Mohammed El Ghzaoui ·
Sudipta Das · Trupti Ranjan Lenka ·
Arindam Biswas *Editors*

Terahertz Wireless Communication Components and System Technologies

Springer

Terahertz Wireless Communication Components and System Technologies

Mohammed El Ghzaoui · Sudipta Das ·
Trupti Ranjan Lenka · Arindam Biswas
Editors

Terahertz Wireless Communication Components and System Technologies

Springer

Editors
Mohammed El Ghzaoui
Faculty of Sciences
Sidi Mohamed Ben Abdellah University
Fez, Morocco

Trupti Ranjan Lenka
Department of Electronics
and Communication Engineering
National Institute of Technology Silchar
Silchar, Assam, India

Sudipta Das
Department of Electronics
and Communication Engineering
IMPS College of Engineering
and Technology
Malda, West Bengal, India

Arindam Biswas
School of Mines and Metallurgy
Kazi Nazrul University
Asansol, West Bengal, India

ISBN 978-981-16-9181-2 ISBN 978-981-16-9182-9 (eBook)
https://doi.org/10.1007/978-981-16-9182-9

This Springer imprint is published by the registered company Springer Nature Singapore Pte Ltd.
The registered company address is: 152 Beach Road, #21-01/04 Gateway East, Singapore 189721, Singapore

Preface

The prime objective of this book is devoted to feature the research developments in the design aspects of advanced components and systems for terahertz wireless technologies. This field of research is becoming quite popular today. Indeed, many THz components have been developed and the research field is still expanding. This is due to that the terahertz communications have a higher frequency than the microwaves and millimeter waves used so far in wireless networks, and therefore, terahertz technology will be the solution to meet the increasing demand for bandwidth. However, this high frequency leads to an increase in complexity to develop THz components. For that reason, the scientific community is intensifying research in the development of THz components and of course its vast applications for the betterment of civilization through the best utilization of advanced technology.

This book gathers scientific and technological innovations and advancements already developed or underdevelopment in the academic, industry, and research communities. This title would involve fundamental ideas and advancements in the terahertz technology covering communication techniques that can be used for THz system, terahertz VCO design, THz detection techniques, antennas for THz system, quantum confined THz materials, micromachining and measurements of THz waveguide components, THz communication system, and terahertz wave source design. In this book, the methodologies for the design of terahertz components and system technologies including emerging applications are discussed. The chapter contents are expected to be based on theoretical, methodological, well-established, and validated empirical work dealing with different topics in the terahertz domain. This book covers a very broad audience ranging from basic sciences to experts and learners in engineering and technology.

The book will be an ideal choice for undergraduate, master's degree, research students, microwave engineers, biomedical engineers, electronics and electrical

engineers interested in fundamental and key advancements in THz science and technology.

Fez, Morocco — Mohammed El Ghzaoui
Malda, West Bengal, India — Sudipta Das
Silchar, Assam, India — Trupti Ranjan Lenka
Asansol, West Bengal, India — Arindam Biswas

Contents

Terahertz VCO Design for High-Speed Wireless Communication Systems

Abdelhafid Es-Saqy, Maryam Abata, Mohammed Fattah, Said Mazer, Mahmoud Mehdi, Moulhime El Bekkali, and Catherine Algani

Abstract The enormous evolution of the IoT and its applications requires highly secure communication with high data rates and high bandwidth. However, current wireless communication systems, based on microwave and millimeter frequencies, are not able to meet these requirements. For this reason, several actors propose the migration to terahertz frequencies. In this chapter, we present the THz domain and its potential applications, we present the impact of the use of THz in 6G, and finally we propose the study and design of a terahertz VCO for the THz band applications. The circuit is designed based on the pHEMT transistor from the United Monolithic Semiconductors foundry. Simulation results show that the oscillation frequency is around 104 GHz, the output power is −11.127 dBm.

Keywords 6G · Terahertz communication · Voltage-controlled oscillator VCO

A. Es-Saqy (✉) · M. Abata · S. Mazer · M. E. Bekkali
AIDSES Laboratory, Sidi Mohamed Ben Abdellah University, Fez, Morocco
e-mail: abdelhafid.essaqy@usmba.ac.ma

M. Abata
e-mail: maryam.abata@usmba.ac.ma

S. Mazer
e-mail: said.mazer@usmba.ac.ma

M. E. Bekkali
e-mail: moulhime.elbekkali@usmba.ac.ma

M. Fattah
Moulay Ismail University, Meknes, Morocco

M. Mehdi
Microwaves Laboratory, Lebanese University, Beirut, Lebanon

C. Algani
ESYCOM Lab, University Gustave Eiffel, CNRS, Le Cnam, Paris, France

M. El Ghzaoui et al. (eds.), *Terahertz Wireless Communication Components and System Technologies*, https://doi.org/10.1007/978-981-16-9182-9_1

1 Introduction

One of the main objectives of communication systems is to be able to transmit data at the highest possible rates. In fact, the continuous increase in data rates in wireless communication systems, for both business and private users, is leading to a significant evolution of the bandwidths used. However, the growing user demand for high-speed wireless communication already exceeds the capabilities of current networks.

In order to overcome this challenge, it is necessary to consider the integration of communication systems based on terahertz (THz) carrier frequencies. These frequencies are sufficiently high to support data rates greater than a hundred gigahertz [1]. On the other hand, the THz beam is more diffractive and less attenuated by dry, non-metallic objects than infrared, which is an advantage for high-speed indoor wireless communication [2, 3]. In addition, short wavelengths require very small antenna sizes [4], which is of great importance in medical imaging and in any application requiring thin materials. However, the main difficulty is to manufacture compact, high performance, and reasonably priced sources, as well as THz-sensitive, integrable, and robust detectors [4–6].

The design of sources for THz communication systems is a major challenge. THz sources are the most difficult components to design and manufacture. There are several techniques for generating THz signals, including Resonant Tunneling Diode [7–9], Photomixer [10–12], On-Chip Antenna using the Metasurface notion [13], and other techniques [14]. The development of the performance of THz sources and detectors will allow the evolution of many fields such as pharmaceutical industry [15], medicine and biology [16], astronomy [17, 18], imaging and spectroscopy [19, 20], giga-bit wireless communication systems [1, 21–23], detection of explosives and weapons [24], and other applications in the field of security and quality control [25], where the THz radiations play a highly important role.

In the field of communication, several research institutes, and industrialists, have been studying the terahertz wave for the past ten years. The goal is to demonstrate that the THz domain can be used for higher speed communication [3]. Several papers covering the different aspects of this subject (communication sources and detectors, modulation systems, wireless communication measurements) are available [23, 26, 27].

In this chapter, we present the THz domain and its different applications. Next, we focus on the development and integration of a high spectral purity and high output power VCO, for wireless THz communication.

2 Terahertz Domain

The THz band, which includes frequencies between 100 GHz and 10 THz [28], i.e., wavelengths between 0.03 and 3 mm, is situated between microwaves and infrared. Actually, THz radiation marks the limit between two physical domains: electronics

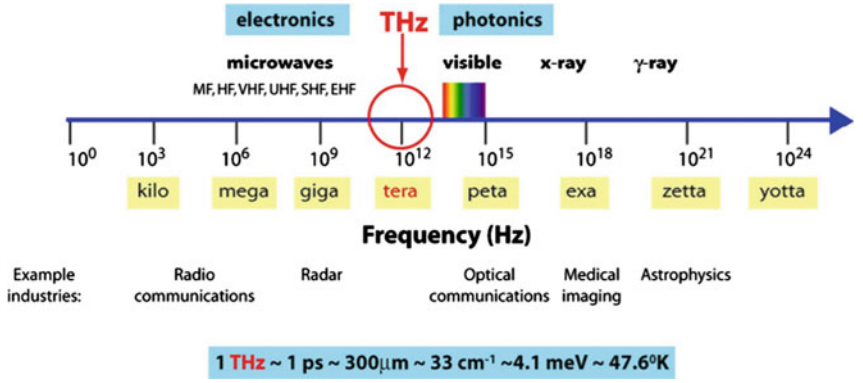

Fig. 1 Representation of the spectrum of electromagnetic waves as a function of frequency

for microwaves and millimeter waves, and optics for infrared (Fig. 1). The importance of THz radiation lies in its four main characteristics [29]:

- They are radiation of very low energy (1 THz $\equiv$ 4.13 meV one million times weaker than X-rays). This low energy has no ionizing effect on biological tissues.
- Have the property of being very penetrating in dielectric or poorly conducting materials.
- Allow the identification of several chemical species, because of their chemical signatures, which characterize each species after interaction with THz waves.
- Have the particularity of being absorbed by polar liquids like water. This feature highlights the potential of THz radiation in many applications and fields.

The THz range represents a very interesting spectral coverage for many applications. In the following paragraph, we give some examples of these applications.

3 THz Radiation Applications

Terahertz (THz) radiation, which ranges from 300 GHz to 30 THz for opticians and between 100 GHz and 10 THz for electronics specialists, has been extensively studied and is about to revolutionize our daily lives by offering a multitude of valuable applications. In every field of activity, THz waves play an increasing role. This section briefly presents the different applications of THz waves.

3.1 THz Spectroscopy

THz spectroscopy is among the most widely used techniques in the biomedical field [19, 30]. Using this technique, chemical analyses can be performed to identify species and molecules present in a sample. This technique also allows the study of the dielectric properties and electrical conductivity of materials [15, 20]. Furthermore, this spectroscopy has the advantage of interacting directly with the vibrational and rotational states of the molecules. Compared to those observed in the ultraviolet, visible spectrum, or infrared, the THz spectroscopy technique provides a complementary signature and fingerprint of the molecule under study [31]. This allows this technique to identify dangerous chemical substances that are difficult to identify with other fields, such as explosives, drugs [15], and other illegal substances. For example, THz spectroscopy can detect substances that are difficult to identify in other fields, such as hydrogen disulfide (H_2S_2) and other illegal substances.

A quick, precise, and efficient qualitative and quantitative technique for studying chiral substances, substances with chiral or asymmetric centers in their structure, proposed by the authors of the paper [32]. The method uses the linearly polarized terahertz spectroscopy.

3.2 Medical Applications

The THz radiation will be the basis for several medical applications, such as the identification of the structural state of proteins, the diagnosis of diseases, and others. In fact, THz radiation is characterized by the frequencies between 100 GHz and 10 THz, i.e., wavelengths between 30 nm and 3 mm, wavelengths that are shorter than those of microwaves, which provides a lateral resolution of 10 μm to be obtained using Optical Rectification Terahertz Imaging (ORTI) technique [33]. The time-domain spectroscopy technique, for example, can provide an absorption spectrum over a band from 100 GHz to 4 THz with a spectral resolution of a few GHz [34, 35].

Furthermore, THz radiation, characterized by its low non-ionizing energy per photon, is safe for biological media, making it more attractive for biological and medical applications [34]. THz radiation seems to be a very favorable choice for the study of living organisms, as it is very low energy radiation (4.13 meV for a frequency of 1 THz) and therefore non-destructive.

3.3 Quality Control and Monitoring for Safety

The properties and performance of THz radiation have made it attractive in the field of safety and quality control [29]. In the pharmaceutical industry, the THz radiation allows the better understanding of the quality and performance of the delivery

mechanisms of active drug ingredients. In fact, the THz radiation penetrates easily through the plastic or polymers used in the pharmaceutical industry and allows the analysis of the active ingredients of most drugs.

In the industrial field, THz waves can be used for the inspection of material or product defects, as well as for the detection of internal defects in encapsulated or packaged products, and the control of purity and contamination of materials such as metal, glass.

In the field of security surveillance, Terahertz radiations provide a key function in the detection of drugs, explosives, dangerous chemical species, and chemical and biological agents. Indeed, each chemical species has its own signature when interacting with THz radiation, so it can be identified from its fingerprint. Furthermore, THz waves can detect these potentially dangerous materials even when they are isolated in a package or hidden in clothing [29].

3.4 Astronomy and Earth Science

Half of the total luminosity in space is in the THz region [36]. Therefore, the THz radiation has long been, and certainly always will be, of interest to astronomers. Thanks to the resources deployed by large organizations such as NASA, THz radiations play a key role in the study and monitoring of the Earth's environment [27]. For example, a laser emitting a THz wave with a 2.5 THz frequency, whose role is the measure of the concentration and distribution of chemical species constituting ozone (from the hydroxyl radical (OH–), a critical component in the ozone cycle), installed on the AURA satellite, whose role is to collect data, was launched by the NASA in 2004. The measurements and data collected will allow us to understand the importance of chemical species in the destruction of ozone in the stratosphere [37].

On the other hand, the AKARI satellite, launched in February 2006, monitors the frequency band between 1.6 and 176 THz, which corresponds to the wavelength range from 1.7 to 180 μm. This has provided information for understanding the formation of galaxies and their evolution over time, as well as for studying the processes of star formation and planetary systems [38].

3.5 THz Communication

Currently, several billion machine-to-machine and IoT communications are needed to meet both the requirements of industry for the development of other technologies, like autonomous cars, smart homes and cities, and E-health services [39], and the requirements of private users of wireless communication; however, the microwave frequency band will be fully occupied over time [40]. The International Telecommunication Union (ITU) has identified five frequency bands for the deployment of 5G networks, launched in 2020: [24.25–27.5 GHz], [37–43.5 GHz], [45.5–47 GHz],

[47.2–48.2 GHz], and [66–71 GHz] [41]. The International Telecommunication Union's goal for 5G wireless communications, in addition to high spectral efficiency and improved coverage, is to achieve throughput in the range of 10 Gb/s for mobile users and connectivity to AI devices, while 5G users need data rates of 5 Gb/s for low mobility and 50 Gb/s for high mobility [42]. However, these new frequencies (millimeter frequencies) will only provide access to about 7 GHz per sub-band. Also, the bandwidth of circuits operating in the millimeter wave band remains limited, generally capped at 10 or 15% around the center frequency. Therefore, an increase in the operating frequency beyond 100 GHz becomes unavoidable to achieve a data transfer rate of several tens of Gbps.

The THz frequency band, which is both the optics of long wavelengths (far infrared) and the electronics of very high frequencies (at the limit of the intrinsic capacities of transistors), may be a very good choice for tomorrow's communication; therefore, the THz frequency range has been the focus of attention for several years now in response to the problem of wireless communications.

4 Impact of THz on 6G Wireless Communication

The 5G network, with its additional new techniques, such as millimeter wave, massive MIMO, beamforming, small cells, and full duplex, will offer revolutionary new features compared to previous generations. Nevertheless, the explosive growth in the number of connected systems could overcome the capabilities of 5G wireless networks. Some recently developed applications, such as virtual reality systems, are required to go beyond 5G because they need a minimum data rate of ten Gbps, which exceeds the capacity of 5G systems [43]. In addition, high-definition video, ultra-high-definition (UHD) devices, and 3-D video are becoming increasingly valuable for mobile users. Uncompressed UHD video can achieve 24 Gb/s data rate, while uncompressed 3-D video with UHD can achieve 100 G/ps [26].

Research into the use of THz radiation in 6G wireless networks has become a daily occupation for researchers and players in the telecommunications field. This technology will revolutionize not only communication systems and their applications, but also business, personal life, lifestyle, and thus society [44]. To meet the expectations of the intelligent information society of 2030. China has launched the "Broadband Communications and New Networks" project for 2030 and beyond. The European Commission's Horizon 2020 program has sponsored multiple B5G projects, like TERRANOVA; a project that aims to develop architectures and technologies capable of delivering optical network quality of experience in 6G wireless communication networks [45]. In the USA, the FCC has already launched studies of 6G networks, and the THz band has already opened. For the FCC, frequencies beyond 5G are reserved for 6G. In Japan, the first 6G projects have already been launched in 2020 [46]. Finland organized the first global summit on 6G wireless technology and launched the 6Genesis project, the first 6G project. The project supports the development of several aspects of wireless communication [47]. The International

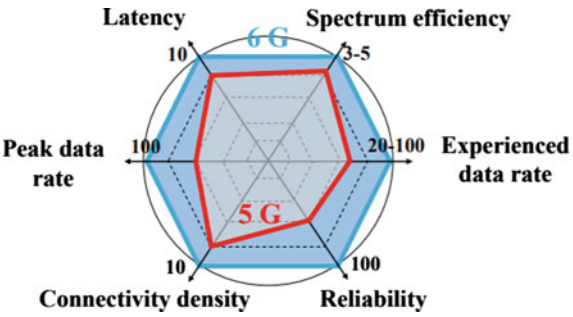

Fig. 2 6G performance compared to the 5G performance

Telecommunication Union (ITU) has established the Focus Group on Network Technologies 2030. It is expected that these new wireless communication networks will improve data rate up to 1 Tbps, reduce latency down to 0.1 ms, increase spectral efficiency above 100 bps/Hz, and provide a huge connectivity density of more than 103 devices per 100 m^2 with a reliability that exceeds 99.9999% (Fig. 2) [45]. And to achieve these goals the use of the THz band is essential for 6G.

5 VCO Design for THz Band

Various electronic and/or photonic systems and technologies have been developed to achieve the first demonstrations of THz communication. Due to the limitation of the operating frequency of the transistors developed by different foundries, most of the published works in the literature propose photonic solutions. Recently, electronic techniques are being developed, and our work is part of the development of an efficient wireless communication system for the terahertz frequency band.

Due to the behavior of passive elements at high frequencies, and the limited cut-off frequency for transistors, the VCO presents one of the most difficult blocks to design in a transceiver system. In this section, we propose the study and design of a VCO, capable to generate a signal with frequencies around 104 GHz.

For the design of a local oscillator that delivers a high-power signal with minimal phase noise, we have opted for the pHEMT (pseudomorphic High Electron Mobility Transistor) of the PH15 process from the UMS foundry. It is characterized by a transition frequency fT = 110 GHz and a gate length of 0.15 μm [48]. In this regard, considering the limitation of the operating frequency of most of the transistors developed so far, we have focused in this chapter on the choice of a structure that favors the second harmonic (Fig. 3). It consists of a LO (Fig. 4) whose fundamental oscillation frequency is 52 GHz and a bandpass filter (Fig. 7), whose passband is around 104 GHz.

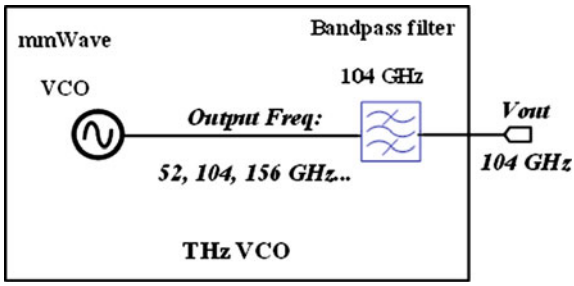

Fig. 3 6G terahertz VCO architecture

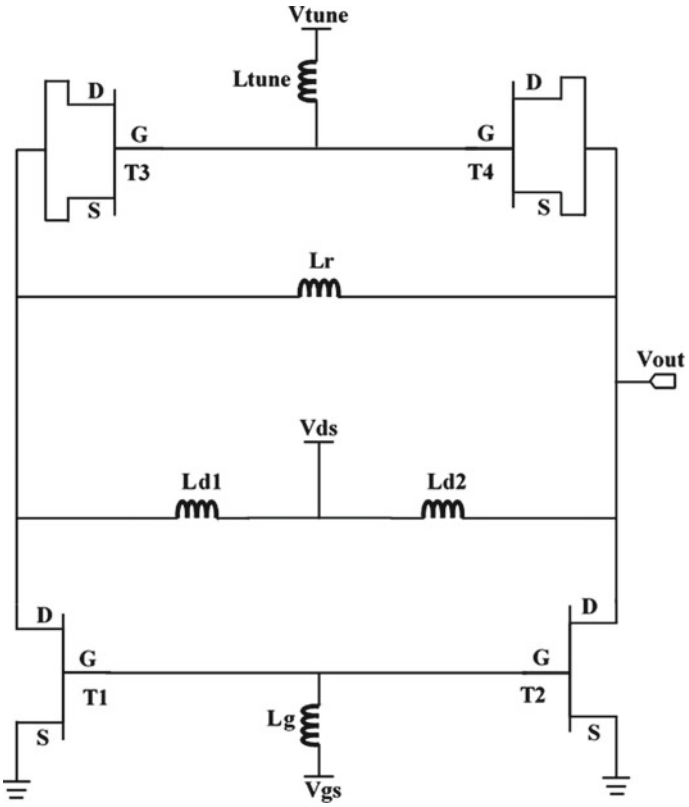

Fig. 4 Circuit of the mmWave voltage controlled oscillator

5.1 mmWave VCO

As shown in Figs. 4 and 5, this is a balanced Colpitts structure based on a pHEMT [39]. The oscillation frequency can be varied by varying the control voltage vtune.

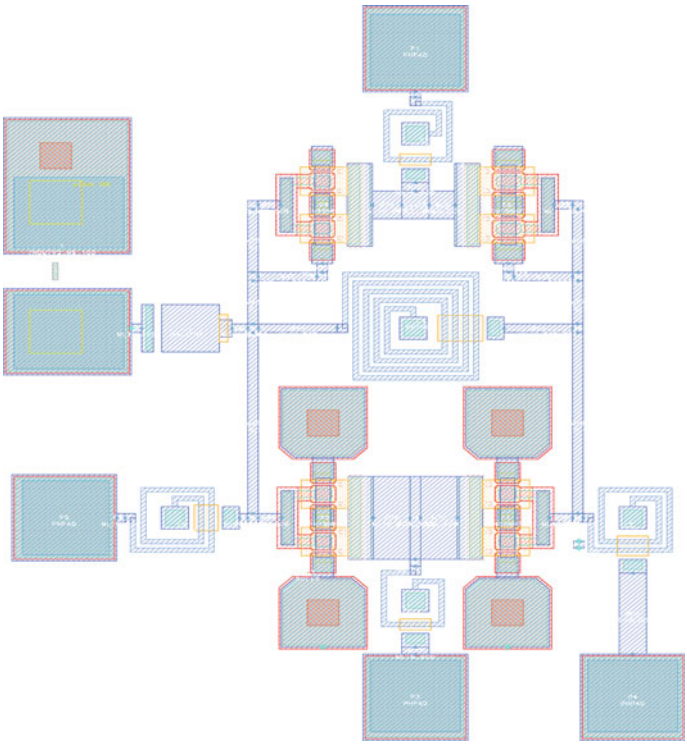

Fig. 5 Layout of the mmWave voltage controlled oscillator

The simulation shows that the power at the fundamental harmonic is −2.768 dBm, and at the second harmonic it is −11.507 dBm (Fig. 6).

5.2 Bandpass Filter

The filter is studied in detail in the paper [49]. Its role is to favor the second harmonic and reject the fundamental and other unwanted harmonics. To accomplish this task, the filter must have a flat frequency response around 104 GHz with a rapid gain drop in the attenuated band. The electrical circuit of the filter is shown in Fig. 7, and the layout is shown in Fig. 8. Actually, the filter is obtained by cascading a low-pass filter, a high-pass filter, and an L4 choke connected with the low-pass filter to perform the rejection. By cascading these two filters, we naturally obtain a bandpass filter, whose passband is the intersection of the passbands of the two filters. Table 1 shows the characteristic values of each component.

The transmission coefficients (S12 and S21) and reflection coefficients (S11 and S22) are presented below. Figures 9 and 10 show that the transmission coefficients

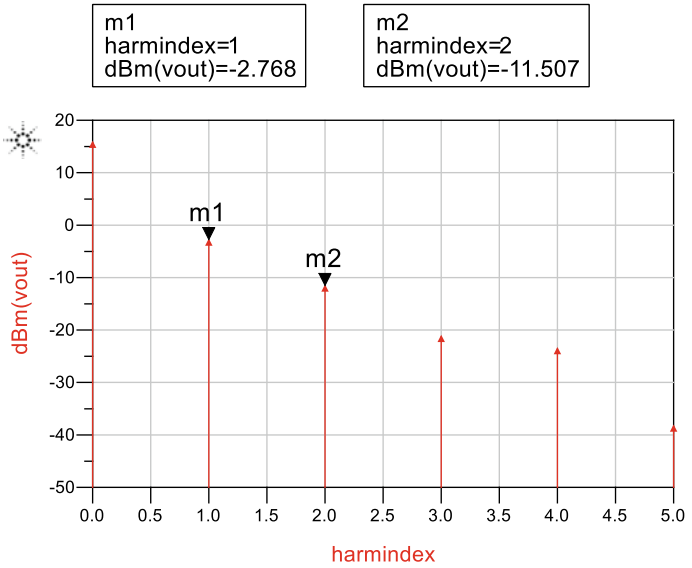

Fig. 6 mmWave VCO output power level for a tuning voltage of 2 V

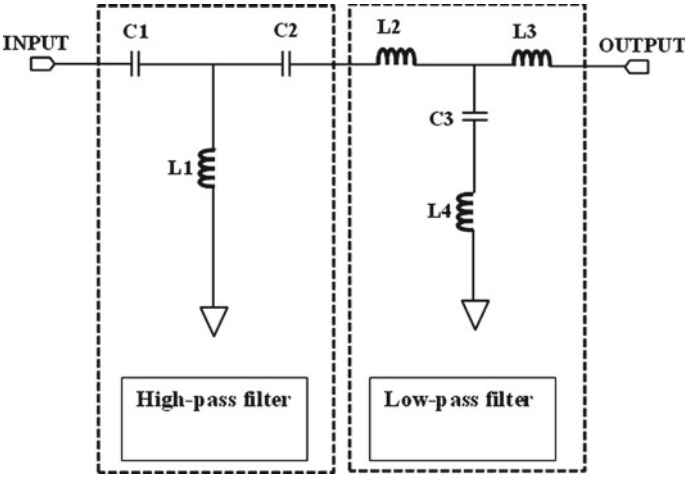

Fig. 7 Circuit of the bandpass filter

have a maximum value at the 104 GHz frequency; it is of the order of −0.542 dB. However, the reflection coefficients (Figs. 11 and 12) have a minimum value at this frequency, −40.25 and −23.49 dB for S11 and S22, respectively.

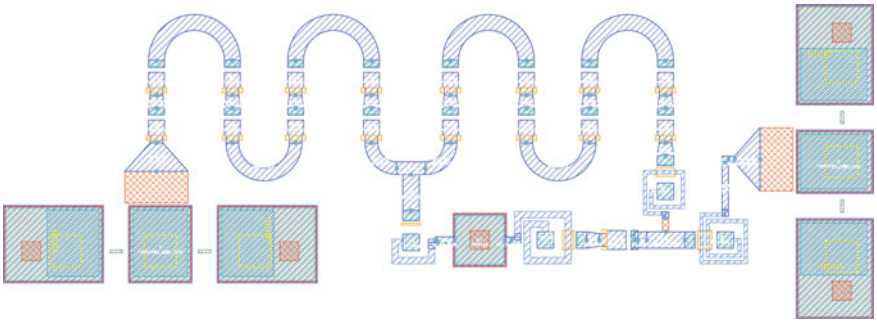

Fig. 8 Layout of the bandpass filter

Table 1 The characteristic values of the passive components forming the bandpass filter

	Parameters	Values
High pass filter	C1	0.017 pF
	C2	0.046 pF
	L1	0.006 nH
Low pass filter	L2	0.025 nH
	L3	0.08 nH
	C3	0.365 pF
Inductance	L4	0.0244 nH

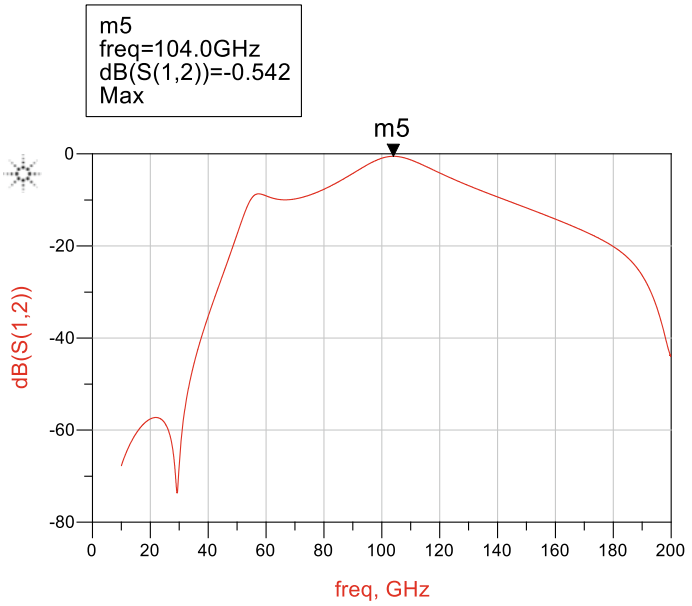

Fig. 9 Transmission coefficient S12 of the bandpass filter

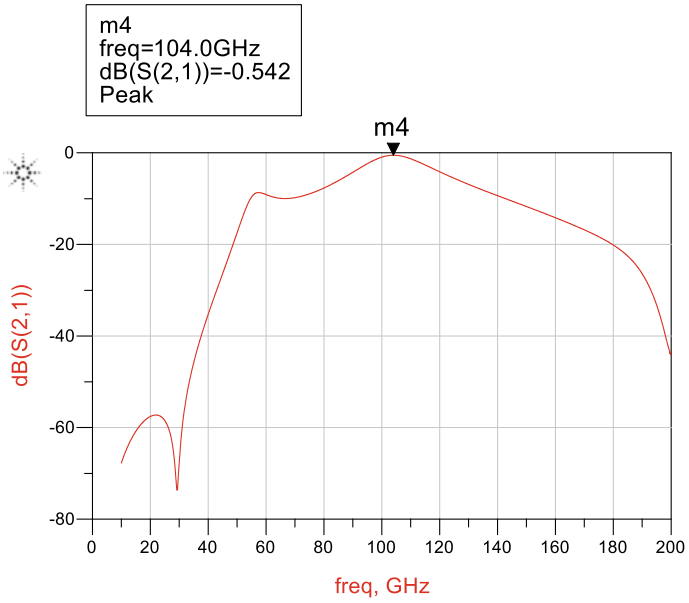

Fig. 10 Transmission coefficient S21 of the bandpass filter

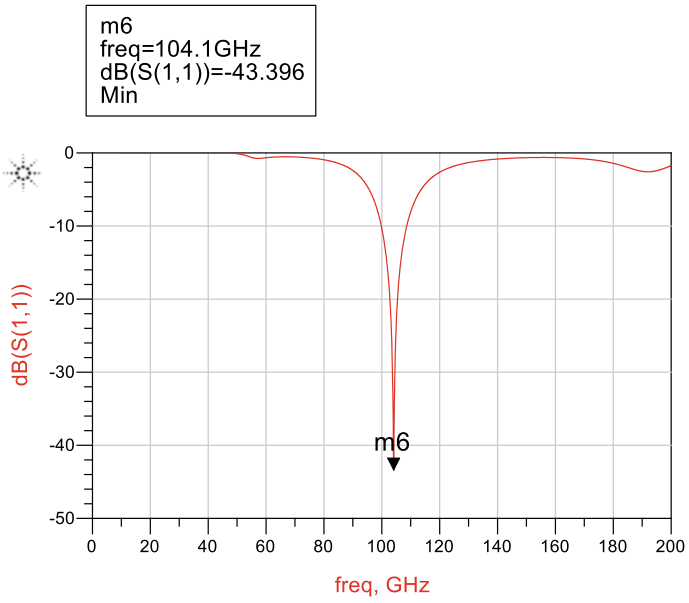

Fig. 11 Reflection coefficient S11 of the bandpass filter

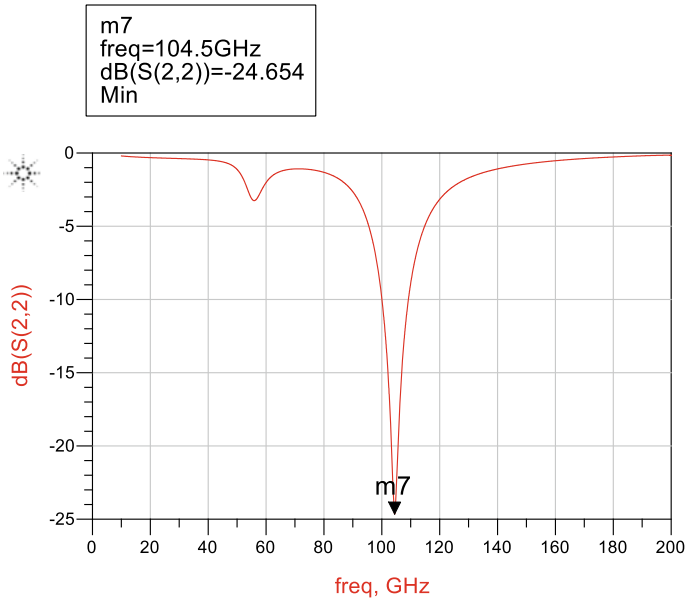

Fig. 12 Reflection coefficient S22 of the bandpass filter

5.3 THz VCO

To overcome the limitation of the operating frequency of the transistors, we propose to highlight the second harmonic from a VCO operating in millimeter band. The cascading of a VCO with an oscillation frequency of 54 GHz, and a bandpass filter with a passband around 104 GHz, has allowed us to enhance the second harmonic of the VCO output spectrum. As we can see in Fig. 13, the fundamental harmonic is attenuated by 19.02 dB: −2.768 dBm before the insertion of the filter, versus −21.792 dB after. However, since the transmission coefficient of the filter is maximum at 104 GHz, the power of harmonic present at this frequency is −11.127 dBm. Compared to most results in the literature, this architecture offers considerable output power.

6 Conclusion

In this chapter, we have defined the THz domain, we have presented different application areas of THz radiation, then we have cited the positive impact of the use of these waves in 6G networks, then we have proposed an architecture of a voltage-controlled oscillator that operates in the THz band. The principle consists in cascading a VCO, whose oscillation frequency is 54 GHz, and a bandpass filter, whose bandwidth is

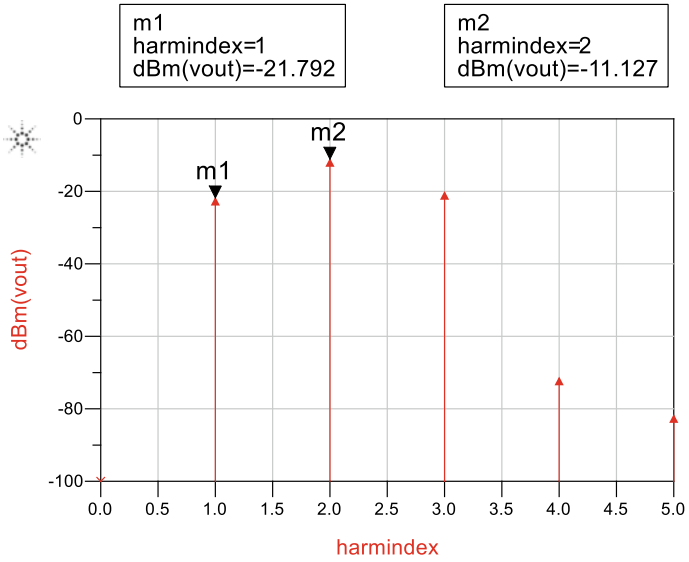

Fig. 13 THz VCO output power level for a tuning voltage of 2 V

around 104 GHz. The result, as previously shown, demonstrates that this technique allows the second harmonic to be favored, and therefore the oscillation frequency of the local oscillator to be doubled, without having to make major modifications to the circuit.

References

1. R. Piesiewicz, M. Jacob, M. Koch, J. Schoebel, T. Kurner, Performance analysis of future multi-gigabit wireless communication systems at THz frequencies with highly directive antennas in realistic indoor environments. IEEE J. Sel. Top. Quantum Electron. **14**(2), 421–430 (2008)
2. C. Jansen et al., Diffuse scattering from rough surfaces in THz communication channels. IEEE Trans. Terahertz Sci. Technol. **1**(2), 462–472 (2011)
3. A. Hirata et al., 120-GHz-band millimeter-wave photonic wireless link for 10-Gb/s data transmission. IEEE Trans. Microw. Theory Tech. **54**(5), 1937–1944 (2006)
4. D. Dragoman, M. Dragoman, Terahertz fields and applications. Prog. Quantum Electron. (2004)
5. M.S. Shur, J.-Q. Lu, Terahertz sources and detectors using two-dimensional electronic fluid in high electron-mobility transistors. IEEE Trans. Microw. Theory Tech. **48**(4), 750–756 (2000)
6. T.W. Crowe, P.W. Porterfield, J.L. Hesler, W.L. Bishop, D.S. Kurtz, K. Hui, *Terahertz Sources and Detectors* (Orlando, Florida, USA, 2005)
7. H. Drexler, J.S. Scott, S.J. Allen, K.L. Campman, A.C. Gossard, Photon-assisted tunneling in a resonant tunneling diode: stimulated emission and absorption in the THz range. Appl. Phys. Lett. **67**, 2816–2818 (1995)
8. R. Izumi, S. Suzuki, M. Asada, in *1.98 THz Resonant-Tunneling-Diode Oscillator with Reduced Conduction Loss by Thick Antenna Electrode*. 2017 42nd International Conference on Infrared, Millimeter, and Terahertz Waves (IRMMW-THz) (Cancun, Mexico, 2017), pp. 1–2

9. K. Kasagi, S. Suzuki, M. Asada, Large-scale array of resonant-tunneling-diode terahertz oscillators for high output power at 1 THz. J. Appl. Phys. **125**(15) (2019)
10. R. Safian, G. Ghazi, N. Mohammadian, Review of photomixing continuous-wave terahertz systems and current application trends in terahertz domain. Opt. Eng. **58** (2019)
11. X. Li, W. Yin, S. Khamas, An efficient photomixer based slot fed terahertz dielectric resonator antenna. Sensors **21** (2021)
12. A. Jumaah, S. Al-Daffaie, O. Yilmazoglu, F. Kuppers, in *Graphene—Nanowire Hybrid Photomixer for Continuous-Wave Terahertz Generation.* 2017 42nd International Conference on Infrared, Millimeter, and Terahertz Waves (IRMMW-THz) (Cancun, Mexico, 2017), pp. 1–2
13. M. Alibakhshikenari et al., Study on improvement of the performance parameters of a novel 0.41–0.47 THz on-chip antenna based on metasurface concept realized on 50 μm GaAs-layer. Sci Rep **10**, 11034 (2020)
14. Z. Vilagosh, A. Lajevardipour, A. Wood, in *Imaging and Lesion Ablation Modeling in Skin Using Freezing to Enhance Penetration Depth of Terahertz Radiation.* Photonics in Dermatology and Plastic Surgery 2019 (San Francisco, United States, 2019)
15. S.K. Mathanker, P.R. Weckler, N. Wang, Terahertz (THz) applications in food and agriculture: a review. Trans. ASABE **56**(3), 1213–1226 (2013)
16. Z. Zhou et al., Multicolor T-ray imaging using multispectral metamaterials. Adv. Sci. **5**(7) (2018)
17. K. Rudakov et al., in *Low-Noise THz-Range Nb Based SIS Receivers for Radio Astronomy*. 2020 45th International Conference on Infrared, Millimeter, and Terahertz Waves (IRMMW-THz) (Buffalo, NY, USA, 2020), pp. 1–2
18. Y. Takashima, S. Sirsi, H. Choi, W.J. Arenberg, D.W. Kim, S.K. Walker, in *All Reflective THz Telescope Design with an Inflatable Primary Antenna for Orbiting Astronomical Satellite for Investigating Stellar Systems (OASIS) Mission.* Astronomical Optics: Design, Manufacture, and Test of Space and Ground Systems III (San Diego, United States, 2021)
19. J.F. Lampin, G. Mouret, S. Dhillon, J. Mangeney, THz spectroscopy for fundamental science and applications. Photoniques **101**, 33–38 (2020)
20. F. Sebastiani et al., Probing local electrostatics of glycine in aqueous solution by THz spectroscopy. Angew. Chem. Int. Ed. **60**(7), 3768–3772 (2021)
21. H.-J. Song et al., 8 Gbit/s wireless data transmission at 250 GHz. Electron. Lett. **45**(22) (2009)
22. T. Nagatsuma et al., in *Giga-Bit Wireless Link Using 300–400 GHz Bands*. 2009 International Topical Meeting on Microwave Photonics (2009)
23. S. Koenig et al., Wireless sub-THz communication system with high data rate. Nat. Photonics **7**(12), 977–981 (2013)
24. M.S. Shamim, M.S., Uddin, M.R. Hasan, M. Samad, Design and implementation of miniaturized wideband microstrip patch antenna for high-speed terahertz applications. J. Comput. Electron. **20**(1), 604–610 (2021)
25. A. Khalatpour, A.C. Paulsen, C. Deimert, Z.R. Wasilewski, Q. Hu, High-power portable terahertz laser systems. Nat. Photonics **15**(1), 16–20 (2021)
26. H.-J. Song, T. Nagatsuma, Present and future of terahertz communications. IEEE Trans. Terahertz Sci. Technol. **1**(1), 256–263 (2011)
27. M.S. Shur, *Terahertz Technology for Space Exploration and Data Communications* (Boston, MA, 2007)
28. A.G. Davies, E.H. Linfield, M.B. Johnston, The development of terahertz sources and their applications. Phys. Med. Biol. **47**(21), 3679–3689 (2002)
29. D.D. Abdelhamid, H. Halima, *Images térahertz et infrarouges pour le contrôle de la qualité intérieure du fruits de dattier* (2020)
30. T. Taniuchi, S. Okada, H. Nakanishi, Widely tunable terahertz-wave generation in an organic crystal and its spectroscopic application. J. Appl. Phys. **95**(11), 5984–5988 (2004)
31. T.R. Globus et al., THz-spectroscopy of biological molecules. Spectrosc. Biol. Mol. **29**, 89–100 (2003)
32. Z. Wang et al., Qualitative and quantitative recognition of chiral drugs based on terahertz spectroscopy. Analyst **12**, 1–12 (2021)

33. G. Soylu, E. Hérault, B. Boulanger, F. Laurell, J.-L. Coutaz, Sub-wavelength THz imaging of the domains in periodically poled crystals through optical rectification. J. Infrared Millim. Terahertz Waves **41**(9), 1144–1154 (2020)
34. A. Ramundo-Orlando, G.P. Gallerano, Terahertz radiation effects and biologic al applications. J. Infrared Milli. Terahz Waves **30**, 1308–1318 (2009)
35. K. Ahi, S. Shahbazmohamadi, N. Asadizanjani, Quality control and authentication of packaged integrated circuits using enhanced-spatial-resolution terahertz time-domain spectroscopy and imaging. Opt. Lasers Eng. **104**, 274–284 (2018)
36. L. Juery, Communication térahertz sans fil à haut débit avec un transistor à haute mobilité électronique comme détecteur. Université Montpellier II—Sciences et Techniques du Languedoc (2014)
37. N.A. Kramarova et al., Validation of ozone profile retrievals derived from the OMPS LP version 2.5 algorithm against correlative satellite measurements. Atmos. Meas. Tech. **11**(5), 2837–2861 (2018)
38. P.H. Siegel, THz instruments for space. IEEE Trans. Antennas Propag. **55**(11), 2957–2965 (2007)
39. A. Es-Saqy et al., 28 GHz balanced pHEMT VCO with low phase noise and high output power performance for 5G mm-wave systems. Int. J. Electr. Comput. Eng. **10**(5), 4623–4630 (2020)
40. A. Es-Saqy et al., 5G mm-wave band pHEMT VCO with ultralow PN. Adv. Sci. Technol. Eng. Syst. J. **5**(3), 487–492 (2020)
41. International Telecommunication Union, *Key outcomes of the World Radiocommunication Conference 2019*. ITU News MAGAZINE 6 (2019)
42. L. Rao, M. Pant, L. Malviya, A. Parmar, S.V. Charhate, 5G beamforming techniques for the coverage of intended directions in modern wireless communication: In-depth review. Int. J. Microw. Wirel. Technol. 1–24 (2020)
43. B. Aghoutane, M. El Ghzaoui, H. El Faylali, Spatial characterization of propagation channels for terahertz band. SN Appl. Sci. **3**, 233 (2021). https://doi.org/10.1007/s42452-021-04262-8
44. S. Nayak, R. Patgiri, 6G communication: envisioning the key issues and challenges. EAI Endorsed Trans. Internet Things **6**(24) (2021)
45. Z. Zhang et al., 6G wireless networks: vision, requirements, architecture, and key technologies. IEEE Veh. Technol. Mag. **14**(3), 28–41 (2019)
46. T. Nakamura, in *5G Evolution and 6G*. 2020 IEEE Symposium on VLSI Technology (2020)
47. M. Kokkonen, S. Myllymäki, H. Jantunen, Focal length of a low permittivity plano-convex lens at frequencies 30–600 GHz. Electron. Lett. **56**(5), 223–225 (2020)
48. United Monolithic Semiconductors, *Take Advantage of Wideband, Low Noise Medium Power UMS PH15 GaAs Process*. Shared Foundry Offer (2018)
49. M. Abata, M. Mehdi, S. Mazer, M. El Bekkali, C. Algani, A V-band two pole high-pass filter for frequency quadrupler design. Int. J. Commun. Antenna Propag. IRECAP **6**(1), 56–60 (2016)

Performance Analysis of EOS and SDI Detectors in THz Band

Mohammed El Ghzaoui

Abstract Over time, scientists and engineers exploited the frequency bands of the electromagnetic spectrum. Starting with the visible spectrum, they gradually developed sources and detectors operating at lower and higher frequencies. First, the frequency band between 0.1 and 30 THz, called terahertz (THz), has not been fully exploited. On the other hand, with the current development of communication and broadband, many parts of the electromagnetic spectrum are saturated. For this, scientists are interested in the terahertz (THz) domain, which, thanks to its high frequencies, offers the possibility of increasing the data rate. Indeed, the transmission of bit rates of the order of one Tbit/s is potentially possible with THz waves, which is advantageous for a wireless communication technology. However, the main difficulty with its use is the lack of compact, powerful, and inexpensive sources and detectors. The objective of this work is to set up detectors that can be used in the THz field. In this chapter, we will begin by describing the terahertz (THz) spectral domain and the applications exploiting this frequency band. We will also list some detectors that currently exist on the market. THz detection methods with equivalent sampling by photoconductive antennas, by electro-optical sampling, and by plasma in air are discussed here. In addition, spectral domain interferometry (SDI) and bolometer detection systems are discussed later in this chapter.

Keywords Terahertz bands · Terahertz detectors · Bolometer detector · SDI for terahertz detection · Photoconductive terahertz detector · Electro-optical detector

1 Introduction

The terahertz frequency domain, commonly called far infrared, extends between 0.3 and 30 THz, i.e., in terms of wavelengths between 1 μm and 1 mm. The rise in frequency to the domain terahertz is interesting because it theoretically allows to have bands passes higher than in microwave [1, 2]. The continuous development of THz radiation detectors and sources is a key point for progress in various fields

M. El Ghzaoui (✉)
Faculty of Sciences Dhar El Mahraz-Fes, Sidi Mohamed Ben Abdellah University, Fez, Morocco

M. El Ghzaoui et al. (eds.), *Terahertz Wireless Communication Components and System Technologies*, https://doi.org/10.1007/978-981-16-9182-9_2

of science and technology, such as security, medical imaging, high resolution radar system, spectroscopy, and telecommunication, … [3, 4]. Since the THz frequency domain lies between microwaves (generated by electronic devices) and medium-IR (where optical sources exist), both domains can be used to create new devices (sources and detectors) capable of operating in THz mode. Thus, electronic or optical skills will be used, directly or indirectly in the generation and detection of the THz signal. Currently, researchers have understood the interests of the neglected THz wave domain, and for about fifteen years tools have emerged. However, the high absorption of terahertz radiation in the atmosphere seems to be a hindrance to its use for long distances [5]. On the other hand, there are still two important obstacles in this field which are the cost and complexity associated with the manufacture of THz detectors.

Nowadays, there are THz wave detectors that operate at cryogenic temperatures and others at room temperature. The latter are interesting because many applications require detectors at room temperature which are very fast and sensitive and which extend their operation in the THz. A number of ambient temperature detectors have been reported for frequencies below 1 THz. Examples include tunneling diodes, field effect detectors, and Schottky diodes [6]. The latter are most sensitive at room temperature for sub-THz frequencies [7]. However, their sensitivities decrease significantly for frequencies above 1 THz since it is limited by the time constant $\tau = RC$. THz detection methods with SDI detection systems, Bolometers, equivalent sampling by photoconductive antennas, electro-optical sampling, and plasma in air are discussed [8, 9].

Initially proposed by AM Song [10], GaAs-based SSDs have already experimentally shown a good sensitivity of 300 V/W at 1.5 THz and this at room temperature [11]. The capabilities of GAN/AlGaN-based SSDs to function as direct detectors and mixers have been experimentally demonstrated [12]. Even though, it has been demonstrated in [13] that heterostructures based on narrow bandgap materials like InAs or InSb are more suitable for applications in THz. In [14] the choice of GaN was made because SSDs based on this material should theoretically be able to generate submillimeter wave oscillations based on the Gunn effect. This will allow the realization of a continuous wave transmitter/detector system THz integrated in the same material and which is simple to realize, compact, operating at room temperature, tunable and powerful but above all to go further in the frequencies and to approach the 1 THz.

Besides, the detection of terahertz waves can be done as in microwave with a heterodyne detection. Antenna can be also a critical element to transmit signal over a communication channel [15, 16]. A THz signal is transposed to microwave frequencies. The signal is multiplied by another signal from a local oscillator so as to transpose the frequency difference to a detection apparatus such as a spectrum analyzer. This type of detection can go up to 3 THz [17]. Another detector is the bolometer which was invented in 1881 by S. Langley. This system makes it possible to measure the amount of electromagnetic energy by absorbing this radiation and measuring the temperature rise. It consists of an absorber whose temperature will increase proportionally to the energy coming from the incident radiation and a thermal bridge

allowing the heat to evacuate to a radiator. A thermometer measures the temperature rise and generates a voltage that can then be amplified to be measured. The bolometer principle can be applied to all frequency ranges of the electromagnetic spectrum which means that a bolometer can detect both a terahertz beam and infrared radiation. A system of filters allowing only terahertz radiation to pass through is therefore necessary to work in this frequency band. The interest of the bolometer is to have a very good sensitivity and a low noise level. The equivalent level of noise NEP 4 is typically of the order of 10e−11W/q (Hz) for a bolometer cooled with liquid Helium. Research is now focused on room temperature bolometers as well as their miniaturization. Such integrable bolometers make it possible to create micro-bolometer grids and therefore real-time imaging to create a real THz camera [18]. Finally, other detectors exist such as the Schottky diode which can detect a signal at 100 GHz. There are also systems based on the Pockels effect that exploit the appearance of birefringence of an electro-optical crystal when it is illuminated by a THz beam. The measurement of this birefringence effect makes it possible to know the intensity of the THz signal.

In this chapter, we will talk about the THz technology, its characteristics opening to fields of application, and different possible ways of detecting THz waves, then, we will introduce the main characteristic of the THz frequency band. After that, we will describe some non-exhaustive methods of detection of THz waves.

2 Handling Terahertz Radiation

The terahertz wave domain is located between infrared and microwave, at the border of optics and radioelectricity, so that the terahertz sources are inspired by those of the two branches of physics. However, their effectiveness here decreases very sharply: this leads to the appearance of the "terahertz gap." This chapter includes a review of different methods for generating and detecting terahertz radiation.

3 Interest, Capacity, and Potential of THz Radiation

THz radiation is attracting increasing interest from public services or industry, and certain application niches are already well targeted. By way of example and to cite the most popular applications, mention should be made of the transmission of data in terahertz mode which will make it possible to increase the currently accessible data rates [19], the study of ultra-fast molecular dynamics [20], the imaging of skin cancer cells [21], the detection of prohibited substances (explosives [22] or narcotic drugs [23]) through their packaging. All those applications need detection method in order to have practical implementation. For that, we will begin by succinctly presenting the different techniques that can be used for the detection of explosives in particular by THz technology. Then we will briefly present the different methods of detection

making it possible to fill the THz gap, showing the interest of THz in the time domain for the detection of explosives.

4 THz Detection Methods

THz detection methods with equivalent sampling by photoconductive antennas, by electro-optical sampling, and by plasma in air are discussed here. In addition, SDI and bolometer detection systems are discussed later in this chapter.

4.1 Equivalent Time Sampling

A THz pulse has a duration of the order of a picosecond, and therefore, standard electronics are not fast enough to sample several points of the same pulse and reconstruct its shape. In this case, equivalent time sampling shall be used. For this, the signal to be measured must absolutely be periodic, which is the case for the pulse THz since it is repeated several times in time (at each pulse of the laser). A delay line is generally used in order to vary the delay between the THz pulse and the probe laser pulse. For each delay, one can sample a different point of the THz wave. By moving the delay line between each measurement, it is therefore possible to sample the waveform THz point by point (see Fig. 1) [24]. Equivalent time sampling is possible because the probe pulse used to sample is much shorter than the THz pulse. Note that this technique is often carried out using a synchronous detection amplifier and that several measurements are then acquired for each position of the delay line in order to reduce the measured noise.

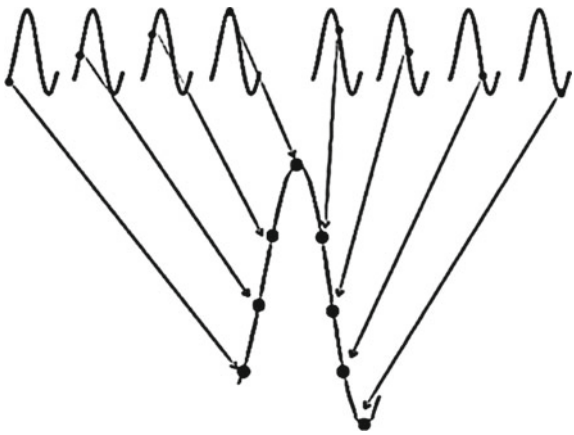

Fig. 1 Equivalent time sampling

4.2 THz Detection by Photoconductive Antennas

The principle of detection by photoconductive antennas is similar to that of generation. As for the generation, a laser pulse (visible or infrared) is sent to the semiconductor component of the antenna, between the two electrodes, in order to reduce its resistance. On the other hand, unlike the generation, no potential difference is imposed between the electrodes; here, it is the incident THz field which acts on the displacement of the photoporters. A current can then pass between the two electrodes. By measuring this current, we can determine the THz field using the expression that binds the two, i.e., [25]:

$$I(t) = \int_{-\infty}^{t} \epsilon\left(t - t'\right) E_{\mathrm{THz}} \mathrm{d}t' \tag{1}$$

where $I(t)$ is the current induced by the THz field, ϵ is the surface conductivity of the semiconductor, and E_{THz} is the electric field THz.

Photoconductive antennas are mainly used for the detection of low and medium high THz electric fields. Indeed, a strong THz electric field could induce nonlinear effects in the semiconductor and the above formula would then no longer be valid [13].

Generally, the detection of terahertz radiation using photoconductive antennas is quite similar to its emission: This time it is the incident terahertz electric field which induces a voltage between two arms of the antenna connected by a transmission line to a current amplifier. Indeed, a laser pulse excites charge carriers beyond the bandgap of the semiconductor photoswitch. The charge carriers are accelerated by the external terahertz field to be detected, such that, still in the context of the Drude model. The current measured by an ammeter is then the convolution of the sampling field $E_S^{(d)}$ and the flow of charge carriers in the detector antenna:

$$I^{(d)}(t) = E_S^{(d)} * \left(en^{(d)}(t)V(t)\right) \tag{2}$$

where $V(t)$ is the speed of the charge carriers and $n^{(d)}$ which is the initial density of the charge carriers in the detector is giving by:

$$n^{(d)}(t) = n_0^{(d)} \exp\left(-\frac{t}{\tau^{(d)}}\right) \tag{3}$$

$\tau^{(d)}$ is the relaxation time of the detector material, possibly different from that of the emitter. Since the electronics associated with the detection antenna are slower than the optical processes, the experimentally measured signal represents a time average of the current $I^{(d)}(t)$.

For the detection of terahertz radiation, a Hertz dipole geometry can be used (Fig. 2) [26]. The semiconductor material is most often low temperature gallium arsenide or silicon on sapphire substrate damaged by radiation (see above for their

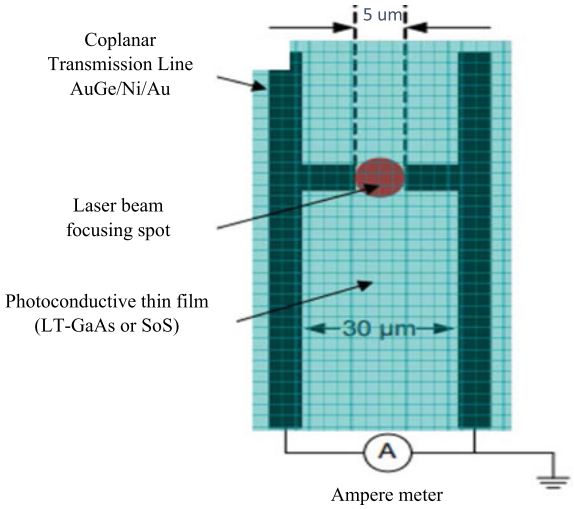

Fig. 2 Diagram of a terahertz detection antenna

electronic characteristics); we use antennas manufactured in LT-GaAs on the technological platform of the IEMN (Villeneuve d'Ascq). The transmission lines form a separation of 5 µm. Once again, a good operation of the circuit can be verified by measuring its resistance which must fall sharply when the antenna is illuminated; typically, it goes from about ten mega-ohms to a few hundred kilo-ohms.

In the same way as in the case of the transmitting antenna, a high-resistivity silicon lens is placed on the surface of the semiconductor and makes it possible to collect more signal. The electric field of the incident beam sampled with a femtosecond laser (typically, 30 mW) induces a current between the two arms of the detector antenna connected by the transmission line to a current preamplifier and a synchronous detection amplifier coupled to a mechanical chopper inserted in the terahertz beam (all three are provided by Stanford Research Systems, USA); this technique makes it possible to considerably increase the signal-to-noise ratio. It should be emphasized that, the current being positive or negative, this type of detector makes it possible to measure the terahertz electric field directly.

The electrooptic detection of the signal is done by the opposite effect to the optical rectification which is the Pockels effect (linear electrooptic effect). The terahertz wave arriving on an electrooptic crystal (typically, ZnTe or GaP) modifies its refractive index and two photodiodes record the difference in intensity of two beams separated by a Wollaston prism, proportional to the terahertz field to be detected. This technique is called optical sampling and was proposed in 1995 by Wu and Zhang [27].

The advantage of this method lies in the low dispersion of certain crystals in the terahertz region. Among the crystals of $LiTaO_3$, $LiNbO_3$, and ZnTe, it is the latter that has shown the most performance for the detection of terahertz pulses. Electrooptic terahertz receivers showed exceptional performance at high frequencies, but could not cover the entire spectral continuum covered by photoconductive receivers. The

reason for this is the absorption of phonons in crystals used in the terahertz region and the strong spectral dependence of electrooptic susceptibility.

4.3 THz Detection by Electro-Optical Sampling

Electro-optical sampling (EOS) is a technique based on the Pockels effect, which is the inverse of optical rectification. The Pockels effect is the induction of birefringence in a nonlinear crystal by a DC wave. In the case of THz detection by electro-optical sampling, it will be approximated that the THz wave is a DC wave since its frequency is much smaller than the visible or near infrared wave used as a probe. The THz wave is therefore sent on a non-centrosymmetric crystal, which induces a change in the polarization ellipsoid in the crystal, and therefore in the ellipsoid of the refractive indices of the crystal. For example, for a ZnTe crystal (or any other crystal with a blende-like structure), the ellipsoid of indices becomes [28]:

$$\frac{\alpha^2+\beta^2+\gamma^2}{n_0^2}+2r_{41}E_\alpha\beta\gamma+2r_{41}E_\beta\alpha\gamma+2r_{41}E_\gamma\alpha\beta=1 \tag{4}$$

where α, β, γ are the spatial coordinates corresponding to the axes of the crystal, n_0 is the refractive index of the crystal without exposure THz, r_{41} is the electro-optical coefficient of the crystal and E_α, E_β, E_γ, are the electric fields THz applied along the axes α, β, γ.

The THz wave thus induces a birefringence in the nonlinear crystal. This birefringence is probed by a second beam sent on the crystal. This beam, visible, or near infrared undergoes a change in polarization during its passage in the birefringent crystal since the optical component parallel to the slow axis of the crystal undergoes a phase delay with respect to the optical component parallel to the fast axis of the crystal [28]:

$$\Delta\varphi=\frac{2\pi L}{d}\Delta n \tag{5}$$

where $\Delta\varphi$ is the induced phase difference, L is the thickness of the crystal d is the central wavelength of the probe pulse and Δn is the difference between the refractive indices of the slow and fast axes of the crystal. For a beam orthogonal to an oriented ZnTe crystal (110) with an electric field oriented along the axis (–110) of the crystal, i.e., the optimal position [29]:

$$\Delta\varphi=\frac{2\pi n_0^3 L r_{41}E_{\mathrm{THz}}}{d} \tag{6}$$

where E_{THz} is the electric field THz.

By measuring the change in polarization, i.e., the phase shift, it is therefore possible to calculate the magnitude of the electric field THz that caused the birefringence. To do this, a balanced detection is generally used. A pair of photodiodes and a Wollaston prism are then used to measure the orthogonal components s and p of the polarization of the laser pulse. The signals from the photodiodes are then directed to a synchronous detection amplifier where they are subtracted and filtered. The difference of the signals is proportional to the THz field provided that the position of the quarter-wave plate of the mounting has been adjusted beforehand so that the difference is zero without a THz field [30]:

$$M = \frac{I_1 - I_2}{I_1 + I_2} = \frac{1}{2}(1 + \sin(\Delta\varphi)) - \frac{1}{2}(1 - \sin(\Delta\varphi)) = \sin(\Delta\varphi) = \Delta\varphi \quad (7)$$

where M is the modulation measured with the photodiodes and I_1 and I_1 are the intensity of photodiode 1 and 2, respectively.

It should be pointed out that $\Delta\varphi \lll 1$ was assumed in order to obtain a linear formula, and therefore, this formula can only be used with small phase differences. By combining Formulas (6) and (7), we obtain:

$$E_{\mathrm{THz}} = \frac{dM}{2\pi n_0^3 L r_{41}} \quad (8)$$

• Over-rotation during electro-optical sampling

It is noted in Formula (7) that the modulation is bounded by -1 and 1 for phase differences of $-\pi/2$ and $\pi/2$, respectively. If the phase difference exceeds $\pi/2$, the modulation decreases instead of increases since it has a sinusoidal behavior. This problem related to electro-optical detection is called over-rotation. Since a large phase difference is usually caused by a high electric field, EOS can only be used for detecting weak THz fields if over-rotation is to be avoided.

There are of course ways to work around the over-rotation problem and detect high THz fields. According to Formula (6), a smaller phase difference can be obtained by using a thinner detection crystal or having a lower electro-optical coefficient. In the first case, it should be known that a THz pulse incident on a crystal always generates reflections, which can also be detected. The thinner the crystal, the closer the reflection is temporally to the main pulse, and therefore, the more it is necessary to reduce the time window of the measurement in order to avoid measuring the reflection. However, a short time window also means a low frequency resolution, which is generally undesirable. In addition, a thinner crystal also means a shorter interaction length of the waves in the crystal, which results in a decrease in the Signal-to-Noise Ratio (SNR). In the second case, it is actually possible to use a crystal with a lower electro-optical coefficient than ZnTe, for example, gallium phosphide (GaP), and with which it is much more difficult to obtain over-rotation. On the other hand, the measured signal-to-noise ratio is then lower.

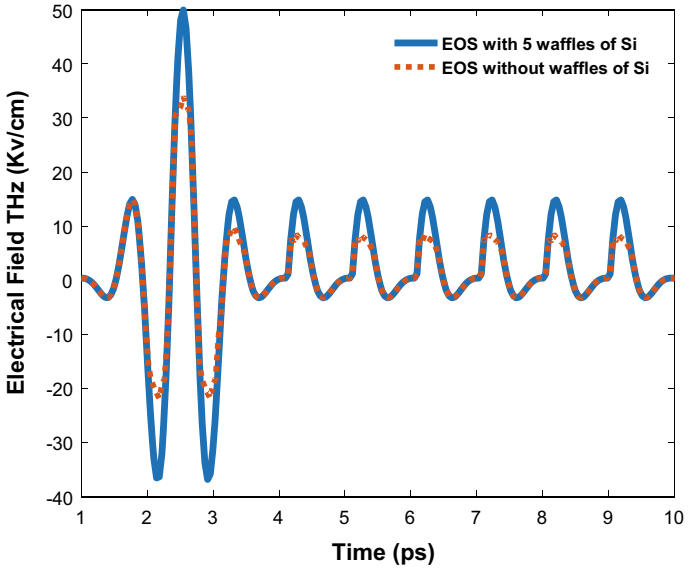

Fig. 3 Over-rotation in a THz pulse measured by EOS

The most common solution to over-rotation is the addition of silicon waffles in the mounting just before the detection crystal (see Fig. 3). Part of the THz pulse (30%) is reflected on each silicon waffle. The goal is to add enough silicon waffles so that the THz field reaching the crystal is both under the over-rotation limit and in the linear regime ($\sin(\Delta\varphi) = \Delta\varphi$). However, adding several silicon waffles may cause some deformations in the detected THz field. In addition, a high THz field can induce nonlinear effects in silicon and the reflection on each waffle is then lower than 30%. Also, multiple THz reflections on the silicon waffles are always at the tail of the main pulse in a measurement, which limits the time acquisition length and therefore the frequency resolution.

Of course, if silicon waffles are added to the assembly, this must be taken into account when calculating the THz field. By also adding the reflection losses on the detection crystal, we obtain:

$$E_{\mathrm{THz}} = \frac{dM}{2\pi n_0^3 L r_{41} \Gamma 0.7^N} \tag{9}$$

where Γ is the transmission coefficient through the detection crystal and N is the number of waffles of Si. Each waffle transmits 70% of the THz wave.

4.4 THz Detection by Plasma in Air

There are two methods of plasma THz detection in air called THz-ABCD. The first is THz Air Breakdown Coherent Detection. The principle is very similar to THz generation by plasma in the air: A femtosecond laser is focused in the air, which generates a plasma whose charges are accelerated. If one sends a THz pulse to be detected on the plasma at the same time (or almost) as the laser pulse, there will be generation of the second harmonic of the laser beam. By detecting this second harmonic using a photomultiplier tube, the THz field can be deduced:

$$I_{2\omega} \propto |E_{2\omega}|^2 \propto \left(W^{(3)} E_\omega E_\omega\right)^2 E_{\mathrm{THz}}^2 \tag{10}$$

where $I_{2\omega}$ is the intensity of the second harmonic of the laser, $W^{(3)}$ is the 3rd order nonlinear coefficient of the plasma, E_ω is the laser electric field, $E_{2\omega}$ is the electric field of the second harmonic of the laser, and E_{THz} is the electric field THz.

Unfortunately, since we only measure the intensity of the second harmonic, we cannot measure the electric field coherently. To achieve consistent detection, a very intense laser intensity must be used. At high pump intensity, the white light generated by the plasma contains a non-negligible second harmonic component that must be considered in the calculation [31]:

$$I_{2\omega} \propto |E_{2\omega}|^2 \propto \left(W^{(3)} E_\omega E_\omega\right)^2 E_{\mathrm{THz}}^2 + 2\left(W^{(3)} E_\omega E_\omega\right) E_{\mathrm{THz}} E_{\mathrm{SH}}^{2\omega} + \left(E_{\mathrm{SH}}^{2\omega}\right)^2 \tag{11}$$

where $E_{\mathrm{SH}}^{2\omega}$ is the electric field of the second harmonic from the plasma.

If the field of the second harmonic coming from the plasma is high enough, the first term of Formula (11) becomes negligible and the intensity detected by the photomultiplier tube is then proportional to the electric field THz, making the detection method consistent. Of course, a drawback is that it is not possible to detect a THz field that is too large (or it is necessary to compensate with the intensity of the pump laser) since the first term of Formula (11) would then no longer be negligible. The second THz method is THz Air Bias Coherent Detection (THz-ABCD). This method requires a lower laser intensity, but an AC electric field must be applied close to the focal point. The intensity detected with a photodetector is then:

$$I_{2\omega} \propto |E_{2\omega}|^2 \left(W^{(3)} I_\omega\right)^2 \left(E_{\mathrm{THz}}^2 + 2E_{\mathrm{THz}} E_{\mathrm{SFI}} + E_{\mathrm{SFI}}^2\right) \tag{12}$$

where E_{SFI} is the alternating electric field imposed on the plasma.

Modulation of the applied electric field makes it possible to use a synchronous detection amplifier in order to measure only the second oscillating term at the frequency of the applied AC signal. An intensity proportional to the electric field THz is thus measured. We then have:

$$I_{2\omega} \propto 2\left(W^{(3)} I_\omega\right)^2 E_{\mathrm{THz}} E_{\mathrm{SFI}} \tag{13}$$

This type of detection makes it possible to improve the bandwidth of the measurement compared with the electro-optical detection seen above. There are also no multiple reflections of the laser on the faces of the electro-optical crystal or the photoconductive substrate, nor any danger of damaging the detector material by too high a laser intensity. On the other hand, the very high laser intensities and the sometimes necessary high voltages are clearly a material limitation.

4.5 Frequency Domain Interferometry THz Detection

Frequency domain interferometry (SDI) is a detection technique used in several fields. A standard assembly based on a Michelson interferometer is shown in Fig. 4. In Fig. 4, a separator blade separates an incident pulse into two pulses. One of the two pulses follows the path of the sample arm while the other follows the reference arm. The two pulses are then recombined by the same separating plate and interfering in a spectrometer.

The principle is first to split in two a beam from a coherent source (often a laser pulse). The first beam is used to probe the sample while the second serves as a reference. In the case presented here, the sample beam is reflected on the sample while the reference beam is reflected on a plane mirror. The two beams are then recombined together and directed to a spectrometer. The spectrometer is typically composed of a diffraction grating, which spatially separates the constituent wavelengths of each of the two beams, followed by an grating of photodetectors, which records the light intensity as a function of the wavelength. Since the beams are coherent, they interfere and the detector therefore measures fringes. After numerical transformation of the

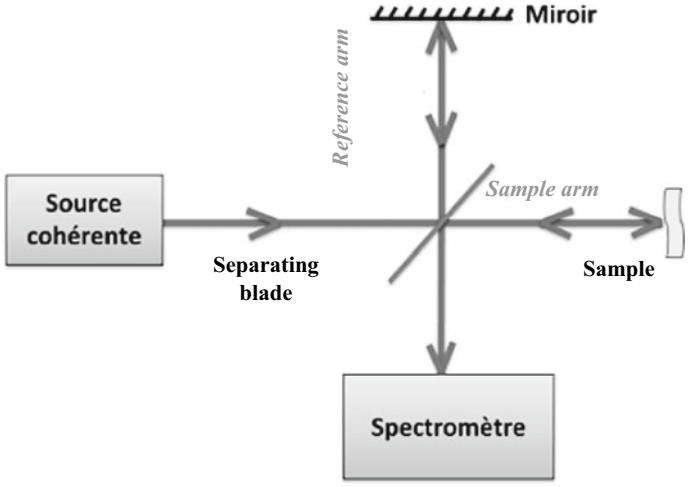

Fig. 4 SDI mounting type

space of wavelengths to the space of wavenumbers ($k = 2\pi\lambda$), the intensity of the fringes can be described by the following formula:

$$I_i(k) = I_p(k) + I_{pr}(k) + 2\sqrt{I_p(k)I_{pr}(k)}\cos(kL + \vartheta_0) \tag{14}$$

where I_i is the intensity of the fringes I_p is the intensity of the pulse reflected on the sample I_{pr} is the intensity of the pulse reflected on the reference, i.e., the mirror k is the wavenumber L is the optical path difference between the sample and reference beams at the spectrometer ϑ_0 is a phase constant.

According to Formula (14), the frequency of oscillation of the fringes is given by the optical path difference between the sample and reference pulses. The frequency can be extracted using a Fourier transform of the interferogram in wavenumber k. It is then possible to deduce therefrom the position of the sample or even the topography of the sample if the latter is displaced laterally between two measurements. SDI detection can be used for several purposes. These include the measurement of small distances at high resolution, atmospheric radar, phase microscopy, and ultrasound imaging of arteries. However, its most common and well-known application is Optical Coherence Tomography (OCT). There are three types of OCT: Time Domain OCT (TD-OCT), frequency Domain OCT (SD-OCT), and frequency swept Source OCT (SS-OCT), which is a variant of SD-OCT.

The SD-OCT mount is the same as shown in Fig. 4. The coherent source is then a broadband infrared source, i.e., it contains a wide frequency range and therefore has a very short coherence length. For this reason, there will be interference between the sample beam and the reference beam only if the optical path difference between the two is smaller or equal to the coherence length of the source. At the spectrometer, instead of observing an infinite number of fringes, we will therefore observe a local interference pattern composed of a finite number of fringes.

Figure 5 illustrates the principle of operation of the SD-OCT. An incident beam on a semi-transparent sample is then reflected by each interface between two different refractive indices. For example, it can be assumed that a first light ray is reflected by the input surface of the sample, a second by an internal structure of the sample, and a third by the output surface of the sample. After being reflected by the sample, these three rays are directed to the spectrometer, where their constituent wavelengths are spatially separated by a diffraction grating. The reference beam also reaches the diffraction grating and then interferes with each of the rays reflected by the sample. Since the optical path traveled by each of the three rays reflected by the sample is different, their optical path difference with the reference beam is also different. The three interference patterns produced will therefore have different oscillation frequencies according to Eq. (14). These three interference patterns are detected and added together by the array of photodetectors. By making the Fourier transform of the total interference pattern, we obtain three peaks corresponding to the three optical path differences, i.e., a depth profile of the sample. A 3D scan of the sample can be obtained by scanning its surface with the sample beam.

OCT in general has been used in a wide range of applications including glaucoma detection, eye tissue movement measurement for eye disease diagnostics, tissue

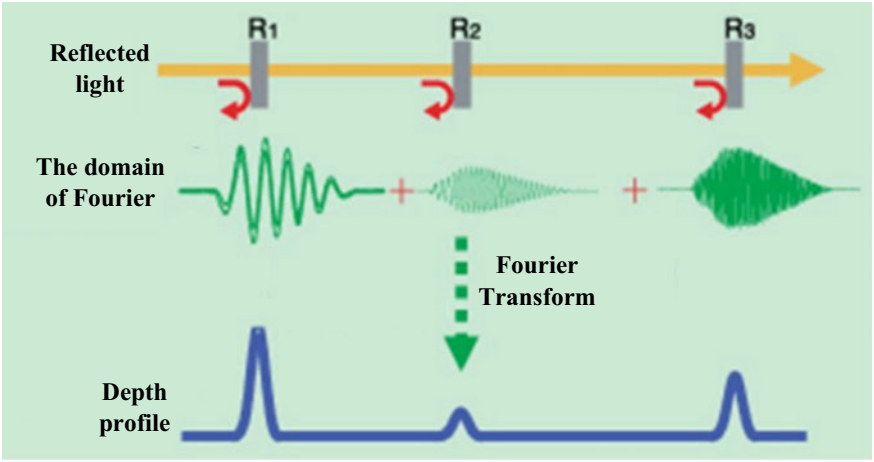

Fig. 5 Principle of operation of the DS-OCT

differentiation, and industrial part metrology [32, 33]. OCT in the frequency domain offers advantages such as better sensitivity and faster acquisition than OCT in the time domain [34].

4.6 Bolometers Detectors

Bolometers are detectors very sensitive to thermal radiation and are among the most widely used infrared detectors in the IR spectrum including the THz frequency range. The detector element is extremely sensitive to temperature change. Their principle of operation is such that the thermal radiation that hits the detector causes a temperature change. This will then lead to a change in resistance which gives access to a variation in the measurement of the voltage across an external reading circuit (Wheatstone Bridge). There are several types of bolometers [35]: • Metallic: the typical metals used in this type are nickel, bismuth, platinum, and titanium. They operate at room temperature and are easily integrated with CMOS technology. They are characterized by low noise, on the other hand, their temperature coefficient is low which decreases their performance.

The semiconductors used amorphous silicon, germanium, and alloys such as SiGe. Their temperature coefficient depends on the manufacturing process but it is of the order of 10 times higher than that of metals. Semiconductor oxides are also used such as GexSi1-xOy or vanadium oxide (V0x). * Hot electron superconductors: For a better bolometer sensitivity, the resistivity of the thermistor material must show a strong temperature dependence. The known high dependence of the resistivity of a superconductor on temperature makes it a natural choice for a thermistor material in bolometers. Note that unlike the other two types of bolometers where the resistance of

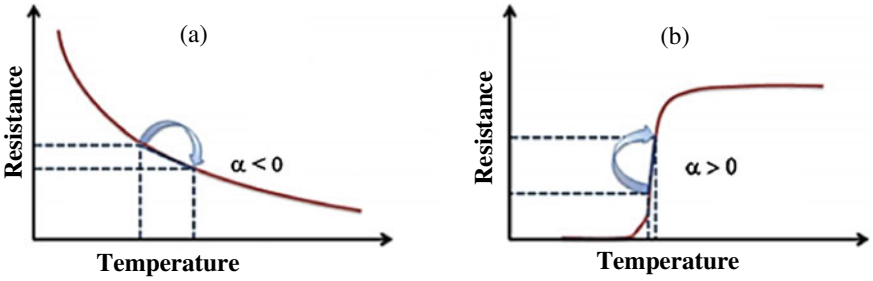

Fig. 6 Resistance variation of **a** semi-conductor, **b** superconductor. α is the variation coefficient of the resistance as a function of temperature

their thermistor decreases with temperature, here the resistance of a superconductor increases with temperature (Fig. 6).

Golay cells and pyroelectrics are the most widely used commercial detectors due to their reasonable sensitivities. On the other hand, their response speeds are too slow (generally of the order of a few milliseconds), and they are very difficult to arrange in matrices which is a handicap for applications such as in imaging; Bolometers although they are capable of detecting frequencies above 2 THz, they require a response time of a few milliseconds, an electrical polarization but also sometimes a cryogenic temperature.

5 SDI Versus EOS Detection

In Sect. 4, we have described several detection methods, the most common of which is electro-optical sampling (EOS). EOS, however, is limited by over-rotation for strong THz fields. While various methods exist for circumventing the over-rotation limit, the latter always have drawbacks such as the reduction of the signal-to-noise ratio, a limited time acquisition length, or the deformation of the detected pulse THz. An alternative electro-optical detection method would therefore be advantageous for the measurement of intense THz fields.

In 2012, Sharma et al. [36] developed a new electrooptic detection method based on an SDI system. The technique makes it possible to measure the phase change undergone by the probe wave when it passes through the electro-optical crystal by interferometry instead of measuring its polarization change with a polarizer.

During THz SDI detection, the probe pulse is temporally divided in half before reaching the detection crystal. The division is carried out using a glass plate: The laser pulse reflects first on the outer face of the glass plate, and then on its inner face, which creates two consecutive pulses. The first pulse reaches the crystal 3 ps before the second pulse. By adjusting the lengths of the probe and THz optical paths, it is possible to obtain that the first probe pulse passes through the crystal before the THz pulse while the second probe pulse passes at the same time as the THz pulse

(see Fig. 7). The first pulse serves as a reference, while the second probe pulse is phase shifted by the birefringent crystal and therefore contains the information to be measured. The two probe pulses are then directed to a spectrometer consisting of a diffraction grating, a cylindrical lens, and a CCD camera. The two probe pulses are diffracted by the grating, after which they interfere together. Fringes are therefore observed on the camera, with an intensity given by the Formula (14). Here, it is the instantaneous phase differences between each of the Fourier components of the two probe pulses that it is desired to extract since they are induced by the THz field and proportional to the latter. Instantaneous phase differences can be extracted as follows:

$$\vartheta = \arctan\left(\frac{\mathrm{Im}(F(I(k)))}{\Re(\mathrm{F(I(k))})}\right) \tag{15}$$

where ϑ is the instantaneous phase difference between the two probe pulses, Im(.) is the imaginary part, $\Re(.)$ is the real part, and $F(I(k))$ is the Fourier transform of the intensity of the fringes $I(k)$ (see Formula (14)).

For the calculation of the instantaneous THz field, the value of the phase shift corresponding to the center frequency of the probe pulse is generally selected. As mentioned in Sect. 4.5 and observed in Fig. 7, the probe pulse is much shorter than the THz pulse, and therefore, it can be approximated that the calculated phase corresponds to a single point of the THz wave. To measure the complete THz wave, the glass plate is placed on a delay line that makes it possible to vary the optical path difference between the probe and THz pulses. For each position of the delay line and therefore for each point of the pulse THz, the phase must be calculated. It is noted that, since the phase is calculated using an inverse tangent function, the result is always between $-\pi/2$ and $\pi/2$. To avoid phase jumps and thus obtain a continuous waveform, a standard phase unwinding algorithm is used.

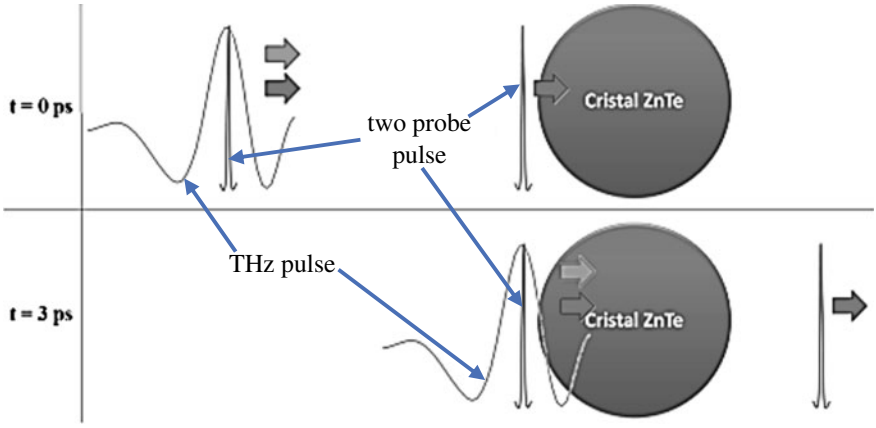

Fig. 7 Synchronization of THz pulses and probe on crystal

During standard electro-optical sampling, it was desired to measure the phase difference between the components s and p of the probe pulse passing through the birefringent crystal. Here, it is rather desired to measure the phase difference between two probe pulses, one having passed through the birefringent crystal and the other having passed through the same crystal but without birefringence. Since the SDI technique is based on interferometry, the maximum detectable phase is theoretically limited by the coherence length of the source. However, the discrete sampling of the interference pattern by the pixels of the CCD camera limits the actual maximum detectable phase to a value lower than this theoretical limit. Indeed, according to Eq. (14), the greater the measured phase, the greater the frequency of oscillation of the fringes becomes. However, according to Nyquist, a signal must be sampled with a frequency at least twice as high as that to be sampled. In other words, an interferogram cannot be sampled if there are too many fringes for the number of pixels in the camera. The maximum phase detectable by the spectrometer is called the depth range. If the spectrometer camera contains N pixels, a maximum of 2 fringes can be sampled according to the Nyquist criterion. In this case, according to Formula (14), we obtain:

$$\Delta_{\text{spectroscopy}} L_{\text{Max}} = 2\pi \frac{N}{2} \tag{16}$$

$$L_{\text{Max}} = \frac{N\pi}{\Delta_{\text{spectroscopy}}} \tag{17}$$

where $\Delta_{\text{spectroscopy}}$ is the spectral range of the spectrometer, L_{Max} is maximum optical path difference detectable, N is the number of pixels of the CCD camera (perpendicular to the fringes).

The spectral range of the spectrometer is chosen as a function of the source used. This is because if the spectral range is too small, part of the spectrum is lost, and if it is too large, the resolution after FFT is reduced. It is therefore established as a criterion that the resolution after FFT must correspond to the axial resolution of the system, i.e., the minimum distance between two objects that can be solved by the spectrometer. Axial resolution is defined as the mid-height width (FWHM) of the source spectrum after FFT. For a Gaussian source, we get [37]:

$$\text{Axial resolution} = \frac{2\lambda_O^2 \ln(2)}{\pi \Delta\lambda_{\text{source}}} \tag{18}$$

where λ_O is the central wavelength of the source and $\Delta\lambda_{\text{source}}$ is the bandwidth of the source.

Since the source used has a wavelength of 790 nm and a bandwidth of 40 nm and the camera has 1024 pixels, the theoretical depth range is 3.53 mm. Considering that a phase difference of 2π corresponds to a wavelength of the laser, the maximum measurable phase difference is therefore 8924π, compared to $\pi/2$ for EOS [36]. Another advantage of the SDI over the EOS is that no synchronous sensing amplifier

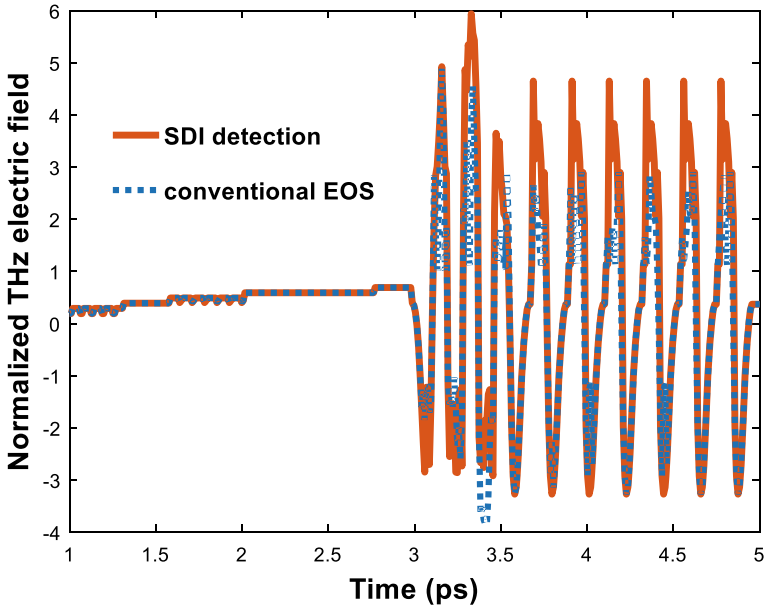

Fig. 8 Terahertz electric field detection using the conventional EOS, and the SDI techniques

is needed, making mounting more accessible. Despite its excellent performance in terms of maximum detectable phase difference, the SDI system also has its drawbacks. The glass is used to temporally separate the probe pulse and limit the temporal acquisition length of the pulse THz. Indeed, the first probe pulse must not be superimposed on the field THz, and therefore, it is possible to acquire only 3 ps of the pulse THz, i.e., the time separating the two probe pulses. The limited time window results in a limited frequency resolution. In addition, the signal-to-noise ratio obtained with SDI detection is much lower than with the standard EOS (see Fig. 8). Sharma et al. [38] attribute a majority of the noise in the signal to mechanical vibrations in the system, in particular the angular vibration of the glass blade. Finally, most of the initial probe pulse is transmitted through the glass slide instead of being reflected there and is therefore not used for detection. The contrast of the fringes on the camera, and therefore the signal-to-noise ratio, is then lower than if 100% of the probe beam were used.

6 Conclusion

In this first chapter, we defined the THz domain and presented its interest thanks to its physical properties. We introduced a number of THz detectors and discussed the pros and cons of each. It is clear that enormous efforts are still to be made and that

recent advances in both electronics and photonics are to be continued even if only by the levels of power/sensitivities achieved by current emitters/detectors. The objective in this work is part of the development of a THz detector with a wide bandwidth, a high response speed, a high cut-off frequency, and above all the ability to operate at room temperature.

References

1. M. El Ghzaoui, S. Das, in *Data Transmission with Terahertz Communication Systems*, ed. by A. Biswas, A. Banerjee, A. Acharyya, H. Inokawa, J. Roy. Emerging Trends in Terahertz Solid-State Physics and Devices (Springer, Singapore, 2020). https://doi.org/10.1007/978-981-15-3235-1_9
2. M. EL Ghzaoui, J. Mestoui, A. Hmamou, S. Elaage, Performance analysis of multiband on–off keying pulse modulation with noncoherent receiver for THz applications. Microw. Opt. Technol. Lett. 1–6 (2021). https://doi.org/10.1002/mop.33051
3. D. Molter, J. Klier, S. Weber, M. Kolano, J. Jonuscheit, G. von Freymann, Two decades of terahertz cross-correlation spectroscopy. Appl. Phys. Rev. **8**, 021311 (2021). https://doi.org/10.1063/5.0037395
4. K. Ahi, S. Shahbazmohamadi, N. Asadizanjani, Quality control and authentication of packaged integrated circuits using enhanced-spatial-resolution terahertz time-domain spectroscopy and imaging. Opt. Lasers Eng. **104**, 274–284 (2018). https://doi.org/10.1016/j.optlaseng.2017.07.007
5. B. Aghoutane, M. El Ghzaoui, H. El Faylali, Spatial characterization of propagation channels for terahertz band. SN Appl. Sci. **3**, 233 (2021). https://doi.org/10.1007/s42452-021-04262-8
6. L. Lv, J. Yu, M. Hu, S. Yin, F. Zhuge, Y. Ma, T. Zhai, Nanoscale, Design and tailoring of two-dimensional Schottky. PN Tunneling Junctions Electron. Optoelectron. **13**, 6713 (2021). https://doi.org/10.1039/D1NR00318F
7. L. Liu, J.L. Hesler, H. Xu, «A broadband quasi-optical terahertz detector utilizing a zero bias Schottky diode.» IEEE Micr. Wirls. Comp. Lett. **20**, 504–506 (2010)
8. N.M. Burford, M.O. El-Shenawee, Review of terahertz photoconductive antenna technology. Opt. Eng. **56**(1), 010901 (2017). https://doi.org/10.1117/1.OE.56.1.010901
9. H. Murakami, K. Mizui, M. Tonouchi, High-sensitivity photoconductive detectors with wide dipole electrodes for low frequency THz wave detection. J. Appl. Phys. **125**(15), 151610 (2019). https://doi.org/10.1063/1.5080750
10. A.M. Song, M. Missous, P. Omling, A.R. Peaker, L. Samuelson, W. Seifert, Unidirectional electron flow in a nanometer-scale semiconductor channel: a self-switching device. Appl. Phys. Lett. **83**, 1881–1883 (2003)
11. C. Balocco, S.R. Kasjoo, X.F. Lu, L.Q. Zhang, Y. Alimi, S. Winnerl, A.M. Song, Room-temperature operation of a unipolar nanodiode at terahertz frequencies. Appl. Phys. Lett. **98**, 223501 (2011)
12. J. Torres, P. Nouvel, A. Penot, L. Varani, P. Sangaré, B. Grimbert, M. Faucher, G. Ducournau, C. Gaquière, I. Iniguez-de-la-Torre, J. Mateos, T. Gonzalez, Nonlinear nanochannels for room temperature terahertz heterodyne detection. Semicond. Sci. Technol. **28**, 125024 (2013)
13. I. Iñig, H. Rodilla, J. Mateos, D. Pardo, A.M. Song, T. González, Terahertz tunable detection in self-switching diodes based on high mobility semiconductors: InGaAs, InAs and InSb. J. Phys. **193**, 012082 (2009)
14. A. Iniguez, I. Iniguez, J. Mateos, T. Gonzalez, P. Sangaré, M. Faucher, B. Grimbert, V. Brandli, G. Ducournau, C. Gaquière, Searching for THz Gunn oscillations in GaN planar nanodiodes. J. Appl. Phys. **111**, 113705 (2012)

15. Y. Ghazaoui, A. El Alami, M. El Ghzaoui, S. Das, D. Baradand, S. Mohapatra, Millimeter wave antenna with enhanced bandwidth for 5G wireless application. J. Instrum. **15** (2020). https://doi.org/10.1088/1748-0221/15/01/T01003
16. B. Aghoutane, S. Das, H. El Faylali, B.T.P. Madhav, M. El Ghzaoui, A. El Alami, Analysis, design and fabrication of a square slot loaded (SSL) millimeter-wave patch antenna array for 5G applications. J. Circ. Syst. Comput. **30**(05), 2150086 (2021). https://doi.org/10.1142/S0218126621500869
17. H. Richter, A.D. Semenov, S.G. Pavlov, L. Mahler, A. Tredicucci, H.E. Beere, D.A. Ritchie, K.S. Il'in, M. Siegel, H.-W. Hubers, Terahertz heterodyne receiver with quantum cascade laser and hot electron bolometer mixer in a pulse tube cooler. Appl. Phys. Lett. **93**(14), 141108 (2008)
18. A.W. Lee, Q. Hu, Real-time, continuous-wave terahertz imaging by use of a microbolometer focal-plane array. Opt. Lett. **30**(19), 2563–2565 (2005)
19. T. Nagatsuma, G. Ducournau, C.C. Renaud, Advances in terahertz communications accelerated by photonics. Nat. Photon. **10**, 371–379 (2016)
20. M.C. Beard, W.T. Lotshaw, T.M. Korter, E.J. Heilweil, Comparative OHD-RIKES and THz-TDS probes of ultrafast structural dynamics in molecular liquids. J. Phys. Chem. A **48**, 9348–9360 (2004)
21. C.D. Sudworth, A.J. Fitzgerald, E. Berry, N.N. Zinov'ev, S. Homer Vanniasinkam, R.E. Miles, M. Chamberlain, M.A. Smith, The optical properties of human tissue at terahertz frequency. SPIE 5143 (2003)
22. K. Yamamoto, M. Yamaguchi, F. Miyamaru, M. Tani, M. Hangyo, T. Ikeda, A. Matsushita, K. Koide, M. Tatsuno, Y. Minami, Noninvasive inspection of C4 explosive in mails by terahertz time-domain spectroscopy. Jpn. J. Appl. Phys. **43**(3B), 414–417 (2004)
23. Y. Ogawat, K. Kawad, M. Yamashita, H. Inoue, Non-destructive inspection techniques for illicit drugs using terahertz imaging. Opt. Express **11**(20), 2549–2554 (2003)
24. M. Caselle et al., An ultra-fast data acquisition system for coherent synchrotron radiation with terahertz detectors. JINST **9**, C01024 (2014)
25. Y.-S. Lee, *Principles of Terahertz Science and Technology* (Springer, New York, 2009), p. 340
26. P.R. Smith, D.H. Auston, M.C. Nuss, Subpicosecond photoconducting dipole antennas. IEEE J. Quantum Electron. **24**, 255–260 (1988)
27. Q. Wu, X.C. Zhang, Free-space electrooptic sampling of terahertz beams. Appl. Phys. Lett. **67**, 3523–3525 (1995)
28. X.-C. Zhang, J. Xu, *Introduction to THz Wave Photonics* (Springer, Boston, 2010), p. 246
29. S. Casalbuoni, H. Schlarb, B. Schmidt, B. Steffen, P. Schmüser, A. Winter, in *Numerical Studies on the Electro-Optic Sampling of Relativistic Electron Bunches.* Proceedings of the 2005 Particle Accelerator Conference (2015), pp. 3070–3072
30. M. Naftaly, *Terahertz Metrology* (Artech House, Boston, 2015), p. 359
31. J. Dai, X. Xie, X.C. Zhang, Detection of broadband terahertz waves with a laser-induced plasma in gases. Phys. Rev. Lett. **97**(10), 8–1 (2006)
32. Thorlabs inc, OCT selection guide. Thorlabs inc. https://www.thorlabs.com/newgrouppage9.cfm?objectgroup_id=5702
33. D. Lorenser, B.C. Quirk, M. Auger, W.-J. Madore, R.W. Kirk, N. Godbout, D. Sampson, C. Boudoux, R.A. McLaughlin, Dual-modality needle probe for combined fluorescence imaging and three-dimensional optical coherence tomography. Opt. Lett. **38**(3), 266–268 (2013)
34. W. Drexler, J.G. Fujimoto, *Optical Coherence Tomography: Technology and Application"s,* 2e édition (Springer, New York, 2008), p. 1346
35. U. Sassi et al., Graphene-based mid-infrared room-temperature pyroelectric bolometers with ultrahigh temperature coefficient of resistance. Nat. Commun. **8**, 14311 (2017). https://doi.org/10.1038/ncomms14311
36. G. Sharma, K. Singh, I. Al-Naib, R. Morandotti, T. Ozaki, Terahertz detection using spectral domain interferometry. Opt. Lett. **37**(20), 4338–4340 (2012)
37. M.E. Brezinski, *Optical Coherence Tomography: Principles and Applications* (Academic Press, San Diego, 2006), p. 480

38. G. Sharma, K. Singh, A. Ibrahim, I. Al-Naib, R. Morandotti, F. Vidal, T. Ozaki, Self-referenced spectral domain interferometry for improved signal-to-noise measurement of terahertz radiation. Opt. Lett. **38**(15), 2705–2707 (2013)

On the Effective Electron Mass in Quantum-Confined THz Materials

R. Paul, M. Mitra, A. K. Pradhan, M. Maiti, S. Mondal, K. Bhattacharyya, S. K. Biswas, and K. P. Ghatak

Abstract The Effective Electron Mass (EEM) is studied in bulk specimens and also under strong magnetic field (B). Taking various THzMs we observe that normalized EEM increases with increasing doping, intensity and wavelength, respectively. The EEM decreases with increasing alloy composition; the EEM exhibits increasing dependence with intensity and wavelength under magnetic quantization. The EEM will change with other physical quantities in various ways which shows their individual quantum signature.

R. Paul
Department of Computer Science and Engineering, University of Engineering and Management, Kolkata 700156, India
e-mail: rajashree.paul@uem.edu.in

M. Mitra
Department of Electronic and Telecommunication Engineering, Indian Institute of Engineering Science and Technology, Shibpur, Howrah 711103, India

A. K. Pradhan
Department of Electronics, Acharya Prafulla Chandra College, New Barrackpore, North 24 Parganas, Kolkata 700131, India
e-mail: ayan@apccollege.ac.in

M. Maiti
Department of Electronics and Communication Engineering, Techno International Newtown, Block DG, Action Area 1, New Town, Kolkata 700156, India

S. Mondal
Purba Banbania Bhagabati Vidyamandir, North 24 Parganas, Habra 743263, India

K. Bhattacharyya
Tamralipta Mahavidyalaya, Abasbari, Tamluk, Purba Medinipur 721636, India

S. K. Biswas
Department of Physics, Calcutta University, 92, Acharya Prafulla Chandra Road, Kolkata 700009, India

K. P. Ghatak (✉)
Department of Basic Science and Humanities, Institute of Engineering & Management, D-1, Management House, Salt Lake, Sector-V, Kolkata, West Bengal 700091, India

M. El Ghzaoui et al. (eds.), *Terahertz Wireless Communication Components and System Technologies*, https://doi.org/10.1007/978-981-16-9182-9_3

Keywords Effective electron mass · Terahertz materials · Magnetic field · Wavelength · Intensity

1 Introduction

The concept of Effective Electron Mass (EEM) is very important in the realm of terahertz materials (THzMs) [1–25]. The THzMs are being widely studied in the literature [13, 26–39], and the EEM affects all other electronic, electrical and thermal properties of the conduction electrons in THzMs. The EEM is studied for THzMs under different physical conditions as stated in the abstract.

2 Method

The EEM in *i*th direction in *k*-space can be defined as [13, 26–39]

$$m_i^*(E_F) = \hbar^2 k_i \frac{\partial k_i}{\partial E_F} \tag{1}$$

where the symbols are defined above.

From (1), we note that the EEM can be derived and for that we need the energy-wave vector relation (EWR) of a particular THzM. By using the different EWR as given in [1–25], we can find out the EEM (denoted by α_1) for various THzMs which are plotted in Figs. 1, 2, 3, 4, 5 and 6. The n_0 has been calculated in each case by using the Uncertainty principle of Heisenberg under different quantization.

3 Result and Discussions

1. From Fig. 1, we note that the normalized EEM increases with increasing n_0 for bulk THzMs.
2. From Fig. 2, we note that the normalized EEM increases with increasing I for bulk THzMs.
3. From Fig. 3, we infer that the normalized EEM increases with increasing λ for bulk THzMs.
4. From Fig. 4, we note that the normalized EEM changes with increasing x for bulk THzMs.
5. Figures 5 and 6 reflect the fact that EEM exhibits increasing dependence with I and λ under magnetic quantization.

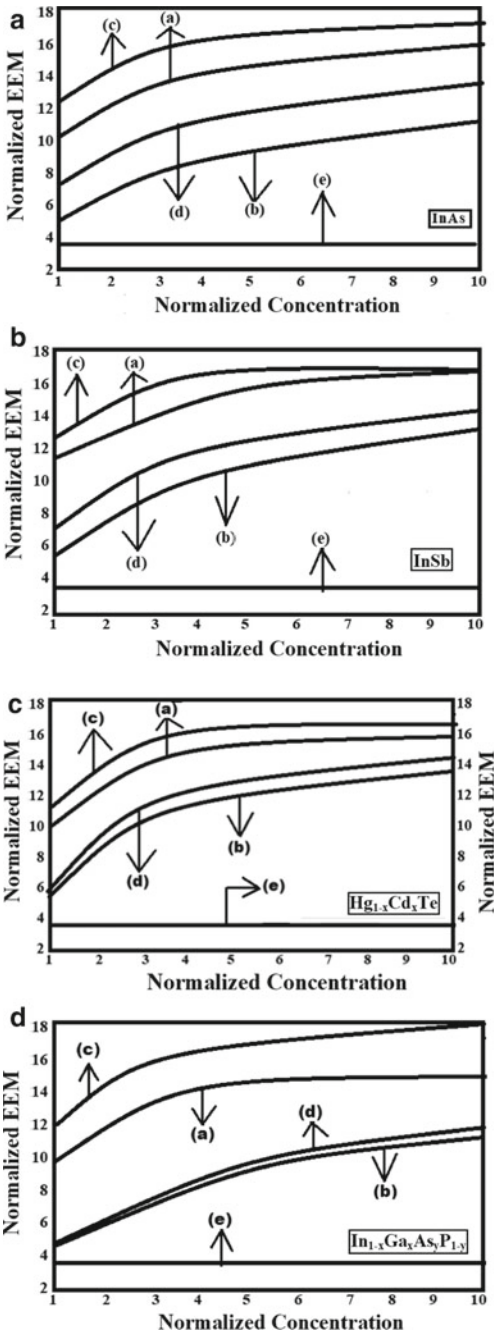

Fig. 1 Plots of α_1 versus n_0 for the indicated materials in figures **a**–**d** for finite I where the graphs **a**, **c** are valid for $\Delta \neq 0$ and $\Delta = 0$. The graphs **b**, **d** show the same when $I = 0$. The graph e is for parabolic energy bands which is valid for both $I = 0$ and $I \neq 0$

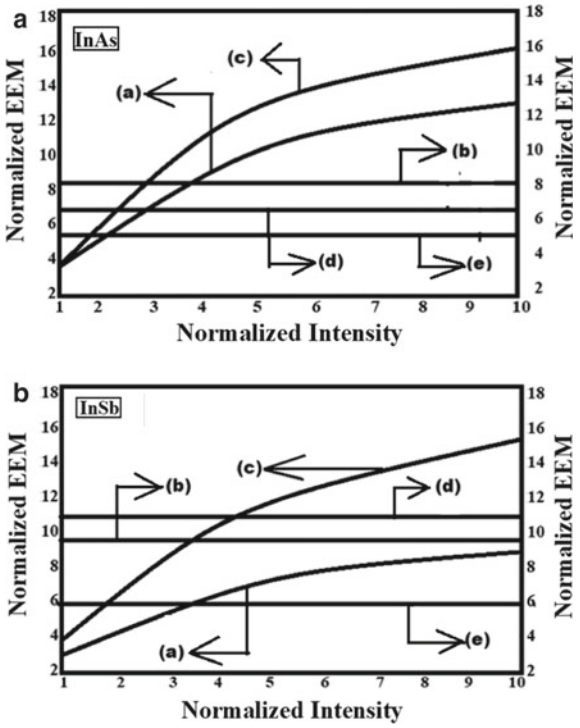

Fig. 2 Plots of α_1 versus I for the indicated materials

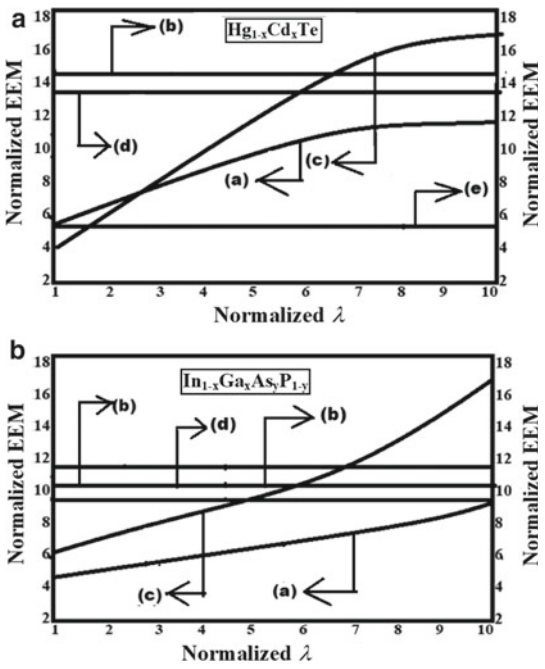

Fig. 3 Plots of α_1 versus λ for the indicated materials

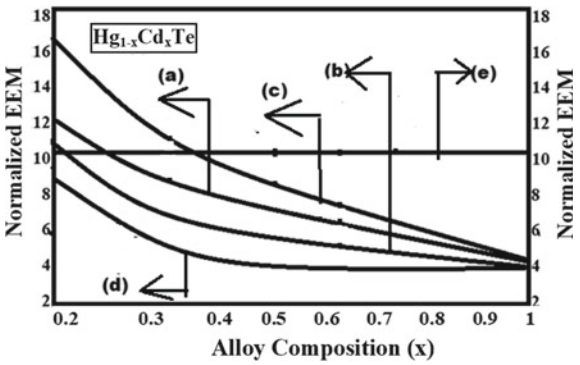

Fig. 4 Plot of α_1 versus x for the indicated material

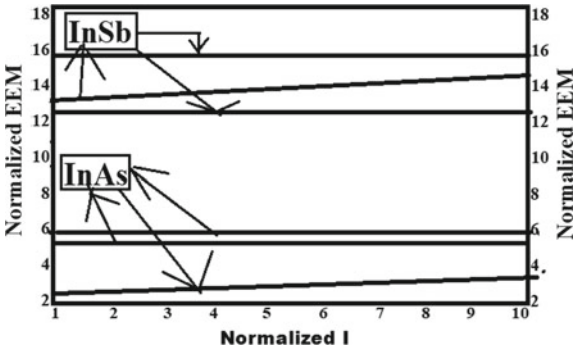

Fig. 5 Plot of α_1 versus I for indicated materials for $I \neq 0$ and finite B

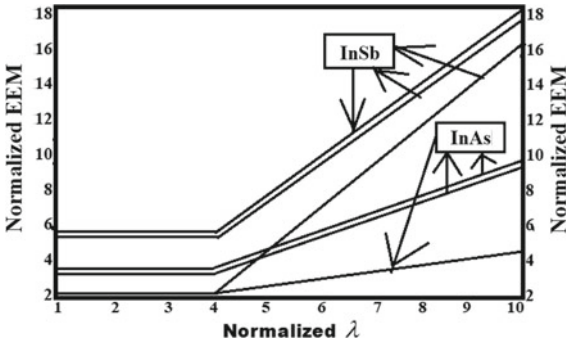

Fig. 6 Plot of α_1 versus λ for indicated materials for $I \neq 0$ and finite B

4 Conclusion

The EEM is studied in bulk specimens and also under strong magnetic field (B). Taking various THzMs, we observe that normalized EEM increases with increasing doping, intensity and wavelength, respectively. The EEM decreases with increasing

alloy composition; the EEM exhibits increasing dependence with intensity and wavelength under magnetic quantization. The EEM will change with other physical quantities in various ways which shows their individual quantum signature.

References

1. S. Bhattacharya, K.P. Ghatak, Effective electron mass in low dimensional semiconductors, in *Springer Series in Materials Sciences*, vol. 167 (Springer, Berlin, Heidelberg, 2013)
2. K.P. Ghatak, Quantum effects, heavy doping, and the effective mass, in *Series on the Foundations of Natural Science and Technology*, vol. 8 (World Scientific Publishing Co. Ltd., Singapore, USA, 2017)
3. K.P. Ghatak, B. Mitra, On the effective electron mass in strained layer superlattices of non-parabolic semiconductors under strong magnetic quantization. Int. J. Electron. **72**, 541–552 (1992)
4. M. Mondal, N. Chattopadhyay, K.P. Ghatak, Theoretical analysis of the effective electron mass in ultrathin films of ternary chalcopyrite semiconductors in the presence of crossed electric and magnetic fields. J. Low Temp. Phys. **66**, 131–143 (1987)
5. P.K. Chakraborty, G.C. Datta, K.P. Ghatak, A simple theoretical analysis of the effective electron mass in heavily doped III–V semiconductors in the presence of band-tails. Physica Scr. **68**, 368–371 (2003)
6. K.P. Ghatak, M. Mondal, Theoretical study of the effective electron mass in ternary chalcopyrite semiconductors in the presence of crossed electric and magnetic fields. Zeitschrift Für Physik B Condens. Matter **69**, 471–473 (1988)
7. B. Mitra, K.P. Ghatak, On the effective electron mass in N-channel inversion layers of Ge. Solid State Electron. **32**, 177–178 (1989)
8. K.P. Ghatak, S. Bhattacharya, S.K. Biswas, A. Dey, A.K. Dasgupta, A simple theoretical analysis of the effective electron mass in III–V, ternary and quaternary materials in the presence of light waves. Physica Scr. **75**, 820–830 (2007)
9. M. Mondal, K.P. Ghatak, On the effective electron mass in ternary semiconductors in the presence of crossed electric and magnetic fields. Phys. Lett. A **131**, 529–532 (1988)
10. A.N. Chakravarti, K.P. Ghatak, K.K. Ghosh, S. Ghosh, A. Dhar, Effect of size quantization on the effective mass in ultrathin films of n-Cd3As2. Zeitschrift Für Physik B Condensed Matter **47**, 149–153 (1982)
11. A. Ghoshal, B. Mitra, K.P. Ghatak, On the effective electron mass in quantum well wires of ternary chalcopyrite semiconductors. Il Nuovo Cimento D **12**, 891–900 (1990)
12. A.N. Chakravarti, A.K. Howdhury, K.P. Ghatak, S. Ghosh, A. Dhar, Oscillatory effective mass in degenerate narrow-gap semiconductors in a quantizing magnetic field. Appl. Phys. **25**, 105–108 (1981)
13. K.P. Ghatak, M. Mondal, Effect of magnetic quantization on the effective electron mass in bismuth. Zeitschrift für Naturforschung A **41**, 881–882 (1986)
14. M. Mondal, K.P. Ghatak, Influence of magnetic quantization on the effective electron mass in ternary semiconductors. Physica Status Solidi (b) **129**, 745–753 (1985)
15. K.P. Ghatak, A. Ghoshal, B. Mitra, Influence of quantization of band states on the effective electron mass in quaternary alloys. Il Nuovo Cimento D **14**, 903–925 (1992)
16. B. Mitra, K.P. Ghatak, Effect of magnetic quantization on the effective electron mass in n-Ge. Solid State Electron. **32**, 515–516 (1989)
17. K.P. Ghatak, A. Ghosal, On the effective electron mass in n-channel inversion layers on ternary semiconductors in the presence of a parallel magnetic field. Physica Status Solidi (b) **151**, K135–K140 (1989)

18. S. Bhattacharya, D. De, S.M. Adhikari, K.P. Ghatak, On the two dimensional effective electron mass in quantum wells, inversion layers and NIPI superlattices of Kane type semiconductors in the presence of strong light waves: Simplified theory and relative comparison. Superlattices Microstruct. **51**, 203–222 (2012)
19. K.P. Ghatak, M. Mondal, Influence of a quantizing magnetic field on the effective electron mass in HgTe/CdTe superlattices with graded structures. Physica Status Solidi (b) **175**, 113–121 (1993)
20. M. Mondal, K.P. Ghatak, Theoretical analysis of the effective electron mass in n-channel inversion layers on ternary chalcopyrite semiconductors. Physica Status Solidi (b) **139**, 185–193 (1987)
21. S. Debbarma, A. Bhattacharjee, S. Bhattacharyya, A. Mondal, K.P. Ghatak, Influence of quantizing magnetic field on the effective electron mass in nonlinear optical, optoelectronic and related materials: Simplified theory and relative assessment. J. Adv. Phys. **1**, 84–109 (2012)
22. D. Bhattacharyya, K.P. Ghatak, On the effective electron mass in quantum wires of non-parabolic semiconductors under a parallel magnetic field. Physica Status Solidi (b) **187**, 523–531 (1995)
23. K.P. Ghatak, A simple theoretical analysis of the effective electron mass in NIPI structures of non-parabolic semiconductors. Acta Physica Hungarica **74**, 257–268 (1994)
24. M. Mondal, K.P. Ghatak, Effect of size quantization on the effective electron mass in ultrathin films of Bismuth. Acta Physica Slovaca **36**, 325–328 (1986)
25. M. Mondal, K.P. Ghatak, Effect off surface electric field on the effective electron mass in inversion layers on small-gap semiconductors. Acta Phys. Pol., A **66**, 47–51 (1984)
26. N. Paitya, K.P. Ghatak, Effective electron mass in quantum wires of III–V, ternary and quaternary materials. J. Nano Sci. Nanotechnol. **12**, 8985–8993 (2012)
27. S.L. Singh, S.B. Singh, K.P. Ghatak, 2D effective electron mass at the fermi level in accumulation and inversion layers of MOSFET nano devices. J. Nanosci. Nanotechnol. **18**, 2856–2874 (2018)
28. S. Bhattachrya, N. Paitya, K.P. Ghatak, Simple theoretical analysis of the effective electron mass in semiconductor nanowires. J. Comput. Theor. Nanosci. **10**, 1999–2018 (2013)
29. K.P. Ghatak, *The EM in Heavily Doped (HD) Non-Parabolic Semiconductors Under Magnetic Quantization, Quantum Effects, Heavy Doping, and the Effective Mass*, vol. 8 (World Scientific Publishing Company, 2017), pp. 259–304
30. K.P. Ghatak, *The EM in Nano-Wires (NWs) of Heavily Doped (HD) Non-Parabolic Semiconductors, Quantum Effects, Heavy Doping, and the Effective Mass*, vol. 8 (World Scientific Publishing Company, 2017), pp. 201–258
31. K.P. Ghatak, *The EM in Accumulation and Inversion Layers of Non-Parabolic Semiconductors, Quantum Effects, Heavy Doping, and the Effective Mass*, vol. 8 (World Scientific Publishing Company, 2017), pp. 169–200
32. K.P. Ghatak, *The EM in Doping Superlattices of HD Non-Parabolic Semiconductors, Quantum Effects, Heavy Doping, and the Effective Mass*, vol. 8 (World Scientific Publishing Company, 2017), pp. 139–168
33. M. Mondal, K.P. Ghatak, Effect of size quantization on the effective electron mass in ultrathin Bi films. Physica Status Solidi (b) **128**, K133–K137 (1985)
34. K.P. Ghatak, On the effective electron mass in semiconductor superlattices. Acta Physica Hungerica **70**, 77–81 (1991)
35. B. Chatterjee, K. Sarkar, K.P. Ghatak, Can photon influence effective mass? Springer Proc. Phys. **166**, 621–628 (2015)
36. A.N. Chakravarti, K.P. Ghatak, K.K. Ghosh, H.M. Mukherjee, Effect of varying the orientation of a quantizing magnetic field on the effective electron mass in degenerate tetragonal semiconductors. Physica Status Solidi (b) **116**, 17–24 (1983)
37. M. Mondal, K.P. Ghatak, Influence of magnetic quantization on the effective electron mass in zero-gap semiconductors. Physica Status Solidi (b) **123**, K143–K148 (1984)

38. M. Mondal, K.P. Ghatak, Influence of magnetic quantization on the effective mass in semiconductor superlattices. Czechoslovak J. Phys. **36**, 1389–1395 (1986)
39. K.P. Ghatak, B. Mitra, A. Ghosal, On the effective electron mass in superlattices of III-V semiconductors in the presence of a quantizing magnetic field. Physica Status Solidi (b) **154**, K121–K126 (1989)

Opportunities and Challenges in THz Communication

M. Bharathi, A. Amsaveni, and R. Priyadharshini

Abstract Terahertz communication is the feasible solution for satisfying the demand for higher bandwidth. However, THz channel is highly different from lower frequency bands and poses lot of technical challenges in the design and deployment of communication system. High path loss and absorption loss is one of the critical challenges to be addressed in THz band. Due to this high absorption loss, THz waves can be used only for short distance (<5 m) Communication. The channel characteristics in THz band have to be investigated thoroughly for reliable communication over this band. As it is possible to obtain Tbits/s data rate over this band, the signal processing algorithms in the higher layers of the communication stack need to be revised to handle terabits level data. Design of transceiver to operate in the THz region with wide bandwidth is another technical challenge to be addressed. Highly directive antenna is needed to overcome the path loss problem. The bandwidth of the antenna should be high enough to handle the range of frequency. Large antenna array with nanomaterials/metamaterials to satisfy the above requirements has to be designed. The size of the antenna poses fabrication challenges. In spite of these technical challenges, the recent advancements in THz channel modeling, signal generation, detection, modulation, and antenna design are closing the THz gap. This chapter defines the challenges in THz communication and reviews the approaches adapted in the literature to address these challenges.

Keywords THz communication · Channel modeling · Molecular absorption · Modulation · Channel coding · MIMO · Antenna design · Transceiver design · Nanodevices

1 Introduction

The demand for wireless communication data rates is ever increasing. This high demand is met to a certain extent by the advancements in the modulation schemes

M. Bharathi (✉) · A. Amsaveni · R. Priyadharshini
Department of Electronics and Communication Engineering, Kumaraguru College of Technology, Coimbatore, India
e-mail: bharathi.m.ece@kct.ac.in

M. El Ghzaoui et al. (eds.), *Terahertz Wireless Communication Components and System Technologies*, https://doi.org/10.1007/978-981-16-9182-9_4

and the signal processing algorithms both at the transmitter and at the receiver ends. However, the available bandwidth sets an upper limit for the achievable data rate. Terahertz communication is one of the feasible solutions to overcome the spectrum scarcity. The wavelength of Terahertz signal is lesser than microwave and ranges from some tens of GHz up to limited range in THz. This band is less explored and not used for active services. Very high data rate up to Terabits per Second (TBPS) over a short range can be achieved using this frequency band. As the wavelength is less in this range, antenna size is very small and hence nanodevices can communicate using this spectrum [1].

THz wireless communications can be explored for AR and VR applications. Chip to-chip-communication, on-chip communication, body area networks, communication between nanothings (IoNT), Remote Sensing, Biological Detection are some of the possible applications in THz frequency. However, there are few technical challenges that need to be addressed to enjoy the benefits of this large spectrum. These challenges include channel modeling, high path loss, antenna design, etc. This chapter discusses a few of these challenges with the present state of development.

2 Channel Modeling

The signal can propagate in either direct (Line of Sight—LOS) or indirect (Non-Line of Sight—NLOS) paths through wireless communication medium. To completely understand and study the channel, both LOS and NLOS paths must be considered [2]. THz frequency waves are extremely absorbed by the molecules in the atmosphere. Molecules in the atmosphere vibrate at certain frequencies and in those frequencies, the absorption is more. Hence the molecular absorption depends on the type of molecules present, the vibrating frequency, temperature, and pressure. High Resolution Transmission Database (HITRAN) is the open source which takes the composition of atmospheric gas as input and predicts the molecular absorption ($\alpha_{\text{mol}}(f, T_k, p)$). For pure water vapor, the absorption coefficient as a function of wavelength is given in Fig. 1. Frequency starting from 0.1 to 1.5 THz is considered for this computation, and the wave numbers corresponding to this frequency start at 3.3 cm^{-1} and go up to 50 cm^{-1}.

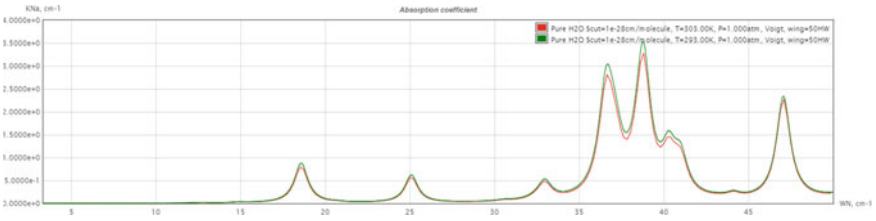

Fig. 1 Water vapor absorption coefficient as a function of wavelength

Absorption coefficient was computed for temperatures 293 degree Kelvin (20 °C) and 303 (30 °C) degree Kelvin and plotted in Fig. 1. From the graph, it is learnt that as temperature increases there is a small decline in the absorption coefficient. However, the peaking happens at same frequency for both temperatures. The peaks occur at frequencies different frequencies spread throughout the region.

The free space absorption of the electromagnetic wave is given by [2]

$$A_{\text{abs}}^{\text{dB}}(f, r) = \alpha_{\text{mol}}(f, T_k, p) r 20 \log e \tag{1}$$

where 'f' is the frequency of the wave and 'r' is the propagating distance.

Expansion of EM wave while propagating produces loss known as spreading loss which is function of the distance traveled, frequency and is given by,

$$A_{\text{spread}}^{\text{dB}}(f, r) = 20 \log_{10} \frac{(4\pi f r)}{c} \tag{2}$$

where $c = 2.9979 \times 10^8$ m/s is the speed of light.

LoS path loss is primarily due to both free space absorption and spreading loss and is given by,

$$A_{\text{dB}}(f, r) = A_{\text{abs}}\text{dB}(f, r) + A_{\text{spread}}\text{dB}(f, r) \tag{3}$$

LoS path loss with respect to frequency is computed for two temperatures 20 and 30 °C and given in Figs. 2 and 3, respectively. Various propagating distances from 0.1 to 100 m are considered for this simulation. Path loss is highly frequency selective and goes more than 100 dB for even for very short distance. At some frequencies,

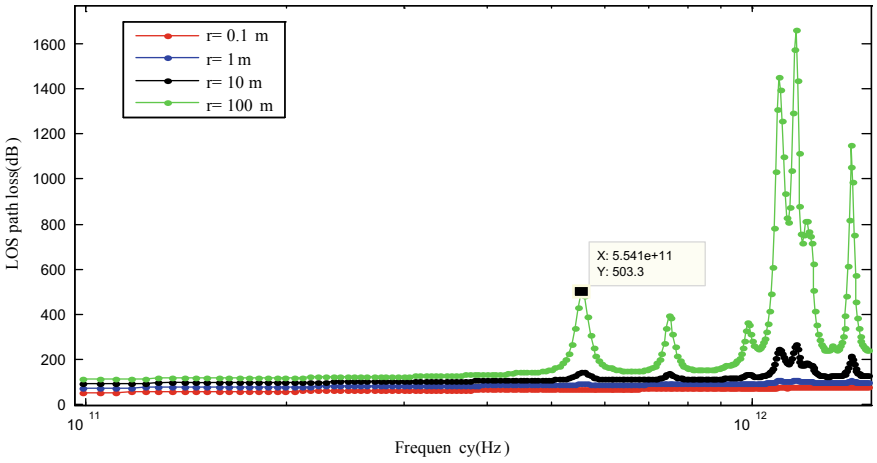

Fig. 2 LOS path loss for 200 °C

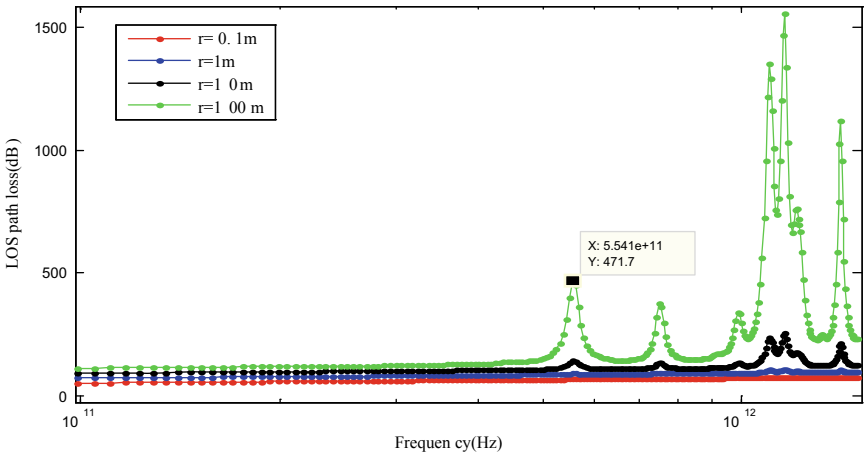

Fig. 3 LOS path loss for 300 °C

loss is too high and this forms transmission windows and over which data can be transmitted effectively [3].

The transfer function of the direct path can be obtained by,

$$H^{\mathrm{LOS}}(f,r) = H_{\mathrm{spread}}(f,r).H_{\mathrm{abs}}(f,r) \tag{4}$$

where

$$H_{\mathrm{spread}}(f,r) = c/4\pi fr \quad \text{and} \quad H_{\mathrm{abs}}(f,r) = e^{-\frac{1}{2}\alpha_{\mathrm{mol}}(f,T_k,p)r}$$

The NLOS path is more crucial in establishing communication in condition where the direct path is blocked due to some obstacles. Electromagnetic wave reflection is the major factor for the NLOS path loss. Reflection depends on the surface roughness σ_{hs} and the length of correlation l_{corr} [2]. Analyzing the reflection properties of the surface helps in understanding the NLOS path loss. Kirchhoff scattering theory can be employed for studying the EM wave scattering at rough surfaces.

The transfer function of the ith NLOS path is,

$$H_i^{\mathrm{NLOS}}(f,r,\xi_i) = H_{\mathrm{ref},i}(f,r_{i2},\theta_{i1},\theta_{i2},\theta_{i3}) \times H_{\mathrm{spread},i}(f,r_{i1},r_{i2}).H_{\mathrm{abs},i}(f,r_{i1},r_{i2}) \tag{5}$$

where

$$H_{\mathrm{ref},i}(f,r_{i2},\theta_{i1},\theta_{i2},\theta_{i3}) = \sqrt{E\left\{R_{\mathrm{power},i}(f,r_{i2},\theta_{i1},\theta_{i2},\theta_{i3})\right\}},$$

$$H_{\text{spread},i}(f, r) = \frac{c}{4\pi f(r_{i1} + r_{i2})}$$

$$H_{\text{abs},i}(f, r_{i1}, r_{i2}) = e^{-\frac{1}{2}\alpha_{\text{mol}}(f, T_k, p)(r_{i1}+r_{i2})}$$

r is the direct distance between the Tx and Rx.
r_{i1} is the distance between the Tx to the ith scattering point.
r_{i2} is the distance between the ith scattering point to the Rx.

Including both LoS and NLoS path, the overall transfer function of the channel is given by

$$HEQ(f, r, \zeta) = H^{\text{LOS}}(f, r)e^{-j2\pi f \tau_{\text{LOS}}} + \sum_{i=1}^{N} H_i^{\text{NLOS}}(f, \zeta_i)e^{-j2\pi f \tau_{\text{NLOS}i}} \quad (6)$$

The vector $\zeta = [\zeta_1, \zeta_2, \ldots \zeta_N]$ gives the coordinates for the scattering points, which accounts for the parameters $[r_{i1}, r_{i2}, \theta_{i1}, \theta_{i2}, \theta_{i3}]$. N is the total number of NLOS paths.

For the simulation of transfer function, a rectangular room of length 5 m, width and height 2.75 m and 2.5 m, respectively, is considered. Four NLOS paths as shown in Fig. 4 are analyzed, and the total path loss is calculated. The transmitter and the receiver are placed 2 m apart. LoS and NLoS transfer function is computed for 300 °C and is given in Fig. 5. It can be observed from the result that LOS path is the predominant factor if exist. Under such condition, transfer function can be approximated to the transfer function of LoS path.

Due to the high path loss in THz region, efficient methods need to be developed to overcome the power loss in this band. High gain directional antenna, efficient channel codes, and modulation schemes are few areas that need to be focused to make THz communication possible.

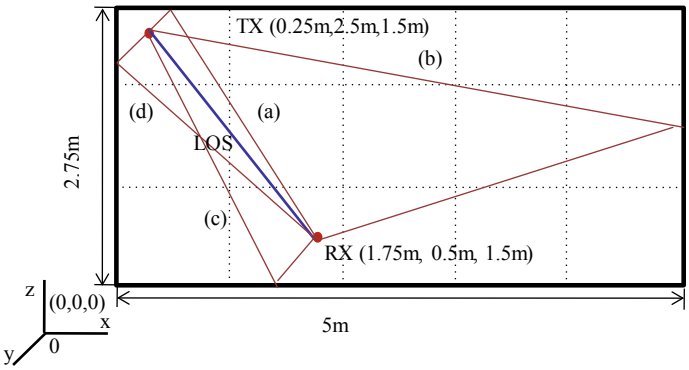

Fig. 4 Indoor scenario

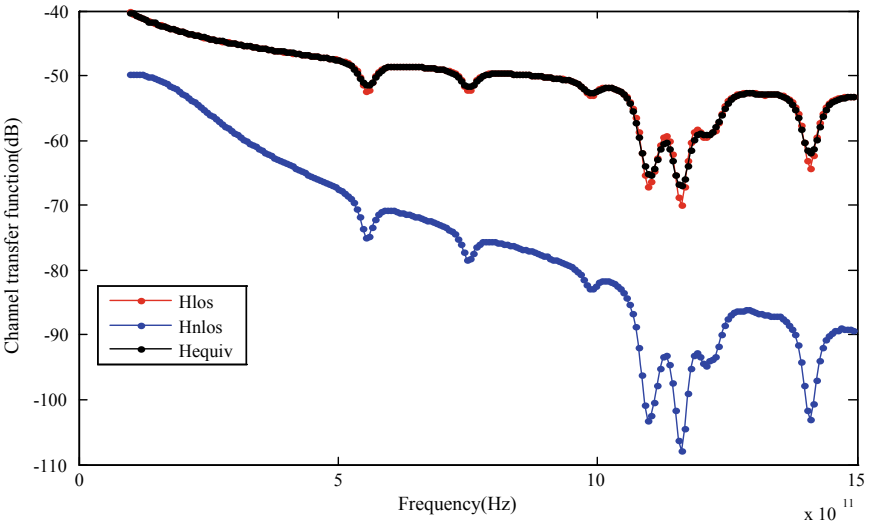

Fig. 5 Channel transfer function

3 Modulation Schemes

To evaluate the performance of Terahertz channel, Binary Phase Shift Keying (BPSK) is used as a modulation scheme. In BPSK modulation technique, to encode each bit a phase shift is introduced over a fixed time interval. The performance of the high frequency channel for various distances is shown in Fig. 6. For small distances like 0.5, 1, and 2 m, the error rate is low and the performance is acceptable. However, with distance due to the absorption attenuation increases. Even with high signal-to-noise ratio, for long distances, the noise floor dominates the signal, and hence, the error rate is more.

Frequency-dependent path loss of THz channel demands novel modulation schemes to be developed. From Fig. 7, it is observed that at some frequencies the transfer function is very low, and these frequencies are not suitable for data transmission. It is the best practice to send data over frequencies where the loss is minimum. The dips in the transfer function create transmission windows. The THz channel needs unique modulation schemes considering these constraints.

The frequency selective nature of the channel is considered for designing the modulation scheme for improving the performance of the system. The width of the high attenuation bands mainly depends on the distance and humidity in the air. Modulation scheme is designed such that these bands are excluded from data transmission. This type of modulation scheme is known as adaptive modulation scheme. Though the amount of data transmission is reduced with adaptive modulation scheme, the Bit Error Rate (BER) is improved with such modulation techniques [2]. Comparison of channel performance with and without adaptive modulation is shown

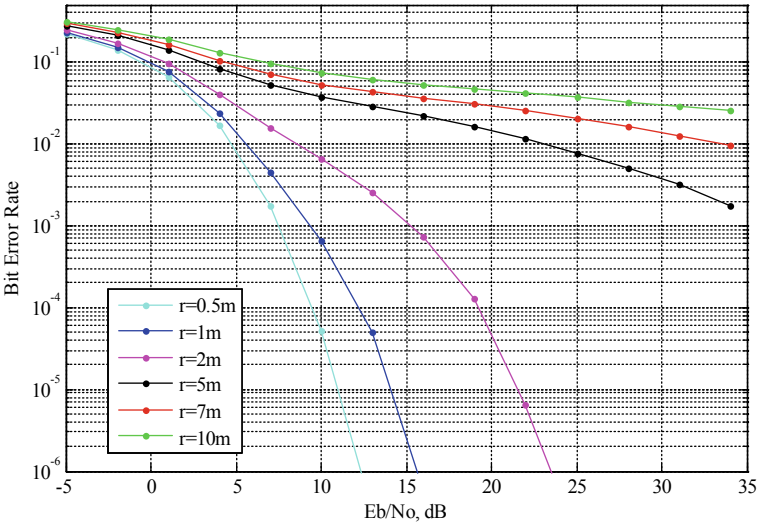

Fig. 6 Performance with BPSK

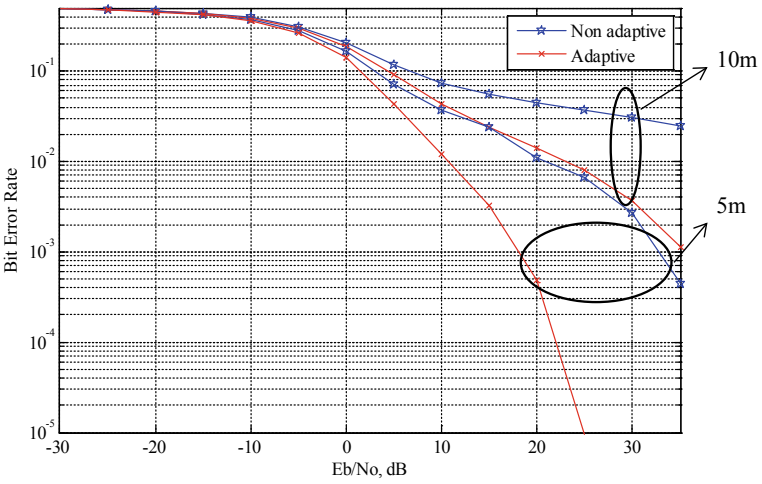

Fig. 7 BER performance with adaptive modulation

in Fig. 6. Significant improvement is observed in the case of adaptive modulation scheme compared to non-adaptive technique. This improvement is observed in both 5 and 10 m propagation distance. In non-adaptive technique, high attenuation bands in the transfer function such as 0.5–0.6 THz, 0.7–0.78, 0.93–0.98, and 1.09–1.2 are not considered for data transmission.

4 Multiple-Input Multiple-Output Systems

In the recent past, the demand for data rate is met with the help of Multiple-Input Multiple-Output (MIMO) systems. MIMO technique exploits the space dimension. Using MIMO technology, capacity of the channel and the spectral efficiency can be improved. This also helps to improve the reliability of the communication medium. MIMO is implemented by deploying Many co-located antennas at the receiver side or/and transmitter side. The key idea behind diversity is that each antenna receives different faded signal and the probability of all of them in deep fade is less. Thus spatial diversity schemes improve reliability by reducing channel fluctuations due to fading.

Figure 8 shows the schematic of THz channel with receiver diversity where multiple antennas are deployed at the receiver side.

The signal received at *i*th antenna at the receiver side is given by

$$y_i = h_i x + n_i \tag{7}$$

In general form,

$$Y = HX + N \tag{8}$$

where

$Y = [y_1 y_2 \cdots y_{Nr}]^{\mathrm{T}}$ is the vector consists of received signal from all antenna.
$H = [h_1 h_2 \cdots h_{Nr}]^{\mathrm{T}}$ is the vector consists of the channel seen by each antenna.
$N = [n_1 n_2 \cdots n_{Nr}]^{\mathrm{T}}$ is the vector of noise on the received signal.

The signal received through each antenna can be combined effectively using various combining techniques. Maximum Ratio Combining (MRC) is the commonly used technique which is optimal in terms of SNR. The transmitted symbol is estimated using,

$$\hat{x} = \frac{H^H Y}{H^H H} \tag{9}$$

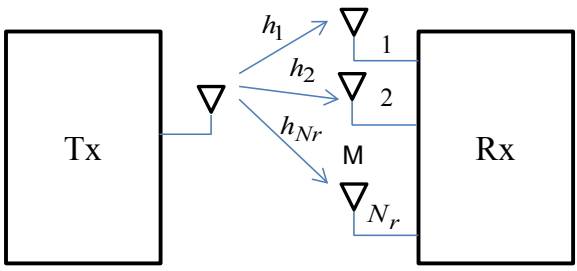

Fig. 8 Schematic of receiver diversity

Deployment of more than one antenna at the transmitter and at the receiver is the feasible solution to achieve better performance in THz environment. Multiple antennas also help to achieve narrow beamwidth. The data throughput of THz band can be increased with the help of MIMO technology. Many users can also be supported in the same environment using MIMO. However, this advantage comes with the cost of complexity. In the recent years to reduce the complexity and cost [4] array of subarrays are used. Nano-sized antennas in this high frequency range lead to ultra-massive architectures. 1024 × 1024 massive MIMO structure was designed and the improvement was analyzed [5] using numeric and analytical examination. This massive structure was capable of achieving a data rate up to 8 Tbps for a distance of about 10 m. However, to improve the data rate and distance, it is not advisable and feasible to increase the array size. As discussed in Chap. 2, adaptive modulation with transmission window can be explored with MIMO system. Adaptive modulation with receiver diversity is analyzed with different number of receiver antennas. The performance of the system with varying receiver diversity is plotted in Fig. 9 and shows the BER of adaptive modulation in combination with receiver diversity. For a distance of 10 m and NRx = 32, there is a 25 dB gain with and without adaptive modulation.

Another promising technology to improve the performance of communication systems is Orthogonal Frequency Division Multiplexing (OFDM). This technology helps to reduce Inter Symbol Interference (ISI) which occurs due to the dispersive nature of the channel. In wideband channel when the delay spread is more than the symbol duration, each symbol will interfere with the neighboring symbol and this reduces the data that can be transmitted. Proper selection of the transmitted symbols and the use of adaptive equalizers at the receiver side reduce the ISI effect. However, the use of adaptive equalizer is complex as it needs high computational power to

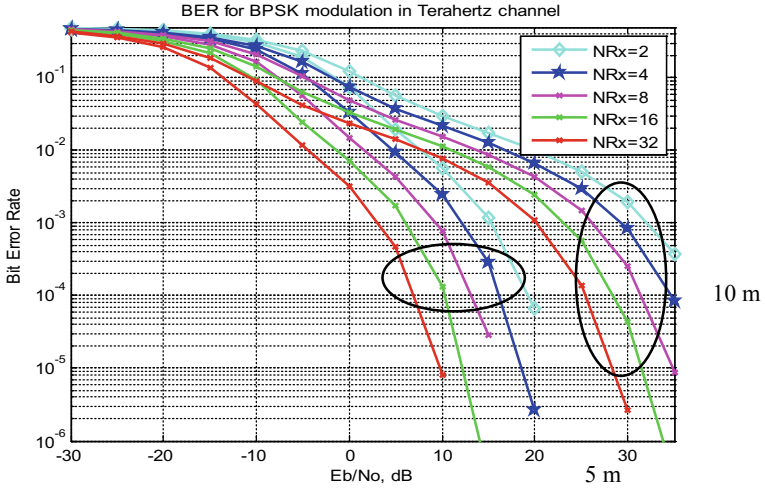

Fig. 9 BER performance with adaptive modulation and receiver diversity

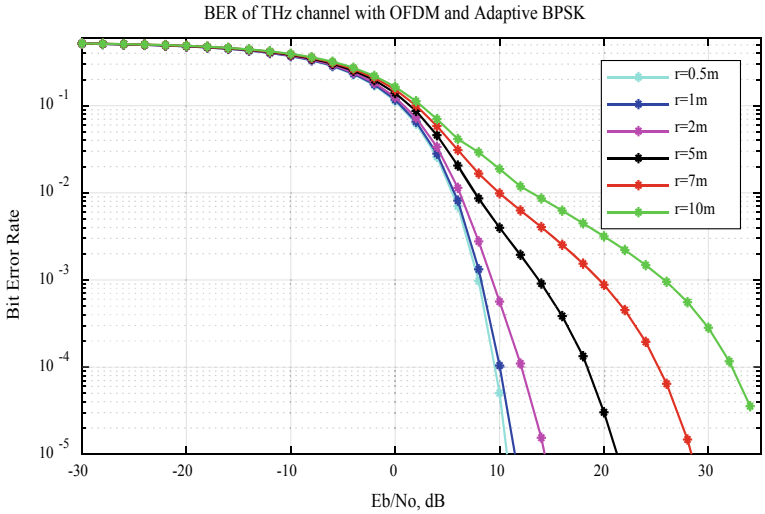

Fig. 10 The BER performance of THZ channel OFDM

update and train the equalizer at regular intervals and reduces the spectral efficiency of the channel. The promising technology to overcome the effect of ISI is multicarrier modulation which converts the wideband channel into parallel multiple narrowband channels. Data is transmitted in each channel independent of the other channel. The narrowband channels will be flat fading, and hence, the frequency-dependent channel is converted to multiple narrowband flat fading channels.

OFDM with adaptive BPSK modulation and MIMO improves the performance of the system. Figure 10 shows the variation of BER with OFDM.

5 Antenna Design

The bandwidth of the THz channel is too high and this can support the growing demand of high data rate. The antenna that is used at THz communication should have wider bandwidth. The directivity of the antenna plays an important role in mitigating the distance constraint due to excessive path loss. Properties of the material are vital in deciding the performance of antenna. Therefore, the impact of material properties might be an interesting area to study further. These two needs can be achieved using graphene-based huge antenna arrays. Surface plasmon polaritons (SPP) waves can propagate at THz frequency with graphene as a material used for antenna design. The velocity of SPP wave in graphene is almost twice compared to the velocity in vacuum. Graphene outperforms copper and carbon nanotubes when it comes to designing antennas with small footprints and great directivity [6]. Nanoelectronic device can employ antenna array made up of graphene for communication. Graphene

also enables the creation of reconfigurable directional antennas in addition to SPP wave propagation. Plasmonic patch antenna based on graphene, a reconfigurable graphene-based Yagi–Uda MIMO antenna, and planar antennas are some of the THz antennas which are studied and explored. Antenna with superstate layers are also explored in THz region to obtain multiple bands.

To counteract the path loss incurred at THz frequencies, a large antenna gain is required, and this can be achieved with large antenna array [7]. Although printed antennas can be used to create a huge antenna array construction, mutual coupling is one of the key concerns in such antenna. Although there is a substantial amount of study on mutual coupling reduction in the literature, it demands special attention in the THz domain.

6 Transceivers Design in Terahertz Band

The development of transceivers with a large bandwidth in the THz frequencies is a significant issue. The THz gap, which means that the frequency band is too high for traditional oscillators and too low for optical photon emitters, makes signal creation at THz frequencies challenging. As molecular absorption and path loss are high in this band of frequencies, high power, high sensitivity, and low noise figure should be taken into consideration while designing THz transceivers. Available oscillators will not be sufficient to generate THz signals. There is considerable research happening in the area of signal generation. However, the available solutions are costly and also complex. Research efforts are needed to reduce the cost and complexity of the available solution. THz signals can be generated either by top-down or by bottom-up approach.

Multiplexers are used to generate THz frequency signal in bottom-up method. Several multiplexers can be used in bottom-up method. With several multiplexers, the total power and the intermodulation products will be more in the generated signal. This results in highly distorted modulation signal with multiple mixers. The number of multiplexers should be limited to avoid distortion created by intermodulation and spurious effects. The top-down approach employs a photonics system in which continuous or pulsed THz radiation is produced by laser stimulation of semiconductors, and non-linear crystals or lasers are operated directly on THz frequencies.

7 Present State of the Art

The performance of the THz channel in terms of the achievable data rates is discussed in this section.

Amplitude Shift Keying is used in frequencies varying between 0.125 and 0.542 THz for distance varying between 0.1 and 5800 m. The data rate achieved with

ASK was varying between 1 and 30 Gbps. OOK modulation scheme was used in frequencies between 220 and 300 GHZ for distance for 0.04 to 60 m. The maximum achievable data rate with OOK was up to 48 Gbps. 8-PSK and QPSK modulation schemes were also explored for THz communication. 16 QAM modulation scheme was also explored by many researchers and the data rate obtained was up to 100 Gbps.

8 Future Research Areas in THz Communication

Research gaps exist in the THz communication although considerable work is available in this spectrum. Focused attention is needed in every aspect of this new and potential technology to make it practical. Figure 11 shows the areas that need to be explored.

Critical issues including modeling of the channel, signal processing, design of transceiver, antenna design, constraints of the physical layer, protocols for the upper layer, security to be studied and analyzed to enjoy the benefits of this wide spectrum and increase the data rates.

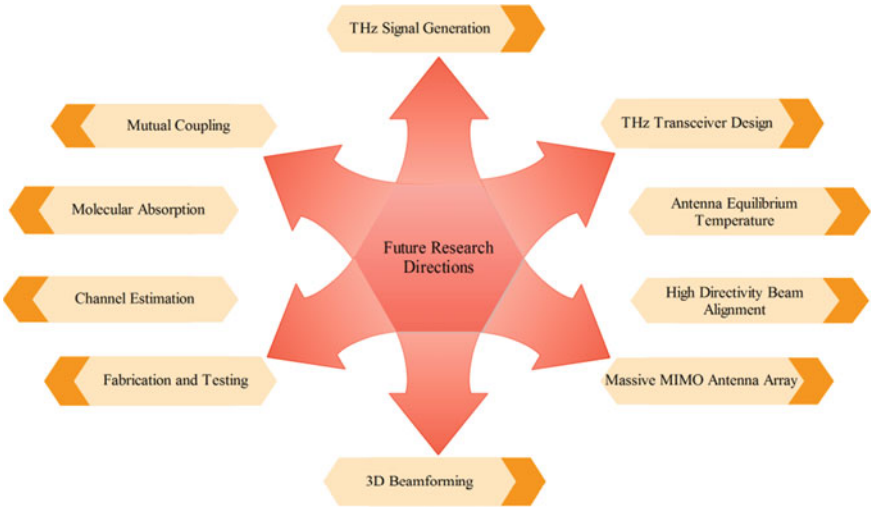

Fig. 11 Research areas in THz communication

9 Conclusion

The demand for data rate is growing exponentially and this can be achieved only with increased bandwidth. The available bandwidth is almost reaching its maximum limit. Due to the growing demand and advancements in smart handheld devices, multimedia services are commonly used in modern wireless communication. The number of people using wireless networks is increasing at a fast rate; today, there are 23 billion devices connected to the internet and the prediction is that this number will reach 75 billion by 2025. Furthermore, when compared to a fixed wired network connected to personal computer, people use mobile devices more and consume more data on the mobile devices. So it is mandate to discover a way to meet this high demand. The unexplored THz spectrum with ultrawide bandwidth enables high data rate communication. Many literature study and analyze the channel and noise properties of THz links, which differ significantly from those of currently used bands. Physical layer requirements as well as the features that the upper layers must contain should be studied in order to construct a proper communication system in THz bands. It is necessary to develop new modulation and channel code schemes that account for physical layer aspects such as energy efficiency, distance, and bandwidth. Because of the significant attenuation inherent in THz bands, the design of amplifiers and antennas is very critical in achieving high gain and directivity. The key issues in the THz bands are signal production, transmission, and sensing; however, recent work on graphene has opened up new vistas in signal generation because graphene permits SPP waves to propagate. Antennas based on graphene are well suited for nanonetworks. In addition to graphene, SiGe, InP, and InGaAs are widely studied materials in transceiver design. Because the investigations have mostly focused on the physical layer, the MAC and above levels must be thoroughly investigated to cope with big bandwidths, high data rates, and a large number of nodes in a seamless manner.

References

1. K. Tekbıyık, A.R. Ekti, G.K. Kurt, A. Görçin, Terahertz band communication systems: challenges, novelties and standardization efforts. Phys. Commun. **35**, 100700 (2019)
2. M. Bharathi, S. Sasikala, J. Vanmathi, Performance of terahertz channel with multiple input and multyiple output techniques. J. Infrared Millimeter Waves **36**(6), 668–672 (2017). ISSN: 1001–9004
3. L. Rothman, I. Gordon, Y. Babikov et al., The HITRAN 2012 molecular spectroscopic database. J. Quant. Spectrosc. Radiat. Transfer **130**, 4–50 (2013)
4. C. Lin, G.Y.L. Li, Terahertz communications: an array-of-subarrays solution. IEEE Commun. Mag. **54**(12), 124–131 (2016)
5. L.M. Zakrajsek, D.A. Pados, J.M. Jornet, Design and performance analysis of ultra-massive multi-carrier multiple input multiple output communications in the terahertz band. Image sensing technologies: materials, devices, systems, and applications IV. Int. Soc. Opt. Photonics **10209**, 102090A (2017)

6. S. Abadal, S.E. Hosseininejad, A. Cabellos-Aparicio, E. Alarcón, in *Graphene-Based Terahertz Antennas for Area-Constrained Applications*. 2017 40th International Conference on Telecommunications and Signal Processing (TSP) (IEEE, 2017, July), pp. 817–820
7. M.A. Jamshed, A. Nauman, M.A.B. Abbasi, S.W. Kim, Antenna selection and designing for THz applications: suitability and performance evaluation: a survey. IEEE Access **8**, 113246–113261 (2020)

Coding and Modulation for Terahertz

Mohamed El Jbari, Mohamed Moussaoui, and Noha Chahboun

Abstract Due to the huger demand for data traffic, today's network devices face great challenges and require urgent development of a high-speed broadband communications network. Efforts should be made to increase channel capacity. As its proportional to the channel bandwidth, the most effective way to rapidly expand channel capacity is to increase the channel bandwidth and expand the available spectrum. In this context, it is inevitable to switch to the terahertz (THz) band of 0.1–10 THz with correspondent wavelength range of 3 mm at 30 μm, which is an area that has not been thoroughly explored and has a very wide application value and development space. THz is a key enabler of future fifth-generation (5G) and sixth-generation (6) wireless communication systems. It shows great potential to mix an incredibly wide variety of applications and devices with Ultra-high Data Rate rates up to Terabits per second. Despite its characteristics of high-speed transmission, wide bandwidth, and high security, terahertz faces various challenges; including the path loss is very sensitive to water concentration and T_X–R_X distance. The frequency and distance dependence of terahertz (THz) propagation channel can seriously degrade the Bit Error Rate (BER) performance. In order to reach Ultra-high Data Rate THz Communication, it is imperative to develop novel modulation schemes and waveform designs that provide a good compromise between low complexity, ultra-high throughput, and low energy consumption. In addition, there is a necessity to modify, adapt, and improve conventional Error-Control Coding mechanisms to find the tradeoffs between error correction capabilities, energy consumption and latency, with the main motivation on improving communication reliability for ultra-high-speed wireless THz communication. This chapter mainly presents the principle of terahertz communication and provides the advances in coding and modulation for ultra-high-speed THz communications.

M. El Jbari (✉) · M. Moussaoui · N. Chahboun
Information and Communication Technologies Laboratory (LabTIC), National School of Applied Sciences of Tangier, Abdelmalek Essaâdi University Tetuan, ENSA of Tangier, Ziaten Road, BP 1818 Tangier, Morocco
e-mail: mohamed.eljbari2@etu.uae.ac.ma

M. Moussaoui
e-mail: m.moussaoui@uae.ac.ma

M. El Ghzaoui et al. (eds.), *Terahertz Wireless Communication Components and System Technologies*, https://doi.org/10.1007/978-981-16-9182-9_5

Keywords Terahertz (THz) · Modulation schemes · Pulse-based modulation · Carrier-based modulation · Forward error correction (FEC) · Turbo codes · LDPC codes · Polar codes

1 Introduction

To meet ultra-high-speed throughput requirements in wireless communication systems, complex digital communication schemes and advanced signal processing techniques have been used to boost the spectral efficiency and the channel capacity [1]. However, as it's proportional to the channel bandwidth, the most effective way to rapidly expand channel capacity is to increase the channel bandwidth and expand the available spectrum to run bandwidth-intensive applications for ultra-broadband wireless communications.

In this context, it is inevitable to switch to THz band which is an area that has not been thoroughly explored, and it has a wide potential applications.

It is for this reason, the IEEE 802.15 terahertz Interest Group has been created in 2008 to study the possibility of the terahertz for networking wireless communication band [2]. As in 2014, there is an official IEEE standardization commission called 100 Gbps.

As shown in Fig. 1, THz and sub-THz communication involve the electromagnetic spectrum domain in the range of 100 GHz (3 mm) to 10 THz (30 μm) and sub-THz conversion range is between 0.1 and 0.3 THz [3].

THz communication systems can use the available bandwidth to attain terabits per second (Tbps) throughput without any additional sophisticated Spectral Efficiency Improving Techniques.

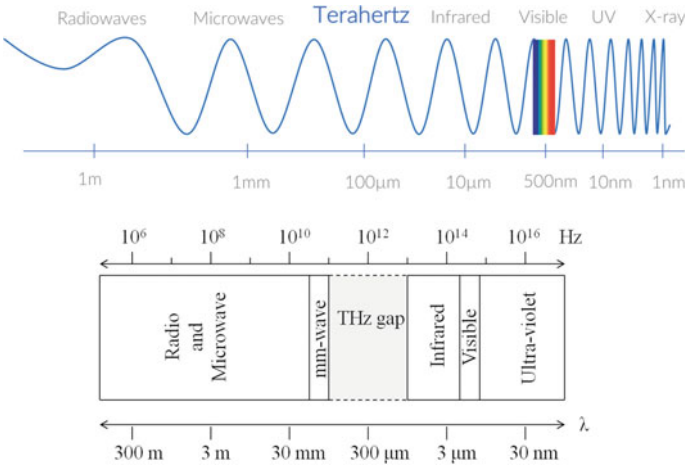

Fig. 1 Diagram showing of location for THz band in the electromagnetic spectrum

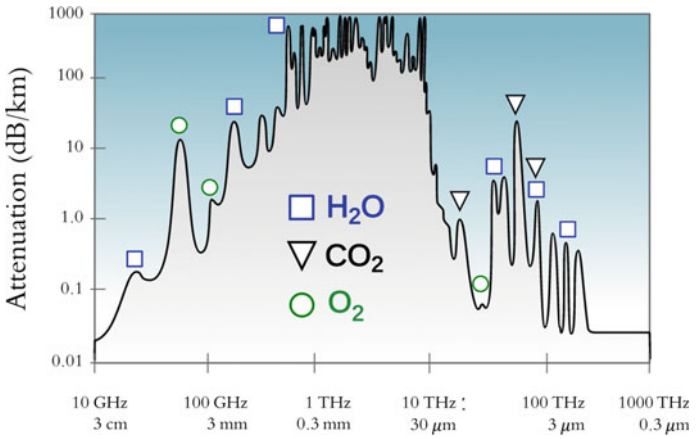

Fig. 2 Atmospheric attenuation (dB/km) at various frequencies

There are many challenges that need to be addressed in signal and communication processing for terahertz (THz) communications.

Figure 2 shows atmospheric attenuation (dB/km) at various frequencies, the signal attenuation clearly peaks between 1 and 10 THz [4]. Propagation losses arise when terahertz waves are absorbed by water vapor, carbon dioxide, and molecular oxygen. As a result, the usable bandwidth is considerably shrinking with distance and ranges.

For very short-range communications less than one meter, molecular absorption loss seems to be insignificant, and thus, the THz band behaves as terahertz wide transmission window [5]. This substantial large bandwidth has encouraged the use of modulation schemes based on exchange of 100 fs-long pulses is TS-OOK [6] that take into consideration the difficulty of generating high-power of carrier signals for THz band frequencies. It has been shown that as the molecular absorption is exponentially increasing with distance; the available bandwidth of the THz transmission is drastically shrinking [7–10]. And thus, the THz band is spited in multiple transmission windows, tens to hundreds of GHz wide each. For longer distances, the modulations that dynamically adjust the transmitted waveform according to the transmission distance appear more convenient and ultra-massive MIMO (UM-MIMO) antenna systems [11–13] are needed to overcome the severe power limitations and path losses.

The path loss and rapid modification of radio waves caused atmospheric scintillation will significantly degrade the signal-to-noise ratio (SNR) and deteriorate the bit error rate (BER) rendering of THz wireless communication.

Error-Control-Coding Techniques can be a favorable solution to increase the system performance in channels. Traditional Error-Control Coding Techniques, such as automatic repeat request (ARQ), forward error correction (FEC), or Hybrid automatic repeat request (HARQ) techniques [14], are most complex and computationally intense components in digital baseband signal processing. Encode-decode of data packet necessity the time longer than that of their transmission. Because of

the very limited computational capability and energy storage capacity of Nano-devices, there is a necessity to modify, adapt, and improve conventional Error-Control Coding mechanisms to find the tradeoffs between error correction capabilities, energy consumption, and latency, with the main goal is to improve communication reliability for ultra-high-speed wireless THz communication. The EPIC project [15, 16] is dedicated exclusively to channel coding and is investigating the coding families' turbo, low-density parity check (LDPC), low-density, and polar codes especially to efficient implementations. This chapter mainly presents the principle of terahertz communication and provides for readers the advances in coding and modulation for ultra-high-speed THz communications.

2 Modulations Schemes for THz Communications

The classical approach used to improve the throughput is based on using higher-order modulation formats and size of MIMO antenna array. Designing similar systems for 100 Tb/s requires an extremely large signal-to-noise ratio (SNR) to ensure high performance. However, the distance and frequency dependent of the THz channel significantly degrade the signal to noise ratio (SNR) and deteriorate the bit error rate (BER) performance. In addition, Carrier-based modulation is particularly challenging at THz band owing to the faculties to generate more than short high-frequency pulses of a few mill-watts (mW). In order to reach Ultra-high Data Rate THz Communication, it is imperative to develop novel modulation schemes waveform design for THz Band communication that provide a concession between low complexity and high throughput with a limited power consumption.

2.1 Pulse-Based Modulation

2.1.1 Time Spread On–Off Keying Modulation

Time Spread On–Off Keying (TS-OOK) is a technical modulation scheme used for short-rang communication, this technique serves to share the channel among different Nano-devices in THz band. TS-OOK is constructed on the transmission and reception of 100 fs-long pulses. Logic '1' is modulated by using 100 fs-long pulse, and the logic '0' is modulated by silence [17].

The time interval between consecutive logical transmissions is fixed such that the apparatus need not sense the channel all the time for all communication, and much longer than the period pulse i.e., silence zones. This technique offers multiple access mechanisms between the communication devices.

A nano-device does not all the time of the detection by channel, but it just delays for the next transmission. The multiple access mechanism does not necessitate close synchronization between nano-devices constantly. Transceivers will be synchronized

about the preamble of the package, in effect, the receiver detects the packet all over the sequence transmission.

In the scheme of TS-OOK modulation, the signal is transmitted on one basis. Since information is encoded in the energy of the signal, demodulation can be realized using an envelope detector [18].

The transmitted signal is given by:

$$s_T^u(t) = \sum_{i=1}^{K} A_i^u \, p(t - iT - \tau^u) \tag{1}$$

where A_i^u mentions to the amplitude of the i-th symbol of transmission u (i.e., '0' or '1'), K is the number of symbols in the packet, p represent a pulse with period time T_p, T_s is inter-arrival time, and τ^u is initial transmission time retard.

The TS-OOK modulation funding a large number about the devices are transmitted concurrently up to a few Tbits/s, since the time period symbols T_s is very longer compared to the pulse period T_p.

The symbol rate as following:

$$\beta = \frac{T_\mathrm{s}}{T_\mathrm{p}} \gg 1 \tag{2}$$

Despite its advantages, TS-OOK suffers of two main drawbacks; firstly, the complexity to detecting the best value from the symbol rate to preserve a greater throughput of the device depending on the number of active devices. i.e, if $\beta = 1$, the communication symbols sent by the device will burst and reach the maximum rate for each device. Therefore, only one device can access the channel at a time. As β increases, the throughput per device is reduced.

Second drawbacks, if the two transmitters T_{x1} and T_{x2} start to transmit at two different times, respectively, τ_1 and τ_2. We will have a collision production between two synchronized communications at the level of the receiver where:

$$(\tau_1 + t_{\mathrm{prop}}^1) \bmod T_\mathrm{s} = (\tau_2 + t_{\mathrm{prop}}^2) \bmod T_\mathrm{s} \tag{3}$$

where t_{prop}^1 and t_{prop}^2 represents the signal propagation time for T_{x1} (resp.T_{x2}) to receiver.

In the case where the transmitters and the receiver are stationary, we fix t_{prop}^1 and t_{prop}^2, the collision make the interest every symbols up to the one of about two communications is completed.

The probabilities of pulses collision and the same channel collision concerning two communications are expressed by:

$$\mathrm{Prob}_{\mathrm{collision}} = \mathrm{Prob}_{\text{co-channel}} = \frac{1}{\beta} = \frac{T_\mathrm{s}}{T_\mathrm{p}} \tag{4}$$

From the co-channel collision, we can check the packet error correction in the receiver, as a critical measuring the quality of the radio access modulation indicates a co-channel collision.

On the receiver side, the signal formula received by a device v can be expressed by:

$$s_R^v(t) = \sum_{i=1}^{K} A_i^v \, p(t - iT_s - \tau^u) * h^{u,v}(t) + n_i^{u,v}(t) \tag{5}$$

where $h^{u,v}$ is the system impulse transfer between the devices u and v, in [8], and be determined by on the optimal conditions and the space from the transmitter–receiver (u, v). $n_i^{u,v}$ is the noise by the transmitter symbol i about (u, v).

Devices start transmission at any time its synchronization or control by same type of the central entity networking, because $T_s \gg T_p$.

However, the possibility of using the channel simultaneously by several devices because of very short $T_p \approx 100\,\text{fs}$, which implies a low probability of collision between the symbols and on the other hand between the silences.

Figure 3 shows an example of TS-OOK modulation for two devices; T_{x1} and T_{x2} which transmit different binary sequences to another device R_x. The higher plot represents the sequence '1011', which is transmitted by T_{x1}. The initial Gaussian pulse define the logical '1', and the logical '0' is defined by silence. This signal propagates in the channel (therefore, deformed and retarded). In parallel, the next plot represents the sequence transmitted by T_{x2}, '1101'. This next plot transmitted is delayed by the receiver whether the first transmitter.

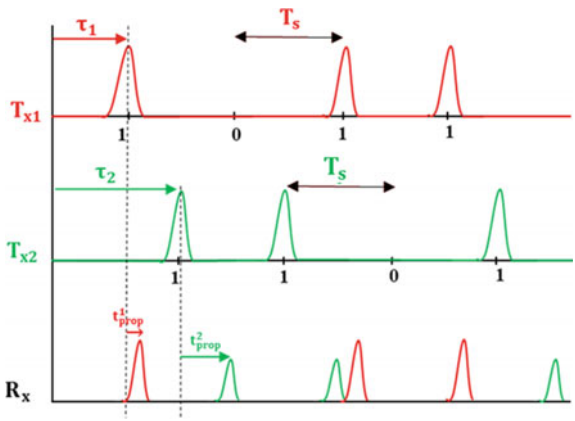

Fig. 3 TS-OOK modulation utilized in terahertz communication

2.1.2 RD-TS-OOK Modulation

TS-OOK has a native limitation in a user data collision during a slot, which results in a collision for all slots. Then, it is necessary to vary the duration of the time slots of the users, i.e., their transmission rate; Rate Division Time Spread On–Off Keying (RD-TS-OOK) is an improvement in terms of TS-OOK, where the transmitter starts by declaring we can use β before sending the data.

RD-TS-OOK can be uses a different symbol rates in terahertz communications by devices reduces the effect of selected interference (co-channel collision) [6].

Certainly, either two communications $C1$ and $C2$ are generated a co-channel collision under the following two conditions:

$$\left[\beta_{C1} \bmod \beta_{C2} = 0 \text{ and } (\tau_1 + t^1_{\text{prop}}) \bmod T_{S_{C1}} = (\tau_2 + t^2_{\text{prop}}) \bmod T_{S_{C2}}\right]$$

or

$$\left[\beta_{C2} \bmod \beta_{C1} = 0 \text{ and } (\tau_1 + t^1_{\text{prop}}) \bmod T_{S_{C1}} = (\tau_2 + t^2_{\text{prop}}) \bmod T_{S_{C2}}\right] \quad (6)$$

In Fig. 2; a collision occurs at a receptor, then the next collision between the nano-devices does not follow, except before a period of least common multiple LCM (β_{c1}, β_{c2}), where:

$$\text{LCM}(\beta_{c1}, \beta_{c2}) = \beta_{c1} \times \beta_{c2} \quad (7)$$

The collision probability in the same co-channel of the RD-TS-OOK modulation is writing as:

$$\text{Prob}_{\text{co-channel}} = \frac{1}{\beta_{\max} - \beta_{\min}} \times \frac{1}{\beta} \quad (8)$$

Figure 4 shows the example of RD-TS-OOK modulation for two devices; T_{x1} and T_{x2} transmit at the same time different binary sequences τ_1 and τ_2 to a third device which receives R_x. The higher plot represents the sequence '1011', which is transmitted by T_{x1} white a symbol rate T_{s1}. This signal propagates in the channel (therefore, deformed and retarded). In parallel, the next plot represents the sequence transmitter by T_{x2} white a different symbol rate T_{s2}, '1101'. This next transmitter is delayed about the receiver whether the first transmitter. In the signal received at R_x, the second symbol of T_{x1} is collided by the second symbol of T_{x2}. To avoid collisions, you have to use different slots duration.

RD-TS-OOK technique has drawbacks. Firstly, we conclude the symbol rate is selected made at random, does not modulate the regular use about the various β. (i.e. induces an unbalancing between devices, using a $\beta_{\min}$ or $\beta_{\max}$). Secondly, The RD-TS-OOK modulation does not keep the consideration of the traffic load, in order to select the value of $\beta_{\min}$ and $\beta_{\max}$.

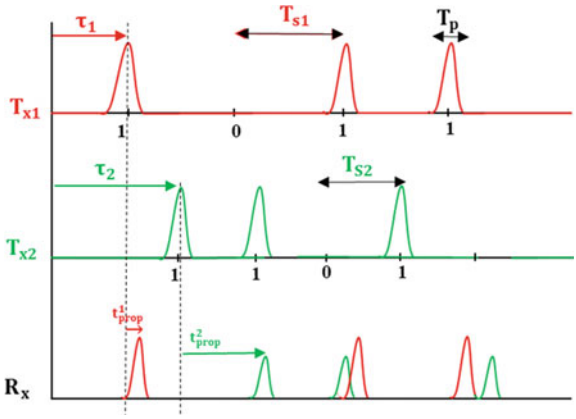

Fig. 4 RD-TS-OOK modulation

2.1.3 DS-OOK Modulation

In Direct Sequence DS-OOK, each transmitter's data with another symbol rates, the access channel is authorized by multiple users concurrently with minimum overlap. DS is used the every codes about the users, in transmission the signal crossing the Thz channel, identical codes are used to dispread the signal at the receiver side [19].

Figure 5 shows DS-OOK communications, the pulse wave for THz-band nano-communication has a Gaussian unicycle with a pulse size of around 100 fs expressed as:

$$p(t) = 2\sqrt{e}A\pi t f_c \exp\left[-2(\pi f_c t)^2\right] \tag{9}$$

where A, and f_c are the amplitude and the frequency, respectively, of the pulse.

The signal propagate by DS-OOK, with the multiplication of all pulse for the user-specific propagate code. The transmitted waveform of the user k is giving by:

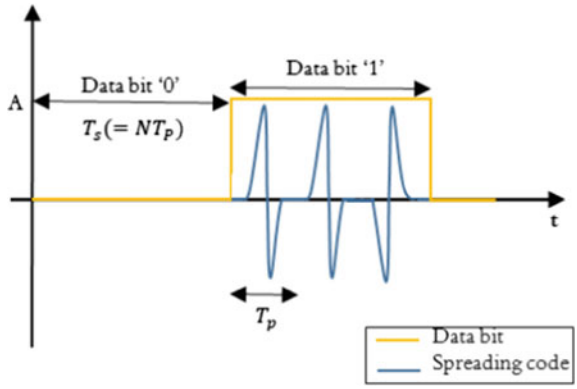

Fig. 5 Signal mechanism of DS-OOK technique

$$s^k(t) = \sum_{i=-\infty}^{\infty} \sum_{n=0}^{N-1} p\left(t - iT_s - nT_p\right) b_j^k a_n^k \tag{10}$$

where the modulated data symbol is b_j^k, and a_n^k is the spreads code about user k. Then, $T_s = NT_p$ is the symbol period, T_p is the single pulse time period, and N number of pulses data bit [20].

On the receiver side, the signal received contain message information on the expected retard and the spread code for the 0-th user. The signal form is represented by:

$$r(t) = s^0(t) * h^0(t) + M(t) + n(t) \tag{11}$$

where $s^0(t)$ is the user's signal and $h^0(t)$ is the channel impulse response. $M(t)$ is multiple-access interference (MAI) at the receiver, such as:

$$M(t) = \sum_{k=1}^{K-1} s^k(t) * h(t) + n(t) \tag{12}$$

where $n(t)$ is the THz band noise.

DS-OOK is a modulation protocol for THz band of multiple-access communications than a correlator receiver.

2.2 Carrier-Based Modulation

Carrier-based modulation techniques enable for the utilization of wider spectrum bandwidths and shorter communication distances at perfect higher frequencies, allowing for effective frequency planning on spectra without absorption and minimizing noisy channel caused noise. At THz frequencies and at long distances, molecule absorption losses outnumber propagation losses. Simple modulation methods that necessitate low-complexity digital demodulation are given priority (binary phase-shift keying and amplitude shift keying).

2.2.1 Single-Carrier

Single-Carrier (SC) modulations are favorable compared to orthogonal frequency division multiplexing (OFDM), despite the difficulty of implementation in terahertz communications. However, can be used in certain indoor THz communications, but with multipath frequency selectivity in the channels, exactly at the receiver side.

2.2.2 Multi-carrier

Multi-carrier reveals to be one of the most promising modulation schemes, and it is defined as a form of multi-carrier modulation of multiple orthogonal sub carrier frequencies of smaller bandwidth. However, there are many challenges remain to be overcome in order to support multi-carrier in the THz region as: high complexity transceiver, high PAPR, and stricter frequency synchronization. In order to address these challenges, one of the promising multi-carrier modulation schemes is the so-called Distance-Aware Multi-Carriers (DAMC) for terahertz communication at distances from meters to kilometers. DAMC modulation allows adaptive transmissions of various symbols on non-overlapping and regularly spaced sub-windows in parallel. The DAMC scheme realized in a centralized control unit was proposed in [21].

Figure 6 shows the three stages of DAMC; in the first step, the available transmission windows identifies and selected by the transmitter at a known communication length and a path loss threshold value. Second step, all window are distributed into some non-interfering sub-windows that are used about the transmission multi-carrier signals. Last step, every carrier signal have a modulation with M-QAM, such as order, M, is dependent on meeting the bit error rate (BER) and transmission power exigency at the receiver (i.e., to maximize the data rate and increase the bandwidth efficiency, thus to minimize power consumption keeping a minimum rate). For example, with 16-ary quadrature amplitude modulation (16-QAM) needs a signal-to-noise ratio (SNR) of 14.9 dB for a bit error ratio (BER) of 10^{-6}.

As Shown in Fig. 7, the transmitter signal $s(r, t)$ is generated by multi-carrier modulator, its expression is given by:

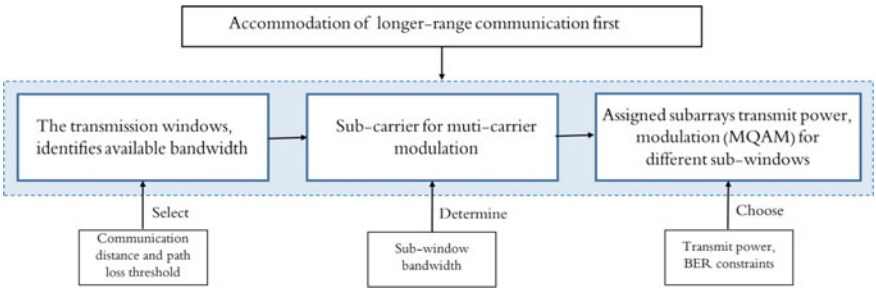

Fig. 6 Planning of DAMC modulation control unit of in THz communication band

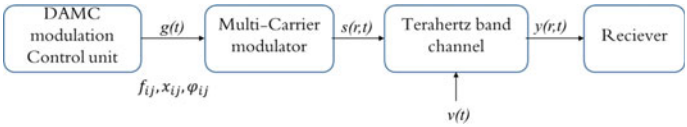

Fig. 7 Schematic model of DAMC modulation communication

$$s(r,t) = \sum_{i=1}^{M(r)} \sum_{j=1}^{N_i} x_{ij}(r) g(t) \cos\left[2\pi f_{ij}(r).t + \varphi_{ij}(r)\right] \tag{13}$$

where M is the total number of transmission windows that is distance-adaptive, N_i is the number of sub-windows in ith transmission window. In the jth sub-window of the ith window x_{ij} is the complex symbol for the long communication length r, f_{ij} and φ_{ij} are the carrier frequency and the phase offset, respectively. $g(t)$ is a raised cosine pulse with roll-off factor that a relates to the sub-window bandwidth

$$BW_g = \frac{1+\beta}{T_s} = (1+\beta) R_s \tag{14}$$

where T_s is the symbol duration, which $0 \leq t \leq T_s$, and R_s is the transmitted symbol rate.

The receiver signal, $y(r,t)$, is writing by:

$$y(r,t) = s(r,t) * h(r,t) + v(t) \tag{15}$$

where h is the transfer function of THz band transfer channel, and v is the total noise with power spectral density Nw, (i.e., the noisy molecular absorption [22] and the thermal noise at the receiver).

As shown in Fig. 8, a Multi-carrier modulation is divided a high density digital stream into several low bit-rate schemes and transmit in parallel (Sub-Carriers).

3 Coding Schemes for THz Communications

Due the very energy storage capacity and limited calculator capability of Nano-devices [23], there is a necessity to modify, adapt, and improve conventional Error-Control Coding mechanisms to find the trade-offs between energy consumption, error correction capabilities, and latency, with the main motivation on improving communication reliability for ultra-high-speed wireless THz communication. The EPIC project [17, 18] is dedicated exclusively to channel coding and is investigating the coding families, LDPC codes, turbo codes; and polar codes, especially to efficient implementations.

Turbo encode-decoding is ingrained serial; and LDPC Code decoding is ingrained parallel. Polar encode-decoding is inherently performant serial on a code tree structure. Thus, the challenges for decoder implementations achieving 100 Gbit/s and beyond are fundamentally different between the different coding schemes (i.e., turbo, LDPC, and Polar codes). The highly parallel nature of LDPC decoding leads to higher throughput [24]. Turbo and Polar codes offer a much greater degree of flexibility in block sizes and code rates [25].

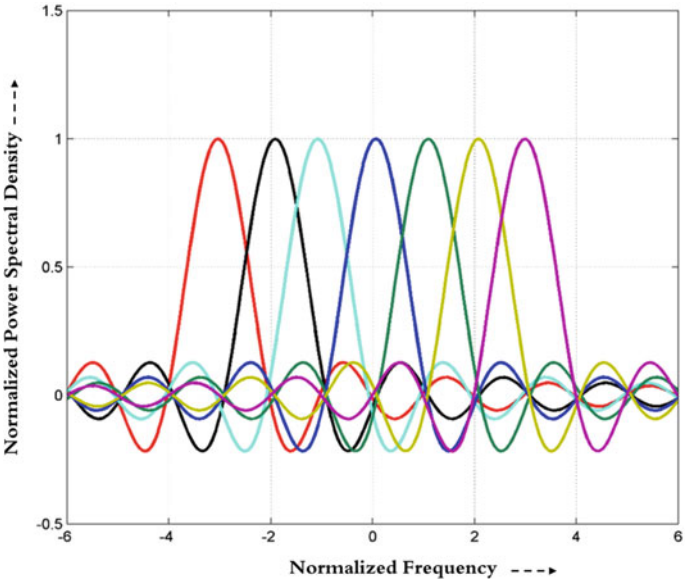

Fig. 8 Power spectral density of mutli-carrier system

3.1 LDPC Code

Low density parity check (LDPC) code is one of the forward error correction (FEC) schemes; it is more effective by their better performance, decoding complexity, and to provide good quality of THz communication band, and LDPC remains a good coding scheme technique. The schema block of LDPC coding based TS-OOK modulation is given in Fig. 9. First rediscovered by Robert Gallager [24], many researches have shown novel LDPC codes which are well generalized providing the practical advantages over turbo codes.

LDPC codes can be used in long distance wireless communication. LDPC code is a linear error-correcting code who has a parity check matrix H, and contains rows and the columns with less to 1's compared to 0's.

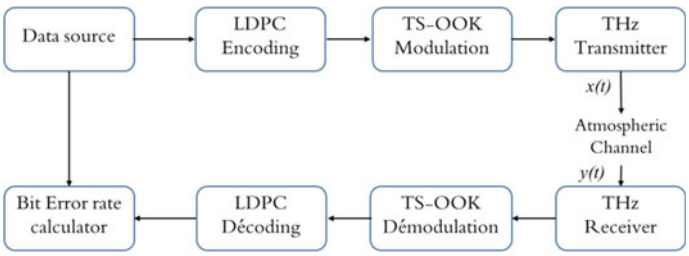

Fig. 9 Schema block of LDPC coding scheme based TS-OOK modulation

LDPC codes are classified into two types of codes; the first is regular LDPC, and the second is irregular LDPC codes. Gallager codes is an original regular binary of LDPC codes. However, the matrix $H_{n\times(n-k)}$ is composed by number w_c of ones in any column and the number w_r of ones in any row, which n is the number of bits in the code-word, and k is bits information symbol [25]. If both conditions are satisfied (i.e., $(n-k)w_r = nw_c$ thus $w_c < w_r$) [21], the parity check matrix is said to be of low density.

We call an LDPC code $(n,\ w_c,\ w_r)$ of length n, and in general the matrix H has a very high dimension, which a very low density of element '1'.

Consider the parity check H matrix, for example, *($n = 20$, $w_c = 3$, $w_r = 4$)* first code proposed with Gallager [26]:

$$\begin{bmatrix}
1&1&1&1&0&0&0&0&0&0&0&0&0&0&0&0&0&0&0&0\\
0&0&0&0&1&1&1&1&0&0&0&0&0&0&0&0&0&0&0&0\\
0&0&0&0&0&0&0&0&1&1&1&1&0&0&0&0&0&0&0&0\\
0&0&0&0&0&0&0&0&0&0&0&0&1&1&1&1&0&0&0&0\\
0&0&0&0&0&0&0&0&0&0&0&0&0&0&0&0&1&1&1&1\\
1&0&0&0&1&0&0&0&1&0&0&0&1&0&0&0&0&0&0&0\\
0&1&0&0&0&1&0&0&0&1&0&0&0&0&0&0&1&0&0&0\\
0&0&1&0&0&0&1&0&0&0&1&0&0&0&1&0&0&1&0&0\\
0&0&0&1&0&0&0&1&0&0&0&1&0&0&0&1&0&0&1&0\\
0&0&0&0&0&0&0&1&0&0&0&1&0&0&0&1&0&0&0&1\\
1&0&0&0&0&1&0&0&0&0&0&1&0&0&0&0&0&1&0&0\\
0&1&0&0&0&0&1&0&0&0&1&0&0&0&0&1&0&0&0&0\\
0&0&1&0&0&0&0&1&0&0&0&0&1&0&0&0&0&0&1&0\\
0&0&0&1&0&0&0&0&1&0&0&0&0&1&0&0&1&0&0&0\\
0&0&0&0&1&0&0&0&0&1&0&0&0&0&1&0&0&0&0&1
\end{bmatrix} \tag{16}$$

The code rate of the linear regular LDPC code $C(n, w_c, w_r)$ is formulated by:

$$\mathcal{R} = \frac{w_r - w_c}{w_r} = \frac{k}{n} \tag{17}$$

For LDPC coding, a generating matrix G is derived from the parity check matrix H to eliminate Gaussian in modulo-2 arithmetic, such that H and G are formed differently. LDPC encoding is giving by matrix multiplication as

$$C = [b|m] = m.G \tag{18}$$

where b is the parity vector corresponding of m message vector.

The matrix generate LDPC codes is giving by:

$$G = \left[P_{k(n-k)}|I_k\right] = \left[H_2 H_1^{-1}|I_k\right] \tag{19}$$

where H_2 is the rectangular parameters matrix $(n-k) \times k$, and H_1 is the square parameters matrix $(n-k)^2$ used in the partitioning of matrix $H^T = \begin{bmatrix} H_1 \\ \vdots \\ H_2 \end{bmatrix}$. Then, $P_{k(n-k)}$ is the coefficient matrix, and I_k is identity matrix.

Many decoding algorithms exist for LDPC codes, but the two well-known types are Sum Product Algorithm (SPA) and Bit Flipping (BF). In this work, we study the SPA algorithms.

First, the bits received from the channel, and which are input to the LDPC decoder, and noisy which are called a posteriori probabilities after demodulation, which can be expressed as Log-likelihood ratios (LLR):

$$\mathrm{LR} = \log\left(\frac{p(x=0)}{p(x=1)}\right) = \log\left(\frac{1-p}{p}\right) \tag{20}$$

As shown in Fig. 10, the decoding procedure is considered as a transfer of some probabilities about the Variable nodes to the Check nodes (VC message) and vice versa (CV message). The SPA is used to maximize a posteriori probabilities (MAP) algorithms [27].

The first step for the VC message at the first iteration is the one-rank matrix of the LLRs:

$$M_{n\times m} = (r_{n\times 1}.1_{1\times m})^T \odot H_{n\times m} \tag{21}$$

where 1 is the matrix or vector of 1's, and $\odot$ denotes Hadamard (element-wise) product.

The algorithm consists of processing the VC message in the probability domain using the relationship between hyperbolic tangents and the neperian logarithm [28]. The transmission operation of the VC message is the multiplication (i.e., the probabilities) of ones elements in each row:

$$E_{r,c} = \log\left(\frac{1+\prod_{c'\in B_{r,c'\neq c}} \tan\left(M_{r,c'}/2\right)}{1-\prod_{c'\in B_{r,c'\neq c}} \tan\left(M_{r,c'}/2\right)}\right) = \log\left(\frac{1+\prod_{c'\in B_{r,c'\neq c}} M'_{r,c'}}{1-\prod_{c'\in B_{r,c'\neq c}} M'_{r,c'}}\right) \tag{22}$$

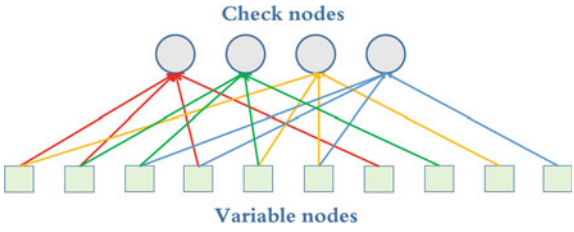

Fig. 10 The VC message flow chart

where r is the number of the row, c is the number of the column, B_r is the set of the 1's elements in r-th row, and $c' \neq c$ means that we exclude c-th variable node from the consideration.

Finally, in the first iteration, LLRs from the channel should be updated. Then, we sum up the information of rows in matrix E.

$$l_c = LR_c + \sum_{r \in A_c} E_{r,c} \tag{23}$$

where A_c is the series of Parity-Check matrix ones elements in the c-th column.

Then, we map up-to-date LLRs to binary symbol by the relationship:

$$z_c = \begin{cases} 0 \text{ if } l_c \geq 0 \\ 1 \text{ if } l_c < 0 \end{cases} \tag{24}$$

Then necessary condition should be checked:

$$s_{m\times 1} = H_{m\times n} \otimes z_{n\times 1} = \begin{cases} 0 & \text{then stop decoding} \\ 1 & \text{then continue decoding} \end{cases} \tag{25}$$

If the syndrome s is not the zero-vector decoding should be continued. Therefore, matrix M should be recalculated (Fig. 11):

$$M_{r,c} = \sum_{r' \in A_{c,r' \neq r}} E_{r',c} + LR_c \tag{26}$$

After that, for the second iteration, we have to repeat the iterations while s is a non-zero vector.

In THz wireless communication, it is necessary to have a long LDPC code length with low code rate. On the other hand, we must be taken into consideration the complexity of the system, the data rate, the transmission delay, and the bit error rate BER performance.

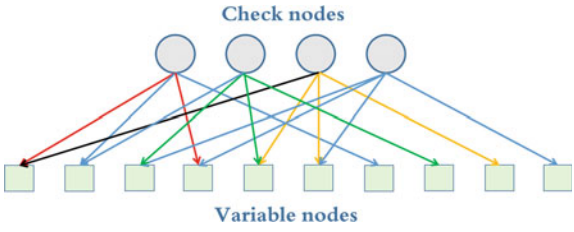

Fig. 11 The CV message flow chart

3.2 Turbo Code

Turbo codes are the groundbreaking codes introduced in [28, 29]. Turbo encoders use the best known systematic convolutional codes. As shown in Fig. 12, the implementation of turbo codes by the parallel concatenation of two recursive systematic convolutional (RSC) encoders. We will see in the following, the turbo encoding and the iterative turbo decoding. The RSCs encoders are a short constraint length to avoid excessive decoding complexity, and it is a code rate 1/3 encoder.

A row column interleave, one finds the data are written by row and read by column, in this way the random interleave provides in the data bits [30]. For a turbo encoder, the generating sequence is the feedback output. Figure 13 shows the recursive systematic convolutional (RSC) encoder [31] for the intended system. The generative sequence used for the encoding algorithm which is defined in the relationship that given by:

$$G(D) = \left[1, \frac{1 + D^2}{1 + D + D^2}\right] \tag{27}$$

where 1 is the systematic output.

Generation of the moderate weight turbo codes is realized by the combination of the low from RSC1 and the high-weight code from RSC2. Finally, one will have the transmission of the original input sequence x next to the two parity bit ranges are transmitted over the channel, where it is dropped to noise interference and attenuation. However, the bit error rates (BER) are different because the BER can be changed, as the input–output of the encoder. At $\frac{E_b}{N_0}$ SNR less, the BER of an RSC code should be minimized. The demodulator can express its trust in the value of each bit by

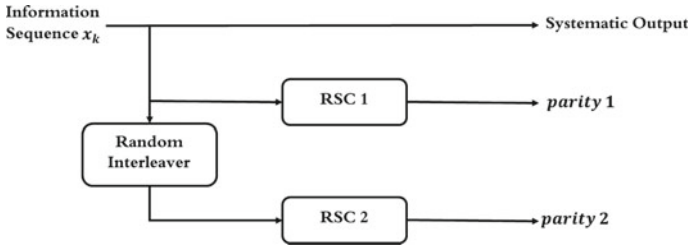

Fig. 12 Schema diagram for turbo encoder

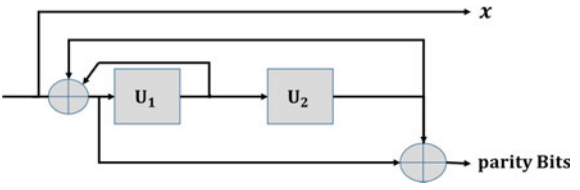

Fig. 13 Schema of (RSC) encoder

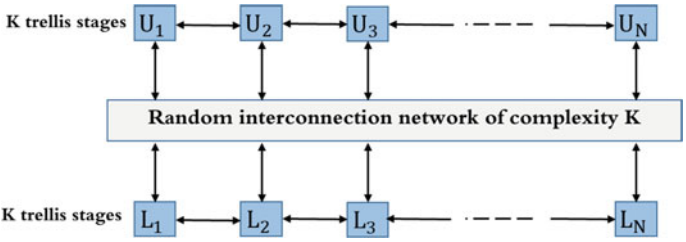

Fig. 14 Turbo decoder scheme

using the corresponding log likelihood ratio (LLR). Each LLR gives the logarithm of the probability ratio of the corresponding bit having the values '0' and '1', which receives the information iteratively, despite the uncertainty of the wireless channel.

The schematic diagram for Turbo decoder represent in Fig. 14. The output decoder produce a soft estimation of systematic bit expressed as LLRs.

$$L_i\left(\hat{x}(n)\right) = \left(\frac{P(x(n)=1|x', p_1', L_a(x)}{P(x(n)=0|x', p_1', L_a(x)}\right); \quad n = 1, 2, \ldots, N \tag{28}$$

where p_1' is the noise of the parity check bits, and the external bits information received by the first decoder is:

$$L_{e1}(x) = L_1(x) - L_a(x) - L_c x' \tag{29}$$

The term $L_c x'$ is the information provided by the noisy observation. The extrinsic information $L_{e1}(x)$ where x is interleaved before applying as input to the Bahl, Cocke, Jelinek, and Raviv algorithm (BCJR) in the second decoder [32].

3.3 Polar Code

Polar code is a novel type channel coding, and it was proposed by Erdal Arikan in 2009 [33]. Polar codes can attain the Shannon capacity for symmetric binary-input memoryless channels as the block dimension is sufficiently large. Low complexity of coding and decoding leads to this codes successful coding.

Throughout polar code length n, k message bits, the binary-input vector $u = (u_1, u_2, u_3, \ldots, u_n)$ may be made up of $(n - k)$ bits, and k information bits, with code rate $R = k/n$. The polar code-word x is defined by

$$x = uG_n \tag{30}$$

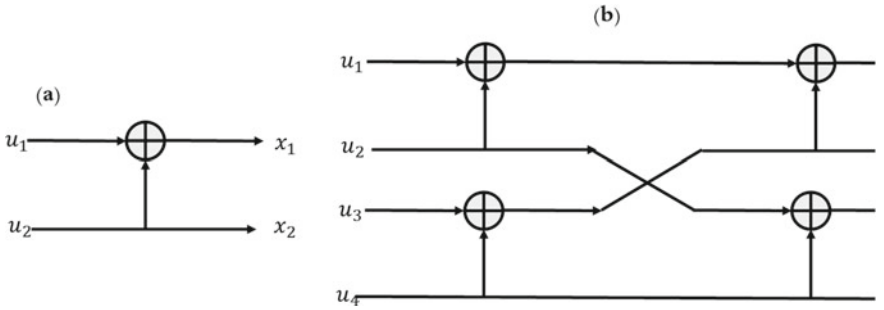

Fig. 15 Examples for polar encoder schemes: **a** $n = 2$, **b** $n = 4$

where G_n are generators matrix.

As shown in Fig. 15, polar decoding has variable node and check node, having a degree of 3 at most. The propagation of LLRs in the decoding butterfly diagram is from right to left. However, the appropriate performant decoding is computing the LLRs at each node. The LLRs is expressed as:

$$L_n^{(i)}(y_1^n, u_1^{i-1}) = \frac{w_n^{(i)}\left(y_1^n, u_1^{i-1} | u_i = 0\right)}{w_n^{(i)}\left(y_1^n, u_1^{i-1} | u_i = 1\right)} \tag{31}$$

where

$$\hat{u}_i = \begin{cases} 0, \text{ if } L_n^{(i)}(y_1^n, u_1^{i-1}) \geq 1 \\ 1, \text{ or else} \end{cases} \tag{32}$$

Polar coding scheme usually approaches with successively cancelation decoder (SCD) as a sub-optimal decoding method [31, 33].

In Fig. 16, we used a successive cancelation list (SCL) of cancelation decoders which is in parallel for a production of a list of candidate decisions and choose the most probable word in the list. This SCL decoder gives a trace of several decoding results in lieu of one. The decoding path is divided into two new paths one ending in '0' and the other ending in '1' for each bit of information; the paths should be pruned to enable the maximum number of paths to list size L.

After reading about the sources of error in THz wireless communication systems, code schemes such as LDPC and turbo and polar codes can be considered as possible coding scheme candidates. Then, the existing coding schemes should be adopted; the disruptive types of channel coding schemes with very low complexity can be developed for THz communications. Finally, the development of FEC technology needs to be validated and demonstrated in future THz chipset.

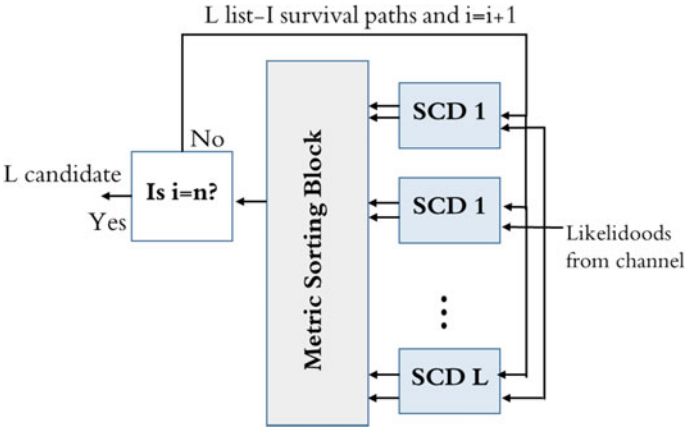

Fig. 16 Illustration diagram SC list decoder

4 Conclusion

The objective of this chapter was to present the efficient modulation techniques that are usable in wireless communication in the terahertz band, as well as the different types of coding that are applicable in the THz band (i.e., forward error correction (FEC), in order to minimize errors at the transmitter–receiver side of communication. Firstly, we give a lecture on the modulation protocols pulse-based modulation (PBM); TS-OOK is characterized by 100 femto-second-long, RD-TS-OOK, and DS-OOK modulation schemes. Carrier-based modulation is treated in two types, single-carrier modulation and multi-carrier modulation in detail. However, multi-carrier schemes are more adaptive and suggested modulation techniques. The second part, we have describe the working principle of each coding scheme, LDPC, turbo, and polar codes. In this work, we conclude that LDPC and turbo codes have a better hardware efficiency, so successive cancelation list SCL decoding is necessary to have a performance at the level of LDPC turbo codes and very low complexity of THz communication. However, a good throughput is achieved by these decoders; it is not like the polar coding that needs improvements made in order to have equality and overcome the problems at the transmission channel. This chapter mainly presents the principle of terahertz communication and provides for readers the advances in coding and modulation for ultra-high-speed THz communications.

References

1. H. Song, T. Nagatsuma, Present and future of terahertz communications. IEEE Trans. Terahertz Sci. Technol. **1**(1), 256–263 (2011)
2. IEEE-802.15-WPAN, Terahertz interest group (IGthz) (2014). [Online]. Available: http://www.

ieee802.org/15/pub/IGthzOLD.html
3. I.F. Akyildiz, J.M. Jornet, C. Han, Terahertz band: next frontier for wireless communications. Phys. Commun. **12**, 16–32 (2014)
4. M.J. Rosker, H.B. Wallace, Imaging through the atmosphere at terahertz frequencies, in *2007 IEEE MTT-S International Microwave Symposium Digest*, art. no. 4263933, pp. 773–776
5. J.M. Jornet, I.F. Akyildiz, Channel modeling and capacity analysis of electromagnetic wireless nanonetworks in the terahertz band. IEEE Trans. Wirel. Commun. **10**(10), 3211–3221 (2011)
6. J.M. Jornet, I.F. Akyildiz, Femtosecond-long pulse-based modulation for terahertz band communication in nanonetworks. IEEE Trans. Commun. **62**(5), 1742–1754 (2014)
7. S. Elaage, M. El Ghzaoui, A. Hmamou, J. Foshi, J. Mestoui, MB-OOK transceiver design for terahertz wireless communication systems. Int. J. Syst. Control Commun. **12**(4), 309–326 (2021). https://doi.org/10.1504/IJSCC.2021.118627
8. C. Han, I.F. Akyildiz, Distance-aware multi-carrier (DAMC) modulation in terahertz band communication, in *Proceedings IEEE International Conference on Communications* (2014), pp. 5461–5467
9. C. Han, A.O. Bicen, I.F. Akyildiz, Multi-wideband waveform design for distance-adaptive wireless communications in the terahertz band. IEEE Trans. Signal Process. **64**(4), 910–922 (2015)
10. M. El Ghzaoui, J. Mestoui, A. Hmamou, E. Serghini, Performance analysis of multiband on–off keying pulse modulation with noncoherent receiver for THz applications. Microwave Opt. Technol. Lett. (2021). https://doi.org/10.1002/mop.33051
11. A. Faisal, H. Sarieddeen, H. Dahrouj, T.Y. Al-Naffouri, M.S. Alouini, Ultramassive MIMO systems at terahertz bands: prospects and challenges. IEEE Veh. Technol. Mag. **15**(4), 33–42 (2020)
12. I.F. Akyildiz, J.M. Jornet, Realizing ultra-massive MIMO (1024 × 1024) communication in the (0.06-10) terahertz band. Nano Commun. Netw. **8**, 46–54 (2016)
13. M. El Ghzaoui, A. Hmamou, J. Foshi, J. Mestoui, Compensation of non-linear distortion effects in MIMO-OFDM systems using constant envelope OFDM for 5G applications. J. Circuits, Syst. Comput. **29**(16), 2050257 (2020)
14. S.A. Busari, K.M.S. Huq, S. Mumtaz, J. Rodriguez, Terahertz massive MIMO for beyond-5G wireless communication, in *Proceedings IEEE International Conference on Communications (ICC)*, May 2019, pp. 1–6
15. M. Patil, R.C. Biradar, Dynamic error control scheme based on channel characteristics in wireless sensor networks, in *IEEE International Conference on Recent Trends in Electronics, Information and Communication Technology* (2018), pp. 736–741
16. N. Wehn, O. Sahin, Next-generation channel coding towards Terabit/s wireless communications, in *European Conference on Networks and Communication (EuCNC)*, Ljubljana, Slovenia, 18–21 June 2018, [online]. https://doi.org/10.5281/zenodo.1346686
17. N. Wehn, Channel coding for Tb/s communications, in *Keynote at 19th International Forum on MPSoC in Hakone, Kanagaw*
18. L. Aliouat, M. Rahmani, H. Mabed, J. Bourgeois, Enhancement and performance analysis of channel access mechanisms in Terahertz band. Nano Commun. Netw. **29**, 100364 (2021). ISSN 1878-7789. https://doi.org/10.1016/j.nancom.2021.100364
19. P. Singh, B.W. Kim, S.Y. Jung, DS-OOK for terahertz band nanonetworks. Natl. Acad. Sci. Lett. **44**, 43–46 (2021). https://doi.org/10.1007/s40009-020-00955-7
20. T. Keller, L. Hanzo, Adaptive multicarrier modulation: a convenient framework for time-frequency processing in wireless communications. Proc. IEEE **88**(5), 611–640 (2000)
21. T. Ohtsuki, Multiple-subcarrier modulation in optical wireless communications. IEEE Commun. Mag. **41**(3), 74–79 (2003)
22. C. Han, I.F. Akyildiz, Distance-aware multi-carrier (DAMC) modulation in terahertz band communication, in *2014 IEEE International Conference on Communications (ICC)* (2014), pp. 5461–5467. https://doi.org/10.1109/ICC.2014.6884190
23. J. Jornet, I. Akyildiz, Channel modeling and capacity analysis for electromagnetic wireless nanonetworks in the terahertz band. IEEE Trans. Wirel. Commun. **10**(10) (2011)

24. S. Weithoffer, M. Herrmann, C. Kestel, N. Wehn, Advanced wireless digital baseband signal processing beyond 100 Gbit/s, in *2017 IEEE International Workshop on Signal Processing Systems (SiPS)* (2017), pp. 1–6
25. R. Gallager, Low-density parity-check codes. IRE Trans. Inf. Theory **8**(1), 21–28 (1962)
26. Z. Tu, S. Zhang, Overview of LDPC codes, in 7*th International Conference on Computer and Information Technology, CIT 2007* (IEEE, 2007), pp. 469–474
27. M.M. Mansour, N.R. Shanbhag, High-throughput LDPC decoders. IEEE Trans. VLSI Syst. **11**(6), 976–996 (2003)
28. S.J. Johnson, *Introducing Low-Density Parity-Check Codes* (University of Newcastle, Australia, 2006), p. V1
29. C. Berrou, A. Glavieux, P. Thithimajshima, Near shannon limit error-correcting coding and decoding: turbo-codes, in *Proceedings of ICC 1993*, Geneva, Switzerland (pp. 1064–1070), May 1993
30. C. Berrou, A. Glavieux, Near optimum error correcting coding and decoding: turbo-codes. IEEE Trans. Commun. **44**(10), 1261–1271 (1996)
31. O. Takeshita, D. Costello, New deterministic interleaver designs for turbo codes. IEEE Trans. Inf. Theory **46**(6), 1988–2006 (2000)
32. K.D. Rao, *Channel Coding Techniques for Wireless Communications*, Forum for Interdisciplinary Mathematics. pp. 272–301, 351–384. https://doi.org/10.1007/978-981-15-0561-4_6
33. Y.D. Beyene, R. Jantti, K. Ruttik, S. Iraji, On the performance of narrow-band internet of things (NB-IoT), in *2017 IEEE Wireless Communications and Networking Conference (WCNC)*, March 2017, pp. 1–6

Terahertz Band Frequency Tuning for a CMOS Active Filter

Imane Halkhams, Wafae El Hamdani, Said Mazer, Moulhime El Bekkali, and Mohammed Fattah

Abstract The Terahertz band, which has remained for a long time little used, is currently in full emergence. In addition to high performance, terahertz (THz) wireless communications appear to be an attractive and complementary technology compared to other less flexible and more expensive technologies. The technological revolution in wireless and high-speed telecommunications applications is pushing researchers to create powerful and compact components. To explore the efficiency of filtering in the Terahertz band, we have designed a frequency tunable bandpass filter. The proposed topology is composed of two transconductances and input and output adaptation stages designing the bandpass filter. The central frequency is 129 GHz, with input and output reflection coefficients of −27.6 dB and −22.86 dB respectively. To tune the filter, a varactor circuit was inserted at its input allowing to vary the centre frequency from 128.2 to 129.8 GHz, a difference of 300 MHz. These performances show that this filter can be widely used in frequency selection applications, low noise amplifiers, and broadband amplifiers bandwidth improvement. The simulations were carried out on the Keysight Technologies Advanced Design System software, using the CMOS 0.35 μm technology from the AMS Australia foundry.

Keywords Terahertz band · Frequency tuning · Active filtering · Active inductor · CMOS

1 Introduction

The THz frequency domain located in the electromagnetic spectrum between the optical domain of the infrared (IR) and the electronic domain of the microwave

I. Halkhams (✉)
LSEED Laboratory, UPF, Fez, Morocco
e-mail: imane.halkhams@usmba.ac.ma

W. El Hamdani · S. Mazer · M. El Bekkali
IASSE Laboratory, USMBA, Fez, Morocco

M. Fattah
IMAGE Laboratory, UMI, Meknes, Morocco

M. El Ghzaoui et al. (eds.), *Terahertz Wireless Communication Components and System Technologies*, https://doi.org/10.1007/978-981-16-9182-9_6

was long called the IR-faraway or submillimetre waves. Confined to the field of astronomical observation, terahertz technologies have exploited the special physical properties related to the terahertz domain to develop new fields of applications, notably that of spectroscopy, imaging, and communication [1, 2].

Certain technological steps have been taken, and components and systems that meet the expectations of the scientific and industrial sectors are now available. In the field of imaging, studies have shown that biological tissues have optical properties in the THz frequency range. Thus, X-rays with ionizing and invasive properties are replaced by terahertz rays which are less ionizing and more transmissible [3].

In the field of spectroscopy, the performance of terahertz techniques is directly related to the generation methods of this radiation. Spectroscopy currently makes it possible to have countless information such as the optical parameters of materials (refractive index, absorption, etc.) and the measurement of thicknesses [4].

For telecommunications, the Earth's atmosphere contains several chemical (gas) absorbent elements that can make the atmosphere almost opaque in specific frequency bands. The water molecule has hundreds of absorption lines that correspond to energy levels of rotation and/or vibration of the molecule that fall within the range of radio and THz waves.

As a result, the potential uses of THz waves in telecommunications exist in these regions and/or at very high altitudes (aircraft, satellite, etc.), where water molecules are rare [5].

In the context of telecommunications, frequency filtering is crucial in the selection of the desired band and the rejection of out-of-band signals. Active filtering is therefore the ultimate solution to this problem. In that connection, we introduce through this article the design and simulations of an active bandpass filter, tunable in frequency and characterized by a high-quality factor. The filter was implemented using active inductor technology, which has the characteristic of being easily integrable and tunable in frequency. However, the parasitic effect of the transistors negatively affects the stability of the circuit and directly impacts the quality factor of the final filter. To remedy this, different techniques are used, including improving the polarization conditions of transistors and adapting them.

2 The THz Domain

Telecommunications include all techniques for transporting data. As current speeds are soon to be exceeded, the emergence of new ultra-fast applications is pushing scientists to develop increasingly fast solutions and systems.

With all these developments, the magnetic spectrum becomes saturated. The research is directed towards bands not (or rarely) allocated in the terahertz domain.

The technological issue is therefore to design active filters that are integrable, reconfigurable, and inexpensive.

The objective of our work is to set up a filter that can be integrated, reconfigured, and intended for THz wireless communication (Fig. 1). Before presenting this study,

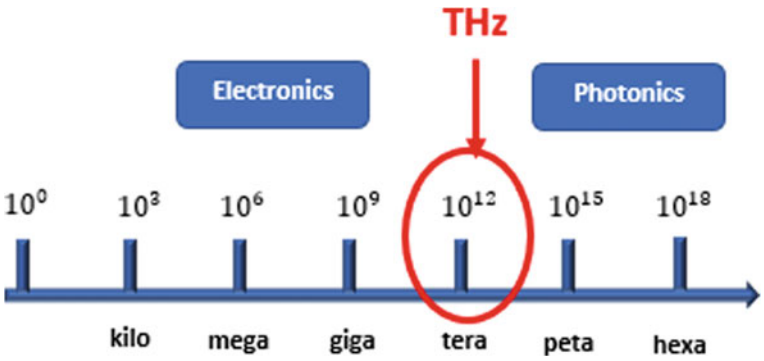

Fig. 1 Electromagnetic spectrum

let us recall some bibliographical elements on the THz domain (advantages, filters, and applications).

For a long time, the researchers developed all types of components and filters at microwave and visible spectrum without taking advantage of the terahertz band, which has undeniable advantages over others.

This area has only been in use for about twenty years [6]. One of the reasons lies in the absence of integrated and tunable filters at a time.

We will start by presenting the different applications using Terahertz waves.

2.1 THz Applications

THz radiation has been widely studied, not only because it is an unknown field, but also for its unique characteristics and wide possible applications. THz waves play an increasing role in different fields of activity.

Their applications are multiple and related in particular to biological detection [7], airport security [8], drug and explosives identification [9], imaging [10], or astronomy [11].

2.1.1 THz Spectroscopy

THz spectroscopy is one of the most commonly used techniques for biomedical applications [12]. It allows chemical analyzes to be carried out to identify and quantify the species present in a sample as well as the study of dielectric properties and electrical conductivity of materials such as semiconductors [13].

For example, THz spectroscopy can detect difficult chemicals to be identified with other areas and other dangerous substances such as gases and explosives or illegal substances such as drugs [14].

2.1.2 Medical Applications

THz radiation is interesting for medical applications since it doesn't present any danger to biological media thanks to its low non-ionizing energy per photon. THz imaging will allow viewing objects in different ways with better spatial resolution [15] since THz radiation makes it possible to get a spatial resolution of a few hundreds of microns [16], much smaller than that of microwaves.

THz radiation appears to be a very favourable alternative because it is non-destructive. THz is used in several medical applications such as diagnosis of diseases, identification of structural state of proteins, effects of radiation on samples and biological processes [13].

2.1.3 Quality Control and Surveillance for Safety

Three important factors have contributed to the use of THz in the field of safety and quality control as well as in military applications:

- To detect potentially hazardous materials, THz radiation is transmitted mostly through non-metallic materials, allowing THz systems to see corrugated boxes, etc. To detect potentially hazardous materials,
- Studies show that THz radiation carries a minimal health risk compared to x-rays.
- Many materials, such as explosives, chemical, and biological agents, have specific characteristics in the THz domain [17], which allow different substances to be detected, even when they are hidden in clothing [8].

One of the most popular security applications is the airport scanner [8].

2.1.4 Astronomy and Earth Science

THz radiation is also used in the study and control of the earth's environment, for example in the study of chemical species that make up the ozone layer [18]. It helps measure the concentration and distribution of chemical species in ozone and understand their importance.

THz technology is also present in astronomy, thanks to the means implemented by large organizations such as NASA.

Its main objectives are to obtain information to apprehend the formation and evolution of galaxies and the study of the processes of formation of stars and planetary systems [19].

2.1.5 THz Communication

Research centres and manufacturers are constantly studying the possibilities of exploiting the terahertz band to develop high-speed communication systems.

A few projects presented transmitters and receivers that operate at 60 GHz [20]. Koch's research published in 2007 states that THz systems will replace the current WIFI systems between 2017 and 2023 [21, 22].

Terahertz systems offering speeds up to GBytes per second will allow several broadband applications to be developed, such as telephony, new generations of wireless networks, HD television (HDTV) [23], etc.

3 Types of Filters

To exploit the terahertz band and develop emerging applications, various types of filters are required.

There are two main families of topologies for making an electromagnetic filter: volume filters and planar filters.

Volume filters are based on the use of electromagnetic resonant modes in a volume which may be a metal cavity or a dielectric resonator. For the design of planar filters, it is done in two dimensions on one or more metal layouts physically spaced by layers of insulators.

3.1 Volume Filters: Based on Waveguide

Waveguide-based filters are composed of resonate cavities delimited generally by conductive walls and coupled by irises or conductive elements.

At frequencies below 30 GHz, these filters are hardly compatible with integrated technologies since they are waveguide and bulky. The main advantage of these structures is that they have a very high-quality factor that can be greater than a few thousand.

To meet the demand for high-quality factor selective filters that can go as far as the terahertz range, different micro-machining techniques are then developed: computer-controlled engraving (CNC-milling) [24], engraving based on synchrotron radiation [25], deep engraving based on reactive ions (DRIE) [26], the use of photosensitive resin SU-8 [27], or etching Tetramethylammonium hydroxide base (TMAH) for example [28].

3.2 Volume Filters: The SIW Filtres

Substrate Integrated Waveguides have a good agreement between electrical performance and integrability. In general, for a SIW structure, the horizontal walls are conductive planes and the vertical ones are made up of a network of vias whose dimensions are chosen to avoid any field leakage.

For the realization of filters, different substrates can be used as the Printed Circuit Board (PCB) [29].

The size of the SIWs remains large compared to conventional volume guides and the different transitions between conventional planar lines (microstrip or coplanar for example) and the mode of propagation must be taken into consideration.

To enhance the integration of this type of filter, heterogeneous integration is increasingly studied [30]. However, despite the possibility of more efficient integration, SIWs remain large and relatively expensive to implement. In a context of maximum integration and low power to convey, the preferred solutions for millimetre wave systems remain planar structures.

3.3 Planar Filters: Localized Element Filters

At very high frequencies, the localized elements will be produced directly on the implementation substrate. For example, the capacitors can be interdigitated as shown in Fig. 2. These allow the synthesized filters to be produced directly using a low-pass prototype.

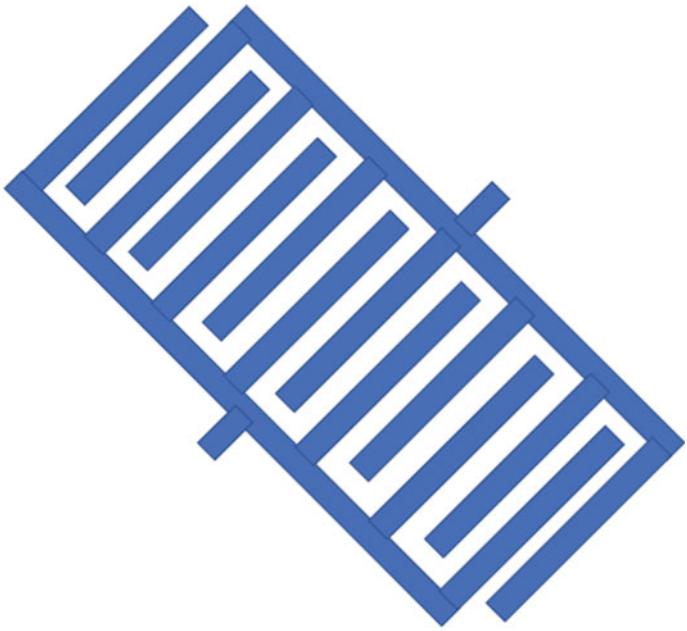

Fig. 2 Interdigitated capacitance topology

However, at such high frequencies, the use of localized elements is relatively problematic because of the losses generated and the complexity of the implementation. Millimetric planar filters are therefore mostly implemented using distributed elements.

3.4 Planar Filters: Distributed Element Filters

Planar transmission lines are an optimal choice for low power integrated millimetre applications. The main technologies used are microstrip lines and coplanar lines also called Coplanar waveguide (CPW). The microstrip lines consist of a dielectric layer separating a conductive strip from the ground plane. Microstrip lines are simple and well modelled so their use is relatively easy.

The main drawbacks are the technological limitation of the range of characteristic impedances and the need to introduce vias (metallized holes) to connect elements located between the signal and the ground.

This technology remains relatively compact and allows great flexibility in filter designs. Although it has very low-quality factors compared to volume technologies, it is a priority for the study of fully integrated systems.

4 Structure and Principle

The proposed analogue filtering mechanism is based on the principle of the gyrator that was invented by S. HARA [31].

This topology designated for microwave applications implements two transistors in AsGa technology connected in a loop and thus constituting a gyrator that delivers an inductive effect as soon as it is closed on a capacitor (Fig. 3).

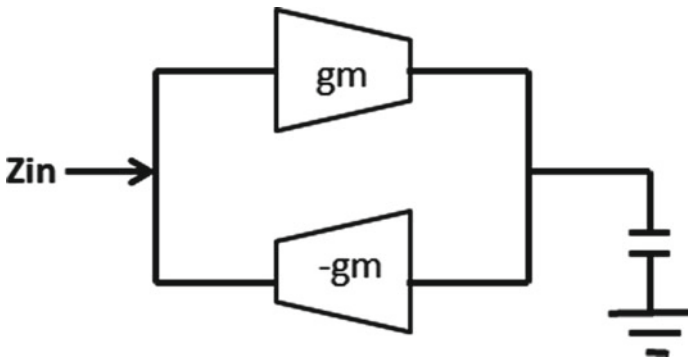

Fig. 3 The first active inductor topology invented by S.HARA

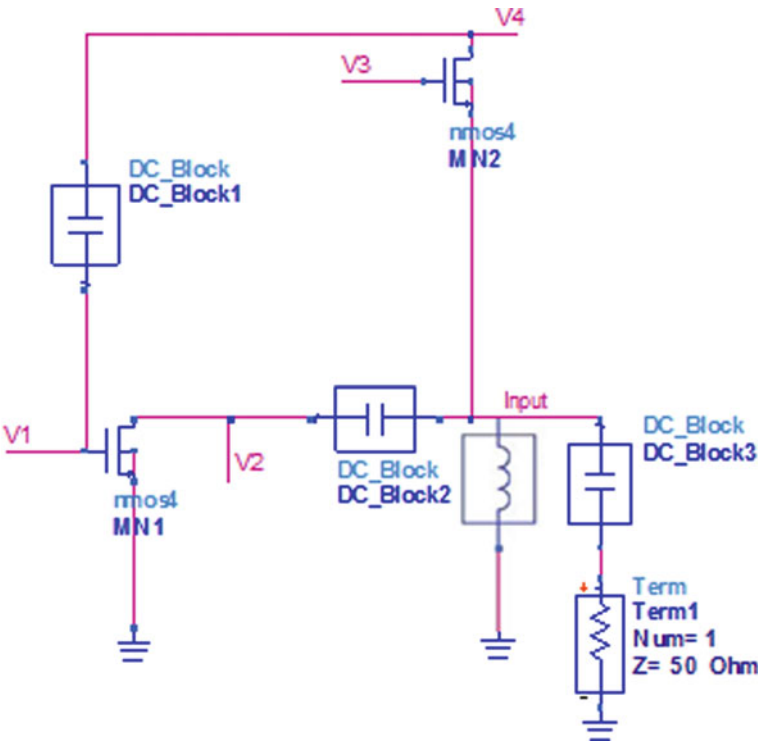

Fig. 4 The active inductor topology

Since then, several works have developed this structure to follow the technological evolution of the bandpass filters [32, 33].

In this paper, we present a topology of the active inductor that is composed of two transistors (Fig. 4).

The first one is common source mounted when the second is common gate mounted. The first transistor's gate to source capacitance delivers the capacitive effect to present an inductive effect at the input of the circuit. V1-V4 exhibit the transistor's biasing.

The role of DC-Block is to block the DC component in an RF signal and to improve measurement accuracy.

The previous circuit has the particularity of simulating an RLC circuit (Fig. 5).

To design the filter, adaptation stages are added in and out. Input and output buffers deliver a 50 Ω impedance to the preceding stage and to the load, respectively (Fig. 6).

The adaptation of the filter's input and output impacts its performance [34]. The insertion, for example, of an output buffer in nMOS technology with a very high Cgs capacitance acts unavoidably on the centre frequency of the filter. Thus, the design of the adaptation circuits must be carefully studied to guarantee the optimum

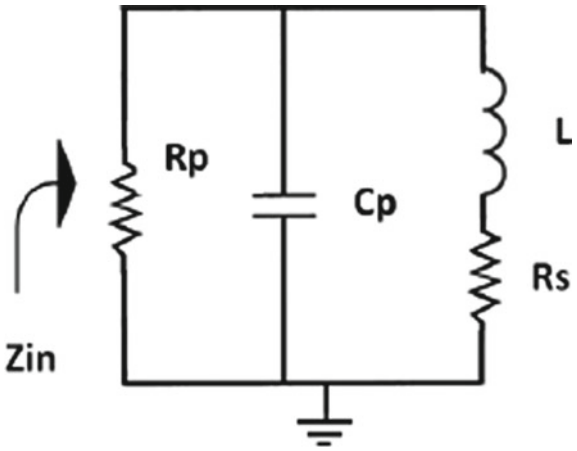

Fig. 5 Equivalent RLC circuit

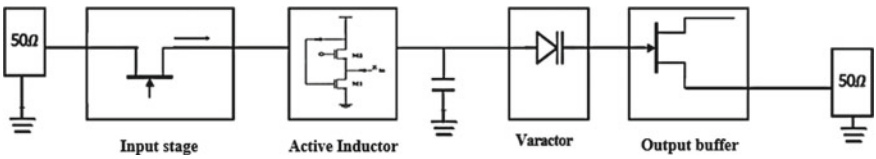

Fig. 6 The active bandpass filter topology

performance of the components without altering their critical characteristics such as the resonance frequency.

In the literature, some research has reported mainly passive circuits, presenting better linearity but which are not adequate for multi-standard applications [35]. Hence, the advantage of active circuits, that are more stable.

At the input, we used a common grid-mounted transistor (Fig. 7). This presents a high input admittance and low output admittance, according to Eqs. (1) and (2)):

$$\mathrm{Ye} \approx \mathrm{gm} + j.w.\mathrm{Cgs}. \tag{1}$$

$$\mathrm{Ys} \approx \mathrm{gds}. \tag{2}$$

where

Ye: input admittance
Ys: output admittance
gm: transistor transconductance
w: Angular frequency
Cgs: grid-source capacity

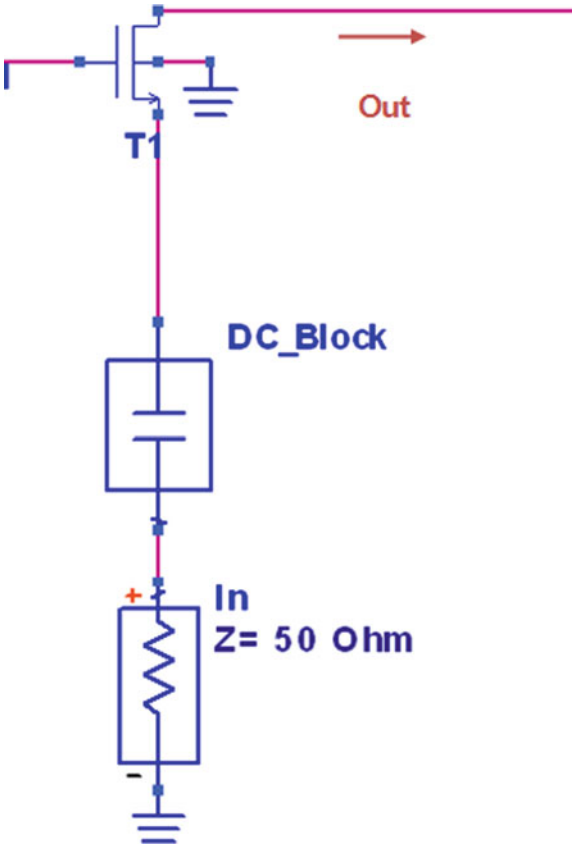

Fig. 7 The input adaptation buffer

gds: output conductance.

In order to obtain an input impedance close to 50 Ω, the capacity Cgs value must be low and the transconductance must be approximately equal to 20 ms.

On the output side, the common drain configuration has a very low input admittance on the active inductor's side and a very high output admittance on the load side, with a voltage gain of the order of the unit (Fig. 8).

5 Simulation Results and Optimization

5.1 S Parameters, Stability, and Noise Figure

To assess the performance of the filters several factors must be taken into account, such as selectivity, which is reflected in the quality factor. In other words, the more

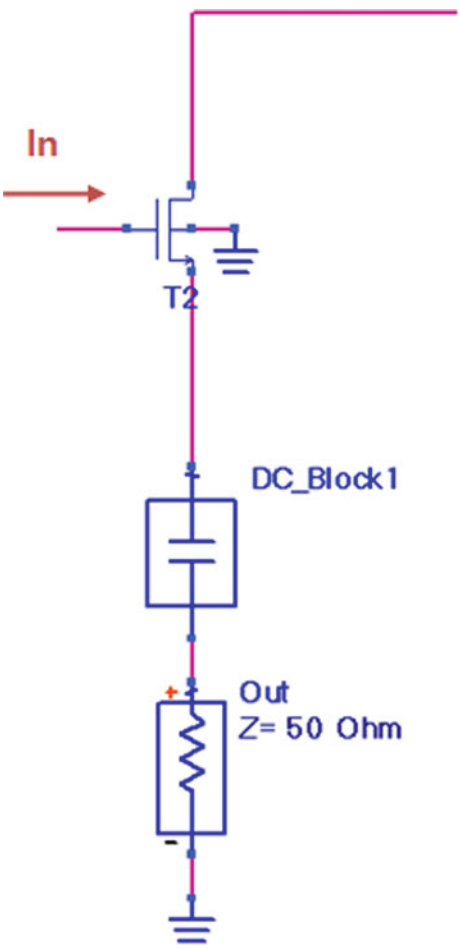

Fig. 8 The output adaptation buffer

selective the filter, the greater its quality factor. The quality factor is the ratio of the centre frequency to bandwidth.

Bandwidth is also crucial, especially for new applications that require increasing bandwidth to meet current communication needs.

We simulated the filter responses, namely the gain (S_{21}) and the reflection coefficients (Fig. 9). The centre frequency is 129 GHz. The simulated bandwidth is 400 MHz. Input and output reflection coefficients are −27.6 dB and −22.86 dB respectively, allowing out-of-band rejection.

The simulated quality factor is 322, which is very suitable for Terahertz applications. This reflects that the designed filter has very good selectivity.

To ensure that the filter is operating correctly across the bandwidth its stability must be evaluated. The stability factor K is inversely proportional to the gain (S_{21}) (3).

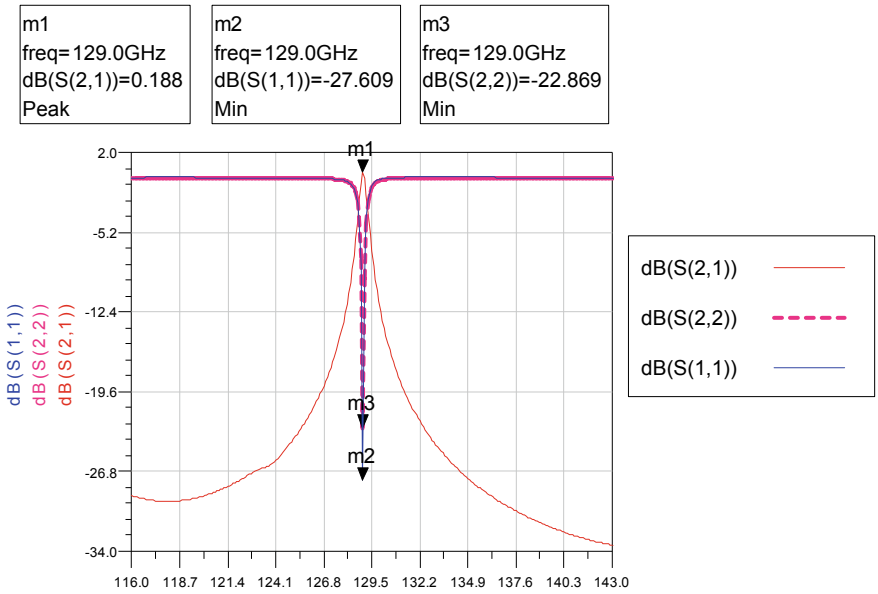

Fig. 9 The active filter's *S* parameters

$$K = \frac{|\Delta|^2 - |S_{11}|^2 - |S_{22}|^2 + 1}{2|S_{12}||S_{21}|} \tag{3}$$

With:

$$\Delta = S_{11}S_{22} - S_{12}S_{21} \tag{4}$$

Thus, the stability factor reaches its minimum at the resonance frequency. However, it should not be less than 0 for the filter to be in the stability zone. The filter stability is shown in Fig. 10.

The curve shows that the stability factor has a minimum of ≈ 1 at the resonance frequency and remains above 1 on the entire frequency range used.

The noise figure shown in Fig. 11 indicates that it reaches its minimum at the resonance frequency.

5.2 *Frequency Tuning*

Communication systems are constantly evolving. Emerging applications continue to consume the available bands, and the need to migrate from one frequency to another is becoming increasingly important.

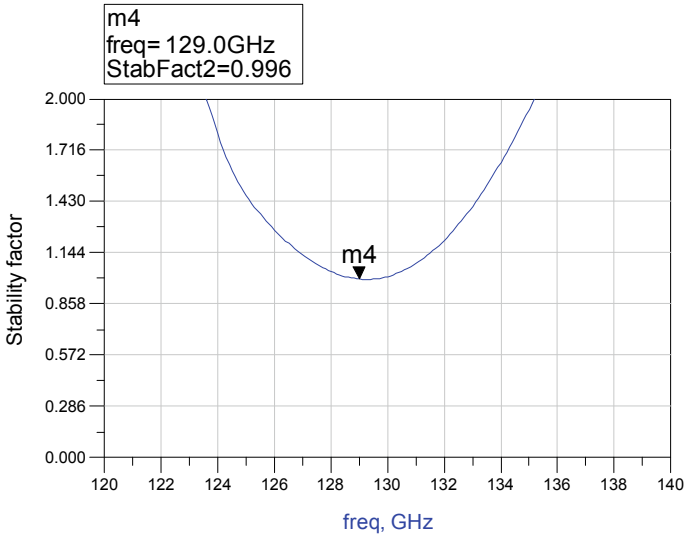

Fig. 10 The active filter's stability factor

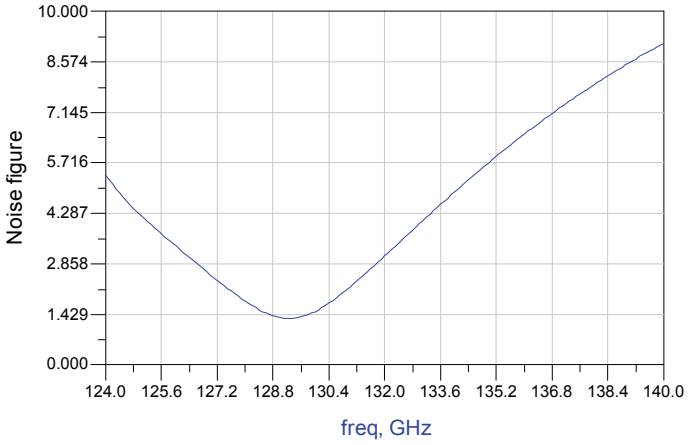

Fig. 11 The active filter's noise figure

For all these reasons, filters need to be more agile and flexible to meet the needs of multi-band applications.

In the literature, several methods exist for frequency tuning [36, 37]. Among the technologies that exist, the most used are semiconductor components, mainly varactor or transistor, as well as their alternative components in MEMS technology.

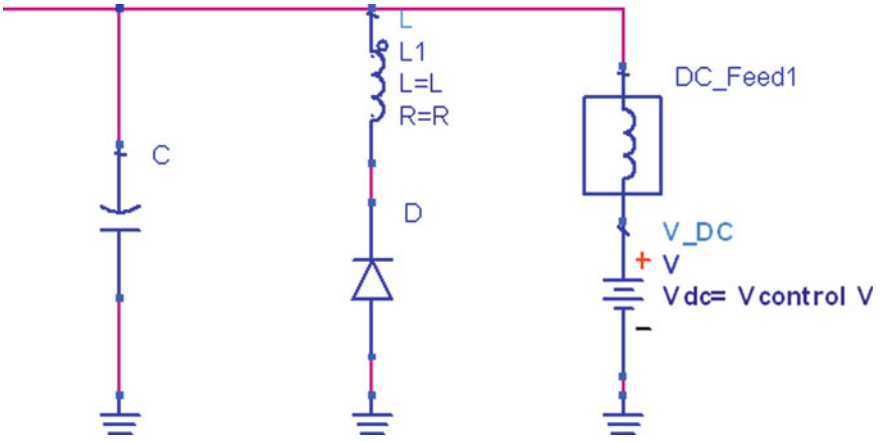

Fig. 12 Varactor's circuit

In our study, we avoided the use of the transistor to avoid the addition of additional noise and consumption in addition to non-linear effects. Our choice was to use a varactor.

To make the filter tunable in frequency, we have added to its input a varactor circuit whose purpose is to adjust the filter's centre frequency. The varactor circuit is shown in Fig. 12.

Using the circuit shown in Fig. 12, which simulates a capacitor whose capacity is variable according to a reverse voltage applied to its terminal, the filter's centre frequency may be tuned by varying the *V* control voltage.

In the following, we examine the effect of the variation of this voltage on the centre frequency of the filter (Fig. 13).

Several simulations were carried out to determine the elements that influence the centre frequency. We started by varying the polarization voltages of the various transistors, starting with those of the active inductor, arriving at those of the input and output buffers.

The results of the simulations made it possible either to vary the centre frequency by a few megahertz or to change the gain value from one frequency to another, which is not recommended for multi-standard applications that require the same gain.

Among all the elements affecting the frequency, the variation of the voltage of the varactor is the only operation allowing to change the frequency over a wide range while keeping the value of the gain fixed.

By varying the Vcontrol voltage in the range [0.1–1 V], the centre frequency of the filter switches from 129.8 V to 128.2, respectively. Note that the filter gain remains constant over the entire range.

Beyond the 130 GHz (1 V) frequency, we observed a decrease in gain as the frequency increased (Fig. 14).

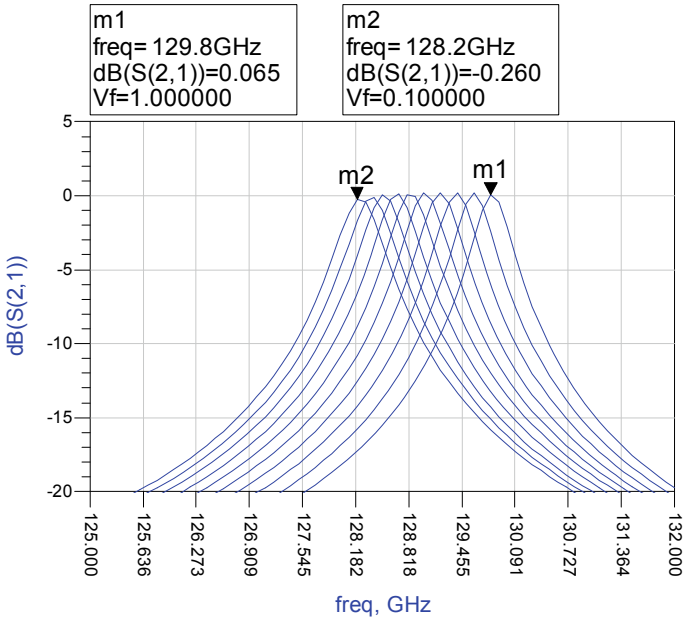

Fig. 13 Frequency tuning

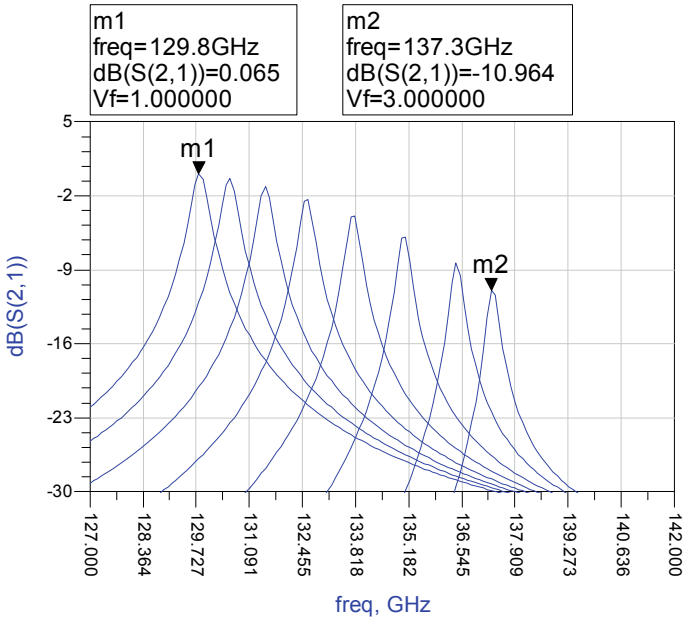

Fig. 14 Gain decrease with frequency increase

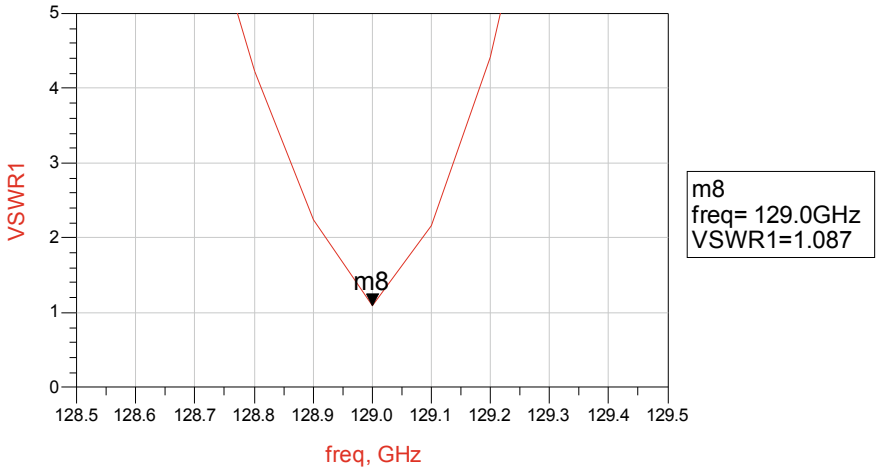

Fig. 15 The active filter's VSWR

In radiofrequency, it is important to minimize the VSWR (Voltage Standing Wave Ratio) when inserting filters. It represents the ratio of the maximum voltage to the minimum voltage present on the line.

When the VSWR is >1, the incident and reflected waves circulate simultaneously in the line. That is the effect of standing waves.

Figure 15 shows a VSWR of ≈ 1 at the centre frequency, which is a perfect match according to IEEE standards [38].

6 Conclusion

We have presented through this paper the research work concerning the operation of analogue filtering in the terahertz band using the principle of the active inductor.

We first gave an overview of the filtering technologies used in this band. We then presented the topology of the filter, the input and output adaptation topologies, and the main results of the different simulations.

The filter provides interesting results for the terahertz band, including gain, out-of-band rejection, noise figure, and stability over the entire frequency band used. In addition, the proposed filter can be easily tuned in frequency according to the desired standard.

Finally, the filter can be used for applications such as mobile and fixed satellite, radio navigation, and radio astronomy [39].

References

1. J.S. Rieh, THz applications, in *Introduction to Terahertz Electronics* (Springer, Cham, 2021), pp. 273–350. https://doi.org/10.1007/978-3-030-51842-4_6
2. J. Hu, Z. Xu, M. Li et al., Detection of foreign-body in milk powder processing based on terahertz imaging and spectrum. J. Infrared Milli. Terahz Waves **42**, 878–892 (2021). https://doi.org/10.1007/s10762-021-00802-w
3. E. Berry, A.J. Fitzgerald, N.N. Zinovev, G.C. Walker, S. Homer-Vanniasinkam, C.D. Sudworth, R.E. Miles, J.M. Chamberlain, M.A. Smith, Optical properties of tissue measured using terahertz pulsed imaging, in *Proceedings of SPIE: Medical Imaging 2003: Physics of Medical Imaging*, vol. 5030, pp. 459–470, 2003
4. M. Naftaly, A. Gregory, Terahertz and microwave optical properties of single-crystal quartz and vitreous silica and the behaviour of the boson peak. Appl. Sci., 116733 (2021). https://doi.org/10.3390/app11156733
5. C. Daher, *Study and realization of terahertz sensors based onasymmetric nanochannels of two-dimensional electron gas (French: Etude et réalisation de capteurstérahertz à base de nanocanaux asymétriques de gaz d'électrons bidimensionnel)* (Université Montpellier, Electronique, 2015)
6. D.L. Woolard, M. Pepper, E.R. Brown, M. Kemp, Terahertz frequency sensing and imaging: a time of reckoning future applications ? Proc. IEEE **93**, 1722–1743 (2005)
7. P.H. Siegel, Terahertz technology in biology and medicine. IEEE Trans. Microw. Theory Tech. **52**(10), 2438–2447 (2004)
8. M.C. Kemp, P.F. Taday, B.E. Cole, J.A. Cluff, A.J. Fitzgerald, W.R. Tribe, Security applications of terahertz technology, in *Proceedings SPIE*, vol 5070, pp. 44–52, 2003
9. Y.C. Shen, T. Lo, P.F. Taday, B.E. Cole, W.R. Tribe, M.C. Kemp, Detection and identification of explosives using terahertz pulsed spectroscopic imaging. Appl. Phys. Lett. **86**(24), 1–3 (2005)
10. W.L. Chan, J. Deibel, D.M. Mittleman, *Imaging with Terahertz Radiation*, 2007
11. A.A. Penzias, R.W. Wilson, *A Measurement of Excess Antenna Temperature at 4080 Mc/s*, 1965
12. J.L. Coutaz, *Optoélectronique Terahertz*. EDP Sciences (2012)
13. V.P. Wallace, B.C. Cole, R.M. Woodward, R.J. Pye, D.A. Arnone, Biomedical applications of terahertz technology, in *The 15th Annual Meeting of the IEEE Lasers and Electro-optics Society*, vol 1, 2002
14. M. Reddy, S.C. Martin, A.C. Molnar, R.E. Muller, R.P. Smith, P.H. Siegel, M.J. Mondry, M.J.W. Rodwell, H. Kroemer, S.J. Allen, Monolithic Schottky-collector resonant tunneldiode oscillator arrays to 650 GHz. IEEE Electron Device Lett. **18**(5), 218–221 (1997)
15. E.R. Mueller, Terahertz radiation: applications and sources. Physicist **9**(September), 27–29 (2003)
16. H.T. Chen, R. Kersting, G.C. Cho, Terahertz imaging with nanometer resolution. Appl. Phys. Lett. **83**(15), 3009 (2003)
17. J.F Federici, B. Schulkin, F. Huang, D. Gary, R. Barat, F. Oliveira, D. Zimdars, THz imaging and sensing for security applications-explosives, weapons and drugs (2005)
18. M. Reddy, S.C. Martin, A.C. Molnar, R.E. Muller, R.P. Smith, P.H. Siegel, M.J. Mondry, M.J.W. Rodwell, H. Kroemer, S.J. Allen, Monolithic Schottky-collector resonant tunnel diode oscillator arrays to 650 GHz. IEEE Electron Device Lett. **18**(5), 218–221 (1997)
19. P.H. Siegel, THz instruments for space, 2007
20. T. Kurner, Towards future THz communications systems. Terahertz Sci. Technol. **5**(1), 11–17 (2012)
21. R. Heidemann, R. Hofstetter, H. Schmuck, Fibre-optic technologies for 30/60 GHz pico-cellular PCN and mobile systems, in *1994 IEEE MTT-S International Microwave Symposium Digest* (Cat. No. 94CH3389-4), 1994
22. M. Koch, Terahertz communications: a 2020 vision, in *Terahertz Frequency Detection and Identification of Materials and Objects* (Springer, Netherlands, Chap. 4, 2007), pp. 325–338 (2007)

23. A. Hirata, T. Nagatsuma, T. Kosugi, H. Takahashi, R. Yamaguchi, N. Shimizu, N. Kukutsu, K. Murata, Y. Kado, H. Ikegawa, H. Nishikawa, T. Nakayama, 10-Gbit/s wireless communications technology using sub-terahertz waves, in *SPIE 6772, Terahertz Physics, Devices, and Systems II*, pp. 67720B, Boston, 2007
24. J.Q. Ding, S.C. Shi, K. Zhou, D. Liu Et, W. Wu, Analysis of 220-ghz low-loss quasi-elliptic waveguide bandpass filter. IEEE Microw. Wirel. Comp. Lett. **27**(7), 648–650 (2017)
25. M. Kishihara, R. Sasaki, T. Yamamoto, A. Yamaguchi, Y. Utsumi Et, I. Ohta, Fabrication of 180 ghz PTFE-filled waveguide and its bandpass filters by SR direct etching, in *2014 Asia-Pacific Microwave Conference*, Sendai, Japan, 2014, pp. 49–51
26. Z. Xing-hai, S. Guang-cun, D. Yi-jia, B. Jing-fu, Z. Hao-shen, Z. Ying-bin, S. Chan-hung Et, C. Yong-sheng, G-band rectangular waveguide filter fabricated using deep reactive ion etching and bonding processes. IET Micro. Nano Lett. **7**(12), 1237–1240 (2012)
27. Y. Wang, M. Ke Et, M.J. Lancaster: Micromachined 60 ghz air-filled interdigital bandpass filter, in *Proceedings of the 2009 International Workshop on Microwave Filters*, Toulouse, France
28. B. Qiong, Z. Binzhen Et, D. Junping, Design of W band rectangular waveguide filter, in *2017 IEEE 9th International Conference on Communication Software and Networks (ICCSN)*, Guangzhou, 2017
29. F.X. Röhrl, R. Sammer, J. Jakob, W. Bogner, R. Weigel, U. HASSEL ET S. ZORN : Cost-effective SIW band-pass filters for millimeter wave applications a method to combine low tolerances and low prices on standard pcb substrates, in *2017 47th European Microwave Conference (EUMC)*, Nuremberg, 2017
30. R. Oikawa, A feasibility study on 100 gbps-per-channel die-to-die signal transmission on silicon interposer-based 2.5-d lsi with a passive digital equalizer, in *2016 IEEE 66TH Electronic Components and Technology Conference (ECTC)*, LAS VEGAS, nv, 2016
31. A.S. Hara, T. Tokumitsu, Broad-band monolithic microwave active inductor and its application to miniaturized wide-band amplifiers. IEEE MTT **36**(12) (1988)
32. I. Halkhams, W. El Hamdani, S. Mazer, M. El Bekkali, M. Fattah, Analytical study of the CMOS active inductor, in *Digital Technologies and Applications*, ed. by S. Motahhir, B. Bossoufi. ICDTA 2021. Lecture Notes in Networks and Systems, vol 211 (Springer, Cham, 2021). https://doi.org/10.1007/978-3-030-73882-2_151
33. Y. Wu, M. Ismail, RF bandpass filter design based on CMOS active inductors. IEEE Trans. Circ. Syst. **50**(12), 942–949 (2003)
34. M. Lahsaini, L. Zenkouar, Interdigital filters for broadband impedance matching of microwave amplifiers. Int. J. Commun. Ant. Propag. **5**(1), 21–27 (2015)
35. J.K. Nai, Y.H. Hsiao, Y.S. Wang, Y.H. Lin, H. Wang, A 2.8–6 GHz high-efficiency CMOS power amplifier with high-order harmonic matching network, in *IEEE MTT-S International Microwave Symposium (IMS)*, 2016
36. M. Marx, D. De Dorigo, S. Nessler, S. Rombach, Y. Manoli, A 27 uW0.06 mm^2 background resonance frequency tuning circuit based on noise observation for a 1.71 mW CT-MEMS gyroscope readout system with 0.9°/h bias instability. IEEE J. Solid-State Circuits **53**(1), 174–186 (2018). https://doi.org/10.1109/JSSC.2017.2747215
37. D. Seo, J. Lee, Frequency-tuning method using the reflection coefficient in a wireless power transfer system. IEEE Microwave Wirel. Compon. Lett. **27**(11), 959–961 (2017). https://doi.org/10.1109/LMWC.2017.2750023
38. EEE standard for methods ofmeasurement of radio-frequencypower-line interference filter in the range of 100 Hz to 10 GHz, in *IEEE Electromagnetic Compatibility Society, IEEE Std 1560*
39. Department of Commerce: The Radio Spectrum, U.S., National Telecommunications and Information AdministrationOffice of Spectrum Management, January 2016

A 10-Element Series Fed Non-uniform High Directional Planar Antenna Array at 0.3 THz

Anveshkumar Nella, Manish Sharma, Vulugundam Anitha, and Tathababu Addepalli

Abstract This work presents a design of 10-element symmetric series fed non-uniform planar antenna array operating at 0.3 THz and exhibiting high directional radiation pattern along the upper hemisphere. An impedance bandwidth of range 0.294–0.313 THz and a peak gain (dBi) of 13.26 at 0.3 THz are noted. Gold material of thickness 5 μm and silicon dioxide (SiO_2) dielectric substrate of 2 mm × 5.5 mm × 0.06 mm dimensions are employed for the proposed antenna array design. Array elements length is considered as quarter of free space wavelength at 0.3 THz while elements width is non-uniform for better impedance bandwidth and directivity. Initially, a 10-element series fed non-uniform array antenna, utilizing the concept of Tschebyscheff polynomials and array factor, is presented. Then, an optimized 10-element series fed antenna array, offering better performance, is discussed. Considering the compact dimensions, higher directivity, resonating characteristics, and better performance proposed antenna array can be a suitable module for various THz applications like imaging, radars, device-to-device communication, THz Wi-Fi, point-to-point communication, etc.

Keywords Array factor · Directional radiation pattern · Non-uniform elements · Series fed · THz applications · Tschebyscheff polynomials

1 Introduction

Micro-strip patch antennas have played a vital role in several microwave band applications, which include applications such as Wi-MAX, WLAN, GPS, Bluetooth, UWB, *X*, *K*, and Ku Bands. The utilization of these antennas based on micro-strip feed has been extended for applications in THz range, which are useful for medical

A. Nella (✉) · V. Anitha
Department of ECE, VIT Bhopal University, Sehore 466114, India

M. Sharma
Chitkara University Institute of Engineering and Technology, Chitkara University, Punjab, India

T. Addepalli
Department of ECE, JNTUA, Anantapur, Andhra Pradesh 515002, India

M. El Ghzaoui et al. (eds.), *Terahertz Wireless Communication Components and System Technologies*, https://doi.org/10.1007/978-981-16-9182-9_7

applications. The THz application oriented micro-strip antennas are used as array so that high gain can be achieved with high directivity. A compact 16 × 12 mm^2 series fed array designed for *X*-Band (8–12 GHz) applications achieves gain of 28.5 dBi at 10 GHz with aperture efficiency of 67% [1]. An integration in lower temperature with co-fired ceramic packages (LTCC) of horn antenna working at 300 GHz offers peak gain of 16 dBi [2], and another high frequency antenna utilizes quartz layers which is useful for *H*-Band (220–325 GHz) application has the capability of suppressing the lower side lobe levels by −4.3 dB at 310 GHz and −8.2 dB at 295 GHz [3]. It is also known that for any fixed wireless communication link compensation of larger path loss for higher frequency, a high gain antenna is desirable which is reported in [4]. It also presents how the designed antenna provides higher-gain of around 20 dBi in both *H*–*E* planes. The coverage area when considered at THz is very restricted in comparison to the existing Wi-Fi systems. But to encounter the demand of higher rate of data transmission under THz bands more progress is observed. A dual-band micro-strip antenna using split-ring resonator provides a −10 dB impedance bandwidth of range 274.10–295.60 GHz and 306.30–313.40 GHz [5]. A compound antenna with resonance at 61 GHz has the capability of beam switching from −32° to 34° [6]. A novel method analyzes linear feeding of micro-strip antenna array thereby resolving complexity in mutual coupling calculations [7, 8]. A very high frequency 300 GHz communication link uses Superhetrodyne system, which achieves a data-rate of 60 Gbit/s covering a maximum range of about 10 mm [9]. The next generation beyond 6G involving frequency band of 0.10–10 THz offers opportunities to exchange (borrow-translate) terrestrial systems [10]. Antenna array with 3 transmitters and 4 receivers utilizes the Dolph-Tschebyscheff distribution for optimization of the papered patch width for application at 77 GHz [11]. The truncated cornered unique series fed micro-strip array for 37/39 GHz beam forming purpose achieves left/right ended polarization (elliptical) [12]. A planar antenna with integration of Schottky barrier diode results in 19 dBi directivity [13]. A collimated beam is produced by the reflectory antenna at 300 GHz [14] and integration of CMOS integrated circuits has proved better performance at 300 GHz band [15]. A dielectric lens antenna designed for 300 GHz measures 21.2 dBi of gain [16] and 300 GHz step-type configured corrugated horn antenna is applicable with high gain and directivity [17]. A 300 GHz with two polarizations is well suited for future generation of micro-machine architecture [18–20]. A uni-traveling photo-diode is reported for high-speed transmission of data at 300 GHz [21] and a FPC (Fabri-Perot Cavity) antenna operation at 300 GHz is constructed by using laser cutting brass technology [22].

In this chapter, the proposed work presents a design of 10-element symmetric series fed non-uniform planar antenna array operating at 0.3 THz and exhibits high directional radiation pattern along the upper hemisphere. An impedance bandwidth of range 0.294–0.313 THz and a peak gain (dBi) of 13.26 at 0.3 THz are noted. Gold material of thickness 5 μm and silicon dioxide (SiO_2) dielectric substrate of height 60 μm are employed for the proposed antenna array design (Ansys HFSS software). Remaining content is arranged as mentioned in the next discussion.

Section 2 presents a discussion on preliminary 10-element series fed non-uniform antenna array structure, dimensions, array factor and Tschebyscheff polynomial design equations, results and discussion. Section 3 reports an optimized antenna array geometry, results, and discussion. Section 4 concludes the work.

2 Preliminary 10-Element Series Fed Antenna Array

Figure 1 shows the 10-element symmetric series fed antenna array printed on silicon dioxide substrate with height given as h_{sub} (0.06 mm) and the overall dimension of the antenna being $L_{sub} \times W_{sub}$ mm^2. The non-uniform radiating patch array is printed on one plane of the substrate of dimensions 2 mm × 5 mm × 0.06 mm and full ground on the opposite plane. The conducting material (patch and ground) is gold with thickness 5 µm, and silicon dioxide exhibits a relative permittivity (ε_r) of 4. The antenna array is designed for 300 GHz as the center frequency. The non-uniform symmetric antenna array shown in Fig. 1 is designed by using Dolph–Tschebyscheff array polynomials where the key parameters like array elements length (l), and width (W_1, W_2, W_3, W_4, and W_5) are obtained from following equations [11, 23–25]. Free space wavelength (λ) as given by Eq. (1), length of each element (l) as given by Eq. (2) and ε_{reff} as given by Eq. (3) are used.

$$\lambda = \frac{c}{f} = \frac{3 \times 10^{11}}{300 \times 10^{9}} = 1\,\text{mm} \tag{1}$$

$$l = \frac{\lambda}{2\sqrt{\varepsilon_{reff}}} = \frac{1}{2\sqrt{\varepsilon_{reff}}} \tag{2}$$

$$\varepsilon_{reff} = \frac{\varepsilon_r + 1}{2} + \frac{\varepsilon_r - 1}{2}\left[1 + \frac{12h_{sub}}{W_1}\right]^{-1/2} \tag{3}$$

where W_1 is width of center element of the array and is calculated by Eq. (4) given as,

$$W_1 = W = \frac{c}{2f\sqrt{\frac{\varepsilon_r+1}{2}}} = 0.3162\,\text{mm} \tag{4}$$

By applying $\varepsilon_r = 4, f = 300$ GHz in Eqs. (4) and (3) we get $W_1 = 0.3162$ mm, $\varepsilon_{reff} = 7.415$. Assuming major-to-minor lobe ratio of 30 dB (31.63 (abs)), knowing the length (l) = 0.183 mm from Eq. (2) the array factor $(AF)_{10}$ is calculated. Spacing between elements (d) as 0.25 *mm* (λ/4), length of feed line (l_f) as 0.5 mm (λ/2), feed line width (W_f) as 0.25 mm and strip line width (a) as 1 mm are considered. The computation of $(AF)_{10}$ for even number of elements [23–25] is given as,

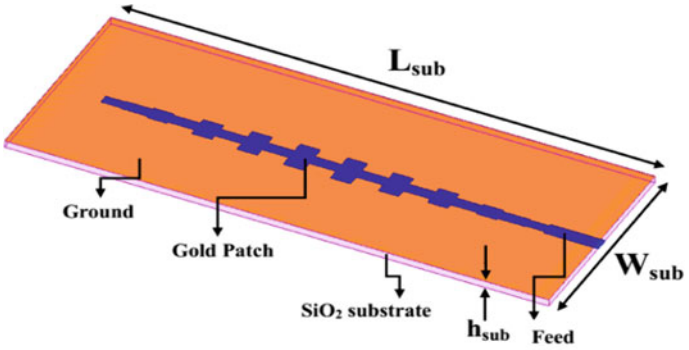

(a)

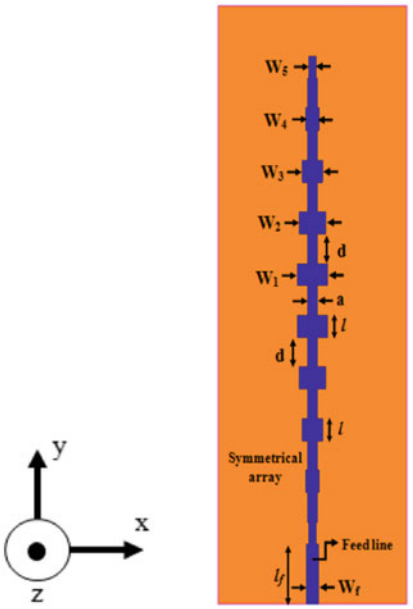

(b)

Fig. 1 Proposed preliminary 10-element series fed antenna array **a** slant view **b** top view

$$\mathrm{AF}_{2M}(\mathrm{Even}) = \sum_{n=1}^{M} a_n \cos[(2n-1)u] \tag{5}$$

$$\text{For 10 elements array, } 2M = 10;\ M = 5 \tag{6}$$

$$\mathrm{AF}_{10}(\mathrm{Even}) = \sum_{n=1}^{5} a_n \cos[(2n-1)u] \tag{7}$$

$$\text{Let, } m = 2n - 1 \tag{8}$$

$$\mathrm{AF}_{10} = \sum_{n=1}^{5} a_n \cos[mu] \tag{9}$$

$$\mathrm{AF}_{10} = a_1 \cos u + a_2 \cos 3u + a_3 \cos 5u + a_4 \cos 7u + a_5 \cos 9u \tag{10}$$

From the theory of array design and applying Dolph-Tschebyscheff theory,

$$\mathrm{AF}_{2M} = T_m(z); \text{ where } m = 2M - 1 \tag{11}$$

So, for $M = 5$ the value of $m = 9$ and hence,

$$\mathrm{AF}_{10} = T_9(z) \tag{12}$$

From the Tschebyscheff polynomials

$$T_m(z) = \cos[m \cos^{-1} z] \quad \text{for } -1 \leq z \leq +1 \tag{13}$$

Now, say $z = \cos u$ and hence,

$$T_m(z) = \cos[mu] \tag{14}$$

If,

$m = 0$ then $\cos[0u] = 1 = T_0(z)$
$m = 1$ then $\cos[1u] = z = T_1(z)$
$m = 2$ then $\cos[2u] = 2z^2 - -1 = T_2(z)$
$m = 3$ then $\cos[3u] = 4z^3 - -3z = T_3(z)$
$m = 4$ then $\cos[4u] = 8z^4 - -8z^2 + 1 = T_4(z)$
$m = 5$ then $\cos[5u] = 16z^5 - -20z^3 + 5z = T_5(z)$
$m = 6$ then $\cos[6u] = 32z^6 - -48z^4 + 18z^2 - -1 = T_6(z)$
$m = 7$ then $\cos[7u] = 64z^7 - -112z^5 + 56z^3 - -7z = T_7(z)$
$m = 8$ then $\cos[8u] = 128z^8 - -256z^6 + 160z^4 - -32z^2 + 1 = T_8(z)$
$m = 9$ then $\cos[9u] = T_9(z)$

$$T_9(z) = \cos 9u = 256\cos^9 u - 576\cos^7 u + 432\cos^5 u - 120\cos^3 u + 9\cos u \tag{15}$$

Hence,

$$T_9(z) = \cos\ 9u = 256\,z^9 - 576\,z^7 + 432\,z^5 - 120\,z^3 + 9\,z \tag{16}$$

From Eq. (10),

$$\mathrm{AF}_{10} = a_1\cos u + a_2\cos 3u + a_3\cos 5u + a_4\cos 7u + a_5\cos 9u \tag{17}$$

In Eq. (17),

$$\cos u = \frac{z}{z_o} \tag{18}$$

$$\begin{aligned}\cos 3u &= 4\cos^3 u - 3\cos u \\ &= 4[z/z_o]^3 - 3[z/z_o]\end{aligned} \tag{19}$$

$$\begin{aligned}\cos\ 5u &= 16\ \cos^5 u - 20\cos^3 u + 5\cos u \\ &= 16[z/z_o]^5 - 20[z/z_o]^3 + 5[z/z_o]\end{aligned} \tag{20}$$

$$\begin{aligned}\cos 7u &= 64\cos^7 u - 112\cos^5 u + 56\cos^3 u - 7\cos u \\ &= 64[z/z_o]^7 - 112[z/z_o]^5 + 56[z/z_o]^3 - 7[z/z_o]\end{aligned} \tag{21}$$

$$\begin{aligned}\cos 9u &= 256\cos^9 u - 576\cos^7 u + 432\cos^5 u - 120\cos^3 u + 9\cos u \\ &= 256[z/z_o]^9 - 576[z/z_o]^7 + 432[z/z_o]^5 - 120[z/z_o]^3 + 9[z/z_o]\end{aligned} \tag{22}$$

where 'Z_o' is calculated by

$$T_9(z_o) = \cos h[9\cos h^{-1} z_o] \tag{23}$$

$$\cos h[9\cos h^{-1} z_o] = 31.63$$

Hence,

$$Z_o = 1.1075 \tag{24}$$

Comparing coefficients of Eqs. (16) and (17)

Table 1 Array coefficients and elements width

Array coefficient	Actual value	Normalized value (a_n)	Width of each element (W_n)	Elements width (mm)
a_1	9.569	1	W_1	$W_1 = a_1 \times W =$ 0.3162
a_2	8.428	0.88	W_2	$W_2 = a_2 \times W =$ 0.278
a_3	6.451	0.674	W_3	$W_3 = a_3 \times W =$ 0.213
a_4	4.161	0.434	W_4	$W_4 = a_4 \times W =$ 0.1372
a_5	2.506	0.261	W_5	$W_5 = a_5 \times W =$ 0.082

$$\frac{256a_5}{z_o^9} = 256 \Rightarrow a_5 = 2.506$$

Similarly,

$$\frac{64a_4 - 576a_5}{z_o^7} = -576 \Rightarrow a_4 = 4.161$$

The same can be followed to obtain antenna array coefficients as $a_3 = 6.451$, $a_2 = 8.428$, $a_1 = 9.569$. The width of array elements is computed as shown in Table 1.

The proposed preliminary series fed antenna array is presenting *S*-parameter, 3D-radiation pattern, and surface current distribution performance as shown in Fig. 2. As per the observations, the proposed design offers poor matching of impedance. At 296 GHz, *S*-parameter corresponds to −11.18 dB and hence there is scope for improvement in the design. Moreover, the radiation pattern is not directional.

3 Modified 10-Element Series Fed Antenna Array

Figure 3 shows the complete design of modified 10-element symmetric array for better matching of the impedance and far-field results. Figure 3a, b shows the top and slant views of the proposed 10-element array. Dimensions of corresponding elements are shown in Table 2. Spacing between the elements (l_1) and elements length (l_1) as 0.25 mm (λ/4), W_f as 0.25 mm (λ/4) and l_f as 0.5 mm (λ/2) are considered.

Figure 3c shows the simulated return loss curve, which provides resonances at 273 GHz, 300 GHz, and 330 GHz. It can be observed that the proposed antenna offers good matching of impedance for the above said three resonating bands. However, better reflection coefficient and directional properties along Phi = 0° and upper hemisphere are obtained at 300 GHz as shown in Fig. 4.

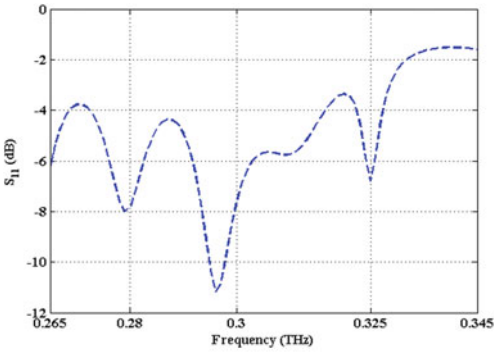
0
-2
-4
-6
-8
-10
-12
S_{11} (dB)
0.265
0.28
0.3
0.325
0.345
Frequency (THz)

(a)

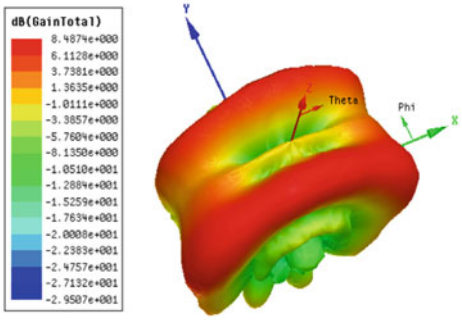
dB(GainTotal)
8.487e+000
6.1128e+000
3.7381e+000
1.3635e+000
-1.0111e+000
-3.3857e+000
-5.760e+000
-8.1350e+000
-1.0510e+001
-1.288e+001
-1.5259e+001
-1.763e+001
-2.0008e+001
-2.2383e+001
-2.4757e+001
-2.7132e+001
-2.9507e+001
Theta
Phi

(b)

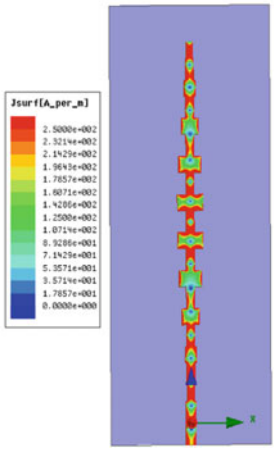
Jsurf(A_per_m)

(c)

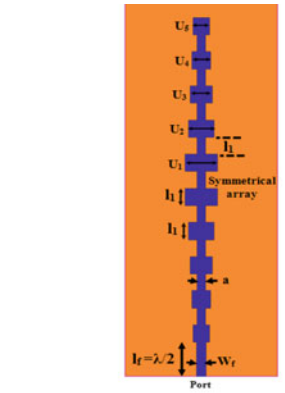

(a)

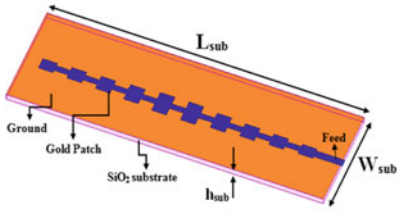

(b)

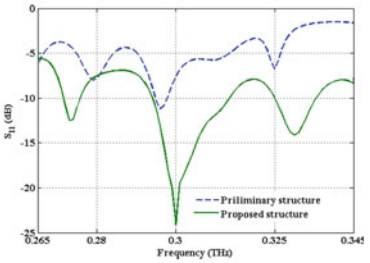

(c)

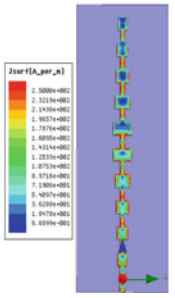

(d)

Fig. 3 Proposed 10-element array **a** top view **b** slant view **c** *S*-parameter performance **d** surface current distribution at 300 GHz

Table 2 Proposed array elements width

Width of each element (U_n)	Elements width (mm) $u = 0.42$ mm
U_1	$U_1 = u = 0.42$
U_2	$U_2 = u/1.25 = 0.336$
U_3	$U_3 = u/1.5 = 0.28$
U_4	$U_4 = u/1.75 = 0.24$
U_5	$U_5 = u/2 = 0.21$

Figure 3d shows the distribution of current on the surface of the radiating patch and the conclusion can be derived that all the array elements are the good radiators at 300 GHz, which results in high gain and achieves the objective of the said above design. Figure 4 shows the plot of far-field results where the study of 3D-radiation pattern and 2D-radiation patterns is shown at various resonant frequencies presenting 273 GHz, 300 GHz, and 330 GHz.

Figure 4 clearly presents required radiation directional characteristics from the proposed antenna at 300 GHz along *XZ* and *YZ* planes. Comparison of proposed work with the existing literature is shown in Table 3, which shows the advantage of proposed work as compared to other THz discussions.

4 Conclusion

This chapter focused on 10-element symmetric series fed planar antenna array for 0.3 THz applications. The antenna array was characterized by using Dolph-Tschebyscheff concept, and all the key parameters obtained are adopted on to the geometry. Initially, a preliminary array of 10-elements is presented based on Tschebyscheff polynomials. However, this structure is not resulting into good S-parameter and radiation characteristics. Then, an optimized 10-element array is reported for achieving better return loss and directional patterns. An impedance bandwidth of range 0.294–0.313 THz and a peak gain of 13.26 dBi at 0.3 THz are noted for the proposed THz array. Gold material of thickness 5 μm and silicon dioxide (SiO_2) dielectric substrate of 2 mm × 5.5 mm × 0.06 mm dimensions are employed. Exhibiting compact structure, dimensions, higher directivity, resonating characteristics, and better performance proposed antenna array can be employed in THz applications like imaging, radars, device-to-device communication, THz Wi-Fi, point-to-point communication, etc.

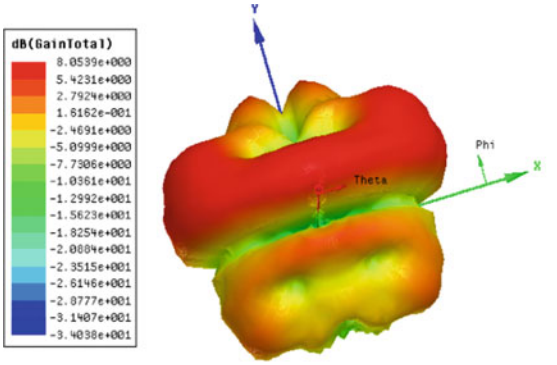

(a)

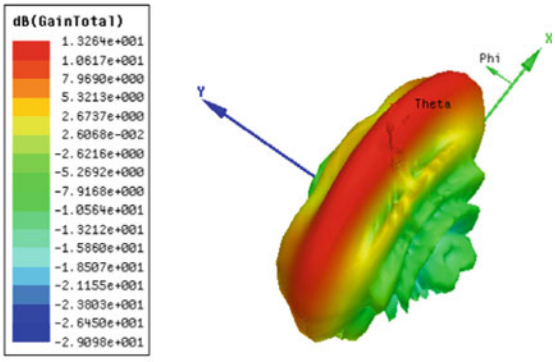

(b)

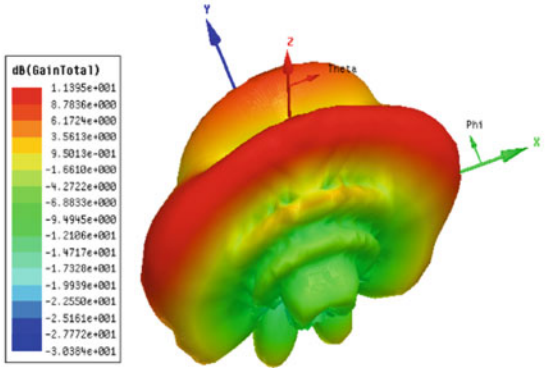

(c)

Fig. 4. 3D-radiation pattern at **a** 273 GHz **b** 300 GHz **c** 330 GHz **d** 2D-radiation pattern at 300 GHz, *XZ*-plane **e** *YZ*-plane **f** *XY*-plane

Fig. 4. (continued)

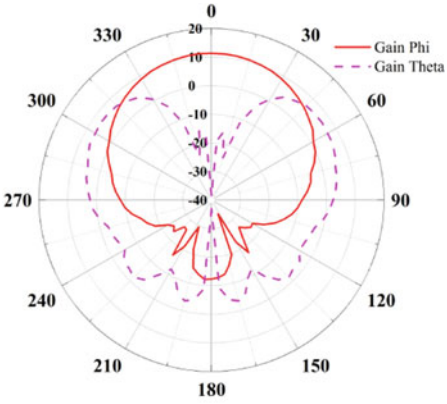

(d)

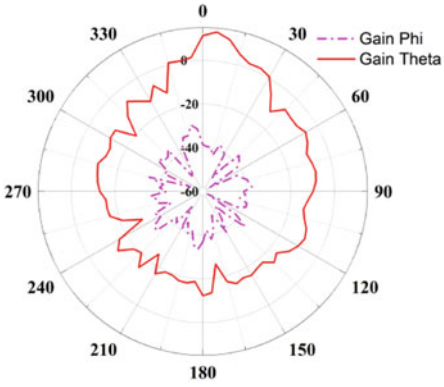

(e)

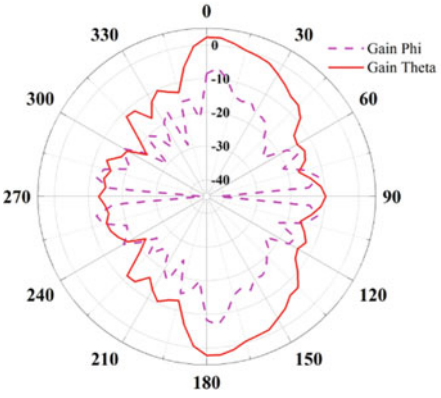

(f)

Table 3 Comparison of proposed work with the existing literature

References	Antenna type	Operating band (THz)	Peak gain (dBi)	No. of layers	Dimensions (mm × mm)	sub
[2]	Horn antenna	0.3	16	3	5 × 5	LTCC
[3]	Stacked patch antenna	0.22–0.32	8.8	2	Top patch 0.208 × 0.153 Bottom patch 0.248 × 0.238	Quartz
[4]	Rectangular Horn antenna, Cassegrain and offset parabolic antennas	0.3	25, 47, 49	1	–	–
[5]	Micro-strip antenna array based on dual surfaced multiple split-ring resonators (DSMSRRs)	0.274–0.295 and 0.306–0.313	–	1	0.423 × 0.345	FR4
[14]	Printed reflect array	0.28–0.32	41	1	0.5 × 0.5	Quartz
[16]	Dielectric lens antenna	0.3	19.7	1	–	PTFE
[17]	Step-profiled corrugated horn antennas	0.3	18	24	5 × 5	LTCC
[18]	Micro-lens antenna	0.3	–	1	Aperture diameter of 2.5 mm	–
[22]	Fabry–Perot cavity (FPC) antenna	0.285–0.31	17.7	7	2.6 × 2.6	Silicon
*	Series fed non-uniform planar antenna array	0.3	13.26	1	2 × 5.5	Silicon dioxide

*Proposed work

References

1. M. Mohammadi Shirkolaei, High efficiency X-band series-fed microstrip array antenna. Progress Electromagn. Res. C. **105**, 35–45 (2020)
2. T. Tajima, H.J. Song, M. Yaita, K. Ajito, N. Kukutsu, 300-GHz LTCC horn antennas based on antenna-in-package technology, in *European Microwave Conference* (2013), pp. 231–234

3. A. Dyck, M. Rosch, A. Tessmann, A. Leuther, M. Kuri, H. Mabler, S. Wagner, D. Meder, B. Weismann-Thaden, M. Schlechtweg, O. Ambacher, A 300 GHz microstrip multilayered antenna on quartz substrate, in *International Workshop on Antenna Technology (iWAT)* (2018), pp. 1–3
4. H. Sawada, A. Kanno, N. Yamamoto, K. Fujii, A. Kasamatsu, K. Ishizu, F. Kojima, H. Ogawa, I. Hosako, High gain antenna characteristics for 300 GHz band fixed wireless communication systems, in *Progress in Electromagnetics Research Symposium* (2017), pp. 1409–1412
5. S. Bie, S. Pu, Array design of 300 GHz dual-band microstrip antenna based on dual-surfaced multiple split-ring resonators. Sensors (Basel) **21**(14) (2021)
6. V. Semkin, F. Ferrero, A. Bisognin, J. Ala-Laurinaho, C. Luxey, F. Devillers et al., Beam switching conformal antenna array for mm-wave communications. IEEE Ant. Wirel. Propag. Lett., 28–31 (2015)
7. S. Sengupta, D.R. Jackson, S.A. Long, A method for analyzing a linear series-fed rectangular microstrip antenna array. IEEE Trans. Ant. Propag. **63**(8), 3731–3736 (2015)
8. R. Zainab Syeda, Design and performance analysis of switched beam series-fed patch antenna array for 60 GHz WPAN applications. pp. 45–54 (2014)
9. L. Dan, G. Ducournau, S. Hisatake, P. Szriftiser, R.P. Braun, I. Kalfass, A terahertz wireless communication link using a superheterodyne. IEEE Trans. Terahertz Sci. Technol. **10**(1), 32–43 (2020)
10. J.F. O'Hara, S. Ekin, W. Choi, I. Song, A perspective on terahertz next-generation wireless communications. Technologies **7**(2), 1–10 (2019)
11. J. Yan, H. Wang, J. Yin, C. Yu, W. Hong, Planar series-fed antenna array for 77 GHz automotive RADAR, in *Sixth Asia-Pacific Conference on Antennas and Propagation (APCAP)* (2017), pp. 1–3
12. H.-C. Chen, T. Chiu, C.-L. Hsu, Design of series-fed bandwidth-enhanced microstrip antenna array for millimetre-wave beamforming applications. Int. J. Ant. Propag., 1–10 (2019)
13. H.J. Song, K. Ajito, A. Wakatsuki, Y. Muramoto, N. Kukutsu, Y. Kado, T. Nagatsuma, Terahertz wireless communication link at 300 GHz, in *2010 IEEE International Topical meeting on Microwave Photonics* (2010), pp. 42–45
14. R. Florencia, R.R. Boix, J.A. Encinar, Design of a reflect array antenna at 300 GHz based on cells with three coplanar dipoles, in *IEEE Antennas and Propagation Society International Symposium (APSURSI)* (2013), pp. 1350–1351
15. M. Fujishima, Future of 300 GHz band wireless communications and their enabler, CMOS transceiver technologies. Japan. J. Appl. Phys. **60**(SB) (2021)
16. I. Abodo, T. Fujimura, T. Miura, A. Shirane, K. Okada, A 300 GHz dielectric lens antenna, in *12th Global Symposium on Millimeter Waves (GSMM)* (2019), pp. 17–19
17. T. Tajima, H.-J. Song, K. Ajito, M. Yaita, N. Kukutsu, 300-GHz step-profiled corrugated horn antennas integrated in LTCC. IEEE Trans. Ant. Propag. **62**(11), 5437–5444 (2014)
18. K. Wang, F. Yang, 300 GHz dual-polarized micro-lens antenna for terahertz integrated heterodyne arrays, in *International Workshop on Antenna Technology (iWAT)* (2018), pp. 1–3
19. A. Munoz-Munoz, M. Sierra-Castaner, J.L. Besada, Antenna measurement system at 300 GHz for the Terasense project, in *Proceedings of the Fourth European Conference on Antennas and Propagation* (2010), pp. 1–5
20. C. Jastrow, K. Münter, R. Piesiewicz, T. Kürner, M. Koch, T. Kleine-Ostmann, 300 GHz transmission system. Electron. Lett. **44**(3) (2008)
21. H.J. Song, K. Ajito, Y. Muramoto, A. Wakatsuki, T. Nagatsuma, N. Kukutsu, 24 Gbit/s data transmission in 300 GHz band for future terahertz communications. Electron. Lett. **48**(15) (2012)
22. B. Aqlan, M. Himdi, H. Vettikalladi, L. Le-Coq, A 300-GHz low-cost high-gain fully metallic Fabry-Perot cavity antenna for 6G terahertz wireless communications. Sci Rep. **11**(1), 7703 (2021)
23. B. Aghoutane, S. Das, H. El Faylali, B.T.P. Madhav, M. El Ghzaoui, A. El Alami, Analysis, design and fabrication of a square slot loaded (SSL) millimeter-wave patch antenna array for 5G applications. J. Circ. Syst. Comput. **30**(5), 2150086 (2021). https://doi.org/10.1142/S0218126621500869

24. M.V. Subbarao, N.S. Khasim, J. Thati, M.H.H. Sastry, Tapering of antenna array for efficient radiation pattern. e-J. Sci. Technol. (e-JST), April (2013)
25. G. Jyothi, K.R. Devi, Design optimization of low side lobe level microstrip antenna array at 28 GHz for 5G application. Int. Res. J. Eng. Technol. (IRJET) **7**(12) (2020). e-ISSN: 2395-0056

Compact Two Ports MIMO Antenna Operating at Terahertz Band

Nour El Houda Nasri, Mohammed El Ghzaoui, and Mohammed Fattah

Abstract The THz frequencies are the new revolution in the telecommunication due to theirs several advantages this paper will propose a MIMO patch antenna polyimide based that is capable to function at THz frequencies. The performance of the proposed antenna has been analyzed in term of multiple antenna characteristics such as impedance bandwidth (GHz), gain (dB), return loss (dB), and VSWR. The Polyimide substrate having thickness of 9 μm and lower dielectric constant, and ε_r of 3.5 has been used in the antenna design. The HFSS (High frequency structure simulator) which is based on the finite element method is used to design and simulate the antenna. In this work, we present the results of a parametric study of a MIMO 2×2 patch antenna in the frequency band Terahertz (THz) ranging from 2.526 to 2.995 THz (a bandwidth of 469 GHz) and has a reflection coefficient of about -21.44 and -29.62 dB and a gain of 6.67 dB at 2.74 THz.

Keywords THz frequencies · Reflection coefficient · Bandwidth · Gain · MIMO

1 Introduction

Telecommunication, a vital sector of the economy of any nation, continues to undergo major changes from a technological point of view. These changes are made necessary by demand and user requirements in terms of services and quality of service. This continuous evolution [1] of the telecommunications field always calls for new frequencies to be used in order to offer the best quality of coverage and therefore of service for the user; and when we talk about coverage implies the use of antennas [2–4], for this we cite MIMO antennas which are the most efficient antennas in the field.

Despite the use of most frequencies on the frequency spectrum there is still a frequency range of THz waves which is not yet overused but this spectrum called *T*

N. E. H. Nasri (✉) · M. Fattah
Moulay Ismail University, Meknes, Morocco

M. E. Ghzaoui
Faculty of Sciences, Sidi Mohamed Ben Abdellah University, Fez, Morocco

M. El Ghzaoui et al. (eds.), *Terahertz Wireless Communication Components and System Technologies*, https://doi.org/10.1007/978-981-16-9182-9_8

waves is a promising spectrum for the future of telecommunications. MIMO is known for its advantages for the telecommunication domain. The microstrip patch antenna is known for its miniaturization compatibility which is perfect for THz frequency.

In fact, many researches have been devoted to the THz patch antennas. Singh and Singh [5] proposed a trapezoidal microstrip patch antenna on photonic crystal substrate for high speed THz applications utilized in the frequency band of 0.88–1.62 THz with a return loss of −13.05. Nickpay et al. [6] designed a wideband rectangular double-ring nanoribbon graphene-based antenna for terahertz communications with an average gain of 2.45 dB is achieved at the operational frequency band of a center frequency of 1 THz. In Anand et al. [7], proposed a graphene nanoribbon based terahertz antenna on polyimide substrate in the 725–775 GHz band, this design has shown a peak gain of 5.71 dB at 750 GHz.

This work proposes a new THz MIMO patch antenna design with a significant bandwidth a relatively standard peak gain and a small size, for THz applications around a resonance frequency of 2.74 THz. The proposed antenna consists of a MIMO 2 × 2 antenna on polyimide ($\varepsilon_r = 3.5$) substrate, the low dielectric substrate is used to improve the radiation in the wanted direction. The antenna is fed by a microstrip line having a power port adapted to 50 Ω. The most important aim of this work is to improve the parameters of the antenna. In order to do this slots were added to the initial antenna.

This paper is divided into 8 sections: the first is dedicated for the THz technology and its applications, the second one is for the advantages of MIMO antenna over SISO antenna, the third one is for MIMO modelization, the fourth one is for the channel characterization for a MIMO antenna, the fifth section is for MIMO gain, the sixth section is for the performance of the MIMO antenna channel, the seventh section is for the antenna gains, and the final one is dedicated for the results and simulations of the proposed antenna.

2 THz Technology

2.1 State of Art of THz Technology

All over the world, several researchers are interested in THz waves since they are able to significantly improve the performance of several devices and also new applications will take place thanks to this technology; unfortunately the design and development of solutions using this technology are manifested always expensive [8].

This interest in THz technologies [9, 10] is due to the fact that THz waves lay between two relevant frequency bands in telecommunication world Fig.1: infrared (30 μm or 10 THz) and microwaves (1 mm or 0.3 THz, approximately) from which they take two interesting characters; firstly, they adopt the ability to focus and access

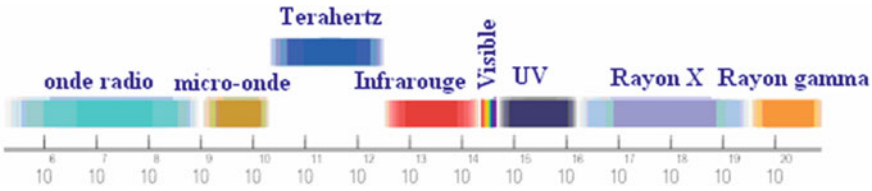

Fig. 1 THz spectrum frequency

a certain submillimeter spatial resolution; secondly, they penetrate dielectric materials, adding to this that they exhibit strong aptitudes for penetrating imagery by emphasizing spectroscopic relevance.

THz technology has several interesting properties:

- The wavelength of THz technology allows waves to penetrate many materials while providing higher spatial resolution than microwaves.
- The penetration depth is relatively large for several non-conductive materials: plastics, ceramics, etc. The THz thickness measurement of multilayer materials is non-destructive.
- Substances subjected to THz radiation exhibit characteristic spectral signatures due to excitation modes of their molecular arrangement. THz spectroscopy also makes it possible to identify substances or their chemical characterization.
- The non-contact measurement character since the propagation of THz waves in the air is low attenuation.
- Their non-destructive and non-ionizing qualities [2].

2.2 THz Applications

Diagnostic imaging

The terahertz will be used in the medical sector [11, 12] to guarantee a more reliable diagnosis with careful results, by combining the THz with existing medical imaging such as MRI the diagnosis will be faster and more precise. The THz will also be used in dentistry to detect quickly the enamel wear and cavities.

Security imaging [13]

Using its property of penetrating dielectric materials, THz will be able to detect all objects under clothing; therefore, it will offer a large number of applications to use in safety the THz will give a clear and high quality image of what is under any non-conductive material; it will be of great service to airport security searches; the THz can also be used by the military to detect any harmful object.

Food and hygiene

Food factories will have the chance to improve their quality and even save time to check through packages using Terahertz to detect the existence of any foreign object in their product and even to monitor their water content.

Material inspection

The biggest evolution that Terahertz will take is its ability to inspect the materials; it will be used as a method of quality control and even in the production process to check if one step is right to move on to the next.

3 Advantage of MIMO Versus SISO System

Unlike the single input single output SISO which is a single antenna for transmission and only one for reception, the MIMO system with several antennas used for transmission and reception achieves a higher throughput thanks to the transmission of data simultaneously on several antennas what is called spatial multiplexing the MIMO system brings other advantages such as the diversity of antennas because each antenna is used with a precise angle [14]. This diversity improves the data link by giving different points of view that an antenna can be affected by an antenna unlike other antennas thanks to the difference in polarization.

Space–time block coding (STBC) is a technique used by MIMO systems which consists of transmitting copies of the same data on all antennas; this technique in combination with spatial multiplexing guarantees the reliability of data transmission. This technique has been able to overcome the problem of interference and obstacles encountered in SISO systems this redundancy in MIMOs guarantees more correct decoding by combining all received copies of the signal.

Another technique that is available with MIMO is beamforming. This method involves emitting individual rays so each lobe will be dedicated to a specific base station.

4 MIMO Modeling

4.1 MIMO 2 × 2 Modeling

In order to model a 2×2 MIMO antenna, the study must focus on two transmitting antennas and two receiving antennas, it is a TITO Fig. 2 (Two Inputs Two Outputs).

The relationship between the x input signals and the y output signals is as follows:

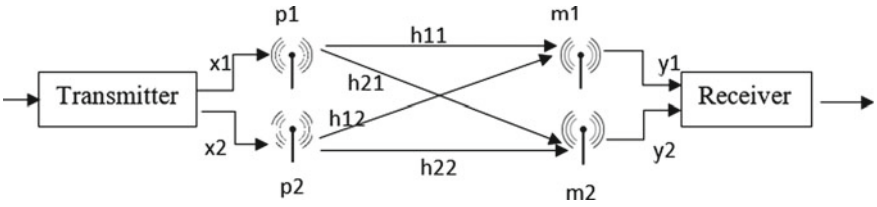

Fig. 2 MIMO 2 × 2 system

$$\begin{bmatrix} y_1 \\ y_2 \end{bmatrix} = \begin{bmatrix} h_{11} & h_{12} \\ h_{21} & h_{22} \end{bmatrix} \begin{bmatrix} x_1 \\ x_2 \end{bmatrix} + \begin{bmatrix} n_1 \\ n_2 \end{bmatrix} \quad \Rightarrow y = Hx + n. \tag{1}$$

where H is the channel matrix of size 2 × 2, and n is the noise vector.

The geometry of the system: two-dimensional 2 × 2 MIMO LOS model shown is in Fig. 3.

The complete geometry of the system is defined from 5 variables $Nt = 2$, $Nr = 2$, ϕt_{11}, ϕr_{11}, and d_{11}.

The first step is to calculate the distances between *Tx* and *Rx* using the formula:

$$\forall i \neq j : d_{ij} = \sqrt{d_{ii}^2 + (|i-j|D_t)^2 + \text{signe}(i-j)2d_{ii}|j-i|D_t\cos(\phi t_{ii})}. \tag{2}$$

In MIMO, 2 × 2 d_{12} and d_{21} are:

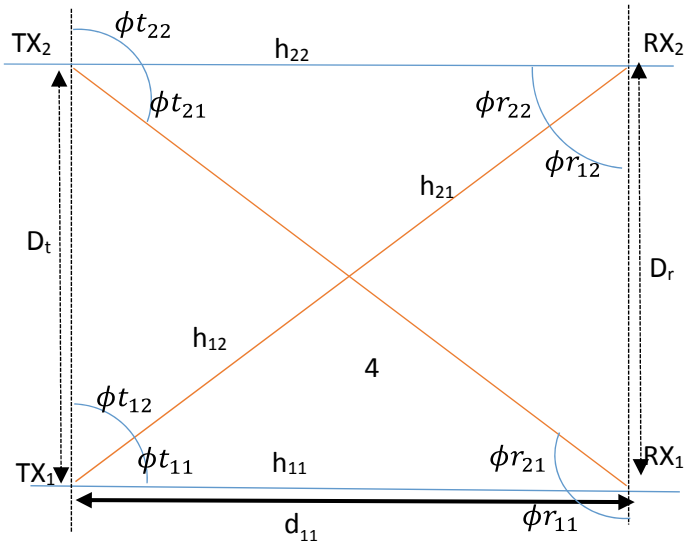

Fig. 3 MIMO LOS 2 × 2 model

$$d_{12} = \sqrt{d_{11}^2 + D_t^2 - 2d_{11}D_t\cos(\phi t_{11})}. \tag{3}$$

$$d_{21} = \sqrt{d_{22}^2 + D_t^2 + 2d_{22}D_t\cos(\phi t_{22})}. \tag{4}$$

d_{ij} allows the calculation of ϕt_{ij}, the angle of arrival (defined on $[0, \pi]$) at the transmitting side between Tx_j and Rx_i using:

$$\phi t_{ij} = \cos^{-1}\left(\text{signe}(i-j)\frac{(|j-i|D_t)^2 + d_{ij}^2 - d_{ii}^2}{2|j-i|D_t d_{ij}}\right). \tag{5}$$

ϕt_{12} and ϕt_{21} are:

$$\phi t_{12} = \cos^{-1}\left(-\frac{(D_t)^2 + d_{12}^2 - d_{11}^2}{2D_t d_{12}}\right). \tag{6}$$

$$\phi t_{21} = \cos^{-1}\left(\frac{(D_t)^2 + d_{21}^2 - d_{22}^2}{2D_t d_{21}}\right). \tag{7}$$

Then ϕr_{ij}, the angle of arrival (defined on $[0, \pi]$) at the reception between Tx_j and Rx_i.

$$\phi r_{ij} = \phi r_{ii} - \phi t_{ii} + \phi t_{ij}. \tag{8}$$

So:

$$\phi r_{12} = \phi r_{11} - \phi t_{11} + \phi t_{12}. \tag{9}$$

$$\phi r_{21} = \phi r_{22} - \phi t_{22} + \phi t_{21}. \tag{10}$$

ϕr_{ii}, ϕt_{ii}, and d_{ii} are calculated using these equations:

$$d_{ii} = \sqrt{d_{1i}^2 + ((i-1)D_r)^2 + 2d_{1i}(i-1)D_r\cos(\phi r_{1i})}. \tag{11}$$

$$\phi r_{ii} = \cos^{-1}\left(\text{signe}(i-1)\frac{(|i-1|D_r)^2 + d_{ii}^2 - d_{1i}^2}{2|j-i|D_t d_{ii}}\right). \tag{12}$$

$$\phi t_{ii} = \phi t_{1i} - \phi r_{1i} + \phi r_{ii}. \tag{13}$$

In this case, $i = 2$:

$$d_{22} = \sqrt{d_{12}^2 + D_r^2 + 2d_{12}D_r\cos(\phi r_{12})}. \tag{14}$$

$$\phi r_{22} = \cos^{-1}\left(\frac{D_r^2 + d_{22}^2 - d_{12}^2}{2D_r d_{22}}\right). \tag{15}$$

$$\phi t_{22} = \phi t_{12} - \phi r_{12} + \phi r_{22}. \tag{16}$$

After having defined all the parameters, they are assembled in the form of matrices:

$$d = \begin{bmatrix} d_{11} & d_{12} \\ d_{21} & d_{22} \end{bmatrix}. \tag{17}$$

$$\phi t = \begin{bmatrix} \phi t_{11} & \phi t_{12} \\ \phi t_{21} & \phi t_{22} \end{bmatrix}. \tag{18}$$

$$\phi r = \begin{bmatrix} \phi r_{11} & \phi r_{12} \\ \phi r_{21} & \phi r_{22} \end{bmatrix}. \tag{19}$$

4.2 MIMO 3 × 3 Modeling

The relationship between the x input signals and the y output signals is as follows:

$$\begin{bmatrix} y_1 \\ y_2 \\ y_3 \end{bmatrix} = \begin{bmatrix} y_{11} & y_{12} & y_{13} \\ y_{21} & y_{22} & y_{23} \\ y_{31} & y_{32} & y_{33} \end{bmatrix} \begin{bmatrix} x_1 \\ x_2 \\ x_3 \end{bmatrix} + \begin{bmatrix} n_1 \\ n_2 \\ n_3 \end{bmatrix} \quad \Rightarrow y = Hx + n. \tag{20}$$

where H is the channel matrix of size 3×3, and n is the noise vector.

Using the same equations in the previous part, the parameters that remain to be calculated are as follows.

Distances are:

$$d_{13} = \sqrt{d_{11}^2 + (2D_t)^2 - 4d_{11}D_t\cos(\phi t_{11})}. \tag{21}$$

$$d_{23} = \sqrt{d_{22}^2 + (D_t)^2 - 2d_{22}D_t\cos(\phi t_{22})}. \tag{22}$$

$$d_{31} = \sqrt{d_{33}^2 + (2D_t)^2 + 4d_{33}D_t\cos(\phi t_{33})}. \tag{23}$$

$$d_{32} = \sqrt{d_{33}^2 + (D_t)^2 + 2d_{33}D_t\cos(\phi t_{33})}. \tag{24}$$

$$d_{32} = \sqrt{d_{13}^2 + 4D_r^2 + 4d_{13}D_r\cos(\phi r_{13})}. \tag{25}$$

For arrival angles:

$$\phi t_{13} = \cos^{-1}\left(-\frac{(2D_t)^2 + d_{13}^2 - d_{11}^2}{4D_t d_{13}}\right). \tag{26}$$

$$\phi t_{23} = \cos^{-1}\left(-\frac{(D_t)^2 + d_{23}^2 - d_{22}^2}{2D_t d_{23}}\right). \tag{27}$$

$$\phi t_{31} = \cos^{-1}\left(\frac{(2D_t)^2 + d_{31}^2 - d_{33}^2}{4D_t d_{31}}\right). \tag{28}$$

$$\phi t_{32} = \cos^{-1}\left(\frac{(D_t)^2 + d_{32}^2 - d_{33}^2}{2D_t d_{32}}\right). \tag{29}$$

$$\phi t_{33} = \phi t_{13} - \phi r_{13} + \phi r_{33}. \tag{30}$$

$$\phi r_{13} = \phi r_{11} - \phi t_{11} + \phi t_{13}. \tag{31}$$

$$\phi r_{23} = \phi r_{22} - \phi t_{22} + \phi t_{23}. \tag{32}$$

$$\phi r_{31} = \phi r_{33} - \phi t_{33} + \phi t_{31}. \tag{33}$$

$$\phi r_{32} = \phi r_{33} - \phi t_{33} + \phi t_{32}. \tag{34}$$

$$\phi r_{33} = \cos^{-1}\left(\frac{(2D_r)^2 + d_{33}^2 - d_{13}^2}{4D_t d_{33}}\right). \tag{35}$$

The matrices of MIMO 3 × 3 are:

$$d = \begin{bmatrix} d_{11} & d_{12} & d_{13} \\ d_{21} & d_{22} & d_{23} \\ d_{31} & d_{32} & d_{33} \end{bmatrix}. \tag{36}$$

$$\phi t = \begin{bmatrix} \phi t_{11} & \phi t_{12} & \phi t_{13} \\ \phi t_{21} & \phi t_{22} & \phi t_{23} \\ \phi t_{31} & \phi t_{32} & \phi t_{33} \end{bmatrix}. \tag{37}$$

$$\phi r = \begin{bmatrix} \phi r_{11} & \phi r_{12} & \phi r_{13} \\ \phi r_{21} & \phi r_{22} & \phi r_{23} \\ \phi r_{31} & \phi r_{32} & \phi r_{33} \end{bmatrix}. \tag{38}$$

5 Characterization of the SISO to MIMO Channel

5.1 Determinist Characterization in the Temporal and Spatial Domains

The propagation channel is mathematically represented by a linear transformation between the input and the output as shown in Fig. 4.

For a stationary and linear propagation medium, the channel is modeled by a filter which takes into account the effect of the antennas of the transmitter, the receiver, and the propagation medium to simplify things the antenna arrays of the transmitter and of the receiver will not be taken into account, and then the propagation channel will depend only on the propagation medium and the geometric configuration, temporal and frequency configuration of the link.

The signals at the input and at the output of this filter are interpreted on both temporal and spatial domains, so to properly characterize the behavior of the propagation channel a joint explanation in both domains is necessary. Therefore, the temporal and spatial domains can be treated separately.

Time domain

Either in the time or in the frequency domain, the representation between the input and output signals is described by four transfer functions. In the time domain there are two pairs of variables which are the reception instant t and the Doppler shift υ and propagation delay τ and the frequency f and by duality properties express the propagation channel. These functions are related by the Fourier transformation that its operators are defined on Table 1.

The representation of the channel in time-delay

The output signals are expressed by:

$$y(t) = \int x(t-\tau)h(t,\tau)\mathrm{d}\tau. \tag{39}$$

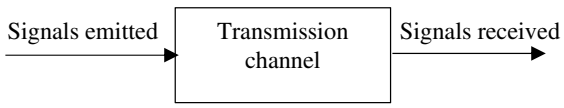

Fig. 4 SISO channel modeling

Table 1 Definition of Fourier transforms in the time domain

Dual domains	Direct transform	Inverse transform
$t \rightleftarrows v$	$\int(.)\exp(-j2\pi vt)\mathrm{d}t$	$\int(.)\exp(-j2\pi v\tau)\mathrm{d}v$
$\tau \rightleftarrows f$	$\int(.)\exp(-j2\pi f\tau)\mathrm{d}\tau$	$\int(.)\exp(-j2\pi f\tau)\mathrm{d}f$

where $x(t)$ is the signal on transmission, $y(t)$ is the signal on reception, $h(t, \tau)$ is the impulse response of the propagation channel without taking into account the gains of the transmitting antenna and receiver, and τ is the propagation delay.

The representation of the frequency-Doppler channel

The characterization of the general channel can also be done with the frequency variables given in the dual character. The output Doppler dispersion function is $h(f, v)$; it allows to observe the Doppler shift phenomenon. The expression of the channel is as follows:

$$y(f) = \int x(f - v)h(f - v, v)\mathrm{d}v. \tag{40}$$

The spectrum of $y(f)$ is a superposition of replicas of the input spectrum $x(t)$ which has been Doppler shifted and filtered.

The representation of the channel in frequency-time

The output time signal $y(t)$ can also be represented by a time-varying transfer function $h(f, t)$ and the spectrum of the input signal $x(f)$ as follows:

$$y(t) = \int x(f)h(t, f)\mathrm{e}^{2j\pi ft}\mathrm{d}f. \tag{41}$$

With

$$h(f, t) = \int h(t, \tau)\mathrm{e}^{-2j\pi f\tau}\mathrm{d}\tau = \int h(f, v)\mathrm{e}^{2j\pi vt}\mathrm{d}v. \tag{42}$$

The representation of the channel in delay Doppler

This last representation is important; it allows to have at the same time the dispersion produced in the transmission channel in the time and frequency domains. The output signal as a function of the Doppler-delay function $h(v, \tau)$ is expressed as follows:

$$y(t) = \iint x(t - \tau)h(v, \tau)\mathrm{e}^{2j\pi vt}\mathrm{d}v\mathrm{d}\tau. \tag{43}$$

Spatial domain

In this part, the study will be done on the characterization of the channel in the space domain. The propagation channel in this domain is modeled by a kernel operator. Knowing that the expression of the monochromatic progressive plane wave is $s(t, \vec{r}) = \mathrm{Re}\left\{A\mathrm{e}^{j\left(\omega t - \vec{k}, \vec{r}\right)}\right\}$, we can have the input–output relations of the channel as following:

Table 2 Definition of Fourier transforms in the spatial domain when the channel response appears in the form of a kernel

Dual domains	Direct transform	Inverse transform
$\vec{r}_{Rx} \rightleftarrows \vec{k}_{Rx}$	$\int(.)\exp\left(-j\vec{k}_{Rx}.\vec{r}_{Rx}\right)\mathrm{d}\vec{r}_{Rx}$	$\int(.)\exp\left(-j\vec{k}_{Rx}.\vec{r}_{Rx}\right)\mathrm{d}\vec{k}_{Rx}$
$\vec{r}_{Tx} \rightleftarrows \vec{k}_{Tx}$	$\int(.)\exp\left(-j\vec{k}_{Tx}.\vec{r}_{Tx}\right)\mathrm{d}\vec{r}_{Tx}$	$\int(.)\exp\left(-j\vec{k}_{Tx}.\vec{r}_{Tx}\right)\mathrm{d}\vec{k}_{Tx}$

$$y(\vec{r}_{Rx}) = \int h(\vec{r}_{Rx}, \vec{r}_{Tx})x(\vec{r}_{Tx})\mathrm{d}\vec{r}_{Tx}. \tag{44}$$

$$y(\vec{r}_{Rx}) = \int h\left(\vec{r}_{Rx}, \vec{k}_{Tx}\right)x\left(\vec{k}_{Tx}\right)\mathrm{d}\vec{k}_{Tx}. \tag{45}$$

$$y\left(\vec{k}_{Rx}\right) = \int h\left(\vec{k}_{Rx}, \vec{r}_{Tx}\right)x(\vec{r}_{Tx})\mathrm{d}\vec{r}_{Tx}. \tag{46}$$

$$y\left(\vec{k}_{Rx}\right) = \int h\left(\vec{k}_{Rx}, \vec{k}_{Tx}\right)x\left(\vec{k}_{Tx}\right)\mathrm{d}\vec{k}_{Tx}. \tag{47}$$

where h is a 3×3 square matrix connecting the 3 orthogonal components of the transmitted signal to those of the received signal. The variables $\vec{r}_{Tx}$ and $\vec{r}_{Rx}$ represent the sending position and the receiving position, respectively, and the variables $\vec{k}_{Tx}$ and $\vec{k}_{Rx}$ are the spatial sending and receiving pulses. The 4 expressions which are equivalent are linked using the Fourier transform in Table 2.

The previous expressions can be simplified in the context of electromagnetic waves in local areas therefore the new expressions:

$$y(\vec{r}_{Rx}) = \int h(\vec{r}_{Rx}, \vec{r}_{Tx})x(\vec{r}_{Tx})\mathrm{d}\vec{r}_{Tx}. \tag{48}$$

$$y(\vec{r}_{Rx}) = \int h(\vec{r}_{Rx}, \Omega_{Tx})x(\Omega_{Tx})\mathrm{d}\Omega_{Tx}. \tag{49}$$

$$y(\Omega_{Rx}) = \int h(\Omega_{Rx}, \vec{r}_{Tx})x(\vec{r}_{Tx})\mathrm{d}\vec{r}_{Tx}. \tag{50}$$

$$y(\Omega_{Rx}) = \int h(\Omega_{Rx}, \Omega_{Tx})x(\Omega_{Tx})\mathrm{d}\Omega_{Tx}. \tag{51}$$

where $h(\vec{r}_{Rx}, \vec{r}_{Tx})$, $h(\vec{r}_{Rx}, \Omega_{Tx})$, $h(\Omega_{Rx}, \vec{r}_{Tx})$, and $h(\Omega_{Rx}, \Omega_{Tx})$ are, respectively, the spatial response, the angular response of emission, the angular response of reception, and the bidirectional response; thus Ω_{Tx} and Ω_{Rx} represent vectors with two elements containing the angles of azimuth and elevation, respectively, at the level of the transmitting site and at the reception site.

Table 3 Definition of Fourier transforms in the spatial domain for the representation

Dual domains	Direct transform	Inverse transform
$\vec{r} \rightleftarrows \vec{\kappa}$	$\int(.)\exp(-j\vec{\kappa}.\vec{r})\mathrm{d}\vec{r}$	$\frac{1}{(2\pi r)^3}\int(.)\exp(-j\vec{\kappa}.\vec{r})\vec{\kappa}$
$\vec{k} \rightleftarrows \vec{\rho}$	$\int(.)\exp\left(-j\vec{k}.\vec{\rho}\right)\mathrm{d}\vec{k}$	$\frac{1}{(2\pi r)^3}\int(.)\exp\left(-j\vec{k}.\vec{\rho}\right)\mathrm{d}\vec{k}$

Other expressions can be deduced from the time domain expressions with an equivalence between the parameters of the two. The instant of reception t, the frequency, the propagation delay τ, and the Doppler shift v which are replaced, respectively, by the reception position r, the spatial pulsation k, the relative position of the emission with respect to the reception ρ, and the spatial Doppler pulse κ. So, the expressions are in the form of a convolution product:

$$y(\vec{r}) = \int h(\vec{r}, \vec{\rho})x(\vec{r} - \vec{\rho})\mathrm{d}\vec{\rho}$$

$$y(\vec{r}) = \int h\left(\vec{r}, \vec{k}\right)x\left(\vec{k}\right)\mathrm{e}^{j\vec{k}.\vec{r}}\mathrm{d}\vec{k}. \tag{52}$$

$$y\left(\vec{k}\right) = \int h\left(\vec{\kappa}, \vec{k} - \vec{\kappa}\right)x\left(\vec{k} - \vec{\kappa}\right)\mathrm{d}\vec{\kappa}. \tag{53}$$

$$y(\vec{r}) = \iint h(\vec{\kappa}, \vec{\rho})x(\vec{r} - \vec{\rho})\mathrm{e}^{j\vec{\kappa}.\vec{r}}\mathrm{d}\vec{\rho}\mathrm{d}\vec{\kappa}. \tag{54}$$

where $\vec{r} = \vec{r}_{Rx}$, $\vec{k} = \vec{k}_{Tx}$, $\vec{\rho} = \vec{r}_{Rx} - \vec{r}_{Tx}$, and $\vec{\kappa} = \vec{k}_{Rx} - \vec{k}_{Tx}$. The 4 expressions introduced in the equations, mathematically equivalent but of complementary physical interpretation, are linked by TF. The TF operators are defined in Table3. The function $h(\vec{r}, \vec{\rho})$ is the impulse response varying in space, the function $h\left(\vec{r}, \vec{k}\right)$ is the transfer function varying in space, the function $h\left(\vec{\kappa}, \vec{k}\right)$ is the two-frequency function in spatial pulsation, and the function $h(\vec{\kappa}, \vec{\rho})$ is the relative position-spatial pulsation spreading function Doppler.

5.2 *Stochastic Characterization in the Temporal and Spatial Domains*

The propagation channel becomes random in the case of environments rich in diffusers then the functions which models the channel are random functions their stochastic explanation is a density function of multidimensional probability equivalent on all the statistical moments. In order to facilitate the characterization, the calculations will be made at the first order which is defined by the mean and at the second

order by the correlation functions. And the propagation medium will be described by Gaussian processes to understand the energetic behavior of the propagation medium.

Time domain

The functions that were introduced in the previous part can be defined as follows:

$$R_h(t, \tau, t', \tau') = E\{h(t, \tau)h'(t', \tau')\}. \tag{55}$$

$$R_h(f, v, f', v') = E\{h(f, v)h^*(f', v')\}. \tag{56}$$

$$R_h(f, t, f', t') = E\{h(f, v)h^*(f', t')\}. \tag{57}$$

$$R_h(\tau, v, \tau', v') = E\{h(\tau, v)h^*(\tau', v')\}. \tag{58}$$

where (t, t'), (τ, τ'), (f, f'), and(υ, υ') are time, delay, frequency, and Doppler, respectively. These functions are linked by a double fourier transform.

Hypothesis of the wide sense stationary channel

The temporal variations of a stationary channel in the wide sense have the statistical characteristics of weak stationary; therefore, the slow variations are neglected and the fast variations are stationary at order 2 and depend on the difference $\Delta t = t' - t$. This means that during Δt the channel fluctuation statistics remain stable. This assumption of a stationary channel in the broad sense is adequate for the decorrelation for two different Doppler components υ.

Hypothesis of uncorrelated scattering channel

The uncorrelated scattering channel hypothesis is an assumption that the inputs from the diffusers that cause different delays are decorrelated. As a result, this channel is stationary in the wide sense over the frequency domain. So, two different delay elements τ are decorrelated. Hence, the simplification of the correlation functions which vary over time with $\Delta f = f' - f$.

Hypothesis of the stationary channel in the wide sense with uncorrelated scattering

This assumption is the combination of the previous two, so the transfer function is analogous to a stationary two-dimensional process in the wide sense according to the variables of time and frequency. The previous correlation functions are reduced to:

$$R_h(t, \tau, t + \Delta t, \tau') = \delta(\tau' - \tau)P_h(\Delta t, \tau). \tag{59}$$

$$R_h(f, v, f + \Delta f, v') = \delta(v' - v)P_h(\Delta f, v). \tag{60}$$

$$R_h(f, t, f + \Delta f, t + \Delta t) = P_h(\Delta f, \Delta t). \tag{61}$$

$$R_h\big(\tau, \upsilon, \tau', \upsilon'\big) = \delta\big(\tau' - \tau\big)\delta\big(\upsilon' - \upsilon\big)P_h(\tau, \upsilon). \tag{62}$$

where $\Delta t = t' - t$ and $\Delta f = f' - f$. The decorrelation for different Doppler and/or delay components is represented by the presence of the Dirac distributions $\delta(\tau' - \tau)$ and $\delta(\upsilon' - \upsilon)$. The equations express time and frequency stationarity well.

Spatial domain

The stochastic characterization of the channel in the spatial domain is expressed with the following functions:

$$R\big(\vec{r}_{Rx}, \vec{r}_{Tx}; \vec{r}'_{Rx}, \vec{r}'_{Tx}\big) = E\Big\{\mathrm{vec}(h(\vec{r}_{Rx}, \vec{r}_{Tx}))\mathrm{vec}\big(h\big(\vec{r}'_{Rx}, \vec{r}'_{Tx}\big)\big)^H\Big\}. \tag{63}$$

$$R\Big(\vec{r}_{Rx}, \vec{k}_{Tx}; \vec{r}'_{Rx}, \vec{k}'_{Tx}\Big) = E\left\{\mathrm{vec}\Big(h\Big(\vec{r}_{Rx}, \vec{k}_{Tx}\Big)\Big)\mathrm{vec}\Big(h\Big(\vec{r}'_{Rx}, \vec{k}'_{Tx}\Big)\Big)^H\right\}. \tag{64}$$

$$R\Big(\vec{k}_{Rx}, \vec{r}_{Tx}; \vec{k}'_{Rx}, \vec{r}'_{Tx}\Big) = E\left\{\mathrm{vec}\Big(h\Big(\vec{k}_{Rx}, \vec{r}_{Tx}\Big)\Big)\mathrm{vec}\Big(h\Big(\vec{k}'_{Rx}, \vec{r}'_{Tx}\Big)\Big)^H\right\}. \tag{65}$$

$$R\Big(\vec{k}_{Rx}, \vec{k}_{Tx}; \vec{k}'_{Rx}, \vec{k}'_{Tx}\Big) = E\left\{\mathrm{vec}\Big(h\Big(\vec{k}_{Rx}, \vec{k}_{Tx}\Big)\Big)\mathrm{vec}\Big(h\Big(\vec{k}'_{Rx}, \vec{k}'_{Tx}\Big)\Big)^H\right\}. \tag{66}$$

where h is a square matrix of dimension 3×3 which links the 3 polarization components of the transmitted signal to that of the received signal, and vec(.) transforms the matrix to a vector into a column. Each correlation function expressed previously gives us a matrix of dimension 9×9 and these matrices contain the functions of autocorrelation and intercorrelation between the nine channels. So, these functions are a global description of the properties of spatial correlations between the different locations of emission and that of reception and the same for the different pulses of emission.

In order to simplify the correlation functions in the spatial domain, the propagation channel is assumed to be stationary in the broad sense on small areas of movement in transmission, and in reception therefore we neglect the slow large-scale variations while the rapid variations are stationary at l order 2. The stationarity in the broad sense makes the functions expressed previously independent of the absolute position variables of reception and emission; therefore, this stationarity is a total decorrelation for different spatial pulsations hence the decorrelation for different directions in emission or on reception, the functions become:

$$R_h(\vec{r}_{Rx}, \vec{r}_{Tx}; \vec{r}_{Rx} + \Delta\vec{r}_{Rx}, \vec{r}_{Tx} + \Delta\vec{r}_{Tx}) = P_h(\Delta\vec{r}_{Rx}; \Delta\vec{r}_{Tx}). \tag{67}$$

$$R_h\left(\vec{r}_{Rx}, \vec{k}_{Tx}; \vec{r}_{Rx} + \Delta\vec{r}_{Rx}, \vec{k}'_{Tx}\right) = \delta\left(\vec{k}_{Tx} - \vec{k}'_{Tx}\right) P_h\left(\Delta\vec{r}_{Rx}, \vec{k}_{Tx}\right). \quad (68)$$

$$R_h\left(\vec{k}_{Rx}, \vec{r}_{Tx}; \vec{k}'_{Rx}, \vec{r}_{Tx} + \Delta\vec{r}_{Tx}\right) = \delta\left(\vec{k}_{Rx} - \vec{k}'_{Rx}\right) P_h\left(\vec{k}_{Rx}; \Delta\vec{r}_{Tx}\right). \quad (69)$$

$$R_h\left(\vec{k}_{Rx}, \vec{k}_{Tx}; \vec{k}'_{Rx}, \vec{k}'_{Tx}\right) = \delta\left(\vec{k}_{Tx} - \vec{k}'_{Tx}\right)\delta\left(\vec{k}_{Rx} - \vec{k}'_{Rx}\right) P_h\left(\vec{k}_{Rx}; \vec{k}_{Tx}\right). \quad (70)$$

So, the channel is spatially stationary in the broad sense with spatially decorrelated diffusers. The four functions are simplified for the context of the characterization of electromagnetic waves in the local area, related to polarization behaviors such as (71–74):

$$R_h(\vec{r}_{Rx}, \vec{r}_{Tx}; \vec{r}_{Rx} + \Delta\vec{r}_{Rx}, \vec{r}_{Tx} + \Delta\vec{r}_{Tx}) = P_h(\Delta\vec{r}_{Rx}; \Delta\vec{r}_{Tx}). \quad (71)$$

$$R_h\left(\vec{r}_{Rx}, \Omega_{Tx}; \vec{r}_{Rx} + \Delta\vec{r}_{Rx}, \Omega'_{Tx}\right) = \delta\left(\Omega_{Tx} - \Omega'_{Tx}\right) P_h(\Delta\vec{r}_{Rx}, \Omega_{Tx}). \quad (72)$$

$$R_h\left(\Omega_{Rx}, \vec{r}_{Tx}; \Omega'_{Rx}, \vec{r}_{Tx} + \Delta\vec{r}_{Tx}\right) = \delta\left(\Omega_{Rx} - \Omega'_{Rx}\right) P_h(\Omega_{Rx}; \Delta\vec{r}_{Tx}). \quad (73)$$

$$R_h\left(\Omega_{Rx}, \Omega_{Tx}; \Omega'_{Rx}, \Omega'_{Tx}\right) = \delta\left(\Omega_{Tx} - \Omega'_{Tx}\right)\delta\left(\Omega_{Rx} - \Omega'_{Rx}\right) P_h(\Omega_{Rx}; \Omega_{Tx}). \quad (74)$$

where Ω_{Tx} and Ω_{Rx} are two-part vectors containing the azimuth and elevation angles, respectively, at the emission site and at the reception site.

6 Gains of the MIMO Channel

The MIMO system was able to improve the communication systems, unlike the old systems MIMO presented a new gain: the multiplexing gain which is added to the already existing gains, the diversity gain and the beamforming gain.

Beamforming gain

Beamforming involves maximizing an accurate signal at reception by applying a rear or filter and a front filter to the transmitter that selects the desired wave propagation paths by eliminating unused paths or interference. The beamforming gain is a development of SNR plus receiver interference.

Spatial diversity gain

Le MIMO antennas make it possible to make copies of the same information these replicas have undergone fading during transmission using an optimal combination; the average error probability of the high SNRs is as follows: Pe $\approx c\text{SNR}^{-d}$ with

c constant linked to channel coding and modulation, SNR signal-to-noise ratio, and diversity gain.

Diversity gain describes how the slope of the error probability as a function of SNR varies with diversity. Considering a $c = 1$ (absence of coding), therefore:

$$d = -\lim_{\mathrm{SNR}\to\infty} \frac{\log \mathrm{Pe(SNR)}}{\log \mathrm{SNR}}. \tag{75}$$

With Pe(SNR) is the error rate for a given SNR.

Spatial multiplexing gain

Spatial multiplexing consists of cutting the message sent into blocks, each block will be sent on an antenna simultaneously, which makes it possible to increase the transmission rate; hence the gain in spatial multiplexing which results in an increase in capacity by using spatial channels parallels. The transmission capacity is directed by the sub-channels r which evolves in log(SNR). at a strong signal to noise. Hence, the total capacity $R \approx r \log(\mathrm{SNR})$. The spatial multiplexing gain r is then expressed in Eq. 76:

$$r = \lim_{\mathrm{SNR}\to\infty} \frac{R(\mathrm{SNR})}{\log_2(\mathrm{SNR})}. \tag{76}$$

With R(SNR) the capacity available at SNR.

Diversity-multiplexing gain trade-off

Unlike the time domain, the spatial domain allows for maximum multiplexing gain and maximum diversity gain with an optimal compromise. The optimum diversity gain for an $N_t \times N_r$ MIMO system is given as a function of the multiplexing gain in:

$$d(r) = (N\boldsymbol{t} - \boldsymbol{r})(\boldsymbol{N}\boldsymbol{r} - \boldsymbol{r}). \tag{77}$$

With $r = 0, \ldots, \min(Nr, Nt)$.

This equation shows that if we have r transmitting and receiving antennas for multiplexing, the others offer transmission diversity with $(N_t - r)$ in transmission and $(N_t - r)$ in reception.

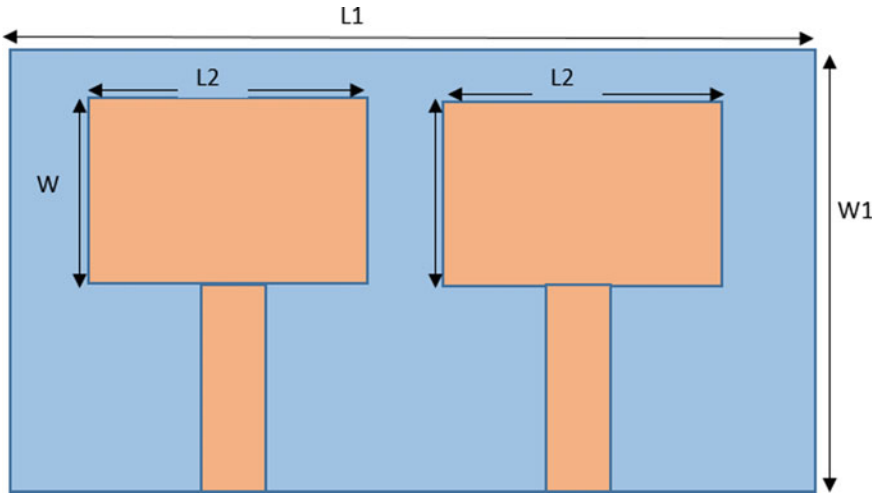

Fig. 5 Initial MIMO antenna

7 MIMO Antenna Design

7.1 The MIMO Antenna Design

The initial MIMO antenna has been made based on polyimide substrate which has a dielectric constant $\varepsilon_r = 3.5$ and thickness of 9 μm, and the antenna dimensions are $W1 \times L1 = 47.916 \times 75.386\ \mu m^2$. With an inter-distance of 38.693 μm. Figure 5 describes the top view of the MIMO proposed antenna design.

The proposed MIMO antenna has a radiating patch in the form of a rectangular with a surface area of $W2 \times L2 = 19.918 \times 28.693\ \mu m^2$. The antenna is fed using a microstrip feedline of width $W_d = 4.8465$ μm with a power port adapted to 50 Ω. The ground plane size for the MIMO antenna is $47.916 \times 75.386\ \mu m^2$. This initial MIMO antenna has a negative peak gain of −11 dB where comes the need for the next step which consists in the optimization of the antenna using the slots as shown in the next paragraph.

7.2 Optimization of the MIMO Antenna and Results

In order to improve the performance of the MIMO antenna of the previous paragraph in term of gain return loss and bandwidth slots were inserted on the radiating elements, the optimization approach followed in inserting slots in the right position with the convenient length and width.

Table 4 The dimensions of the slots

Slot	Length (μm)	Width (μm)
1	8.82675	7.2675
2	6	5
3	6	12
4	7	5
5	10	5

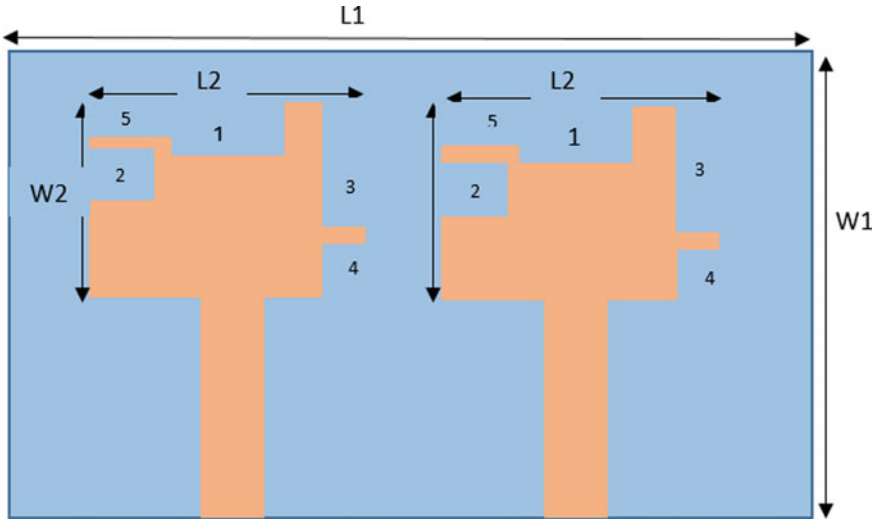

Fig. 6 MIMO antenna with slots

This methodology is the simplest way to impact significantly the performance of the antenna. We ended up adding 5 slots with widths and lengths shown in Table 4 to the antenna as shown in Fig. 6.

7.3 Results and Simulations

The antenna has been simulated using HFSS. The main characteristics that evaluate the radiation performance of the antenna are return loss, VSWR, gain, *E*-plane, and *H*-plane radiation pattern.

The return loss of an antenna describes the reflection of the wave by the impedance discontinuity in the transmission medium in dB. It will be referred to it as $S11$ (dB) and $S22$ (dB); their value have to be less than −10 dB in order to have an effective antenna. Figure 7 represents the return losses for the proposed antenna which are –21.44 dB and −29.62 dB, respectively. The antenna has a bandwidth of 469 GHz

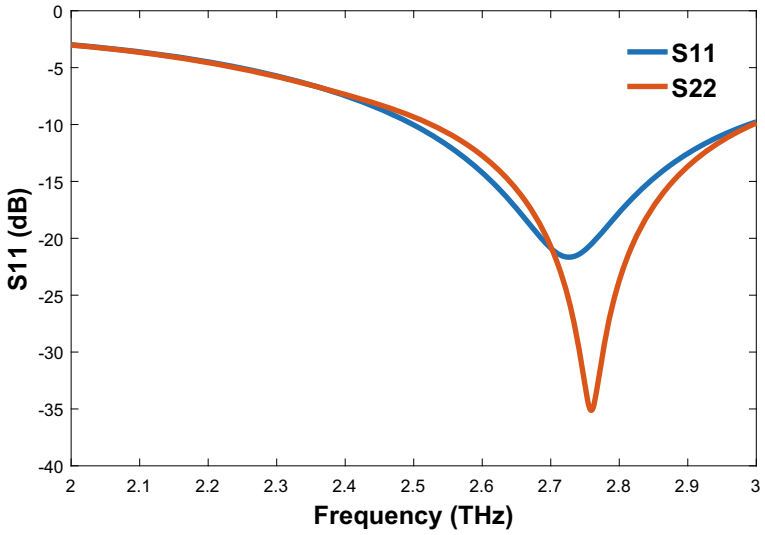

Fig. 7 Return loss $S11$ of the THz antenna

(impedance bandwidth of 17.11% in the range of 2.526–2.995 THz) with a center frequency of 2.74 THz. The voltage standing wave ratio (VSWR) is the standard to judge the impedance matching between the transmission line and antenna which is a crucial factor to rate the performance of the antenna; the value of this ratio has to be below 2 [6, 16] to meet the requirements.

The designed antenna VSWRs are 1.18 and 1.07 at 2.74 THz. In perfect conditions, VSWR = 1 which means no reflection and all the power is endured [17]. Up to now, all the important performance parameters have been discussed. The peak gain of the proposed antenna is also a crucial parameters is 4.65 dB (Table 5).

The *E*-plane *H*-plane far field radiation patterns of the proposed antenna at 2.74 THz are shown in Figs. 10 and 11. These patterns show that the antenna has a minimum back lobe in the chosen band (Figs. 8 and 9).

The performance comparison is based on $S11$, Gain (dB), and BW (GHz). This comparison proves that the designed antenna offered a larger bandwidth and a higher resonant frequency.

Table 5 Comparison of the designed MIMO antenna with other existing work

Antenna	Resonant frequency (THz)	S11 (dB)	Gain (dB)	BW (GHz)
[5]	0.96	−13.05	7.3	
[6]	0.750	−35	5.09	
[7]	1.06	−41.65	2.45	50
Proposed antenna	2.74	−34	4.65	469

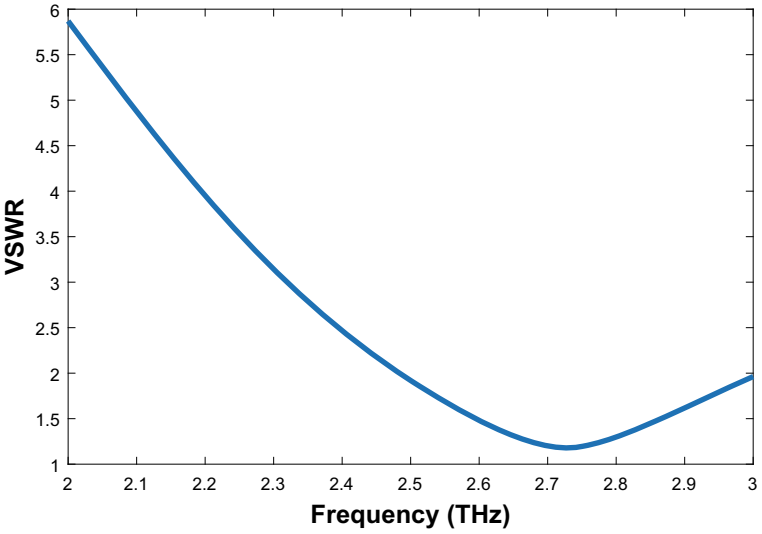

Fig. 8 VSWR of the THz antenna

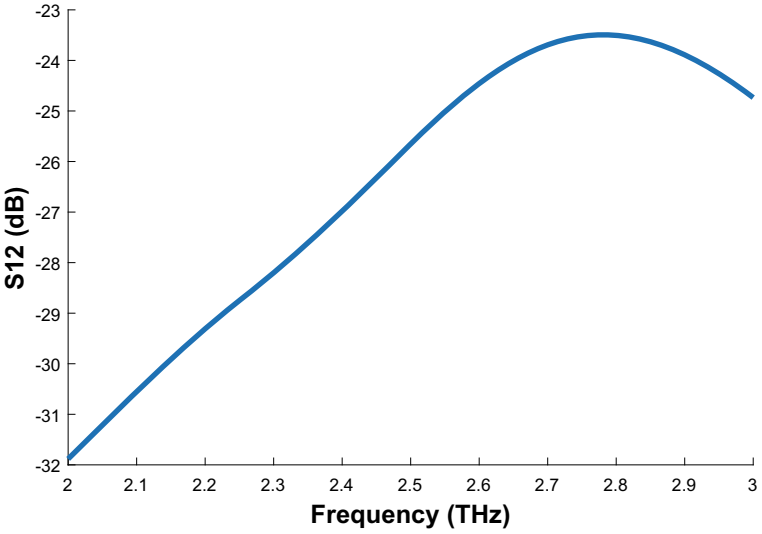

Fig. 9 *S*12 plot for the proposed THz antenna

8 Conclusion

This work proposed a new MIMO antenna structure that has been analyzed and simulated for THz applications at 2.74 THz. The approach to do this work mainly

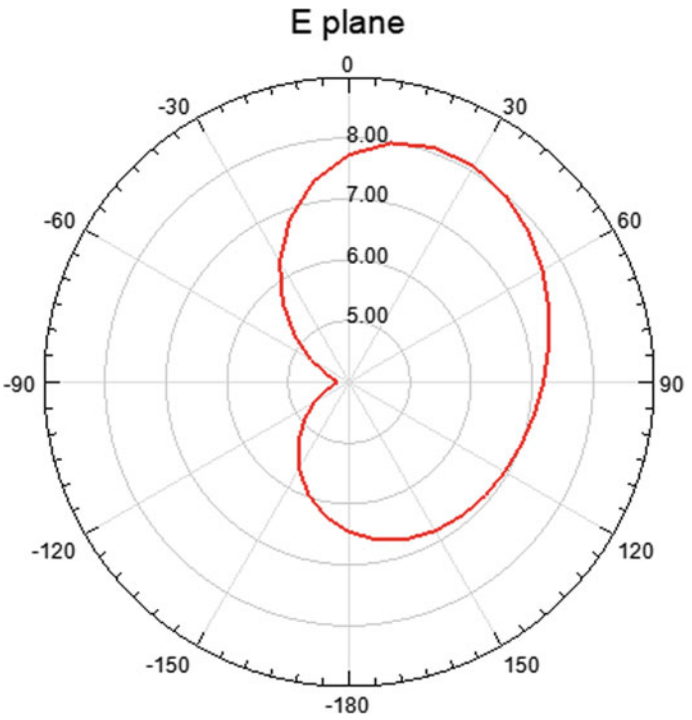

Fig. 10 *E*-plane radiation for the THz antenna

focused on the optimization of a simple rectangular antenna by inserting slots on the radiating element in the right position with a convenient length and width for these slots. This approach has improved the peak gain to be 4.65 dB. This antenna has a bandwidth of 469 GHz and a reflection coefficients of −21.44 dB and − 29.62. Furthermore, the proposed antenna has shown good results comparing to other existing antenna at a higher frequency.

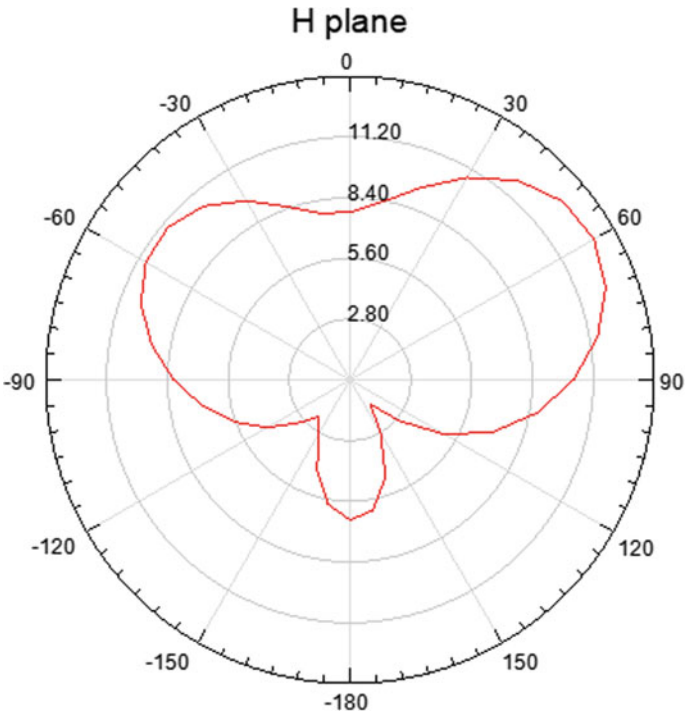

Fig. 11 *H*-plane radiation for the THz antenna

References

1. M.A.K. Khan, T.A. Shaem, M.A. Alim, Analysis of graphene based miniaturized terahertz patch antennas for single band and dual band operation. Optik **194**, 163012 (2019)
2. J.H. Son, Terahertz electromagnetic interactions with biological matter and their applications. J. Appl. Phys. **105**(10), 102033 (2009)
3. Y. Ghazaoui, A. El Alami, M. El Ghzaoui, S. Das, D. Baradand, S. Mohapatra, Millimeter wave antenna with enhanced bandwidth for 5G wireless application. J. Instrum. 15 (2020). https://doi.org/10.1088/1748-0221/15/01/T01003
4. B. Aghoutane, S. Das, H. El Faylali, B.T.P. Madhav, M. El Ghzaoui, A. El Alami, Analysis, design and fabrication of a square slot loaded (SSL) millimeter-wave patch antenna array for 5G applications. J. Circ. Syst. Comput. **30**(05), 2150086 (2021). https://doi.org/10.1142/S0218126621500869
5. A. Singh, S. Singh, A trapezoidal microstrip patch antenna on photonic crystal substrate for THz application. Photonics Nanostruct. Fundam. Appl. **14** (2015)
6. M.R. Nickpay, M. Danaie, A. Shahzadi, Wideband rectangular double-ring nanoribbon graphene-based antenna for terahertz communications. IETE J. Res. (2019)
7. S. Anand, D.S. Kumar, R.J. Wu, M. Chavali, A graphene nanoribbon based terahertz antenna on polyimide substrate. Optik Intern. J. Light Electron. Optic **125**, 19 (2014)
8. B. Aghoutane, M. El Ghzaoui, H. El Faylali, Spatial characterization of propagation channels for terahertz band. SN Appl. Sci. **3**, 233 (2021). https://doi.org/10.1007/s42452-021-04262-8

9. M. EL Ghzaoui, J. Mestoui, A. Hmamou, S. Elaage, Performance analysis of multiband on–off keying pulse modulation with noncoherent receiver for THz applications. Microw. Opt. Technol. Lett. **2021**, 1–6 (2021). https://doi.org/10.1002/mop.33051
10. A. El Fatimy, *Terahertz Emission and Detection by Plasma Waves in Nanometer HEMT Transistor* (2007)
11. Z. Li, L. Guan, A. Radwan, A secure intelligent spectrum control strategy for future THz mobile heterogeneous networks, IEEE Commun. Mag. **56**(6), 116–123 (2018)
12. H. Zhang, Z. Li, F. Hu, B. Qin, Y. Zhao, T. Chen, C. Hu, Sensitive distinction between herbs by terahertz spectroscopy and a metamaterial resonator. Spectrosc. Lett. **51**, 174–178 (2018)
13. R.K. Kushwahaa, P. Karuppanana, L.D. Malviyab, Design and analysis of novel microstrip patch antenna on photonic crystal in THz. Physica B Condeses Matter **545** (2018)
14. M. El Ghzaoui, A. Hmamou, J. Foshi, J. Mestoui, Compensation of non-linear distortion effects in MIMO-OFDM systems using constant envelope OFDM for 5G applications. J. Circ. Syst. Comput. **29**(16), 2050257 (2020)
16. G. Kaur, V. Mehta, E. Sidhu, in *Rectangular Terahertz Microstrip Patch Antenna Design for Vitamin K2 Detection Applications*. 2017 1st International Conference on Electronics, Materials Engineering and Nano-Technology (IEMENTech) (IEEE, 2017), pp. 1–3
17. Q.-Y. Tang, Y.-M. Pan, Y.C. Chan, K.W. Leung, Frequency-tunable soft composite antennas for wireless sensing. Sens. Actuat. A Phys. **179** (2012)

High Gain of a Canine MIMO Antenna for Terahertz Applications

Bilal Aghoutane, Hanan El Faylali, and Sudipta Das

Abstract The antennas can equip everyday objects of all kinds. They are used for various applications ranging from telecommunications to medicine, transport and even manufacturing. In the context of a generalization of wireless communication systems, the need to miniaturize antennas to allow their integration on small objects at Terahertz frequencies is building. This chapter investigates the probability of designing a MIMO antenna for terahertz applications on Rogers substrate across a broad frequency spectrum, with a thickness of 0.508 μm. The antenna element includes five steps. The beginning is the usual patch antenna. Next, we add rectangular and triangular slots size 5×1 μm^2 and 4.05 μm^2 on the patch near the feed line, respectively. Also, on the right and left of the antenna is loaded with added a triangular slot size. Before the last, the antenna was close to construction, further adding a polygon with a number of segments equaling six. Whereas a ground plan comprise 12.871×14.051 μm^2. With relative dielectric permittivity equal to 2.33 and tangent loss equal 0.012 to operate on Terahertz. Patch has a much better impedance matching. This antenna is simulated before implementing a two-element MIMO antenna, which is our goal. In the design of the MIMO antenna, one of the more significant elements is the monopole. This is operated under the λ/2 mode. Moreover, archived that the optimized proposed has significant bandwidth and return loss equal 0.61 THz and −36.9 dB, respectively, at operating frequency 0.75 THz, with the high gain and current distribution showing good directional radiation pattern. The proposed MIMO antenna is simulated in HFSS and can be used for THz Applications.

Keywords High gain · THz · MIMO antenna · 6G

B. Aghoutane (✉) · H. E. Faylali
Faculty of Sciences, University Ibn Tofail, Kenitra, Morocco
e-mail: bilal.aghoutane@uit.ac.ma

S. Das
Department of ECE, IMPS College of Engineering and Technology, Azimpur, West Bengal, India

M. El Ghzaoui et al. (eds.), *Terahertz Wireless Communication Components and System Technologies*, https://doi.org/10.1007/978-981-16-9182-9_9

1 Introduction

In this part, we will focus on wireless communication systems. The different fields of application covered by this term will be quickly presented and recent developments in these technologies will be discussed. Current reflections on wireless local networks fil will be more particularly developed, since the present study is situated in this context. A state of the art of research carried out in the millimetre wave band (or EHF, Extra High Frequency: 30–300 GHz), and more particularly around 60 GHz, will end this chapter. Electromagnetic waves are various powerful mechanisms for studying. The broad range of the electromagnetic spectrum offers many applications, such as the subject of galaxies in astronomy, between different wavelength ranges of the electromagnetic spectrum. First of all, we will start with a semantic precision about the term communication. It often happens that scientific jargons use certain words in everyday language with special meaning. This is the case with communication. Much like the word information used by Shannon in information theory, the word communication in communication systems is devoid of any connotation about the content or value of communication. They are simply systems allowing the exchange of data (in digital form for most current technologies) between several devices. This reminder is to be seen in relation to the extensive and complex use of the term communication in current language ("communication era", "communication society", etc.). The word is now loaded with various meanings that have become a fact of society.

The THz frequencies are between the frequencies 0.1 and 10 THz. Figure 1 illustrates the location of THz frequencies in the electromagnetic spectrum. We can see that the THz frequencies are located between infrared waves and microwaves. To better define the THz frequency range, the duration of a cycle electromagnetic at

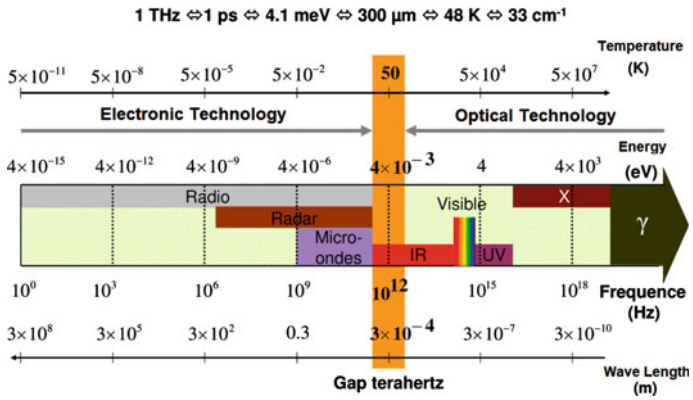

Fig. 1 Schematics representation of the electromagnetic spectrum with a highlighting of the frequencies, energies, temperatures and wavelengths associated with each type of radiation. An equivalence between these different parameters is given for 1 THz [3]

1 THz is one ps, the wavelength is 300 μm, the energy is 4.1 meV and the temperature is 48°K.

The exploitation of millimetre-frequency bands is one of the research topics commonly studied in the field of electronics [1, 2]. Millimetre frequencies are emerging as the apparent solution to the exponential increase in speed demands for wireless communications due to the large bandwidths available at these frequencies. The significant development of printed antenna technologies such as HFSS and ADS software has enabled the conception of radiofrequency designs with exciting performances and costs. Likewise, in these frequency bands, antennas with large gains and directional beams can be designed with reasonable dimensions. These two parts have contributed significantly to the emergence of several millimetre-band wireless communications applications such as high-speed short distance communications, 5G networks and ultra-high definition television.

However, several challenges arise regarding integrating circuits with antennas in wireless transmission applications at millimetre frequencies. Losses are one of the main difficulties encountered in these frequency bands. As for the T_x chain, they force very high power amplifiers to maintain a sufficient transmission power level and ensure the desired throughput. However, the difficulties in making such amplifiers are significant in these frequency bands, especially when high levels of linearity are required. On the R_x side, the noise level of the circuits and the losses between the antenna and the input amplifier significantly limit the receiver's noise figure. To minimize these losses, several techniques must be jointly considered. Among them, they are minimizing the distance between the antenna and integrated circuits, reducing interconnection losses and increasing the efficiency of the antenna. Antenna architectures integrated on a circuit (Antenna-on-Chip, AoC) and antennas integrated with the box (Antenna-in-Package, AiP) allow compromises between these different options. They also make it possible to reduce the volume of the front-end module and its manufacturing cost.

One of the essential parameters in building a millimetre-frequency wireless link between two T_x and R_x antennas is Free Space Attenuation (FSA). The power P_{RX} received by the antenna R_x is defined by the FRIIS Eq. (1) also called the telecommunications equation:

$$P_{RX} = P_{TX} G_{TX} G_{RX} \left(\frac{\lambda_0}{4\pi R} \right)^2 \tag{1}$$

With P_{RX} the transmit power, λ_0 the wavelength in free space, G_{TX}, G_{RX} the gains of the T_x and R_x antennas, respectively, and R the distance between the two antennas. The free space loss is defined in Eq. (2):

$$\text{FSA} = -10\text{Log}_{10} \left(\frac{\lambda_0}{4\pi R} \right)^2 \tag{2}$$

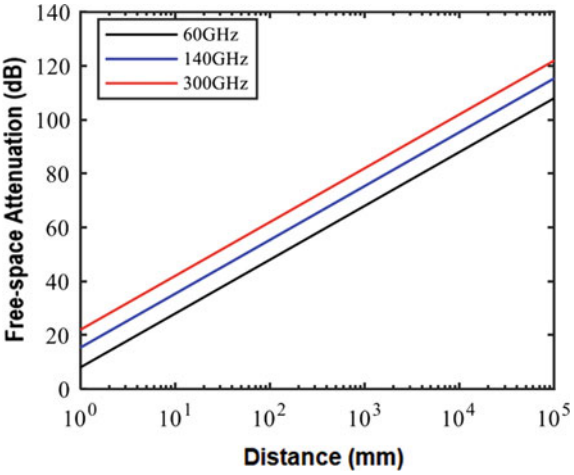

Fig. 2 Attenuation in free space as a function of distance at 60, 140 and 300 GHz (abscissa represented in logarithmic scale)

To quantify the importance of this term at millimetre frequencies, the free space attenuation is plotted in Fig. 2 for three typical frequencies (60, 140 and 300 GHz) and for distances ranging from millimetres to hundreds of metres. For example, 10 cm away, the FSA equals 48 dB at 60 GHz, 55 dB at 140 GHz and 62 dB at 300 GHz. At 1 m distance, the FSA is 20 dB higher, and at 10 m, it is 40 dB higher.

2 Smart Antenna THz

Smart antennas are devices capable of reacting automatically and in real time as the propagation channel or environment changes. Operation by adjusting one or more electrical or radiating characteristics of the antenna. In reality, the antennas are not brilliant, but the digital signal processing capability, along with the associated active antennas, makes the system intelligent. The term smart antenna incorporates all situations in which a system adjusts the electrical characteristics or radiation properties of a single antenna or an array of antennas dynamically as needed. This implies that this system can operate in any environment and extract valuable signals in the presence of interference and noise. Generally, there are two categories of intelligent antennas: adaptive antenna systems and switched beam antenna systems. The main objective of both methods is to increase the gain in the user's direction (useful) while cancelling the power in the order of the interference. Smart antennas offer important advantages for the design of wireless systems, which can be summarized as follows:

- Increased Antenna Gain: This helps increase the coverage of modern telecommunications systems, prolong battery life, and leads to smaller, lighter designs.
- Interference Rejection: The zeros created by the antenna pattern can be generated to interference sources by electronically scanning the radiation pattern, reducing

the interference seen by the base station. Such interference reductions improve the Carrier-to-Interference Ratio (CIR), which in turn leads to increased capacity.
- Diversity: This greatly minimizes fading and other unwanted effects of multipath propagation. The different types of diversity and their advantages will be dealt with later in this chapter.
- Possibility to communicate between several users at the same time or to follow a target in real time.

3 Recent Work

Recent developments in integrated antenna and process technologies and assembly and integration processes have allowed the emergence of serval channel applications in Terahertz bands [4]. Among them, very high-speed point to point communications [5, 6], 5G networks [7–10] short distance communications such as WLAN networks, high definition television (HDTV) and ultra-high definition (UHDTV) [11, 12] and high-speed wireless interconnections [13, 14]. The performances demonstrated by these technologies, particularly the high bandwidths, the high level of integration and the reduction in cost, also make it possible to envisage future communications networks beyond 5G and 6G [15, 16].

In addition to wireless communications, several other applications have emerged in the millimetre-wave spectrum, such as 77 GHz automotive radars [17, 18], detection radars [19, 20] and imaging for safety and security monitoring [21, 22].

The millimetre-wave spectrum is divided into several bands, the main ones being the V band (40–75 GHz), E band (60–90 GHz), D band (110–170 GHz) and H band (220–325 GHz). The H band can also be considered as part of the submillimetre or terahertz bands [23]. This chapter gives particular interest to wireless communications applications operating in the D and H bands.

4 THz Wave

In conventional material characterization techniques (microscopy, spectroscopy), the determination of the specific losses of a material consists of measuring the decrease in signal between transmitter and detector when a material is placed in the path of the beam. These measurement techniques bring together in the magnitude “loss” or “absorption” contributions related to the pure absorption of the material, to the reflection at its interfaces and to the scattering at the interfaces (diffuse reflection) that to through the material (diffuse transmission). However, the distinction between diffusion and inherent absorption of materials may be necessary and important for some applications. This is, for example, the case in applications such as telecommunications [24], isolation [25] or even metrology [26] and scene simulation [27] where it is useful to know the properties of the materials carefully to be traversed.

Studies on the scattering of the THz wave by materials were carried out by Cheville et al. [28]: they showed, by measuring the THz signal backscattered on a sphere, that it is possible to temporally separate the different waves responsible for the halo phenomenon. Pearce and Mittleman studied the propagation of THz radiation in a complex medium. They show in particular that time-domain THz spectroscopy can be used to study transport (ballistic and diffuse) in complex media [29, 30]. Shen et al. (Teraview) [31] have shown that the spectral signatures of inhomogeneous materials can be changed by scattering THz radiation by particles of comparable size at wavelength.

5 MIMO Antenna Design and Analysis

The proposed antenna was designed on Roger RT/duriod 5870 substrate with a thickness of 0.508 μm. The antenna element includes five steps. The beginning is the usual patch antenna, as shown in Fig. 3a. Next, in Fig. 3b and c, we add rectangular and triangular slots size $5 \times 1\ \mu m^2$ and $4.05\ \mu m^2$ on the patch near the feed line, respectively. Also, on the right and left of the patch is loaded with added a triangular slot size as shown in Fig. 3d. Before the last, the antenna was close to construction, further adding a polygon with a number of segments equaling six, as shown in Fig. 3e. Whereas a ground plan comprise $12.871 \times 14.051\ \mu m^2$. Relative permittivity equal to 2.33 and tangent loss equal to 0.012 to operate at terahertz, the patch has better impedance matching. This antenna is simulated before implementing a two-element MIMO antenna, which is our goal. In the design of the MIMO antenna, one of the more significant elements is the monopole. This is operated under the λ/2 mode. The configuration and the optimized value of the parameters for the proposed MIMO have been presented in Fig. 4 and Table 1.

In Fig. 5 shows the comparison of reflection coefficient between the first design (Ant-1), second design (Ant-2) and third design (Ant-3). As we can see, the designed antenna (Ant-3) has a greater bandwidth with return loss equal to −12.5 dB. On the contrary, other designs.

Further to improve the performance of an antenna, in the fourth and fifth steps, the developed patch antenna is transformed. Also, from Fig. 6, it is noted that on adding a polygon of the slot, the resonating frequency is slightly shifted towards the right side near 0.5 THz. After the simulation of the two elements, the result is shown in Fig. 7 and compared with the single element in Fig. 8. From Fig. 7, it is observed that the optimized proposed have great bandwidth and return loss equal 0.61 THz and −36.9 dB, respectively, at operating frequency 0.75 THz.

Moreover, Fig. 8 shows all coefficient reflection, the total bandwidth of the proposed antenna are enhanced from 0.05 THz to 0.61 THz. Also, the maximum achieved gain is improved from 27 to 34 dBi, as illustrated in Fig. 9.

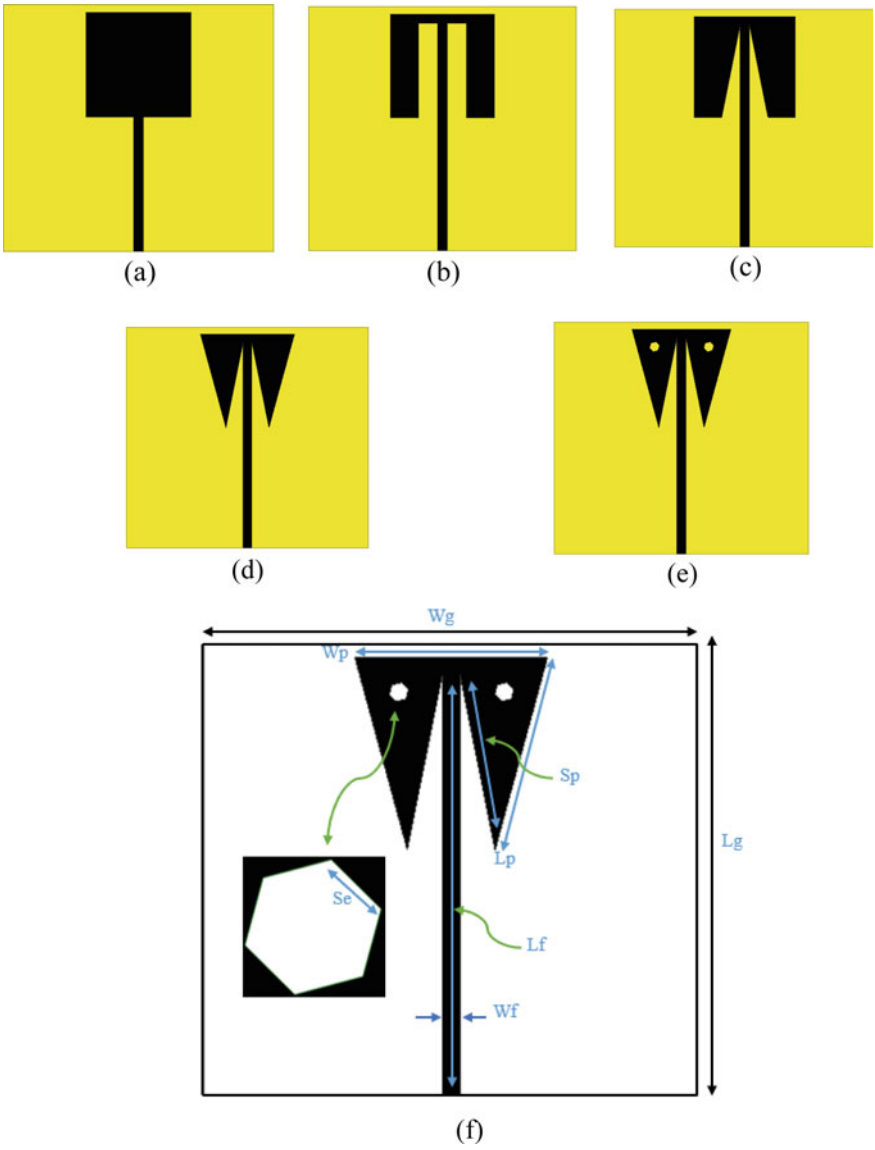

Fig. 3 Antenna geometry steps. **a** Ant-1, **b** Ant-2, **c** Ant-3, **d** Ant-4, **e** Ant-5 and **f** optimized design

6 Simulation Results and Optimization

The proposed antenna is simulated, modelled and optimized by using the High-Frequency Simulation Software (Ansys HFSS). The proposed MIMO antenna is analyzed and validated in HFSS. The microstrip port feed, the real port formed

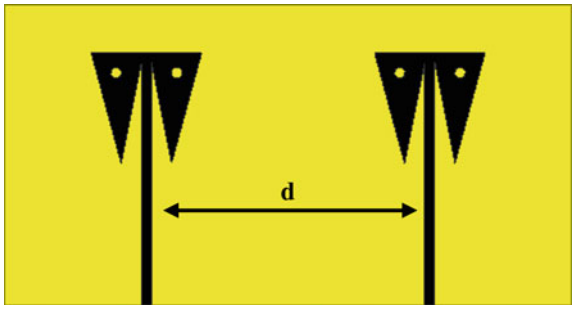

Fig. 4 Proposed MIMO antenna for THz

Table 1 The optimised dimensions of the single and two elements antenna

Parameters	Dimensions (μm)
W_p	5.48
L_p	6.25
W_f	0.5
L_f	12.48
W_g	14.051
L_g	12.851
S_e	1.953
S_p	4.896
D	14.051

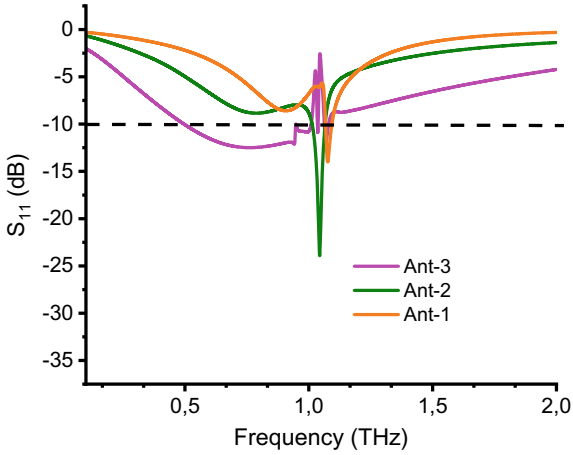

Fig. 5 Comparison reflection coefficient between Ant-1, Ant-2 and Ant-3

through lines, is used to feed the antenna. The particular lines circling the waveguide port define the EM distribution on the waveguide port. In this section, the development of the proposed optimized antenna design MIMO is discussed.

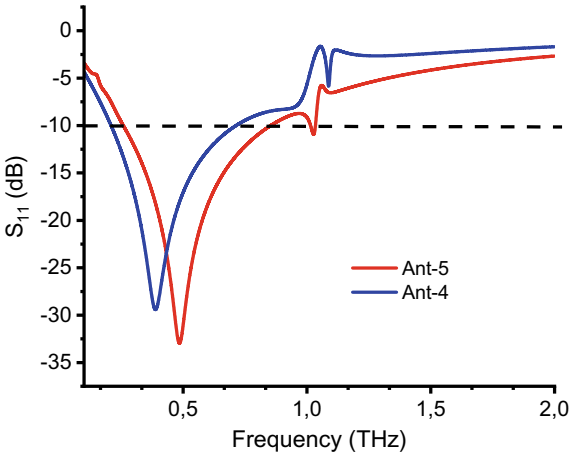

Fig. 6 Comparison reflection coefficient between Ant-4 and Ant-5

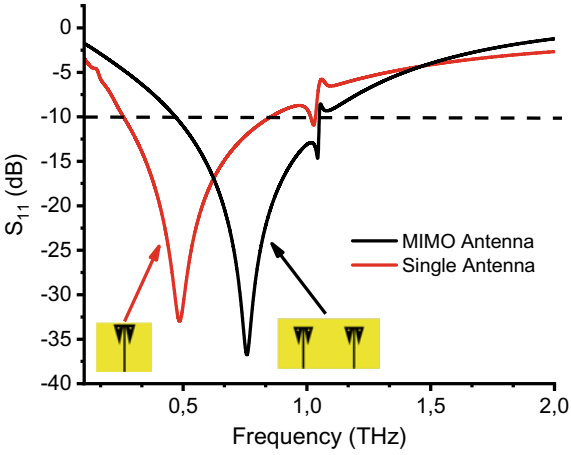

Fig. 7 Comparison of reflection coefficient for the single element antenna and MIMO antenna

To identify the radiation pattern of optimized MIMO antenna design, the E and H plane, as shown in Fig. 10, is plotted at resonating frequency 0.25 THz, 0.5 THz, 0.75 THz and 1 THz of the proposed antenna. From the radiation pattern, it is a noticeably advanced MIMO antenna with a multi-side lobe character, which is not acceptable. To reduce the side lobe in a realistic situation, some algorithms can be used.

Some other methods are available to overcome the sidelobe levels same filling the antenna layout, including the metamaterial lens or metamaterial structures, which assists in decreasing the sidelobe levels of the before-mentioned proposed antenna.

Figure 11 shows the current distribution of the proposed MIMO antenna at 0.25 THz, 0.5 THz, 0.75 THz and 1 THz is diverse due to the difference in the conine patch and feed line width. In uniform power distribution, the impedance to all the

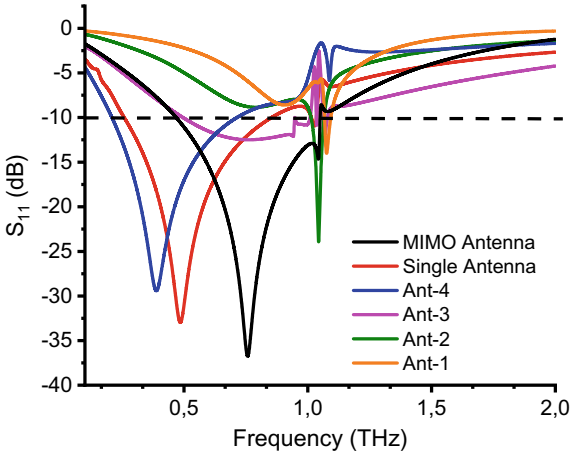

Fig. 8 S_{11} for Ant-1, Ant-2, Ant-3, Ant-4, single antenna and MIMO antenna

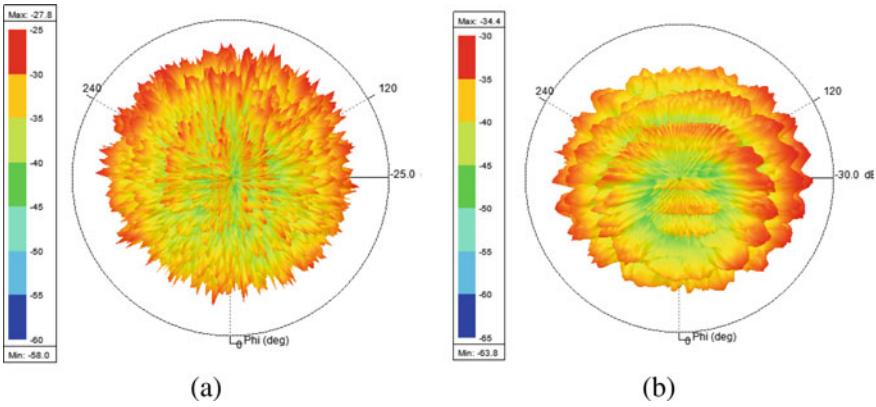

Fig. 9 Gain 3D for **a** single element and **b** MIMO antenna

transmitting feed lines is the same. In contrast, each transmitting feed line impedance is different with a different width to the feed lines, as shown in Fig. 11a–d.

7 Conclusion

The probability of a MIMO antenna proposed model is studied for THz applications. The MIMO antenna is designed on Roger RT/duriod 5870 substrates with a thickness of 0.508 μm. The antenna uses a mircostrip feed line with 50 Ω. The proposed MIMO antenna has a size $12.871 \times 14.051 \times 0.508\ \mu m^3$ operate across 0.75 THz. Moreover,

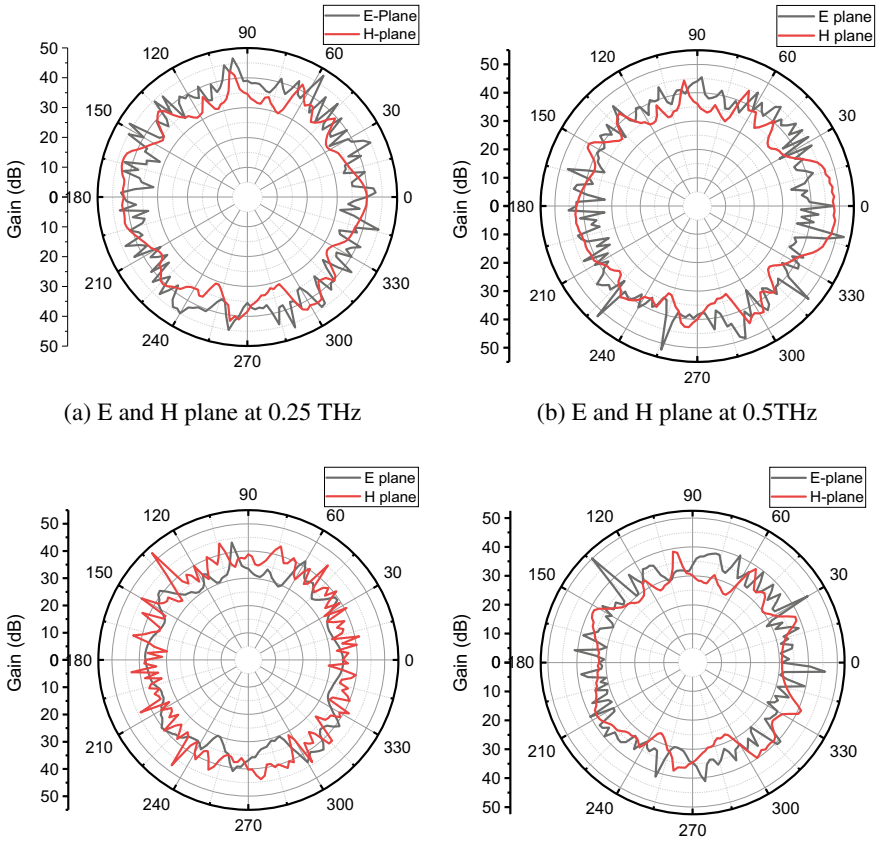

(a) E and H plane at 0.25 THz

(b) E and H plane at 0.5THz

(c) E and H plane at 0.75THz

(d) E and H plane at 1THz

Fig. 10 Radiation pattern for E and H plane of MIMO antenna

archived that the optimized proposed has significant bandwidth and return loss equal 0.61 THz and −36.9 dB, respectively, at operating frequency 0.75 THz, with the high gain and current distribution showing good directional radiation pattern. The proposed MIMO antenna is simulated in HFSS and can be used for THz Applications.

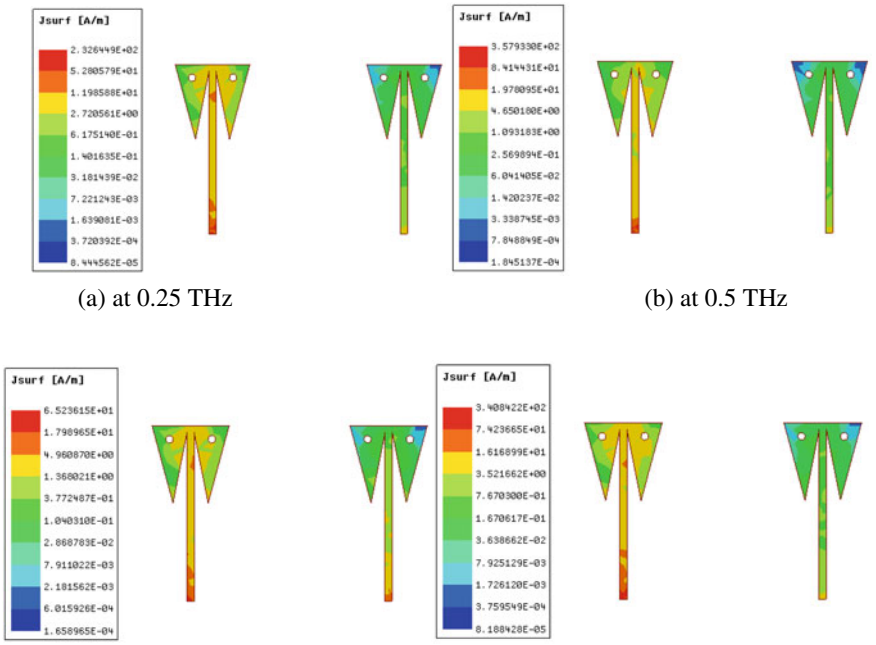

(a) at 0.25 THz (b) at 0.5 THz

(c) at 0.75 THz (d) at 1 THz

Fig. 11 The current distribution of the proposed antenna

References

1. S. Elaage, M.E. Ghzaoui, A. Hmamou, J. Foshi, J. Mestoui, MB-OOK transceiver design for terahertz wireless communication systems. Int. J. Syst. Control Commun. **12**(4), 309–326 (2021). https://doi.org/10.1504/IJSCC.2021.118627
2. M.E. Ghzaoui, J. Mestoui, A. Hmamou, E. Serghini, Performance analysis of multiband on–off keying pulse modulation with noncoherent receiver for THz applications. Microwave Opt. Technol. Lett. (2021). https://doi.org/10.1002/mop.33051
3. D. Oustinov, *Study of quantum cascade lasers using terahertz time-domain spectroscopy*. Doctoral Thesis-Paris VI, 8 (2011)
4. B. Aghoutane, M. El Ghzaoui, H. El Faylali, Spatial characterization of propagation channels for terahertz band. SN Appl. Sci. **3**, 233 (2021). https://doi.org/10.1007/s42452-021-04262-8
5. A. Smale, Point-to-point communications—the role of radio. Trans. South African Inst. Electr. Eng. **50**(1), 3–10 (1959)
6. N. Mehravari, Performance and protocol improvements for very high speed optical fiber local area networks using a passive star topology. J. Lightwave Technol. **8**(4), 520–530 (1990). https://doi.org/10.1109/50.50758
7. B. Aghoutane, N. Meskini, M. Elghzaoui, H.E. Faylali, Millimeter-wave microstrip antenna array design for future 5G cellular applications, in 2018 International Conference on Electronics, Control, Optimization and Computer Science (ICECOCS), pp. 1–4 (2018). https://doi.org/10.1109/ICECOCS.2018.8610507
8. B. Aghoutane, S. Das, H. El Faylali, B.T.P. Madhav, M. El Ghzaoui, A. El Alami, Analysis, design and fabrication of a square slot loaded (SSL) millimeter-wave patch antenna array for

5G applications. J. Circ. Syst. Comput. **30**(05), 2150086 (2021). https://doi.org/10.1142/S0218126621500869
9. Y. Ghazaoui, A. El Alami, M. El Ghzaoui, S. Das, D. Baradand, S. Mohapatra, Millimeter wave antenna with enhanced bandwidth for 5G wireless application. J. Instrum. **15** (2020). https://doi.org/10.1088/1748-0221/15/01/T01003
10. M. González-Palacio, L. Sepúlveda-Cano, R. Montoya, *Simplified Path Loss Lognormal Shadow Fading Model Versus a Support Vector Machine-Based Regressor Comparison for Determining Reception Powers in WLAN Networks* (2021). https://doi.org/10.1007/978-3-030-68285-9_41
11. Y. Shishikui, Y. Sawahata, Quality of 8K ultra-high-definition television viewing experience in practical viewing conditions. IEEE Trans. Broadcas. https://doi.org/10.1109/TBC.2021.3105031
12. P. Duy Tung, C.W. Jung, Highly transparent planar dipole using liquid ionized salt water under surface tension condition for UHD TV applications. IEEE Trans. Antennas Propag. **69**(1), 35–42 (2021). https://doi.org/10.1109/TAP.2020.3008637
13. G. Calò, G. Bellanca, M. Barbiroli, F. Fuschini, G. Serafino, D. Bertozzi, V. Tralli, V. Petruzzelli, Design of reconfigurable on-chip wireless interconnections through optical phased arrays. Opt. Express **29**, 31212–31228 (2021)
14. M. Ahmed, A. Vashist, S.M. Pudukotai Dinakarrao, A. Ganguly, Architecting a secure wireless interconnect for multichip communication: an ML approach, in *2020 Asian Hardware Oriented Security and Trust Symposium (AsianHOST)*, pp. 1–6 (2020). https://doi.org/10.1109/AsianHOST51057.2020.9358256
15. M.S. Sim, Y. Lim, S.H. Park, L. Dai, C. Chae, Deep Learning-based mmWave beam selection for 5G NR/6G with sub-6 GHz channel information: algorithms and prototype validation. IEEE Access **8**, 51634–51646 (2020). https://doi.org/10.1109/ACCESS.2020.2980285
16. R. Shafin, L. Liu, V. Chandrasekhar, H. Chen, J. Reed, J.C. Zhang, Artificial intelligence-enabled cellular networks: a critical path to beyond-5G and 6G. IEEE Wirel. Commun. **27**(2), 212–217 (2020). https://doi.org/10.1109/MWC.001.1900323
17. Y. Wang, W. Wang, M. Zhou, A. Ren, Z. Tian, Remote monitoring of human vital signs based on 77-GHz mm-wave FMCW radar. Sensors **20**(10), 2999 (2020). https://doi.org/10.3390/s20102999
18. U. Chipengo, A. Sligar, S. Carpenter, High fidelity physics simulation of 128 channel MIMO sensor for 77GHz automotive radar. IEEE Access **8**, 160643–160652 (2020). https://doi.org/10.1109/ACCESS.2020.3021362
19. B. Jokanović, M. Amin, Fall detection using deep learning in range-doppler radars. IEEE Trans. Aerosp. Electron. Syst. **54**(1), 180–189 (2018). https://doi.org/10.1109/TAES.2017.2740098
20. M. Stephan, A. Santra, G. Fischer, Human target detection and localization with radars using deep learning. in *Advances in Intelligent Systems and Computing*, eds. by M.A. Wani, T.M. Khoshgoftaar, V. Palade, Deep Learning Applications, vol 2, 1232 (Springer, Singapore, 2021). https://doi.org/10.1007/978-981-15-6759-98
21. S. Marathe, Leveraging drone based imaging technology for pipeline and RoU monitoring survey. in *Paper presented at the SPE Symposium: Asia Pacific Health, Safety, Security, Environment and Social Responsibility, Kuala Lumpur, Malaysia,* April 2019. https://doi.org/10.2118/195427-MS
22. J.T. Vasquez, J. Rivero, R. Scapaticci, L. Farina, L. Crocco, F. Vipiana, Monitoring of food contamination via microwave imaging, in *2019 International Applied Computational Electromagnetics Society Symposium (ACES)*, pp. 1–2 (2019)
23. A.S.H. Ahmed, U. Soylu, M. Seo, M. Urteaga, M.J. W. Rodwell, A compact H-band power amplifier with high output power, in *2021 IEEE Radio Frequency Integrated Circuits Symposium (RFIC)*, pp. 123–126 (2021). https://doi.org/10.1109/RFIC51843.2021.9490426
24. R. Piesiewicz, T. Kleine-Ostmann, N. Krumbholz, D. Mittleman, M. Koch, T. Kurner, Terahertz characterisation of building materials. Electron. Lett. **41**(18), 1–2 (2005)
25. R. Piesiewicz, C. Jansen, S. Wietzke, D. Mittleman, M. Koch, T. Kurner, Properties of building and plastic materials in THz range. Int. J. Infrared Milli. Waves **28**,363–371 (2007)

26. C.R. Dietlein, J.E. Bjarnason, E.N. Grossman, Z. Popovic, Absorption, transmission and scattering of expanded polystyrene at millimeter-wave and terahertz frequencies. Proc. Of SPIE **6948**, 1–9 (2008)
27. A. Neil Salmon, Scene simulation for passive and active millimetre and sub-millimetre wave imaging for security scanning and medical applications. Proc. SPIE **5619**, 1–7 (2004)
28. R.A. Cheville, R.W. McGowan, D. Grischkowsky, Time resolved measurements which isolate the mechanisms responsible for terahertz glory scattering from dielectric spheres. Phys. Rev. Lett. **80**(2), 269–272 (2008)
29. J. Pearce, Z. Jian, D.M. Mittleman, Statistics of multiply scattered broadband terahertz pulses. Phys. Rev. Lett. **91**(4), 1–4 (2003)
30. J. Pearce, D.M. Mittleman, Using terahertz pulses to study light scattering. Physica B **338**, 92–96 (2003)
31. Y.C. Shen, P.F. Taday, M. Pepper, Elimination of scattering effects in spectral measurement of granulated materials using terahertz pulsed spectroscopy. Appl. Phys. Lett. **92**(051103), 1–3 (2008)

Terahertz Band for Wireless Communication—A Review

Ram Krishan

Abstract In wireless communication, the exchange of data traffic has increased significantly in modern days as the public produces, transmits, and uses this information. Following this transformation, the demand for faster wireless networking has been increasing rapidly that can be utilized anywhere. Wireless data amount has quadrupled in the course of recent many years, moving toward the limit of wired transmission organizations. If the current patterns proceeds, wireless Terabit-per-second (Tbps) connections are supposed to be the reality in the following five to ten years. Advanced physical layer technologies, particularly current spectral bands, would be needed to help these amazingly high data rates. Terahertz (THz) band networking is imagined as a basic wireless innovation to address this demand, easing bandwidth depletion and power limitations in current wireless networks and empowering a huge number of applications in a wide scope of areas. Terahertz is a spectral band with frequencies ranging from 0.1 THz to 10 THz. The frequencies ranges above and below of this band have gotten a lot of interest, but this is the band that is the least researched. This chapter explores the THz band communication systems and their features for future wireless communication.

Keywords Wireless communication · Data transmission · Terahertz (THz) · Frequency band

1 Introduction

Terahertz [1] radiations lies in 100 GHz (3 mm) to 10 THz (30 μm) on the electromagnetic spectrum, and this frequency range falls in between the millimeter and infrared as depicted in Fig. 1. The other names of the THz band [2] are close millimeters wave, sub-millimeter, and far-infrared [3].

This piece of the electromagnetic range is the least examined region when contrasted with neighbor locales, i.e., the microwave and optical groups [4]. This

R. Krishan (✉)
Mata Sundri University Girls College, Mansa, Punjab, India
e-mail: ramkrishan@pbi.ac.in

M. El Ghzaoui et al. (eds.), *Terahertz Wireless Communication Components and System Technologies*, https://doi.org/10.1007/978-981-16-9182-9_10

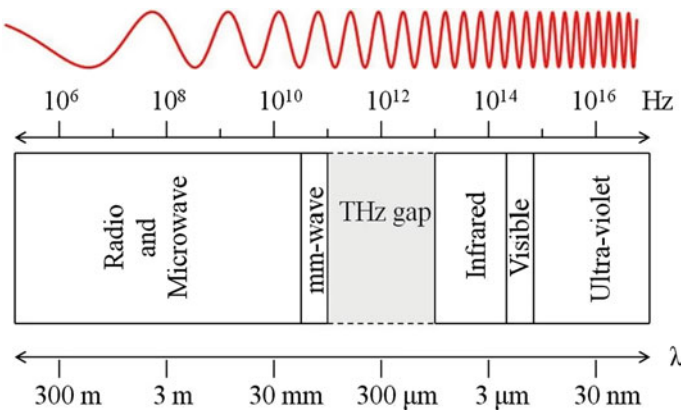

Fig. 1 Terahertz radiation spectrum

is the reason the expression "THz hole" is utilized to clarify the early stages of this band when contrasted with all around created adjoining ghastly locales. This has driven specialists from different followers (like physical science, material science, gadgets, optics, and science) to research different neglected or less-investigated parts of THz waves.

1.1 Properties of Terahertz Waves

A critical inspiration for this is the uncommon wave properties and huge potential applications in the THz frequency range. THz waves [5–7] have mid-qualities of the two groups they have sandwiched in the middle. These properties can be summed up as follows:

1. **Penetration**: The frequency of THz radiation is longer than the infrared frequency; henceforth, THz waves have less dissipating and better infiltration profundities (in the scope of cm) contrasted with infrared ones (in the scope of μm). Subsequently, dry and non-metallic materials are straightforward in this reach yet are murky in the noticeable range.
2. **Resolution**: The THz waves have more limited frequencies in contrast with the microwave ones; this gives a superior spatial imaging goal.
3. **Security**: In the THz band, the photon energies are a lot lower than X-beams. Consequently, the radiations of THz are said to be non-ionizing.
4. **Spectral fingerprint**: In numerous particles, inter and intra-vibrational method lies in the THz range.

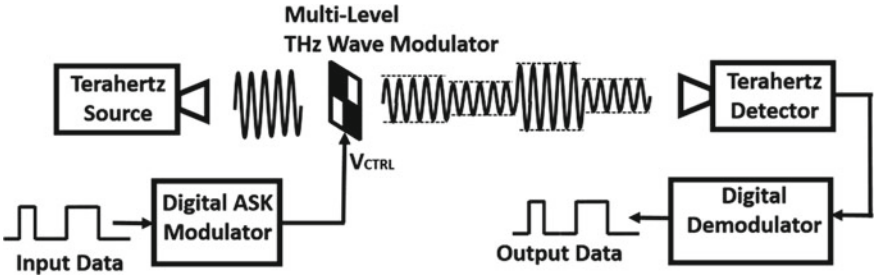

Fig. 2 Block diagram of terahertz communication

2 Terahertz (THz) Band in Wireless Communication

The Terahertz Band (0.1–10 THz) is anticipated to satisfy the need for Tbps wireless connectivity in the near future [8]. THz Band connectivity can overcome the spectrum shortage and power limitations that currently exist in wireless systems, allowing for a variety of applications such as ultra-fast huge data transfers between neighboring devices or videoconferencing of HD quality across personal mobile devices in small cells [9–11]. Furthermore, new nanoscale networking paradigms such as Nano Sensor in wireless networks and the Nano Internet of Things may be enabled by the THz Band.

Figure 2 shows the block diagram of the terahertz communication process. The increased interest in wireless communication pushed the required wireless connectivity speed to more than 100 Gbit/s. To convey the expansive data transfer capacity [12] vital for communication in future, specialists are investigating new resources of the frequency, like terahertz (THz), which is characterized as over 300 gigahertz (GHz) [13]. Already shown in [13] that the transmission in the 300 GHz must be done over transmission windows in order to realize a reliable transmission. There has been a surge in interest in this frequency band, and considerable efforts are being put into creating efficient sources, sensitive detectors, and suitable modulators in this frequency band [14, 15].

3 Terahertz Radiation Sources

THz technologies have a long history in space, owing to research applications such as astronomy and earth monitoring [16]. Increased commercial exploitation of space, for example, in support of weather forecasting and future ultra-high-frequency telecommunications, has a lot of potentials. Next-generation instrumentation, on the other hand, would be compatible with low-mass, small-volume, and low-power satellite payload systems. Higher-frequency sensors would be developed for increased sensitivity and imaging capabilities, as well as enhanced optical signal processing. These

advances provide major challenges, requiring improvements in detector components, circuit downsizing, sophisticated machining, lightweight composites, and improved cooling technologies, to mention a few. Addressing these problems will enable more widespread usage of the THz domain from space, and considerable work is being done in this area across the globe. In the next decades, THz research in space will flourish, providing both technical and economic advantages. To illustrate the advances and possible dangers in THz protection systems, we utilized the paradigm of standoff imaging systems. Though solid-state transistors would most likely replace Schottky diodes as sources and receivers in active systems, the large number of receivers (thousands) required for fair contrast in passive systems above 150 GHz means bolometer arrays will remain critical until packaging allows MMICs to compete. With cautious optimism, we anticipate integrated circuit and packaging technologies to remain the top research challenges for both active and passive devices to achieve reduced prices and more widely accessible capabilities. THz systems will enable sensory modalities that are just not possible in any other electromagnetic spectrum, regardless of the direction THz technology takes. A key impetus for THz communication system development is the requirement for bandwidth to allow high-capacity wireless data transfer. A multitude of communication windows in the band below 400 GHz will help short-range and indoor wireless networks.

4 Challenges for Terahertz Technology

The two most critical challenges for the commercialization of this technology are,

1. Development of effective THz sources with output power levels up to 100 mW.
2. The development of compact antenna arrays to reduce wireless connection degradation.

Terahertz (THz) waves, also known as underdeveloped electromagnetic waves, have made considerable scientific progress lately. Apart from laser-based THz production, progress is being made in THz generating techniques using electronic devices and accelerators, and a range of THz optical components are being actively manufactured. THz technology is currently being used in a growing number of applications. As a result, new research organizations faced a significant barrier to entry. A new spectroscopic technique was developed in the late 1980s, which led to a significant rise in jumpin operations. It took a few years, however, for the first commercially viable portable gadget to be released. While academics strive to expand the available power of spectrum below 10 GHz, we may be nearing physical capacity limitations, as well as the economic feasibility of increasing capacity in low and mid-band spectrum below 10 GHz. Advances in modulation and coding methods, as well as tiny cells, antenna beam shaping, virtualization, and other approaches, are improving the signal-to-interference-noise ratio (SINR) [17]. If we reach physical limitations in terms of SINR reduction, the only option to increase capacity is to increase available bandwidth. Obtaining large continuous networks, which are

required for greater data rate services, becomes more costly, if not impossible, as a result. The electronics industry has moved on to the next phase. Photonic circuits, high-precision infrared sensors, quantum computing, and a host of other technologies will emerge as a result of this process, which would have been unimaginable only a decade ago. At the heart of this endeavor are issues that mankind has yet to solve. For example, a Terahertz diode is a diode that can function in the Terahertz range. This method has a lot of promise as the next big thing. This paper examines the most recent developments in the field as well as a brief review of the basics. Terahertz diodes are diodes that operate at a Terahertz frequency. Schottky diodes and other PN-junction diodes have a sluggish response time. At such high frequencies, they are unable to adapt, requiring the creation of a new kind of diode built especially for switching at this level. Another significant reason for their present research is the use of THz diodes in Rectenna applications. Rectennas, also known as rectifying antennas, are signal-rectifying antennas. Instead of employing photovoltaics, we'll utilize rectifying antennas to collect light and then directly correct it using these diodes to produce energy from sunshine.

5 Terahertz Communication Systems

Figure 3 presents the terahertz communication system, the future of wireless technology. In future, 6G communications aim to provide an increased data rate and latency efficiency while allowing for ubiquitous connectivity.

Furthermore, 6G communications would use innovative techniques to enable modern networking experiences, such as virtual presence and universal presence,

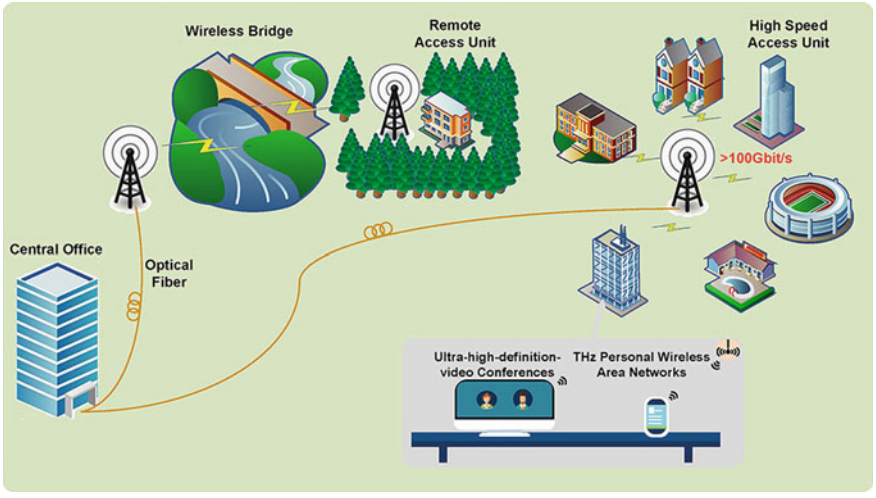

Fig. 3 THz wireless communication system

which would be accessible from anywhere. 6G communications also include notable technologies like holographic messaging, flying networks, and teleoperated vehicles. In addition, when compared to conventional wireless networks, 6G is said to be more efficient and secure. THz and Artificial Intelligence (AI) are, however, the most intriguing of all 6G-related technological developments. These advancements are said to be ground-breaking in the area of cellular networks. Business experts would need to enhance their architectural ideas significantly for these new technologies to be incorporated into prospective networks. 6G broadband networks are expected to go through a transformation that will set them apart from previous generations and revolutionize the wireless shift from "connected objects" to "connected knowledge." Not only that, but 6G communications may have capabilities beyond mobile Internet, enabling ubiquitous AI connection to be provided from the central network, which includes data centers, through delivery backhauls, and finally to end-users.

This presents challenging issues such as spatial-spectral efficiency and communication frequency ranges. As a consequence, a broad bandwidth is required, which may be accommodated by THz bands, which are classed as a distance band between microwave and optical spectra and are the subject of this study. THz waves are high-frequency waves with a very small wavelength. THz waves, as compared to mm waves, have a greater frequency.

As a consequence, 6G may be described as an ultra-dense network with enhanced capabilities that can integrate various technologies to execute and fulfill a wide range of service orchestration requirements. THz band coordination may also be used for a broad variety of applications, including macro and micro scale ones. Video transmission requires a large amount of bandwidth, which is one of the reasons why earlier wireless generations' internet video delivery services were delayed. Existing high-rate systems, such as 60 GHz IEEE 802.11ad mm-Wave Wi-Fi, can only provide 6.8 Gbps on average.

In other words, the bandwidth of existing channels has been exhausted, requiring the search for an additional spectrum. The THz bands, which are proficient to provide multi-gigahertz continuous bandwidths sufficient to support uncompressed video data rates of multi Gbps and Tbps are the only feasible option.

6 Conclusion

In this review chapter, we have explored the various research work is in progress toward terahertz wireless communication. THz waves may transmit the data at a faster speed at the expense of a shorter signal transmission wavelength. THz waves may resolve the issue of lower throughput of data or latency that 5G will not be able to handle, as they are fully deployed and integrated with cellular networks. As a consequence, service providers may look forward to THz waves as a way of addressing the lower electromagnetic spectrum's impending bandwidth constraint. Technology will spread into a wide digital gadgets era with the emergence of smart society, culminating in a multiplicity of devices being linked, resulting in enormous quantities

of data. 6G is expected to offer enormous power and a secure wireless connection between humans and machines like robotic and autonomous drone systems develop. The current Internet of Things (IoT) model will be replaced by the Internet of All (IoE) paradigm in future. Table 1 shows the comparison of different wireless technologies.

Table 1 Comparison of different wireless technologies

Technology	mmW	THz band	Infrared	Visible light communication (VLC)	Ultra-Violet
Range of frequency	30–300 GHz	100 GHz–10 THz	10–430 THz	430–790 THz	790 THz–30 PHz
Distance covers	Small distance	Small/Medium	Small/Extended	Small distance	Small distance
Power utilization	Average	Average	Low	Low	Likely to low
Topology	Point-to-multipoint	Point-to multipoint	Point-to-point	Point-to-point	Point-to multipoint
Source of noise	Thermal noise	Thermal noise	Sun/Ambient Light	Sun/Ambient Light	Sun/Ambient light
System security	Average	High	High	High	To be observed

References

1. M. Shafi, A.F. Molisch, P.J. Smith, T. Haustein, P. Zhu, P. De Silva, F. Tufvesson, A. Benjebbour, G. Wunder, 5G: a tutorial overview of standards, trials, challenges, deployment, and practice. IEEE J. Sel. Areas Commun. **35**, 1201–1221 (2017)
2. H. Elayan, O. Amin, R.M. Shubair, M. Alouini, Terahertz communication: the opportunities of wireless technology beyond 5G terahertz communication: the opportunities of wireless technology beyond 5G (2018)
3. J. Federici, L. Moeller, J. Federici, L. Moeller, Review of terahertz and subterahertz wireless communications. Appl. Phys. Rev. Focused Rev. **111101**(2010) (2016). https://doi.org/10.1063/1.3386413
4. W. Communications, *Utilizing Terahertz Band for Local and Personal Area Wireless Communication Systems*, pp. 330–334
5. K. Shinohara, D. Regan, Y. Tang, A. Corrion, D. Brown, J. Wong, J. Robinson, H. Fung, A. Schmitz, T. Oh, S. Kim, P. Chen, R. Nagele, A. Margomenos, M. Micovic, Scaling of gan HEMTs and schottky diodes for submillimeter-wave mmic applications. IEEE Trans. Electron. Devices **60**(10), 2982–2996 (2013)
6. C. Campbell, M. Kao, S. Nayak, High efficiency Ka-band power amplifier MMICs fabricated with a 0.15 nm GaN on SiC HEMT process, in *IEEE MTT-S International Microwave Symposium Digest* (2012)
7. M. Micovic, A. Kurdoghlian, A. Margomenos, D. Brown, K. Shinohara, S. Burnham, I. Milosavljevic, R. Bowen, A. Williams, P. Hashimoto, et al. 92–96 GHz GaN power amplifiers, in *IEEE MTT-S International Microwave Symposium Digest*, pp. 1–3 (2012)
8. I.F. Akyildiz, J. Miquel, C. Han, Terahertz band: next frontier for wireless communications. Phys. Commun. **12**, 16–32 (2014). https://doi.org/10.1016/j.phycom.2014.01.006
9. V. Radisic, K. Leong, X. Mei, S. Sarkozy, W. Yoshida, W. Deal, Power amplification at 0.65 THz using inp HEMTs. IEEE Trans. Microw.Theory Tech. **60**(3), 724–729 (2012)
10. I. Kallfass, J. Antes, D. Lopez-Diaz, S. Wagner, A. Tessmann, A. Leuther, Broadband active integrated circuits for terahertz communication, in *Proceedings of 18th European Wireless Conference European Wireless, EW*, pp. 1–5 (2012)
11. Y. Kawano, H. Matsumura, S. Shiba, M. Sato, G.-S. Park, Y.H. Kim, H. Han et al., Eds., *Convergence of Terahertz Sciences in Biomedical Systems* (Springer, 2012)
12. J.F. Federici, B. Schulkin, F. Huang et al., THz imaging and sensing for security applications—explosives, weapons and drugs. Semicond. Sci. Technol. **20**(7), S266–S280 (2005)
13. B. Aghoutane, M. El Ghzaoui, H. El Faylali, Spatial characterization of propagation channels for terahertz band. SN Appl. Sci. **3**, 233 (2021)
14. D.H. Auston, K.P. Cheung, P.R. Smith, Picosecond photoconducting Hertzian dipoles 13. in *Study of High-Power Wideband Terahertz-Pulse Generation Using Integrated High-Speed Photoconductive Semiconductor Switches*, eds by P. Kirawanich, S. Yakura, N. Islam, IEEE Trans. Plasma Sci. **37**(1), 219–228 (2009)
15. C. Lombardi, S. Manzini, A. Saporito, M. Vanzi, A physically based mobility model for numerical simulation of nonplanar devices. IEEE Trans. Comput.-Aided Des. Integr. Circ. Syst. **7**(11), 1164–1171 (1988)
16. M. Lundstrom, *Fundamentals of Carrier Transport* (Cambridge University Press, 2009)
17. J.D. Morse, R.P.J. Mariella, G.D. Anderson, R.W. Dutton, Picosecond optoelectronic gating of silicon bipolar transistors by locally integrated gaas photoconductive devices **12**(7), 379–381 (1991)

Nonconventional Heterostructure Tunnel FET for Sensitive Tera Hertz Detection

Ritam Dutta

Abstract A novel extended gate with source splitted nonconventional heterostructured tunnel field effect transistor (TFET) device is proposed in this chapter. A deliberate gate extension utilizes corner effect and can eventually increase the band-to-band-tunneling (BTBT) phenomenon for a n-type heterostructured TFET. The splitted source with ultra-thin barrier width results better digital and analog performance, which can be useful for electrical and high frequency applications. In this chapter, the figure of merits (FOM) of such typical TFET viz. transconductance (g_m), overall gate capacitance (C_{gg}), cutoff frequency (f_t) and gain bandwidth product (GBP) has been discussed and analyzed using TCAD device simulator. The cutoff frequency (f_t) of our proposed nonconventional heterostructured TFET device is recorded as 0.563 THz which makes it suitable for sensitive tera hertz detection.

Keywords TFET · BTBT · FOM · Transconductance · GBP · Cutoff frequency · TCAD · Tera hertz detection

1 Introduction

Nanodevice modeling has been trending research in the field of nanoscience and nanotechnology. With the advent of nanodevice modeling, the device dimensions have been scaled from millimeter to nanometer regime. Though downsizing of MOSFET devices is facing short channel effects (SCE) and drain induced barrier lowering (DIBL) effects, that limits its growth for low power and high frequency applications [1, 2]. Therefore, a new device physics-based approach using quantum tunneling developed several typical homo/hetero structures of tunnel field effect transistors (TFETs), which has been a real alternative of MOSFET for low power and high frequency applications [3–7].

This chapter presents a nonconventional heterostructure of a tunnel FET having extended gate with splitted source electrode, suitable for tera hertz applications.

R. Dutta (✉)
Center of Intelligent Systems and Robotics—ITER, Siksha 'O' Anusandhan (Deemed to be University), Bhubaneswar, Odisha 751030, India

M. El Ghzaoui et al. (eds.), *Terahertz Wireless Communication Components and System Technologies*, https://doi.org/10.1007/978-981-16-9182-9_11

There have been several research articles describe the high frequency applications of lateral conventional structures [8–12]. These conventional TFET device structures gathered much attraction for ease of physical fabrication process. Several modified conventional TFET structures have been studied and inferences have been taken from such literature surveys [5, 13–19]. But there is not much literature survey available for typical nonconventional TFET structures for high frequency applications. The figure of merits (FOM) of such typical TFET viz. transconductance (g_m), total gate capacitance (C_{gg}), cutoff frequency (f_t) and gain bandwidth product (GBP) has been discussed and analyzed using TCAD device simulator.

2 Device Structure and Simulation Strategy

A conventional TFET device structure shaped like English letter 'L' with source splitted is shown in Fig. 1. All necessary device dimension parameters and their associated electrical parameters have been taken from recent established device model [20], shown in Tables 1 and 2 respectively.

A unique feature of L-shaped TFET model is its physical device structure, where due to the L-type structure the BTBT tunneling can happen perpendicular to the channel. Such quantum tunneling across the tunneling junction results thousand times larger drive current (I_{ON}) in comparison to any conventional TFETs [21]. This phenomenon motivated us to modify the structure in nonconventional way, i.e., the gate terminal has been extended from its original position to sandwiched between

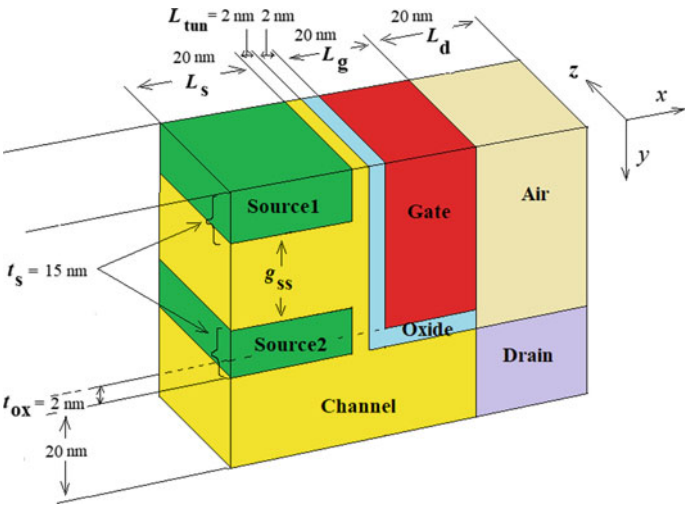

Fig. 1 L-shaped tunnel FET with source splitted device model

Table 1 Device parameters used for nonconventional heterostructure tunnel FET

Device parameters	Values
Gate length (L_g)	20 nm
Tunneling length (L_{tun})	2–8 nm (variable)
Gate oxide thickness (t_{ox})	2 nm
Source thickness (t_{ox})	5–20 nm (variable)
Gap between splitted sources (g_{ss})	10–40 nm
Gate length extension (L_{eg})	2–8 nm (variable)

Table 2 Electrical parameters used for nonconventional heterostructure tunnel FET

Electrical parameters	Values
Intrinsic channel doping (N_{ch})	1×10^{15} cm^{-3}
Source doping (N_s)	1×10^{20} cm^{-3}
Drain doping (N_d)	1×10^{18} cm^{-3}
Metal contact work function (ϕ_m)	4.5 eV
Gate voltage (V_G)	1 V
Supply voltage (V_{DD})	0.5–0.7 V

the splitted source electrodes. The modified nonconventional heterostructured TFET device is proposed in Fig. 2.

The major reason behind the variable gate electrode extension between a thin passage of splitted source electrodes is to utilize maximum source-channel area,

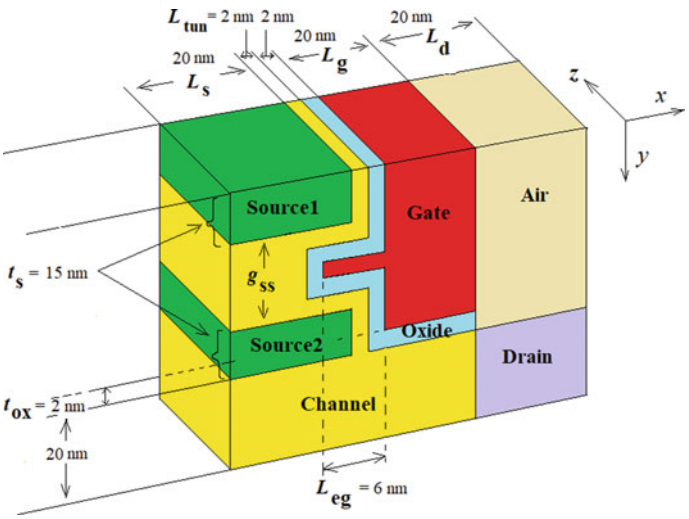

Fig. 2 Proposed nonconventional heterostructured TFET with extended gate and splitted source device model

through which maximum BTBT tunneling can be performed. Moreover, the corner effect also boosts the ON-state current (I_{ON}) as well as turns ON voltage (V_{ON}) for a nonconventional TFET device up to larger extent [22]. The typical device and electrical parameters have been detailed in Tables 1 and 2 respectively.

The proposed nonconventional heterostructured TFET device model is simulated by two-dimensional numerical device simulator, namely TCAD. The Shockley Read Hall (SRH) model is used to assimilate recombination effects between the carriers. Here n-type tunneling FET has been considered for ease of understanding. The Bandgap Narrowing (BGN) model is used for quantum tunneling at ultra-thin tunneling junctions.

2.1 Simulation Framework

The numerical device simulator is based on command and structure files as input peripherals, and log and solution files work as output peripherals. In ATHENA the fabrication process is performed virtually and using tony plot the graphical representations of possible output(s) can be achieved. The entire software environment is termed as technology computer aided design (TCAD) [23] (Fig. 3).

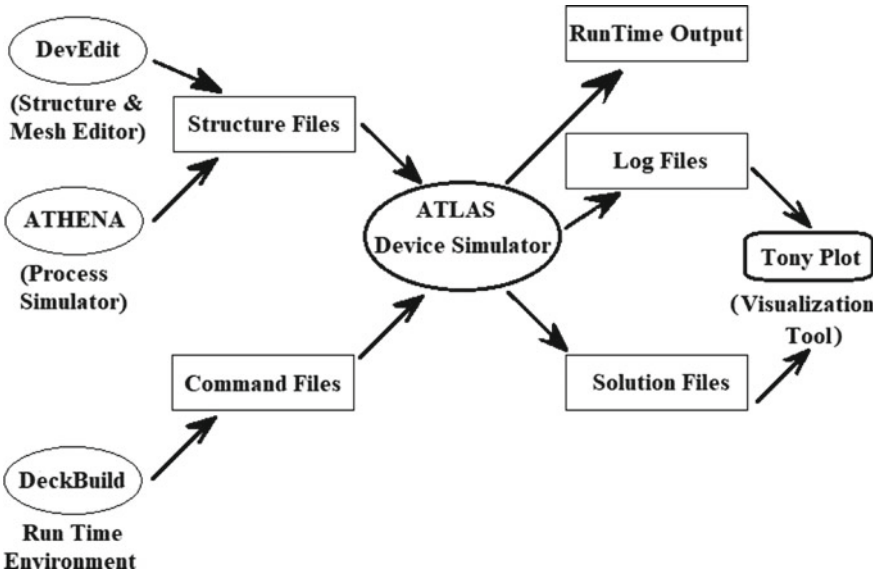

Fig. 3 ATLAS device simulator with its peripherals

2.2 Electric Field Distribution

To study the device performances, firstly the 2D Poisson's equation needs to be solved with determined boundary conditions [24]. Kane's model is used for non-local BTBT tunneling [25, 26]. After bias applied to the proposed device models, the electric field distribution contour plots provide the expanded lateral and vertical electric field emerged around tunneling region for the proposed nonconventional heterostructured TFET device model.

Moreover, the E_{flat} and E_{cor} indicate the electric field distributed at flat surface of source-channel junction and electric field distributed at corner surfaces of source-channel junction regions. Due to current crowding phenomenon, the electric field has got largely distributed at corner regions in comparison with flat source-channel junction regions (Fig. 4).

3 Simulation Results and Discussion

All electrical characteristics and small signal analysis have been performed in detail in this section.

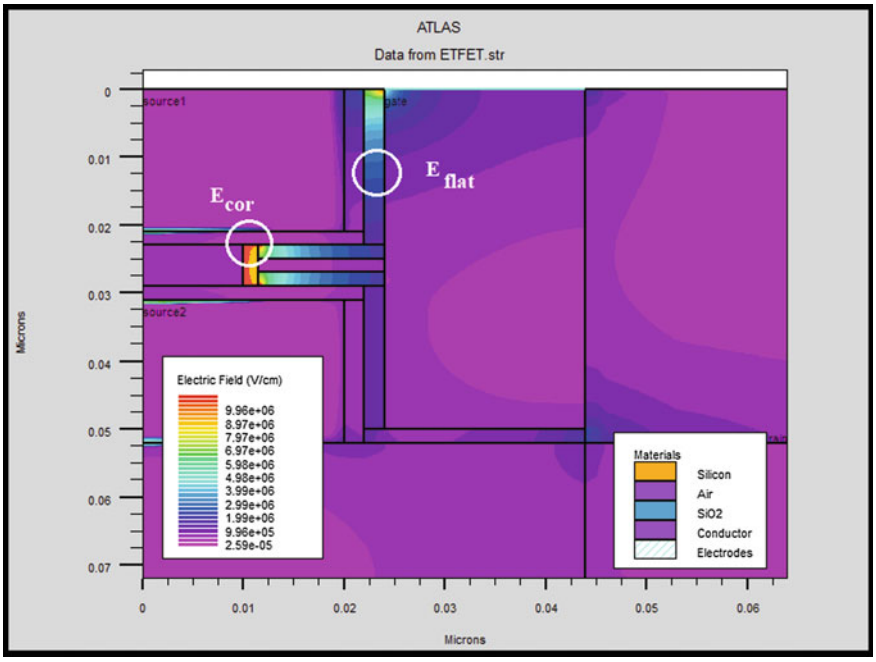

Fig. 4 Electric field distribution captured in contour plots for proposed TFET structure

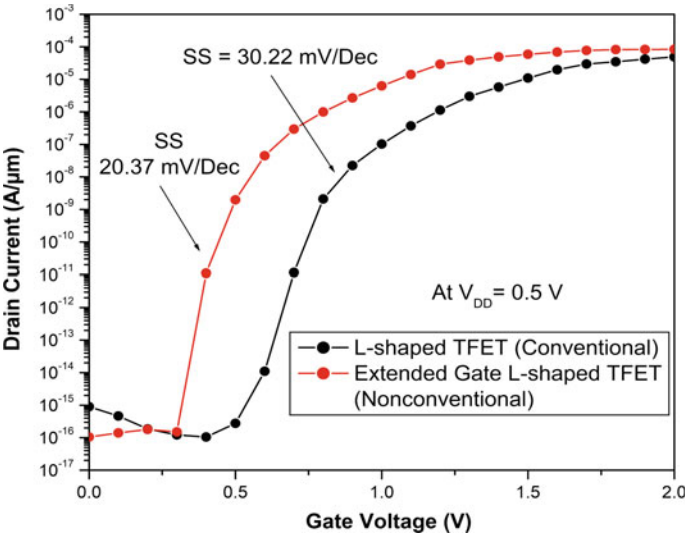

Fig. 5 Transfer characteristics analysis between conventional and nonconventional TFET structure

3.1 Transfer Characteristics

The transfer characteristics depict the variation of ON-state current with varied gate voltage (V_g) at $V_{DD} = 0.5$ V.

From Fig. 5 it can be observed that the red colored solid line rises much earlier at 0.3 V gate voltage. This red color solid line represents our nonconventional heterostructured TFET, which provides 20.37 mV/decade of subthreshold swing (SS), much less compared to 30.22 mV/decade of SS offered by conventional L-shaped TFETs. Moreover, the proposed TFET device offers better leakage current of 1.12×10^{-16} A/μm.

3.2 Surface Potential and Electric Field Distribution Analysis

The surface potential distribution along the channel especially in lateral direction and the electric field distribution analysis plays critical role in determining the suitable physics-based device structure for better device performance.

In Fig. 6, the surface potential distribution has been analyzed at supply voltage kept minimum of 0.5 V for both the conventional L-shaped tunnel FET with our proposed nonconventional TFET device model. From the graphical representation, it can be clearly understood that the extended varied gate electrode placed between the splitted source of our heterostructured TFET device produces steep rise in the tunneling

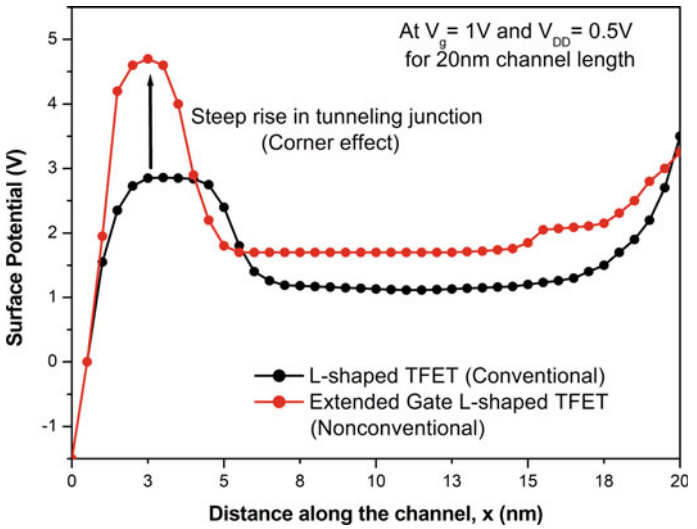

Fig. 6 Surface potential distribution analysis between conventional and nonconventional TFET structure

junction due to corner effect. The current crowding occurring at the source-channel corner region results this steep rise.

The lateral and vertical electric field distribution analysis is shown in Figs. 7 and 8 respectively. In Fig. 7, the noticeable sharp spike has been generated due to the extended gate structure of our proposed device model, recorded best at 1×10^{-4} V/cm

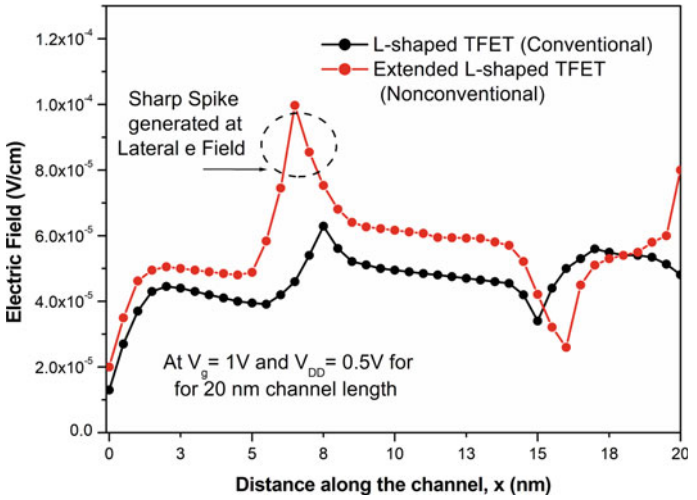

Fig. 7 Lateral electric field distribution analysis between conventional and nonconventional TFET structure

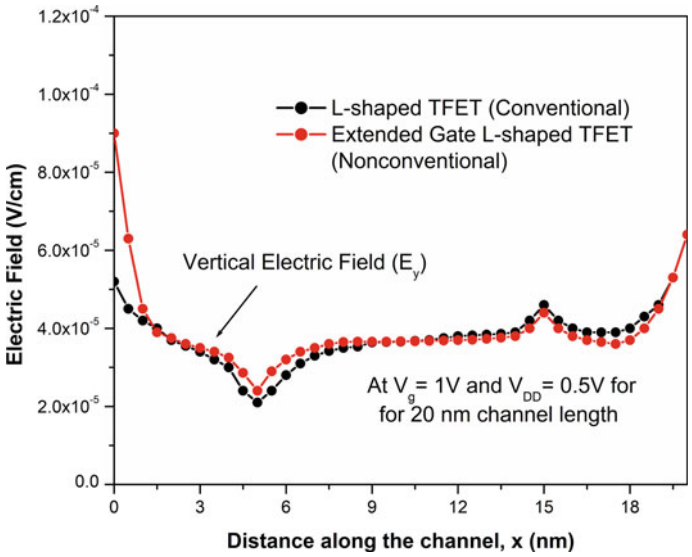

Fig. 8 Vertical electric field distribution analysis between conventional and nonconventional TFET structure

shown using red color solid line, whereas the conventional L-shaped TFET device model shows only 6×10^{-5} V/cm at tunneling regions.

The vertical electric field for both the device models has got distributed almost equally along the channel length.

3.3 Small Signal Analysis

The proposed nonconventional heterostructured tunnel FET device model's small signal analysis is studied by investigating its analog parameters.

Earlier the proposed device model has offered better ON-state current in transfer characteristics analysis, and in addition to this, due to typical corner regions of extended gate, steep subthreshold slope has also been obtained.

The small signal analysis includes transconductance (g_m), capacitance between gate to drain (C_{gd}), capacitance between gate to source (C_{gs}), cutoff frequency (f_t), maximum oscillation frequency ($f_{\max}$) and gain bandwidth product (GBP). The total gate capacitance (C_{gg}) must be less to achieve the superior device performance for high-speed applications. The figures of merits (FOM) are assessed at 1 MHz small signal input frequency. C_{gd} acts like parasitic capacitance at reduced gate voltages, and it acts like an inversion capacitance at higher gate potential for small signal analysis.

3.3.1 Transconductance Analysis

The transconductance (g_m) is defined as the ability of a device to reflect gate voltage (V_g) into drain current (I_d). After bias is applied, g_m can be calculated from transfer characteristics (Fig. 5) using Eq. 1.

$$g_m = (dI_d/dV_g)V_{\mathrm{DS}} \tag{1}$$

The transconductance (g_m) has been simulated and shown in Fig. 9. It can be observed that, at $V_{\mathrm{DD}} = 0.5$ V and with drain to source voltage (V_{DS}) varied between 1–0.5 V, the subthreshold slope gets affected.

Hence, a precise adjustment of V_{DS} can deliver steeper slope with restricted leakage current. The proposed nonconventional heterostructured TFET provides g_m of 12.25×10^{-5} S at $V_{\mathrm{DS}} = 1$ V and $V_{\mathrm{DD}} = 0.5$ V.

Now, after finding g_m, the f_t can be achieved from Eq. 2.

$$f_t = g_m 2\pi(C_{gs} + C_{gd}) \tag{2}$$

$$f_t = g_m 2\pi C_{gg} \tag{3}$$

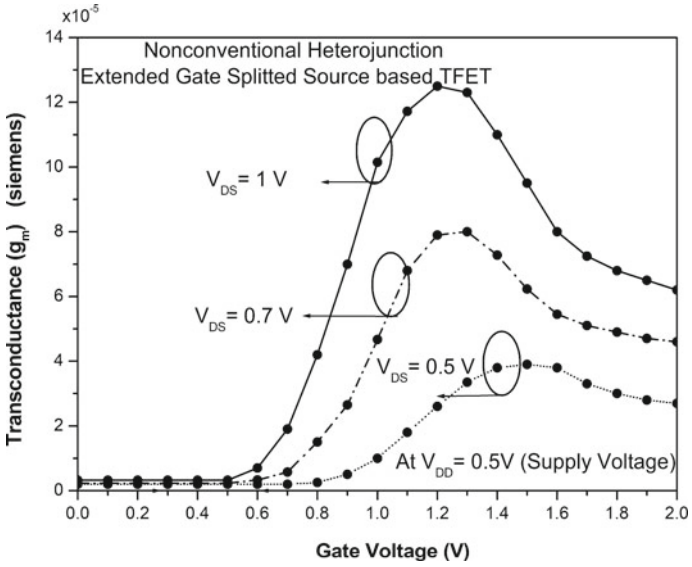

Fig. 9 Transconductance Analysis of proposed TFET model at 0.5 V Supply voltage with varied V_{DS} (0.5–1 V)

where C_{gs} and C_{gd} are the gate to source and gate to drain capacitances, respectively. The total gate capacitance (C_{gg}) is the summation of C_{gs} and C_{gd} of our proposed nonconventional heterostructured TFET device model i.e., ($C_{gg} = C_{gs} + C_{gd}$).

3.3.2 Capacitance–Voltage Characteristics Analysis

Keeping each gate bias of 1 MHz frequency source, small signal analysis can be performed by the internal capacitances i.e., C_{gs} and C_{gd} along with g_m are utilized to evaluate f_t. It is evident that, lower the C_{gg} and higher the g_m helps to achieve excellent high frequency performance.

From Fig. 10, it can be noted that our proposed device model produces less C_{gs} with respect to C_{gd}. Now, with variation in V_{DS} from 0.5 V to 0.7 V, the C_{gd} can be reduced from 1.83×10^{-16} F to 0.57×10^{-16} F at 0.5 V of V_{DD}. C_{gg} can be reduced with higher g_m. The combined attempt of increasing g_m by reducing C_{gg} elevate f_t. The nonconventional heterostructured TFET device model delivers $f_t = 0.563$ THz at $V_{DS} = 0.7$ V, $V_{DD} = 0.5$ V, which is suitable for tera hertz applications.

$$\text{GBP} = \frac{g_m}{2\pi 10 C_{gd}} \tag{4}$$

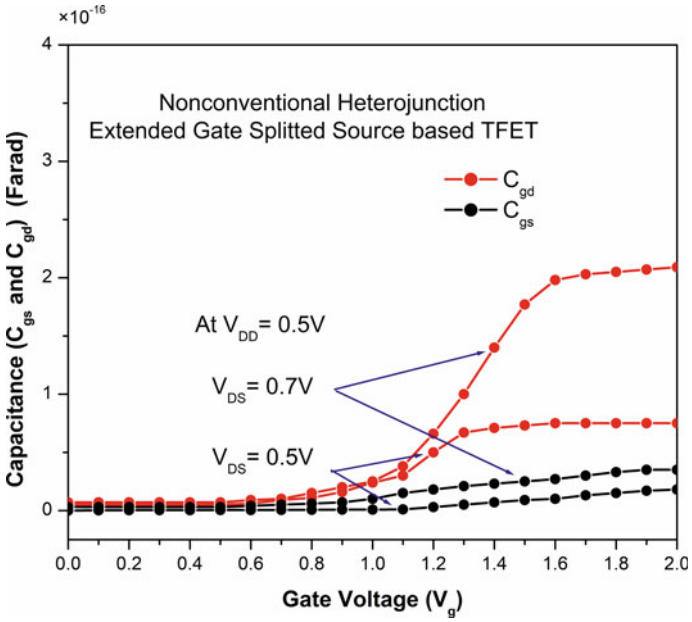

Fig. 10 Capacitance–gate voltage characteristics of proposed device with varied V_{DS} (0.5 V–0.7 V) at 0.5 V supply voltage

$$f_{\max} = \frac{f_t}{8\pi \times C_{gd} \times R_{gd}} \tag{5}$$

Moreover, the GBP and $f_{\max}$ can be computed from Eq. 4 and 5 respectively. The $f_{\max}$ has been given by the equation number (5) and optimum value of R_{gd} have been considered as 1.2 KΩ for calculating $f_{\max}$.

4 Conclusion

The nonconventional heterostructured TFET device's electrical and small signal analysis is performed thoroughly. The corner effect resulting current crowding effect offered larger band-to-band tunneling. At supply voltage of 0.5 V, the SS becomes 20.37 mV/decade which is much lower than conventional TFET structure.

Our proposed model provides g_m of 12.82×10^{-5} S at $V_{DS} = 1$ V and $V_{DD} = 0.5$ V and cutoff frequency of 0.563 THz at $V_{DS} = 0.7$ V, $V_{DD} = 0.5$ V, which can be applied for tera hertz applications. GBP is recorded as 45.5 GHz.

Acknowledgements The research work has been supported by Center of Intelligent Systems and Robotics, Institute of Technical Education and Research–Siksha 'O' Anusandhan (Deemed to be University), Bhubaneswar–751030, Odisha, India.

References

1. T. Nirschl, S. Henzler, J. Fischer, Scaling properties of the tunneling field effect transistor (TFET): device and circuit. Solid State Electron. **50**(1), 44–51 (2006)
2. N. Thomas, H.S. Philip Wong, The end of Moore's law: a new beginning for information technology. IEEE J. Comput. Sci. Eng. **19**(2), 41–50 (2017)
3. Q. Zhang, W. Zhao, A. Seabaugh, Low-subthreshold-swing tunnel transistors. IEEE Electron Device Lett. **27**(4), 297–300 (2006)
4. W.Y. Choi, B.G. Park, J.D. Lee, Tunneling field effect transistor (TFET) with subthreshold swing (SS) less than 60mV/dec. IEEE Electron Device Lett. **28**(8), 743–745 (2007)
5. A.S. Verhulst, D. Leonelli, R. Rooyackers, G. Groeseneke, Drain voltage dependent analytical model of tunnel field-effect transistors. J. Appl. Phys. **110**(2), 024510 (2011)
6. S. Brocard, M. Pala, D. Esseni, Design options for heterojunction tunnel FETs with high on current and steep sub-VT slope. in *Proceedings of IEEE International Electron Devices Meeting (IEDM), San Francisco, CA, USA*, pp. 5.4.1 (2012)
7. W. Lee, W.Y. Choi, Influence of inversion layer on tunneling field-effect transistors. IEEE Electron Device Lett. **32**(9), 1191–1193 (2011)
8. R. Dutta, S.C. Konar, N. Paitya, Influence of gate and channel engineering on multigate tunnel FETs: a review. Computational advancement in communication circuits and systems. Lecture Notes Electr. Eng. (LNEE) **575**, 345–355 (2018). https://doi.org/10.1007/978-981-13-8687-9_31
9. R. Dutta, N. Paitya, Effect of pocket intrinsic doping on double and triple gate tunnel field effect transistors, communication, devices and computing. Lecture Notes Electr. Eng. (LNEE) **602**, 249–258 (2019). https://doi.org/10.1007/978-981-15-0829-5_25

10. P. Wisniewski, M. Majkusiak, Modeling the tunnel field-effect transistor based on different tunneling path approaches. IEEE Trans. Electron. Devices **65**(6), 2626–2631 (2018)
11. R. Dutta, N. Paitya, *Analysis of InN-based Surrounded Gate Tunnel Field-Effect Transistor for Terahertz Applications, Emerging Trends in Terahertz Solid-State Physics and Devices* (Springer 2020), pp. 77–84. https://doi.org/10.1007/978-981-15-3235-1_6
12. R. Dutta, N. Paitya, Novel InAs/Si heterojunction dual gate triple metal P-i-N tunneling graphene nanoribbon field effect transistor (DG-TM-TGNFET) for high frequency applications. Generation, detection and processing of terahertz signals. Lecture Notes Electr. Eng. (LNEE) **794**, 251–262 (2021). https://doi.org/10.1007/978-981-16-4947-9_17
13. V. Chandan, K. Nigam, D. Sharma, Approach on electrically doped TFET for suppression of ambipolar and improving RF performance. IET Circuits Devices Syst. **13**(6), 787–792 (2019). https://doi.org/10.1049/iet-cds.2018.5394
14. R. Dutta, N. Paitya, Performance study of Ambipolar conduction suppression for dual gate tunnel field effect transistors. Advances in communication, devices and networking. Lecture Notes Electr. Eng. (LNEE) **776**, 27–35 (2021)
15. R. Dutta, N. Paitya, TCAD performance analysis of P-i-N tunneling FETs under surrounded gate structure. in *Proceedings of 2nd International Conference (ICAST-2019). Engineering Research Network (SSRN)—Elsevier, Mumbai, India* (2019). https://doi.org/10.2139/ssrn.3370766
16. S. Cho, J.S. Lee, K.R. Kim, B.-G. Park, J.S. Harris, I.M. Kang, Analyses on small—signal parameters and radio-frequency modeling of gate-all-around tunneling field effect transistors. IEEE Trans. Electron. Devices **58**(12), 4164–4171 (2012)
17. R. Dutta, N. Paitya, Electrical characteristics assessment on heterojunction tunnel FET (HTFET) by optimizing various high-κ materials: HfO_2/ZrO_2. Int. J. Innovative Technol. Explor. Eng. **8**(10), 393–396 (2019)
18. R. Dutta, T.D. Subash, N. Paitya, Extended gate with source splitted tunnel field effect transistor for improved device performance. Mater. Today Proc. **43**(6), 3715–3719 (2021). https://doi.org/10.1016/j.matpr.2020.10.983
20. R. Dutta, T.D. Subash, N. Paitya, Improved DC performance analysis of a novel asymmetric extended source tunnel FET (AES-TFET) for fast switching application. Silicon (2021). https://doi.org/10.1007/s12633-021-01147-8
20. S. Yun, J. Oh, S. Kang, Y. Kim, J.H. Kim, G. Kim, S. Kim, F-Shaped tunnel field-effect transistor (TFET) for the low-power application. Micromachines **10**, 760 (2019)
21. S.W. Kim, J.H. Kim, T.K. Liu, W.Y. Choi, B. Park, Demonstration of L-shaped tunnel field-effect transistors. IEEE Trans. Electron. Devices **63**(4), 1774–1778 (2016)
22. J.G. Fossum, J.W. Yang, V.P. Trivedi, Suppression of corner effects in triple-gate MOSFETs. IEEE Electron. Device Lett. **24**, 745–747 (2003)
23. TCAD Atlas Manual, Silvaco, Inc., CA 95054, USA (2015)
24. C. Shen, S.-L. Ong, C.-H. Heng, G. Samudra, Y.-C. Yeo, A variational approach to the two-dimensional nonlinear Poisson's equation for the modeling of tunneling transistors. IEEE Electron. Device Lett. **29**, 1252–1255 (2008)
25. E.O. Kane, Theory of tunneling. J. Appl. Phys. **32**(1), 83–91 (1961)
26. E.O. Kane, Zener tunneling in semiconductors. J. Appl. Phys. Chem. Solids. **12**(2), 181–188 (1960)

Study and Design of the Microstrip Patch Antenna Operating at 120 GHz

Salah-Eddine Didi, Imane Halkhams, Mohammed Fattah, Younes Balboul, Said Mazer, Moulhime EL Bekkali, and Sudipta Das

Abstract In this chapter, we will present a study concerning the design of a microstrip patch antenna with a rectangular slot intended for the wireless technology terahertz. This antenna operates for a frequency located in the terahertz band (120 GHz). The designed slot allows improving the characteristics of the antenna. The dimensions of this type of antenna for the terahertz band are reduced compared to conventional antennas. The patch and feeder cable sizes are small and difficult to manufacture. In this paper, we use a three-dimensional high-frequency structure simulator (HFSS) tool. The substrate chosen for this design is the rubber hard one with permittivity $\varepsilon r = 3$ and its height ($h = 0.1$ mm). The overall size of this antenna is 0.9 mm × 0.7 mm × 0.1 mm. It resonates at a frequency of 119.79 GHz, with a reflection coefficient (S11) of less than minus 10 dB throughout the resonant frequency range (S11 reflection coefficient of −21.36 dB), a bandwidth of 3.11 GHz, VSWR of 1.18, gain of 7.9 dB, and efficiency of 99.5%.

Keywords THz · 120 GHz · Microstrip patch antenna · Slot · HFSS

1 Introduction

Terahertz (THz) waves define the range of the electromagnetic wave spectrum between 20 and 0.1 THz, which corresponds to wavelengths between 15 and 3000 μm. Figure 1 shows this spectrum as a function of frequency and wavelength. The THz band is bounded there by the purple square, which extends from radio waves

S.-E. Didi (✉) · Y. Balboul · S. Mazer · M. EL Bekkali
IASSE Laboratory, Sidi Mohamed Ben Abdellah University, Fez, Morocco
e-mail: salaheddine.didi@usmba.ac.ma

I. Halkhams
LSEED Laboratory, UPF, Fez, Morocco

M. Fattah
IMAGE Laboratory, Moulay Ismail University, Meknes, Morocco

S. Das
Department of ECE, IMPS College of Engineering and Technology, Azimpur, W.B., India

M. El Ghzaoui et al. (eds.), *Terahertz Wireless Communication Components and System Technologies*, https://doi.org/10.1007/978-981-16-9182-9_12

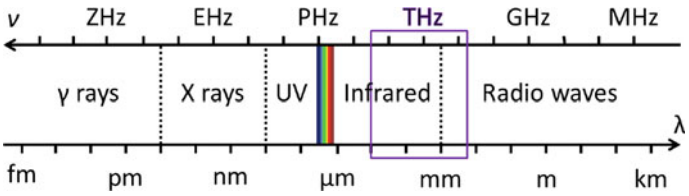

Fig. 1 Representation of the spectrum of electromagnetic waves as a function of frequency and wavelength. The purple frame delimits the THz domain

in the electrical band (<0.1 THz) to infrared waves in the optical band (>20 THz). The THz range covers a spectral area of great interest for many uses in spectroscopy, imaging, and telecommunications [1].

The development of THz spectroscopy began in the late 1980s with the time-domain spectroscopy (TDS) technique [2]. For example, it allows the identification of absorption lines of the polar molecule of water corresponding to the excitation of molecular rotations [3] or the absorption due to phonons or free carriers in metals or doped semiconductors.

Among the most common applications of THz spectroscopy is in the pharmaceutical industry. This application exploits the fact that the absorption lines of water are very well defined and more easily identified in the THz domain than in the optical spectrum [3]. Thus, the presence of water in pharmaceutical products can be identified during the control of a pharmaceutical process [4].

Like X-rays, THz waves have a high penetrating power. They can penetrate plastic and clothing fabrics, for example. Thus, they can be used to make deep images. However, unlike X-rays, THz waves only partially penetrate metals or skin. On the other hand, they have the advantage of being low energy, so they do not ionize the skin and allow body imaging without damaging cells.

These properties offer a great potential to THz sources, which are used for different needs: insecurity [5], industry [6], medicine [7], or art [8].

Telecommunications are an example. The bandwidth of radio waves is limited to 10% of the carrier frequency, which is 10 GHz [1], which limits the data transmission rate. However, by using a higher frequency wave, such as THz waves, the bandwidth is increased, which allows increasing the data rate transmitted by a wireless network.

In the terahertz frequency range, the most commonly used antennas are planar are the planar type and the dipoles (Hertz dipoles) built monolithically on the substrate. On this substrate are active components for radiation generation or detection with a hemispherical silicon lens placed on the backside of this substrate. Even though these antennas are not really "broadband", they have so far provided the best results in pulsed Terahertz spectroscopy. However, on the other hand, their poor efficiency makes them unsuitable for use in continuous operation, where the powers involved are low.

In this chapter, we present a design of a rectangular patch antenna with a rectangular-shaped groove, suitable for the terahertz operating frequency. The structure of this antenna is 0.9 mm × 0.7 mm × 0.1 mm. This paper is structured as

follows: The first step presents a general introduction of this paper, the second step is devoted to the different applications related to Terahertz frequencies, the third step presents the Terahertz radiation sources, the fourth step is devoted to the design of a Terahertz slot patch antenna, finally, the fifth step ends with a conclusion.

2 Applications of Terahertz Frequencies

A. Biomedical

Currently, different medical imaging techniques coexist. The first X-ray images were made in 1895 by Wilhelm Rontgen. A century later, the first demonstrations of imaging using terahertz frequency waves were performed [9]. X-ray imaging uses photons with quantum energies above a hundred eV, whereas in the terahertz range the energy is less than 1 eV (see Fig. 2). Since molecular ionization requires several eV, terahertz waves can currently be considered as non-ionizing electromagnetic radiation. However, the strong absorption of terahertz waves by water molecules and the high water content of the human body limit the applications of terahertz imaging to surface examinations.

Initially, the applications were focused on the examination of the skin. The control of the water content of the cells on the surface allows the detection of a deterioration of the skin. In the case of skin cancers, the use of terahertz imaging allows the early detection of this type of cancer undetectable by X-rays but also to monitor their evolution. In the case of wounds and burns, this detection can be used to evaluate the extent of the deterioration but especially to control the state of healing of the skin without removing the dressings [10]. As skin cancer is one of the most common cancers, its early detection is a significant advance in the biomedical field.

More specific applications have been demonstrated, notably in dentistry. Dentin has different water contents when it is healthy or not. This variation makes it possible to detect the depth of evolution of a cavity or the presence of dental tumors [11] while limiting the use of X-rays. These specific applications may allow an improvement of the current systems on X-ray exposure. Proofs of concept are a first step toward the democratization of these systems.

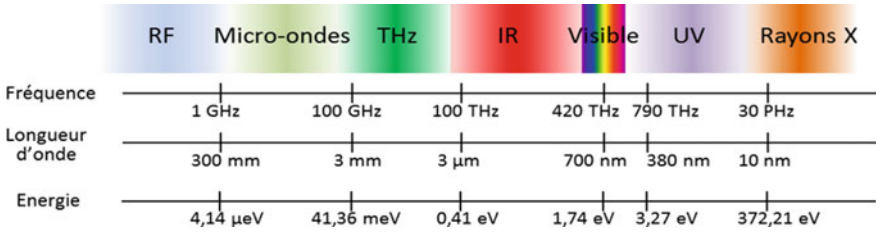

Fig. 2 Electromagnetic spectrum ($\lambda = c/f$; $E = hf$)

Early detection of plantar perforation disease or diabetic foot syndrome was the subject of a proof of concept in 2017 [12]. Thus, detection of arch dehydration, caused by vascular and neurological deterioration, can prevent susceptibility to this syndrome affecting people with diabetes. It could help avoid the amputation required in 15% of cases. The coupling of this type of imaging with other medical techniques increases the scope of application of these frequencies, in particular with endoscopy systems to visualize colon cancer cells [13].

The terahertz domain also has applications in biomedical research. In particular, terahertz spectroscopy allows the non-destructive analysis of tumors in vitro but also the analysis of nerve cells to improve the understanding of neurodegenerative diseases [14]. Biomedical studies using terahertz spectroscopy are now increasingly common in the research field but remain marginal in industry. The use of terahertz waves in the biomedical field contributes to the analysis of the human body and the establishment of medical diagnoses. Proofs of concept for these applications are essential elements for their deployment.

B. **The industry**

The propagation of terahertz waves in different media presents absorption and reflection spectra unique to each medium. This characteristic makes it possible to identify and differentiate each molecule, which is used for spectroscopy. Thus, opaque media in the visible range is transparent for specific THz frequencies. This advantage, applied to non-destructive testing, is of great interest to the industry. The reduction of terahertz waves allows determining the spectra associated with the absorption of products and consequently, their composition or their thickness.

The quality control of a product allows guaranteeing that it fulfills the desired functions. It can be divided into two types of inspection, destructive and non-destructive. In the majority of the mass distribution industries listed in Table 1, the inspection of a percentage of the elements of a batch is sufficient to guarantee the quality of all the elements of the batch. Thus, destructive quality control results in financial losses

Table 1 Industrial applications of non-destructive testing at terahertz frequencies

Sector	Principle
Alimentary	E-coli contamination, underpack control, quality control, fruit deterioration, genetically modified food, product origin presence of insects, plastic, presence of insecticide
Armory	Deteriorations, micro-cracks
Automotive	Degraded paint
Building	Cracks in cement under the plaster, thermal properties of walls
Pharmaceutical	Quality control
Photovoltaic	Local conversion efficiency
Plastic	Thickness of plastic bottles
Semiconductor	Lithography control package control, defect control during axial epic growth, counterfeit detection

depending on the percentage applied. Terahertz imaging in the industry finds its main applications in non-destructive testing which allows the use of the analyzed parts. This type of control is very attractive because of the financial advantage it offers. The cost of the inspection equipment is a key point since it must be lower than the financial losses estimated for destructive inspection. Some sectors, such as nuclear, construction, or space, produce a more limited volume of parts whose manufacturing cost is higher. The criticality of action in these sectors requires 100% control of the parts produced, non-destructive testing is therefore essential.

C. Security and defense

Spending in the security and defense sector in France was 32.7 billion euros in 2017. Two points must be dissociated, the security of citizens and the defense of the territory.

The observation of the French airspace by the radars contributes to the defense of the territory. The detection of an object by radar is possible when the waves emitted by the latter are reflected. Their attenuation makes it possible to determine the distance, speed, and size of the detected object. The use of coatings on moving objects, absorbing over a wide range of frequencies, limits the radar systems capable of detecting them. Thus, as coatings evolve, the frequency ranges used by radars are adjusted. Currently, the lack of terahertz sources limits their use, but a major issue for defense is the increase in the frequency of radar systems [15].

The ability of terahertz waves to image optically invisible elements is a considerable advantage for the security of citizens. For example, determining the contents of a package, envelope, or suitcase without opening it by using terahertz waves guarantees the safety of the control agents. The absorption spectra of drugs, explosives, and chemical agents are studied by the scientific community to realize security scanners applied to containers or individuals [16]. These scanners allow the detection of weapons concealed under clothing by THz cameras and increase security in public places.

Another aspect of security is that of the communications channels. Terahertz beams can be directional and point-to-point terahertz communications limit the possibility of intercepting the signal by an unauthorized person. Marginal use of terahertz waves limits the ability to properly receive the signal and thus increases the security and privacy of communications. More specific examples are developed, in particular, to contribute to the complexity of counterfeit money [17] by applying a resin patch on banknotes that can be deciphered by terahertz spectroscopy.

D. Telecommunications

The rate carried by optical fibers reaches Pb/s in the laboratory. But the lack of optoelectronic converters supporting these speeds limits the bandwidths currently used. In recent years, the growth in the number of connected objects predicts the saturation of Wi-Fi. Eldholm's law predicts a convergence of the necessary data rates in wired, nomadic, and wireless networks by 2030 [17]. Notably, improved video quality goes hand in hand with a need for higher throughput. Currently, devices associated with 4 K are being deployed and 8 K displays are available for purchase.

4 K requires 6 Gbps. A format in development called Super High Vision requires 24 Gbps illustrating this growth in throughput needed shortly. The occupation and allocation of the frequency bands currently in use limit the available frequency bands. An increase in carrier frequencies to terahertz frequencies increases the width of the frequency bands and represents a solution to the growing data rate demand.

Terahertz frequencies are for now not exploited and not assigned above the 275 GHz frequency band. Therefore the range of frequency comprised around the frequency of 275 GHz and 1 THz is possible to set up high-speed data communications. The losses seen at the heart of the atmosphere are due to the frequency of the scattered waves [18, 19] as well as to the peaks of the resonance peaks of all the chemical components that compose it. The movement of water molecules causes several absorption peaks in the terahertz band, but certain frequency ranges can be used and are presented in Table 2. The frequencies above 1 THz are not classified because of numerous peaks associated with phenomena called absorption that renders these frequencies unacceptable for high-speed and long-range communications. The loss suffered by terahertz waves through the atmosphere implies that we need robust and compact terahertz sources for use in actual environments.

Ultrafast non-wireless communications will likely require both low-range and long-range data transfers. Indeed, these very short-distance transmissions have various properties in electronic systems that are very applicable to them. Frequency increases have a significant effect on the amount of loss incurred when information flows through electrical circuits, increasing energy demand, and phenomena related to thermal effects while reducing device characteristics. Wireless communication distances sometimes reaching centimeters, combined with high data transmission rates and short "wireline" type links can replace the electrical interconnections employed within systems running in the multi GHz range [20].

Wireless communication systems that have very high data rates and low data carriers over short lengths of less than a meter make it possible to quickly download data, like magazines or HD movies, past a download kiosk. By augmenting the coverage length to a distance between 1 and 100 m and more, these uses are likely to involve a ward or apartment containing environmentally isolated transmission paths [21]. The scientific literature also mentions the possibility of achieving data transfers at rates ranging from 100 to 120 Gbps [22]. The distance needed to achieve these

Table 2 Usable frequency bands for wireless communications up to 1 THz

Frequency band (GHz)	Bandwidth (GHz)	Attenuation
215–315	100	2 à 4 dB/km
330–365	35	5 dB/km
390–435	45	9 dB/km
450–515	65	11 à 12 dB/km
625–725	100	11 dB/km
790–900	110	12 dB/km
925–950	25	15 dB/km

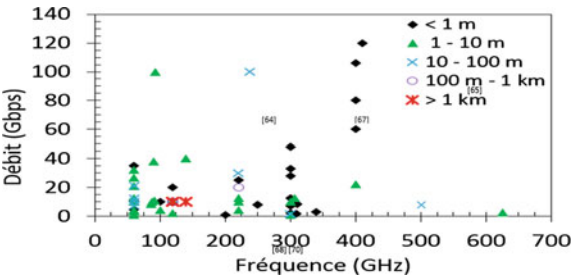

Fig. 3 Report on non-wireless communications operating in the 60 GHz–1 THZ frequency range for data transfer rates above 1 Gigabit

objectives can be estimated as 0.5 to 20 m. Figure 3 shows the results obtained in the field of wireless communications, at a frequency of 60 to 1 THz.

The main link network is essentially made up of non-wireless communications covering a larger area of more than a hundred meters and allowing for large transmission flows with considerable data rates. The progressive development of this type of grid consists in compensating for the change from microwave fireplaces to higher frequency fireplaces. In a more distant future, and to meet the data and information flow needs of users, we must consider a progressive evolution of the technology, particularly in the direction of terahertz frequencies and sources. Scientific research reports high performances reaching 10 Gbps at 120 and 140 GHz for distances between 5.8 and 1.5 km [23].

3 Terahertz Radiation Sources

THz waves can be generated from different types of sources. We will describe here the main ones:

- There are thermal sources that are based on black body radiation. The latter emits in the THz range at a very low intensity from 2 K [24]. For example, a mercury lamp has a spectrum extending over the entire THz range. However, its energy is low and the waves generated are incoherent.
- Electronic sources such as Gunn diodes, high-frequency transistors, and frequency multipliers allow the generation of a monochromatic wave up to 1 THz. We also note the existence of Backward Wave Oscillators (BWO), allowing to generate coherent fixed radiation of up to 2 THz.
- Quantum cascade lasers, based on inter-subband transitions in semiconductor quantum wells, allow the generation of monochromatic waves in the THz domain whose frequency depends on the semiconductor structure. The efficiency of these lasers is of the order of 10^{-5}, for generated powers of the order of a few milliwatts, and their tunability, which ranges from 1.2 to 4.9 THz [25], depends on the structure of the semiconductor used. It should be noted that the design of a quantum cascade laser relies on the dimensions of the wells, which must have nanometric precision. This precision must be even finer for THz generation because the

inter-subband transition is made between two states very close in energy. Therefore, the population inversion between the two sub-bands is very complicated to realize experimentally. The same is true for tunability. Finally, quantum cascade lasers generally operate at low temperatures [26], which limit their use for certain applications.

- Gas lasers also allow the generation of a THz wave by optical pumping of gas molecules. The latter presents a strong rotational transition in the THz domain so that a laser transition between two vibrational levels and the emission of a photon in the THz domain is possible. The most commonly used gases are CH_3F, CH_3OH, NH_3, COOH, and CH_2F_2 [24]. They are commercially available. The best efficiencies obtained with optically pumped gas lasers are of the order of 10^{-2}–10^{-3}, for generated powers of the order of 100 mW. Their emission can range from 0.1 to 8 THz; each gas has its emission line. Gas lasers have three major drawbacks. First, no tunability is possible because the generated spectrum depends on the intrinsic properties of the gas used. Second, optical pumping must be done at high wavelengths, around 9–11 μm, to excite the rotational energy levels [24]. Finally, the combination of a pump laser and a gaseous amplifying medium makes gas lasers very bulky sources.
- Optoelectronic sources are currently the most widely used for the generation of a THz wave. It is a photo computer, also called "THz antenna". It consists of two metallic electrodes separated by a few tens of microns and deposited on a semiconductor substrate, as described in Fig. 4a [24]. The emission is based on a DC bias current applied across the electrodes, so that the antenna behaves like a capacitor in the circuit shown in Fig. 4b. An ultrashort infrared pulse, 20–200 fs,

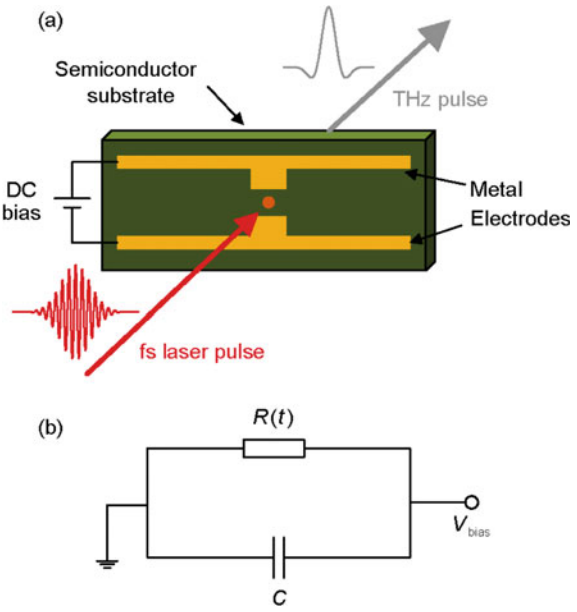

Fig. 4 Schematic of a THz antenna (**a**) and equivalent RC circuit (**b**) [24]

focused between the two electrodes closes the circuit for a short time. The sudden change of polarization current leads to the generation of THz radiation. An antenna generates a THz wave with a very broad spectrum, which can extend from 0.1 to 5 THz if very short femtosecond pulses are used. This results from the fact that a bias current is applied across the antenna electrodes, during the duration _t of the laser pulse. The shorter _t is, the wider the spectrum is, another important parameter is the carrier lifetime of the semiconductor used. The best conversion efficiencies are obtained in the laboratory with THz antennas; they are of the order of 10^{-2} [27].

- Finally, some sources generate a THz wave from a quadratic Frequency Difference Generation (FDG) process in a nonlinear crystal. Two visible or infrared laser optical fields create an induced polarization that generates a coherent electromagnetic wave in the THz domain. These sources are called "parametric sources". The maximum powers of these sources depend in part on the value of the optical damage threshold of the crystal. Two configurations are possible depending on whether the DFG is produced between two monochromatic laser pulses in the nanosecond regime or between two Fourier components within the same femtosecond laser pulse. In the first configuration, the THz source is monochromatic, in the second it is polychromatic.

4 Application

A. Procedure for designing a microstrip patch antenna

For the design of a microstrip patch antenna, we follow the following procedure. Firstly we choose the material needed for the printing that is to say the substrate in this document, we choose the Rubber_hard substrate with permittivity $\varepsilon r = 3$ and its height ($h = 0.\ 1$ mm). Indeed the height of the substrate has a very important role concerning the general characteristics of microstrip antennas, the formula used to determine the maximum value of the substrate height has been established by the relationship of [28, 29]. In the second step, we determine the dimensions of the radiated element (patch) its width and length. In the third step, we also calculate the dimensions of the ground plane, and finally, we choose the type of power supply in this work we use the power supply by micro ribbon line, applying the formulas of [28] at 120 GHz.

$$E_s \leq \frac{0.3c}{2\pi f_{\text{res}}\sqrt{\varepsilon_r}} \tag{1}$$

$$W_p = \frac{c}{2f_{\text{res}}}\sqrt{\frac{2}{\varepsilon_r + 1}} = \frac{\lambda}{2}\sqrt{\frac{2}{\varepsilon_r + 1}}$$

$$\varepsilon_{\text{eff}} = \frac{\varepsilon_r + 1}{2} + \frac{\varepsilon_r + 1}{2}\left(1 + 12\frac{E_s}{W_p}\right)^{\frac{-1}{2}} \tag{2}$$

$$L_{\text{eff}} = \frac{c}{2f_{\text{res}}}\varepsilon_{\text{eff}}^{-\frac{1}{2}} \tag{3}$$

$$\Delta L_p = 0.412\frac{(\varepsilon_{\text{eff}} + 0.3)\left(\frac{W_p}{E_s} + 0.264\right)}{(\varepsilon_{\text{eff}} - 0.258)\left(\frac{W_p}{E_s} + 0.8\right)} \tag{4}$$

$$L_p = L_{\text{eff}} - 2\Delta L_p = \frac{c}{2f_{\text{res}}\sqrt{\varepsilon_{\text{eff}}}} - 2\Delta L_p \tag{5}$$

$$W_g = W_p + 6E_s \text{ and } L_g = L_p + 6E_S \tag{6}$$

$$W_{\text{fed}} = \frac{2h}{\pi}\left[B - 1 - \ln(2B - 1) + \frac{\varepsilon_r - 1}{2\varepsilon_r}(\ln(B - 1) + 0.39 - \frac{0.61}{\varepsilon_r})\right] \tag{7}$$

$$B = \frac{60\pi^2}{z_c\sqrt{\varepsilon_r}} \tag{8}$$

$$L_{\text{fed}} = 3h,\ \text{Z}_{\text{C}} = 50\ \Omega \tag{9}$$

$$|S_{11}|^2 = \frac{|Z_e - Z_c|^2}{|Z_e + Z_c|^2} \tag{10}$$

- E_s: the thickness of the substrate
- C: speed of light such that $c = 3 \times 108$ m/s
- f_{res}: resonance frequency
- ε_r: dielectric constant
- W_P: width of the patch
- L_p: length of the patch
- ε_{eff}: effective dielectric constant
- ΔL_p: the extension of the patch length
- L_g: the length of the ground plane
- W_g: width of the ground plane
- W_{fed}: the width of the feed line
- L_{fed}: the length of the feeder line
- S_{11}: return loss

The formulas in the above table were used to obtain the values of the different parameters that are presented in Table 3, that is to say, the overall sizes of the considered device. Figure 5 illustrates the structure obtained after calculating the dimensions of the various components of this antenna. The results obtained are used

Table 3 The parameters of the proposed antenna

Parameters	Values (cm)
L_g	0.2
W_g	0.22
H	0.01
W_p	0.09
L_p	0.07
L_{fed}	0.093
W_{fed}	0.028
Y_0	0.071
Y_1	0.056
L_f	0.01
W_f	0.04

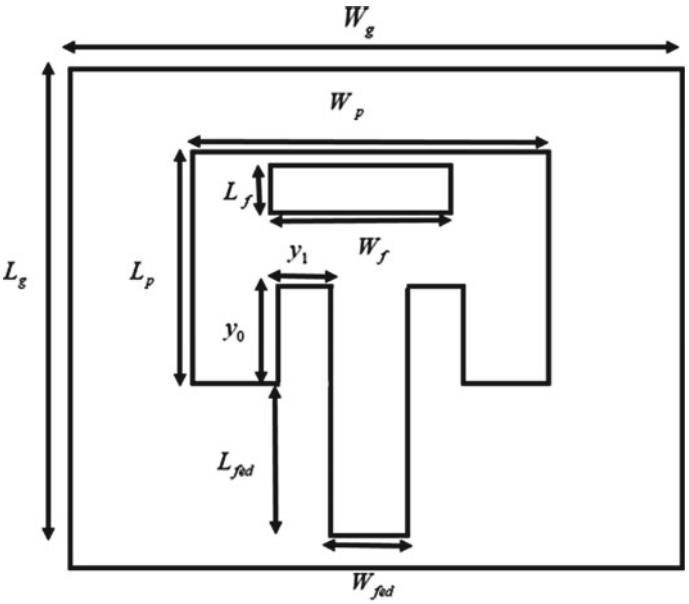

Fig. 5 Geometry of this proposed antenna

here to enhance the overall characteristics of this antenna, especially concerning its bandwidth and size reduction.

B. **Results of the simulations and discussions**

Figure 6 illustrates the result of the simulation of the reflection coefficient curve associated with the proposed antenna. This reflection coefficient S11 is used to check the matching properties provided by the antenna with a load or with a power cable.

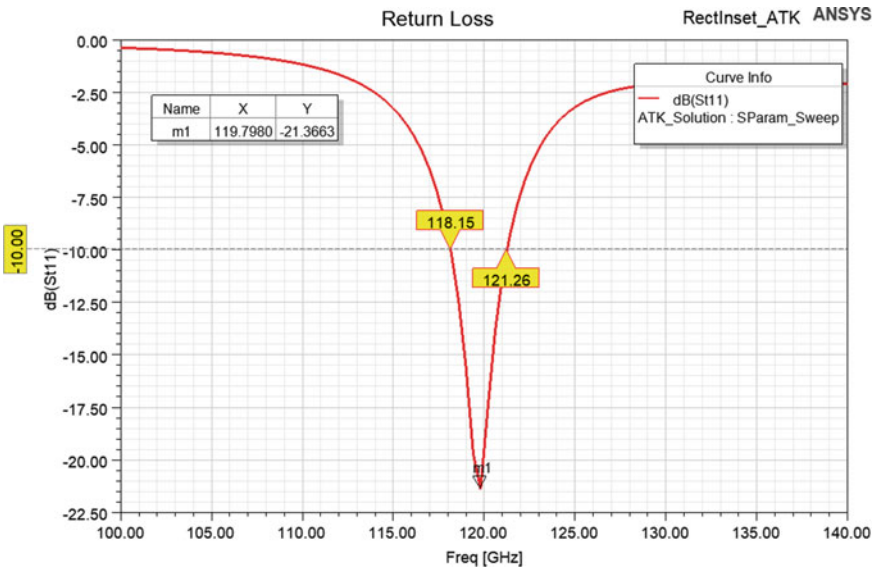

Fig. 6 Diagram of S11

The latter is related to both the input impedance Ze and that associated with the antenna load Zc. Its value is expressed in dB and is constantly negative. It simply corresponds to the relationship existing at the entry port. This relationship consists of the relationship between the reflected power and the incident power. Moreover, if the value of the reflection coefficient S11 < −10 dB it means that the exciting power is transmitted at 90%, which is the case of the designed antenna.

This antenna resonates at 119.79 GHz, with a reflection coefficient (S11) lower than minus 10 dB in the whole resonant frequency range, a bandwidth of 3.11 GHz, a gain of 7.9 dB. These results are validated by simulating the voltage standing wave ratio (VSWR) using the HFSS tool (see Fig. 7). The VSWR reflects the presence of standing waves in the transport cable attached to the electronic system in this case, namely an antenna. The VSWR is therefore obtained directly from the reflection coefficient. The standing wave ratio results from the phenomenon of reflection of a significant amount of the energy produced. This SWR must have a value between 1 and 2 within the bandwidth. Indeed this ratio must tend toward 1 when we want to maximize the power transmission of the antenna. As shown in Fig. 7 at the operating frequency of this antenna, we obtain the value of this SWR of 1.18.

The radiation pattern is a curve describing the radiation properties of antennas as a function of variations (θ, φ), that is to say in the polar plane. This radiation pattern can be in two-dimensional or three-dimensional form and is usually defined in the far field. The gain $G(\theta, \varphi)$, as well as the directivity, is parameters very close to each other, moreover, there is a related relationship between them, this one allows to determine the total efficiency of the antenna as $G(\theta, \varphi) = \eta D\ (\theta, \varphi)$ where η is the efficiency of the antenna, taking into account the losses in the conductors and

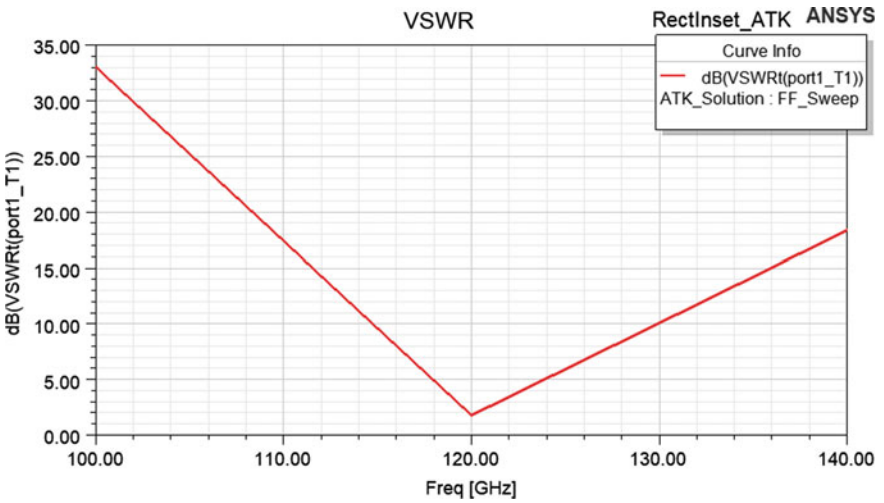

Fig. 7 Diagram of VSWR

dielectrics as well as the mismatch losses. Figure 8 shows the three-dimensional and two-dimensional gain patterns at 120 GHz for this examined microstrip patch antenna.

C. Comparison of the results of this work with those obtained in the available literature

In this section, we will compare the electrical performance of antennas in the terahertz frequency band, such as directivity, gain, reflection coefficient, VSWR, bandwidth, and efficiency of the proposed terahertz antenna with various existing works. The antenna [35] has a better reflection coefficient, VSWR, and bandwidth than the other papers, that is to say, the antennas [30–34] as well as the proposed antenna, as shown in Table 4. Antenna [31] has a very high bandwidth compared to antenna [30, 32–34], but its performance, such as gain and reflection coefficient, is low compared to

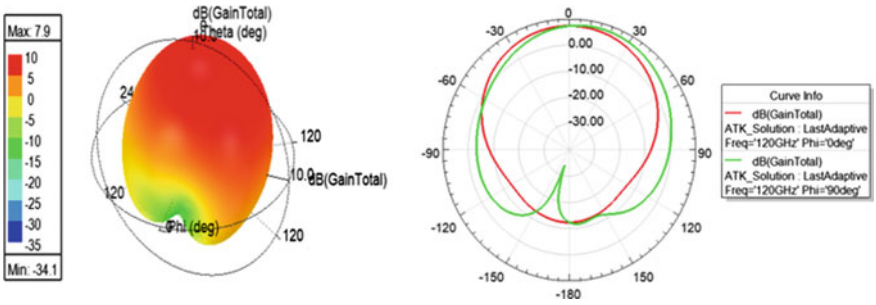

Fig. 8 The 3D and 2D gain pattern of this antenna suggests

Table 4 Comparison of the result of this antenna with the existing result

Refs.	Frequency band (GHz)	Directivity (dB)	VSWR	S11 (dB)	gain (dB)	Bandwidth (GHz)	Efficiency (%)
[30]	150–500	–	–	−16.23	5.17	2.2	–
[31]	960	–	1.3	−13.05	3.8	310	–
[32]	2.7	6.91	1.524	−13.66	6.59	90	92.9
[33]	0.750	5.71	–	−35	5.09	–	86.58
[34]	2.59	7.19	–	−35.183	5.03	–	60.8
[35]	6.994	7.408	1.0003	−75.66	7.286	386	97.21
Proposed	120	–	1.18	−21.36	7.9	3.11	99.5

antenna [30, 32–34]. Thus antenna [34] has a smaller efficiency than antenna [32, 33, 35] and the proposed antenna but offers a much better reflection coefficient than antenna [30–33] and the proposed antenna. While the proposed antenna achieves better results than the other antennas especially in terms of gain and efficiency. In addition, this antenna has a better reflection coefficient compared to antennas [31, 32] and its bandwidth is higher than that of the antenna [30] as shown in Table 4.

5 Conclusion

In this chapter, we present research concerning the THz frequency domain (more than 100 GHz) as well as applications related to terahertz frequencies and terahertz radiation sources. We design a two-slot microstrip patch antenna for the terahertz domain with an operating frequency of 120 GHz. In this chapter, we used the simulation software HFSS (High-Frequency Structure Simulator). The results obtained with this proposed antenna are remarkable with a small and compact size.

The simulation results obtained in this paper are reflection coefficient S11 = −21.36 dB, the bandwidth of 3.11 GHz (from 185.15 GHz to 121.26 GHz), standing wave ratio VSWR = 1.18, the gain of 7.9 dB, and efficiency of 99.5%. This antenna applies to the terahertz frequency range.

References

1. D. Guillaume, S. Pascal, P. Fabio, P. Emilien, Z. Mohammed, B. Denis, B. Alexandre, A. Tahsin, L. Jean-François, L. Jean-François, THz communications using photonics and electronic devices: the race to data-rate. J. Infrared, Millimeter TeraHertz Waves **36**, 198–220 (2015)
2. J. Valdamis, G. Mourou, C. Gabel, Subpicosecond electrical sampling. IEEE J. Quantum Electron. **19**(4), 664–667 (1983)

3. E. Martin van, C.H. Fattinger, D. Grischkowsky, Terahertz time-domain spectroscopy of water vapor. Opt. Lett. **14**(20), 1128–1130 (1989)
4. H.-B. Liu, Y. Chen, X.-C. Zhang, Characterization of anhydrous and hydrated pharmaceutical materials with THz time-domain spectroscopy. J. Pharm. Sci. **96**(4), 927–934 (2007)
5. Y.C. Shen, T. Lo, P.F. Taday, B.E. Cole, W.R. Tribe, M.C. Kemp, Detection and identification of explosives using terahertz pulsed spectrocopic imaging. Appl. Phys. Lett. **86**(241116), 1–3 (2005)
6. O. Frank, Z. Wissem, B. Rene, M. Carsten, J. Joachim, R. Benoit, G. Jean-Paul, M. Patrick, V. Wouter, B. Pablo Venegas, G. Laura Vega, L. Ion, E. Rafael Martinez, S. Yehuda, V. Marijke, Aeronautics composite material inspection with a terahertz time-domain spectroscopy system. Opt. Eng. 53(3), 1–14, 031208 (2014)
7. P. Jae Yeon, C. Hyuck Jae, N. Gi-Eun, C. Kyoung-Sik, S. Joo-Hiuk, In vivo dual-modality terahertz/magnetic resonance imaging using superparamagnetic iron oxide nanoparticles as a dual contrast agent. IEEE Trans. Terahertz Sci. Technol. **2**(1), 93–98 (2011)
8. J.-P. Guillet, M. Roux, K. Wang, X. Ma, F. Fauquet, H. Balacey, B. Recur, F. Darracq, P. Mounaix. Art painting diagnostic before restoration with terahertz and millimeter waves. J. Infrared, Millimetre TeraHertz Waves 38(4) (2017)
9. B.B. Hu, M.C. Nuss, Imaging with terahertz waves. Opt. Lett. OL **20**(16), 1716–1718 (1995)
10. G. Yuan, Z. Reza, Millimeter wave reflectometry and imaging for noninvasive diagnosis of skin burn injuries. IEEE Trans. Instrum. Measur. **66**(1), 77–84 (2017)
11. J.S. Karsten et al., All-optoelectronic continuous-wave THz imaging for biomedical applications. Phys. Med. Biol. **47**(21), 3743 (2002)
12. G.G. Hernandez-Cardoso et al, Terahertz imaging for early screening of diabetic foot syndrome: a proof of concept. Sci Rep **7**, févr (2017)
13. D. Pallavi, A. Karim, C.S. Joseph, R.H. Giles, Terahertz polarization imaging for colon cancer detection. in *Millimeter, and Submillimeter-Wave Technology and Applications VII* ed by, R.F Terahertz, **8985**, 89850K (2014)
14. B. Tyler, C. Tanny, K. Kamrul, W. Jingxian, C. Avishek, R. Narasimhan, B. Keith, O.E. Magda, Pulsed terahertz imaging of breast cancer in freshly excised murine tumors. JBO, JBOPFO, **23**(2), 026004, févr (2018)
15. M.G. Thomas, C.D. Jason, W. Jerry, E.N. William, 1.56-THz compact radar range for W-band imagery of scale-model tactical targets. *Algorithms Synthetic Aperture Radar Imagery VII* **4053**, 615–623 (2000)
16. O.A. Maryam, M.S. Raed, R.R. Nadeen, A. Ghadah, Terahertz spectroscopy and imaging for the detection and identification of illicit drugs. 2017 Sens. Netw. Smart Emerg. Technol. (SENSET) 1–4 (2017)
17. H.J. Shin, M.-C. Lim, K. Park, S.-H. Kim, S.-W. Choi, G. Ok, Invisible security printing on photoresist polymer readable by terahertz spectroscopy. Sensors **17**(12), 2825, déc (2017)
18. B.J. Puttnam et al., 2.15 Pb/s transmission using a 22 core homogeneous single-mode multi-core fibre and wideband optical comb. in *2015 European Conference on Optical Communication (ECOC)*, 1–3 (2015)
19. A.S. Gustavo, R. Jose Manuel, G.P. Padro, Atmospheric attenuation in wireless communication systems at millimeter and THz frequencies [wireless corner]. IEEE Antennas Propag. Mag. **57**(1), 48–61, févr (2015)
20. G. Thierry Le, M. Pierre-Marie, A 45-GHz wireless transmission for a wireless interconnect network-on-board. in *2017 IEEE 21st Workshop on Signal and Power Integrity (SPI)*, 1–2 (2017)
21. P. Vitaly, K. Joonas, M. Dmitri, L. Janne, K. Yevgeni, J. Markku, Last meter indoor terahertz wireless access: performance insights and implementation roadmap. arXiv:1708.02963 [cs], août (2017)
22. S. Koenig et al., Wireless sub-THz communication system with high data rate. Nature Photonics **7**(12), 977–981 (2013)
23. W. Cheng, L. Changxing, C. Qi, L. Bin, D. Xianjin, Z. Jian, A 10-Gbit/s wireless communication link using 16-QAM modulation in 140-GHz band. IEEE Trans. Microwave Theory Tech. **61**(7), 2737–2746 (2013)

24. K. Zhong, W. Shi, D. Xu, P. Liu, Y. Wang, J. Mei, C. Yan, S. Fu, J. Yao, Optically pumped terahertz sources. Sci. China Technol. Sci. **60**(12), 1801–1818 (2017)
25. S.V. Miriam, S. Giacomo, W. Benjamin, D.N. Paolo, Quantum cascade lasers: 20 years of challenges. Optics Express **23**(4), 5167–5182 (2015)
26. B. Mikhail, C. Federico, New frontiers in quantum cascade lasers: high-performance room temperature terahertz sources. Phys. Scripts **90**(118002), 1–13 (2015)
27. Y. Shang-Hua, R.H. Mohammad, W.B. Christopher, J. Mona, 7.5photoconductive emitters with three-dimensional plasmonic contact electrodes. IEEE Trans. Terahertz Sci. Technol. **4**(5), 575–581 (2014)
28. D. Salah-Eddine, H. Imane, F. Mohammed, B. Younes, M. Said, E. Moulhime, Design of a microstrip antenna two-slot for fifth generation applications operating at 27.5 GHz. in *Springer International Conference on Digital Technologies and Applications(ICDTA), Lecture Notes in Networks and Systems, Fes, Morocco* **211**, 1081–1089 (2021)
29. E. Abdelhafid, A. Maryam, F. Mohammed, M. Said, E. Moulhime, A 5G mm-wave compact voltage-controlled oscillator in 0.25 μm pHEMT technology. Int. J. Electr. Comput. Eng. (IJECE) 11(2), 1036–1042 (2021)
30. R. Bhatoa, E. Sidhu, Novel terahertz microstrip patch antenna design for detection of biotin applications, in *2017 International Conference on Big Data Analytics and Computational Intelligence (ICBDAC)* (2017), pp. 289–292
31. A. Singh, S. Singh, A trapezoidal microstrip patch antenna on photonic crystal substrate for high-speed THz applications. Photonics Nanostruct. Fundam. Appl **14**, 52–62 (2015)
32. R. Bala, A. Marwaha (2015) Development of computational model for tunable characteristics of graphene-based triangular patch antenna in THz regime. Springer J. Computat. Electr. ISSN : 1569–8025, indexed by SCI, Thomson Reuter Journal list, Impact Factor 1.520, https://doi.org/10.1007/s10825- 015-0761-6, Print ISSN 1569-8025, Online ISSN 1572-8137, pp 1.6, online 2015
33. S.S. Anand, D.S. Kumar, R.J. Wu, M. Chavali, Graphene nanoribbon based terahertz antenna on polyimide substrate, Optik. Sci. Direct **125**, 5546–5549 (2014)
34. S. Mrunalini, A. Manoharan, Dual-band re-configurable graphene-based patch antenna in terahertz band for wireless network-on-chip applications. IET Microwaves, Antennas Propag. **11**(14), 2104–2108 (2017). https://doi.org/10.1049/iet-map.2017.0415
35. M.A.K. Khan, M.I. Ullah, R. Kabir et al., High-performance graphene patch antenna with superstrate cover for terahertz band application. Plasmonics **15**, 1719–1727 (2020). https://doi.org/10.1007/s11468-020-01200-z

Development of Dissimilar-Shaped 8-Patch Massive MIMO Antenna for Various Application with Enhancement of Bandwidth and ECC

Shrenik S. Sarade and S. D. Ruikar

Abstract In this paper, a compact closely spaced multiband wideband dissimilar eight-elements massive MIMO antenna with inset feed are developed. This antenna is useful for 5G-band n77, Wi-MAX, WLAN and C-band application. This antenna contains 8-dissimilar radiating elements that are designed for different frequency, which are 2.54 GHz, 3.45 GHz and 6 GHz which are optimized using the rectangular shaped with transmission line model. The rectangular shaped cut slots are introduced in the radiating elements for multiband operation. This antenna have designed using FR-4 substrate with permittivity 4.4 and height 1.6 mm. This antenna has radiates multiband frequency. A rectangular-shaped defected ground structure have been used for the improvement of the mutual coupling between the radiating patch. The evaluation of antenna shows that, −10 dB isolation, −10.98 dB total active reflection coefficients, 0.00093 correlation coefficients and 0.00000086 envelope correlation coefficients are achieved for all radiating bands. The antenna is working on wide band, having bandwidth greater than 182 MHz (3.02%) for respective operating bands.

Keywords MIMO · TARC · ECC · CC · RL

1 Introduction

In wireless communication technology, there is requirement of high data rate and reliability for the rapid outgrowth of users. The MIMO antenna system (MAS) has provided the better channel capacity and reliability. The MAS has contains, multiple antennas at transmitter and receiver side to enhance the data rate. Meanwhile, the design of wireless systems is requires the antenna to radiate on multiple frequency band.

In MIMO antenna, the radiating elements are closely placed; therefore, enhancing the isolation between the radiating elements is critical. Due to high isolation, the performance of antenna was reduced. In recent years, the researcher has investigated

S. S. Sarade (✉) · S. D. Ruikar
WCE, Sangli, Maharasthra, India

M. El Ghzaoui et al. (eds.), *Terahertz Wireless Communication Components and System Technologies*, https://doi.org/10.1007/978-981-16-9182-9_13

the techniques to enhancements of isolation parameters. In paper [1–3], the isolation parameter is enhanced using the decoupling structure (DS). This DS decouples the input parts of closely spaced antenna. The decoupling network is used with matching network for proper matching of input port. In paper [4–7], the different-shaped structure cut slot is provided in the ground plane for improvement of isolation that is called as DGS techniques. The mutual coupling (MC) has reduced using the defects within the ground. This defect is acts as band reject filter, that reduces MC between the radiating elements. This technique effects the parameters like capacitance, inductance and dielectric constant of microstrip line.

The paper [8] researcher has used electromagnetics bandgap (EBG) for improvement of mutual coupling between the radiating elements. In paper [9], the metamaterial technique is used for the improvement of mutual coupling between the radiating methods. The neutralization line (NL) [10, 11] is used for enhancement of mutual coupling. In these techniques, the current is taken from a specific location of the radiating elements and then inverts the phase of current using the length of NL, then fed this inverted current to a nearby antenna. The MC between the RPE is reduced using the parasitic structure (PS) [12, 13]. This PS are cancel the couple field between the elements. This PS has created the opposite electric field that reduces the original fields and thus reduces the MC between the RPE. The traditional methods are used for enhancements of isolation [14].

In this paper, the dissimilar-shaped 8-elements massive MAS is designed for various application. The 8-elements of antenna are designed for different frequency, which are 2.54, 3.45 and 6 GHz. The antenna geometry structure is designed using the transmission line model (TLM). The 8-elements are energized using inset feed methods. The DGS techniques are used for the enhancements of isolation, correlation coefficients (CC) and envelope correlation coefficients (ECC). In wireless technology, the antenna is operated on single band or dual band, therefore the size, weight and cost of devices are high. However, today's wireless technologies demand the antenna, which operates on the multiband frequencies. Because, the wireless technology having characteristics like size, weight and cost reduces rapidly. Therefore, there is requirement of design antenna having size, weight and cost is less with radiating on different frequency band (multiband).

2 Massive MIMO antenna system(MAS) Design

The massive MAS as shown in Fig. 1 is investigated for multiband wideband operation of various application. This is consists of 8-different-structured radiating patch (RP). The RPs are designed for different frequency, which are 2.54 GHz, 3.45 GHz and 6 GHz as shown in Table 1. The RP-1 and RP-3 is optimized for 2.54 GHz; RP-2 and RP-4 is optimized for 3.45 GHz; and RP-5, RP-6, RP-7 and RP-8 have optimized for 6 GHz frequency.

The geometrical structure (GS) i.e. W_{rp}, L_{rp}, W_{pf} and L_{pf} of 8-different-shaped elements are calculated for 2.54 GHz, 3.45 GHZ and 6 GHz frequency are as shown

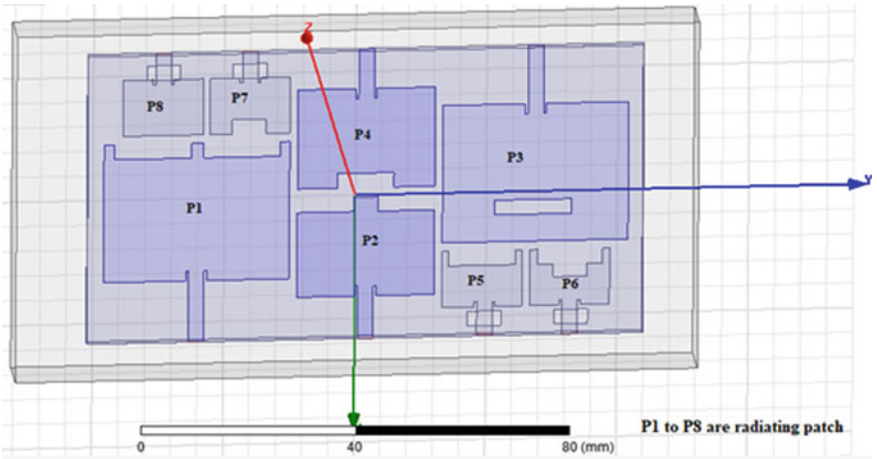

Fig. 1 8-different structured radiating patch (RP) of massive MAS

Table. 1 Radiating patches designed for different frequency

Sr. No.	Patch name	Patch designed frequency (GHz)
1	RP-5 (P5), RP-6 (P6), RP-7 (P7) and RP-8 (P8)	6
2	RP-2 (P2) and RP-4 (P4)	3.45
3	RP-1 (P1) and RP-3 (P3)	2.54

in Table 2 using rectangular-shaped transmission line model (TLM) Eqs. 1 to 5. The FR4 substrate is used for designing of antenna having characteristics shown in Table 3.

Table 2 The geometrical structure of RP for different frequency

Parameter	Values of parameter		
Frequency (*fd*)	2.54 GHz	3.45 GHz	6 GHz
*W*rp	*W*rp2 = 35.40 mm	*W*rp3 = 26.16 mm	*W*rp1 = 15.21 mm
*L*rp	*L*rp2 = 27.82 mm	*L*rp3 = 20.07 mm	*L*rp1 = 11.34 mm
*W*pf	*W*pf3 = 2.95 mm	*W*pf2 = 2.88 mm	*W*pf1 = 2.942 mm
*L*pf	*L*pf3 = 14.64 mm	*L*pf2 = 10.76 mm	*L*pf1 = 6.387 mm

Table. 3 Characteristics of substrate

Sr. No.	Parameter	Values
1	Height (hs)	1.6 mm
2	Dielectric Constant (DC) (ε0s)	4.4

The different rectangular cut slot i.e. A, B, C, D, E, F, G and H are introduced in the RPs as shown in Figs. 1 and 2. The dimensions of rectangular cut slot are as shown in Table 4. In patch-1, the two rectangular-shaped cut slot (CS) is provided at the upper edge, having dimensions are width 'A' and length 'B'. In patch-2, the two rectangular-shaped cut slot is provided at the upper edge, having dimensions are width 'G' and length 'H'. In patch-3, the one rectangular-shaped cut slot is provided, having dimensions are width 'A' and length 'B'. In patch-4, the one rectangular-shaped cut slot is provided, having dimensions are width 'G' and length 'H'.

In patch-5, the one rectangular-shaped cut slot is provided at the upper edge, having dimensions are width 'E' and length 'D'. In patch 6, the two rectangular-shaped cut slot is provided at the upper edge, in which one slot having dimensions are width 'F' and length 'D'; another slot are width 'C' and length 'D'. In patch-7, the one rectangular-shaped cut slot is provided at the upper edge, having dimensions

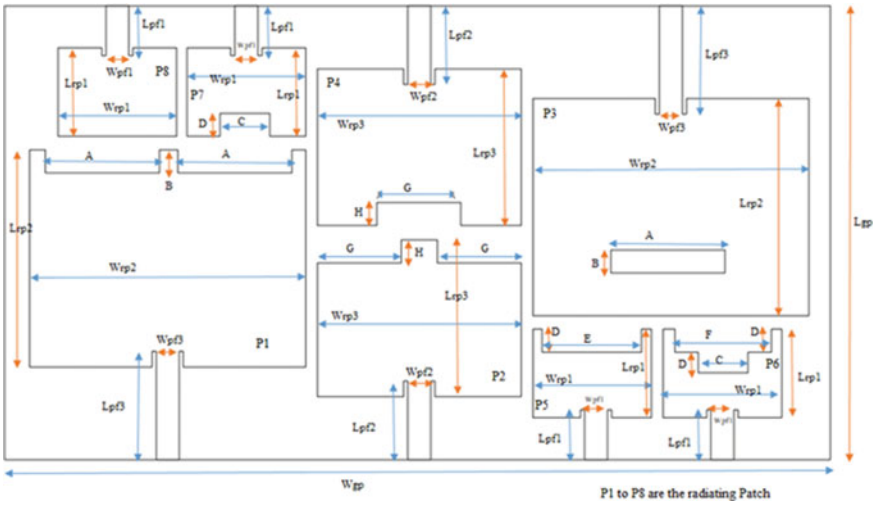

Fig. 2 Massive MAS with dimensions

Table. 4 Dimensions of cut slot in radiating patch

Parameter	Values (mm)
A	14.64
B	2.95
C	6.387
D	2.942
E	12.75
F	12.38
G	10.76
H	2.88

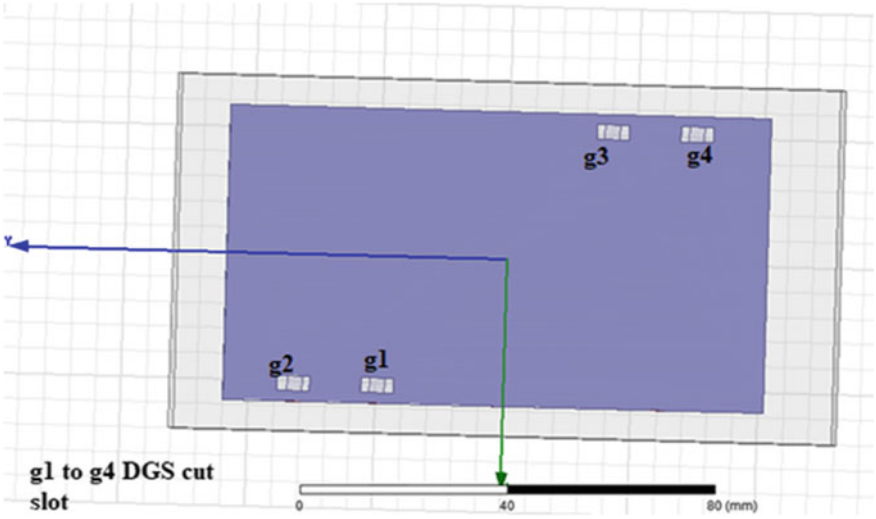

Fig. 3 GP with DGS-CS

are width 'C' and length 'D'. In patch-8, there is no any cut slot. The inset line feed (ILF) is used to apply the RF electrical energy to RP, having dimensions (i.e. W_{pf} and L_{pf}) are calculated using Eqs. 8 to 10 as shown in Table 2

The designed massive MAS structure is 58.16 mm × 105.92 mm × 1.6 mm. The RPs are separated by less than 0.066λ with respect to 6 GHz. This antenna is designed using HFSS software as shown in Fig. 1.

The microstrip patch antenna has limitations i.e. single band frequency, minimum bandwidth, low gain, high isolation and larger size. Therefore, for improvements of above parameter, the DGS techniques are used.

The DGS has been introduced in the ground plane (GP) with the transmission line (TL). A DGS is disturb the current distribution in the GP and changes the characteristics of TL [15].

The GP with dimensions W_{gp} and L_{gp} is calculated using Eqs. 6 to 7 as shown in Fig. 3. The DGS cut slots (CS) of rectangular shape (g1 to g4) are provided in the GP as shown in Fig. 4 and dimensions shown in Table 5. The DGS cut slot (i.e. g1, g2, g3 and g4) having dimensions are width 'C' and length 'D'. The DGS working operation shown in Flow Chart 1.

2.1 Rectangular-Shaped TLM for Radiating Patch

The geometrical structure is calculated using Eqs. 1 to 7.

$$\text{Width } (W_{rp}) = \{[1/2 * f_d * \sqrt{(\mu\varepsilon)}] * [2/\sqrt{(\varepsilon_{0s} + 1)}]\} \quad (1)$$

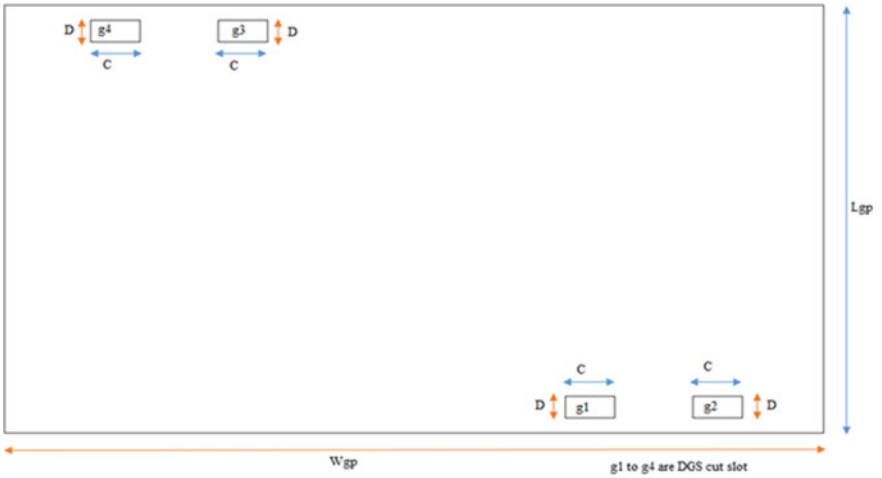

Fig. 4 GP with DGS-CS dimensions

Table. 5 Dimensions of DGS cut slot in ground plane

Parameter	Values in mm
*L*gp	58.16
*W*gp	105.92
Length of DGS (g1 to g4) CS	$D = 2.95$
Width of DGS (g1 to g4) CS	$C = 6.38$

$$L_{\text{change}} = \left\{(4.12/10) * h_s * \left\{\left[(\varepsilon e + (3/10)) * \left((W_{\text{rp}}/h_s) + (2.64/10)\right)\right]/\left[(\varepsilon_e - 0.258) * \left(\left(W_{\text{rp}}/h_s\right) + 0.8\right)\right]\right\}\right\} \quad (2)$$

$$\text{Effective length of RP } (L_e) = L_{\text{rp}} + 2L_{\text{change}} \quad (3)$$

$$\varepsilon_e = \left\{0.5 * \left[(\varepsilon_{0s} + 1) + \left((\varepsilon_{0s} + 1)/\sqrt{(1 + 12 * \left(h_s/W_{\text{rp}}\right))}\right)\right]\right\} \quad (4)$$

where,

W_{rp} = Width of RP
L_{rp} = Width of RP
ε_{0s} = DC of substrate
ε_e = Effective DC

The length (*L*gp) and width (W_{gp}) of GP are computed using the following equation,

$$L_{\text{gp}} = L_{\text{rp}} + 6h_s \quad (5)$$

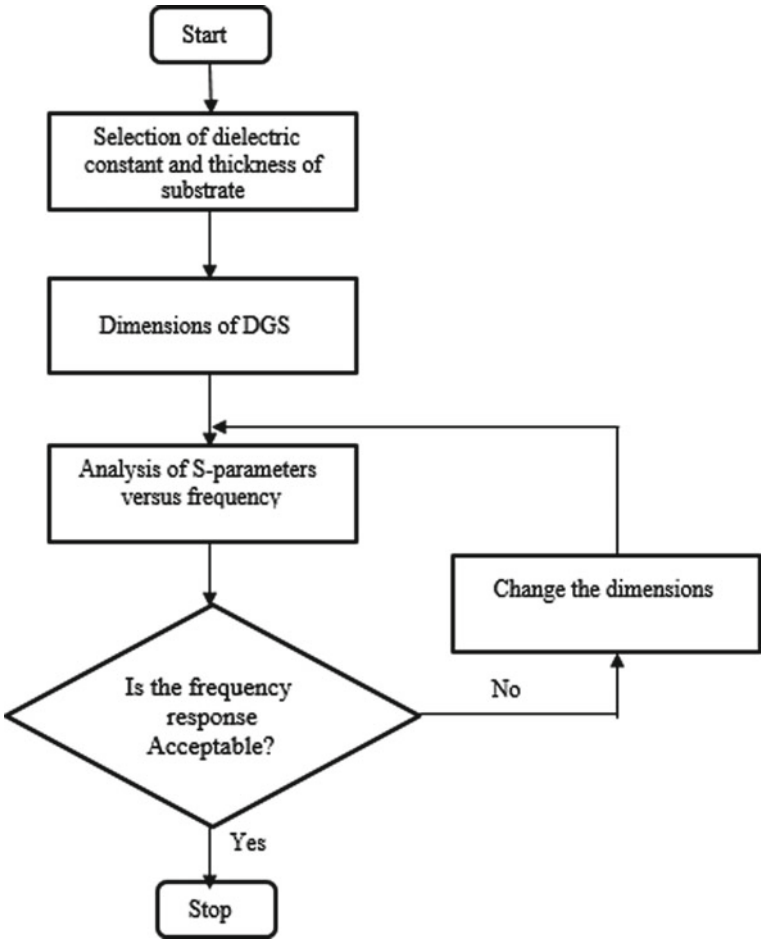

Flow Chart 1 DGS working principle

$$W_{\text{gp}} = W_{\text{rp}} + 6h_s \tag{6}$$

where,

L_{gp} = Length of GP
W_{gp} = Width of GP

The length (L_{pf})length and width (W_{pf}) length for IFL are calculated using the following equation to excite the RPs of antenna.

$$\text{Feed line length } (L_{\text{pf}}) = (\lambda_w/4) \tag{7}$$

$$\text{Guided wavelength } (\lambda_w) = (\lambda_g/4) \tag{8}$$

$$W_{\text{pf}} = \{0.636 * h_s * [(592.19/(Z_0 * \sqrt{(\varepsilon_{0s})}) - -0.7 - -\ln((2 * 377\,\Pi)/ (2 * Z_0 * \sqrt{(\varepsilon_{0s})}) + 1)] + (2 * h_s/\Pi) * [(((\varepsilon_{0s} - 1)/2\,\varepsilon_{0s}) * (\ln[(592.19/(Z_0 * \sqrt{(\varepsilon_{0s})}) - 1]) - - (0.6/\varepsilon_{0s})]\} \tag{9}$$

where,
Characteristics Impedance = $Z0 = 50\ \Omega$

2.2 *Isolation and Bandwidth Improvements*

The isolation or MC is improved, by increasing the distance between the radiating elements, because of that the area of antenna is increases, means compactness of antenna decreases. Therefore, the isolation or MC between the radiating elements is improved using the DGS. Because of DGS, the radiating patches of antenna are placed very close to each other. Therefore, antenna is become compact and isolation has been improved.

The patch antenna has operating on the narrow band. Therefore, there is a requirement to improve the bandwidth [16, 17]. The bandwidth of antenna is improved using DGS.

3 Result Analysis

After simulation of designed massive MAS using high-frequency structure simulator (HFSS), the evaluation of antenna shows that, the RL and isolation in the following figure. This antenna is operated on multiple radiating frequency, which are 3.6 GHz, 3.8 GHz, 4.7 GHz, 4.9 GHz, 5.2 GHz, 5.8 GHz, 6.1 GHz, 6.4 GHz, 6.5 GHz and 6.6 GHz as shown in Figs. 5, 6, 7, 8, 9, 10, 11, 12 and in Tables 6, 7, 8, 9, 10, 11, 12, 13.

The RL of RP-1 to RP-8 and having related isolation as shown in Figs. 5, 6, 7, 8, 9, 10, 11, 12 respectively (Points m1 to m8 show the values on graph). In addition, all values of RL, isolation and bandwidth are shown in Tables 6, 7, 8, 9, 10, 11, 12 and 13, respectively, for radiating frequency.

The simulation of antenna shows less than −10 dB RL and −10 dB isolation. The analysis shows that, bandwidth is in between 182 MHz (3.02%) and 480 MHz (8%). Therefore, this antenna is operated on wide band.

The RL S_{11} and related isolation of RP-1 are shown in Fig. 5 (circle with m1 to m6 shows the point on the graph). The less than −13 dB RL and less than −18 dB isolation are shown in Table 6.

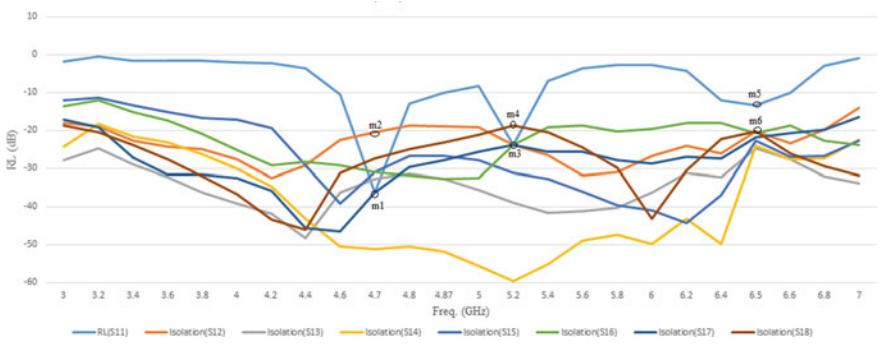

Fig. 5 RL and isolation of patch-1

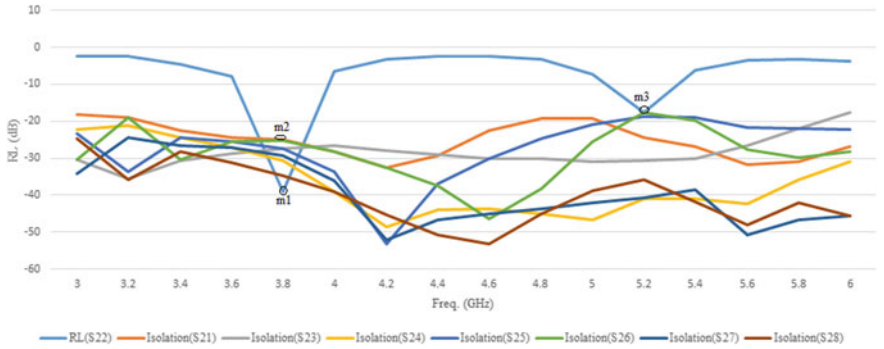

Fig. 6 RL and isolation of patch-2

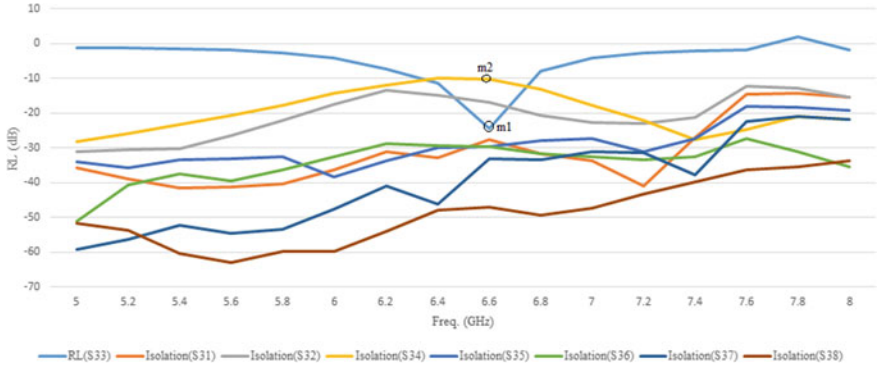

Fig. 7 RL and isolation of patch-3

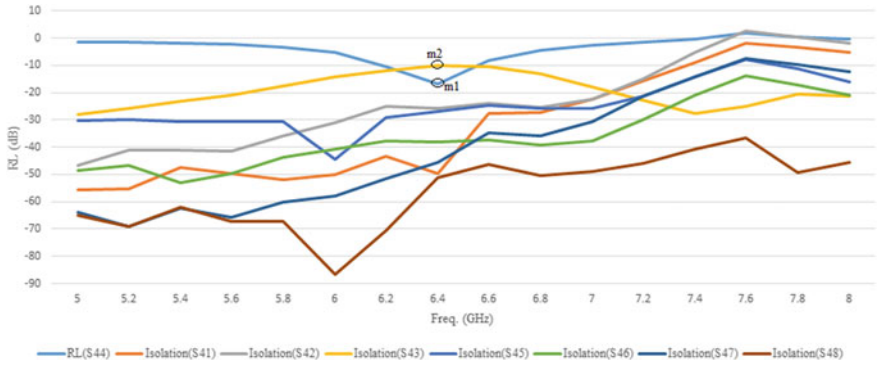

Fig. 8 RL and isolation of patch-4

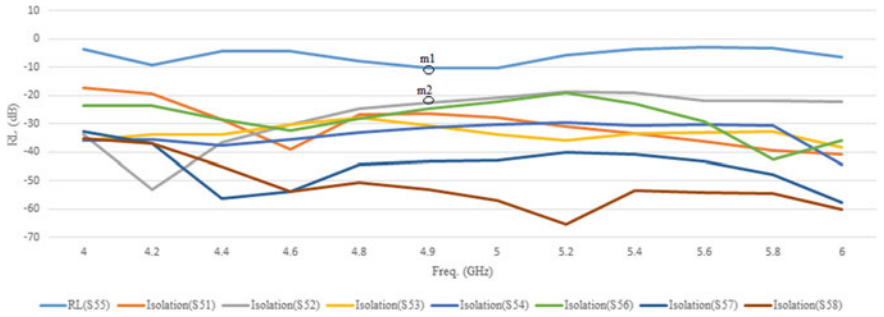

Fig. 9 RL and isolation of patch-5

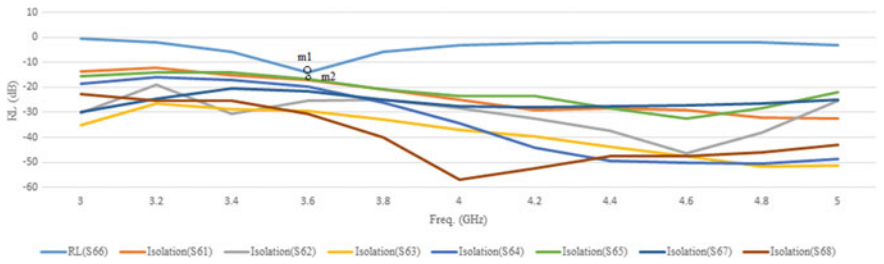

Fig. 10 RL and isolation of patch-6

For good operation of antenna, the standard value defined for RL and isolation is −10 dB. The bandwidth for RP-1 is 342 MHz (5.7%) for resonating at 4.7 GHz, 289 MHz (4.82%) for resonating at 5.2 GHz, 203 MHz (3.39%) for resonating at 6.5 GHz.

Bandwidth is optimized using the Eqs. 14 and 15.

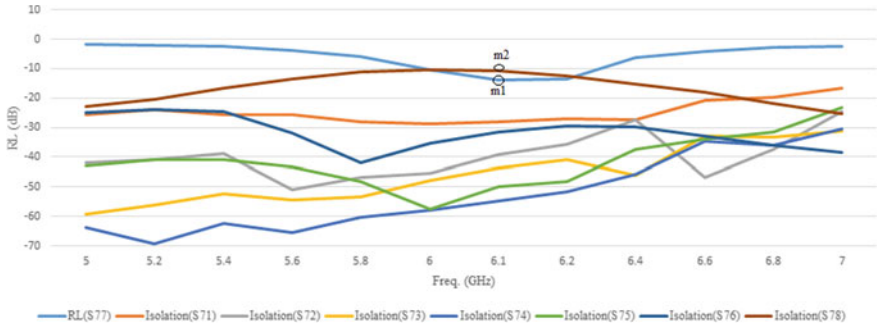

Fig. 11 RL and isolation of patch-7

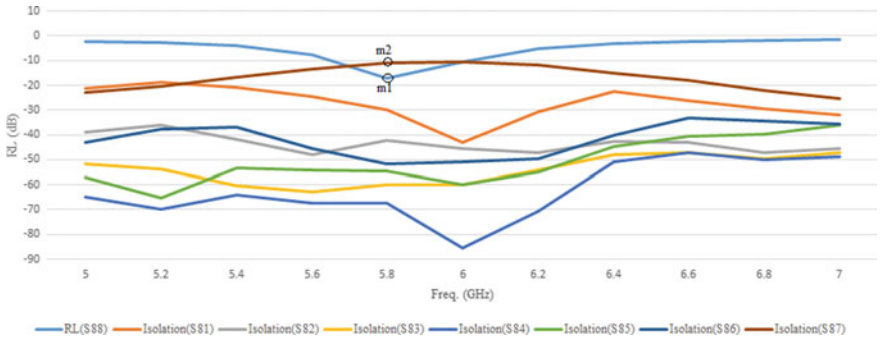

Fig. 12 RL and isolation of patch-8

Table. 6 RL and isolation of patch-1

Parameter	Frequency (GHz)	Values
S11	4.7 (m1), 5.2 (m3) and 6.5 (m5)	−36.29 dB, −23.79 dB and −13.44 dB
S12 (m2), S13, S14, S15, S16, S17 and S18 (m4 and m6)	4.7 (m2), 5.2 (m4) and 6.5 (m6)	less than −20.53 dB, less than −18.80 dB and less than −20.36 dB
Bandwidth	4.7, 5.2 and 6.5	342 MHz (5.7%), 289 MHz (4.82%) and 203 MHz (3.39%)

Table. 7 RL and isolation of patch-2

Parameter	Frequency (GHz)	Values
S22	3.8 (m1) and 5.2 (m3)	−39.13 dB and −17.64 dB
S21 (m2), S23, S24, S25, S26 (m3), S27 and S28	3.8 (m2) and 5.2 (m3)	less than −25.06 dB and less than −17.64 dB
Bandwidth	3.8 and 5.2	329 MHz (5.49%) and 278 MHz (4.64%)

Table. 8 RL and isolation of patch-3

Parameter	Frequency (GHz)	Values
S33 (m1)	6.6	−24.39 dB
S31, S32, S34 (m2), S35, S36, S37 and S38	6.6	less than −10.30 dB
Bandwidth	6.6	366 MHz (6.1%)

Table. 9 RL and isolation of patch-4

Parameter	Frequency (GHz)	Values
S44 (m1)	6.4	−16.86 dB
S41, S42, S43 (m2), S45, S46, S47 and S48	6.4	less than −10.09 dB
Bandwidth	6.4	480 MHz (8%)

Table. 10 RL and isolation of patch-5

Parameter	Frequency (GHz)	Values
S55 (m1)	4.90	−10.31 dB
S51, S52 (m2), S53, S54, S56, S57 and S58	4.90	less than −22.68 dB
Bandwidth	4.90	182 MHz (3.02%)

Table. 11 RL and isolation of patch-6

Parameter	Frequency (GHz)	Values
S66 (m1)	3.6	−13.94 dB
S61, S62, S63, S64, S65 (m2), S67 and S68	3.6	less than −16.49 dB
Bandwidth	3.6	317 MHz (5.28%)

Table. 12 RL and isolation of patch-7

Parameter	Frequency (GHz)	Values
S77 (m1)	6.1	−13.94 dB
S71, S72, S73, S74, S75, S76 and S78 (m2)	6.1	less than −10.82 dB
Bandwidth	6.1	313 MHz (5.21%)

Table. 13 RL and isolation of patch-8

Parameter	Frequency (GHz)	Values
S88 (m1)	5.8	−17.15 dB
S81, S82, S83, S84, S85, S86 and S87 (m2)	5.8	less than −11.10 dB
Bandwidth	5.8	329 (5.47%)

The RL S22 and related isolation of RP-2 are shown in Fig. 6 (m1 to m3 shows the point on the graph). The −17 dB RL and less than −17 dB isolation are shown in Table 7. The bandwidth for patch-1 is 329 MHz (5.49%) for resonating at 3.8 GHz and 278 MHz (4.64%) for resonating at 5.2 GHz.

The RL S_{33} and related isolation of RP-3 are shown in Fig. 7 (m1 to m2 shows the point on the graph). The −24 dB RL and less than −10 dB isolation are shown in Table 8.

The bandwidth for patch-3 is 366 MHz (6.1%) for resonating at 6.6 GHz.

The RL S_{44} and related isolation of RP-4 are shown in Fig. 8 (m1 to m2 shows the point on the graph). The −16 dB RL and less than −10 dB isolation are shown in Table 9. The bandwidth for patch-4 is 480 MHz (8%) for resonating at 6.4 GHz.

The RL S_{55} and related isolation of RP-5 are shown in Fig. 9 (m1 to m2 shows the point on the graph). The −10 dB RL and less than −22 dB isolation are shown in Table 10.

The bandwidth for patch-5 is 182 MHz (3.02%) for resonating at 4.98 GHz.

The RL S_{66} and related isolation of RP-6 are shown in Fig. 10 (m1 to m2 shows the point on the graph). The −13 dB RL and less than −16 dB isolation are shown in Table 11. The bandwidth for patch-6 is 317 MHz (5.28%) for resonating at 3.6 GHz.

The RL S_{77} and related isolation of RP-7 are shown in Fig. 11 (m1 to m2 shows the point on the graph). The −13 dB RL and less than −10 dB isolation are shown in Table 12. The bandwidth for patch-7 is 313 MHz (5.21%) for resonating at 6.1 GHz.

The RL S_{88} and related isolation of RP-8 are shown in Fig. 12 (m1 to m2 shows the point on the graph). The −17 dB RL and less than −11 dB isolation are shown in Table 13.

The bandwidth for patch-8 is 329 MHz (5.47%) for resonating at 5.8 GHz.

The Fig. 13 shows that the voltage standing wave ratio (VSWR) and values of all patches are shown in Table 14. The analysis shows the absolute values of VSWR between 1.04 and 3.52 (Points m1 to m11 shows the values on graph) of a radiating frequency.

The Fig. 14 shows the directivity and radiation pattern of antenna. The directivity of antenna is 1.042 dB as shown in Table 15.

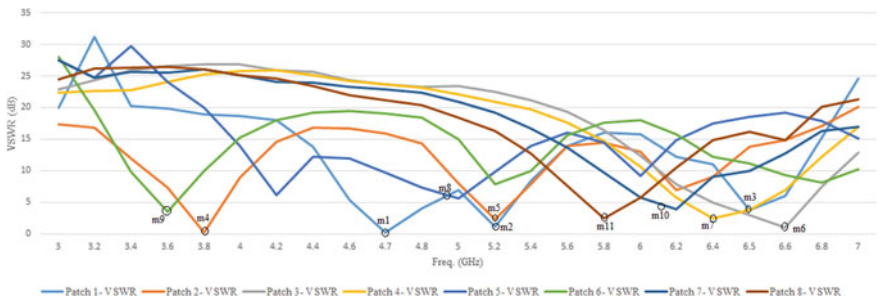

Fig. 13 VSWR

Table 14 VSWR

Parameter	Frequency (GHz)	Values (dB)	Absolute Values
RP-1 VSWR	4.7 (m1), 5.2 (m2) and 6.5 (m3)	0.26, 1.12 and 3.75	1.06, 1.29 and 2.37
RP-2 VSWR	3.8 (m4) and 5.2 (m5)	0.19 and 2.3	1.04 and 1.69
RP-3 VSWR	6.6 GHz (m6)	1.04	1.27
RP-4 VSWR	6.4 GHz (m7)	2.50	1.77
RP-5 VSWR	4.9 GHz (m8)	5.47	3.52
RP-6 VSWR	3.6 GHz (m9)	3.5	2.23
RP-7 VSWR	6.1 GHz (m10)	3.5	2.23
RP-8 VSWR	5.8 GHz (m11)	2.42	1.74

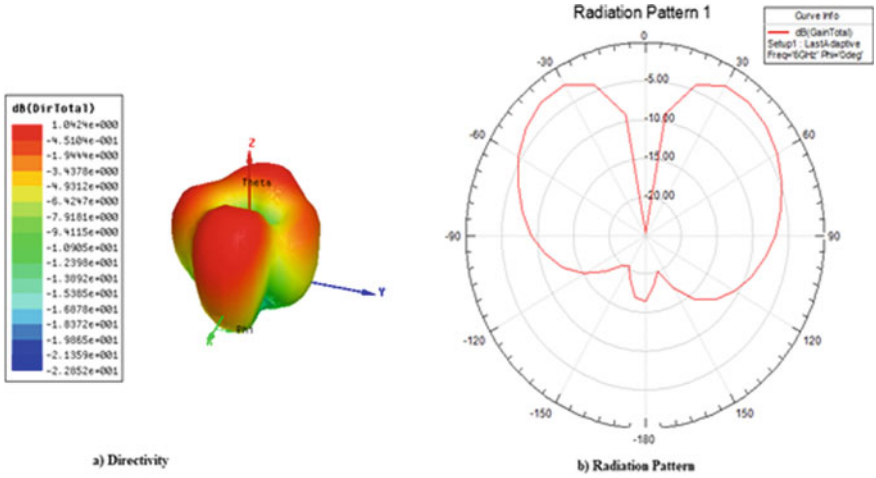

a) Directivity b) Radiation Pattern

Fig. 14 Directivity and radiation pattern

Table. 15 TARC, CC and ECC

Parameter	Values
Directivity	1.042 dB
TARC	Less than 0.079 (−10.98 dB)
CC and ECC	Less than 0.00093 and less than 0.00000086

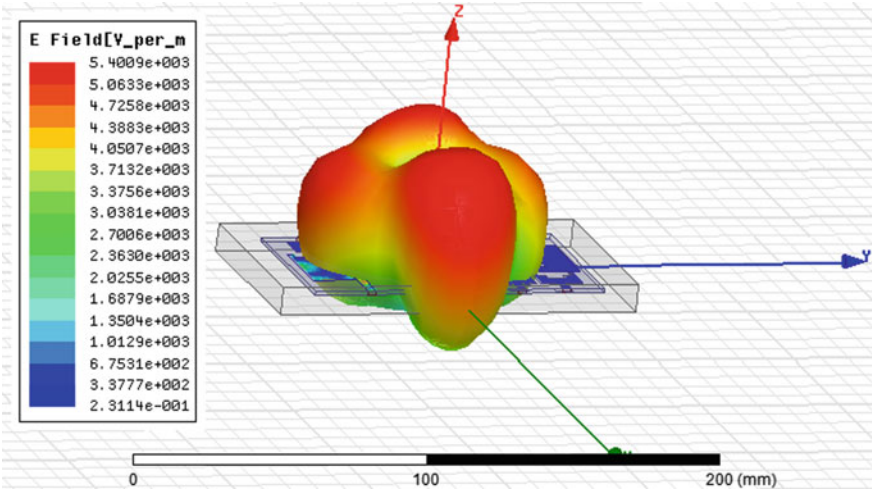

Fig. 15 Electric field intensity on MAS

The Total active reflection coefficients (TARC), correlation coefficients (CC), envelope correlation coefficients (ECC) and diversity gain (DG) are calculated using Eqs. 11 to 13 having values shown in Table 15.

The CC and ECC are required between the zero and one. If this value is close to zero, then all energy is transferred in free space (means, no energy is correlated with others radiating patch).This antenna is very good for operation.

If this value is close to one, then all energy is correlated with nearest radiating elements. This antenna is lost all energy. No any energy is transferred in free space.

So, designed massive MIMO antenna analysis shows that, less than 0.00093 CC, less than 0.00000086 ECC and less than 0.079 (−10.98 dB) TARC. Therefore, this antenna is useful for wireless communication.

The electric field intensity of antenna in free space is 5.4 V/m as shown in Fig. 15.

The current flow in the RP od antenna is as shown in Fig. 16.

3.1 Isolation and Bandwidth Improvements

The parameter of antenna is calculated using the following equation.

(1) Total active reflection coefficients (TARC)

TARC is calculated using Eq. 10.

$$\text{TARC} = \{[\sqrt{[((S_{\text{mm}} + S_{\text{mn}}(e^{\ominus}))^2) + ((S_{\text{nm}} + S_{\text{nn}}(e^{\ominus}))^2)]}]/\sqrt{2} \qquad (10)$$

where:

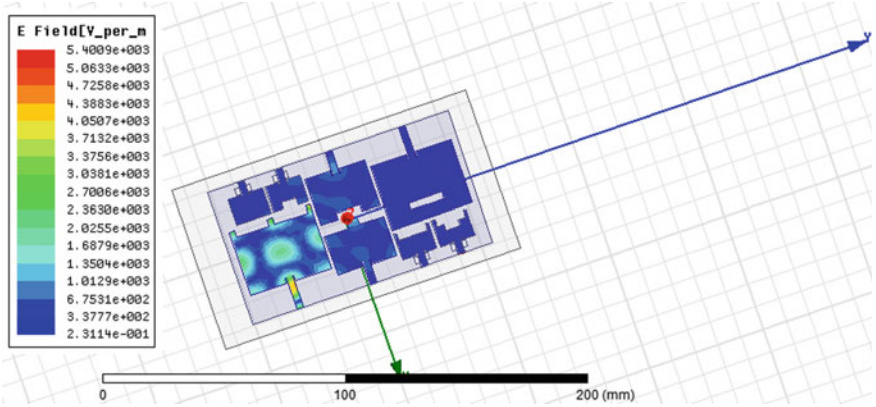

Fig. 16 Electric field flow in MIMO antenna

Θ = Phase of the input feeding
S_{mm} and S_{nn} = Reflection coefficient for $m = 1$ and $n = 2$
S_{mn} and S_{nm} = Isolation

(2) Correlation coefficients (CC) and Envelope correlation coefficients (ECC)

CC and ECC are found out by using the Eq. 11 for 2-element.

$$\mathrm{CC}^2 = \mathrm{ECC} = \left\{\left[(S_{mm} * S_{mn} + S_{nm} * S_{nn})/\sqrt{[(1-(S_{mm})^2 - (S_{nm})^2)\left(1-(S_{nn})^2 - (S_{nn})^2\right)\right]}\right\}^2 \tag{11}$$

(3) Diversity Gain (DG)

DG of the antenna is dependent on ECC.

$$\mathrm{DG} = 10\sqrt{\left(1-(0.99\mathrm{ECC})^2\right)} \tag{12}$$

(4) Bandwidth

The fractional Bandwidth is calculated by following.

$$\%\mathrm{BW} = \{[(F_h - - F_l)/F_0] * 100\} \tag{13}$$

$$F_0 = \{[F_l + (F_h - - F_l)/2]\} \tag{14}$$

where:

BW = Bandwidth
F_h = Higher frequency
F_l = Lower frequency
F_0= Centre frequency

3.2 Flowchart of Antenna Design

The Flow Chart 2 is shown the massive MAS design procedure.

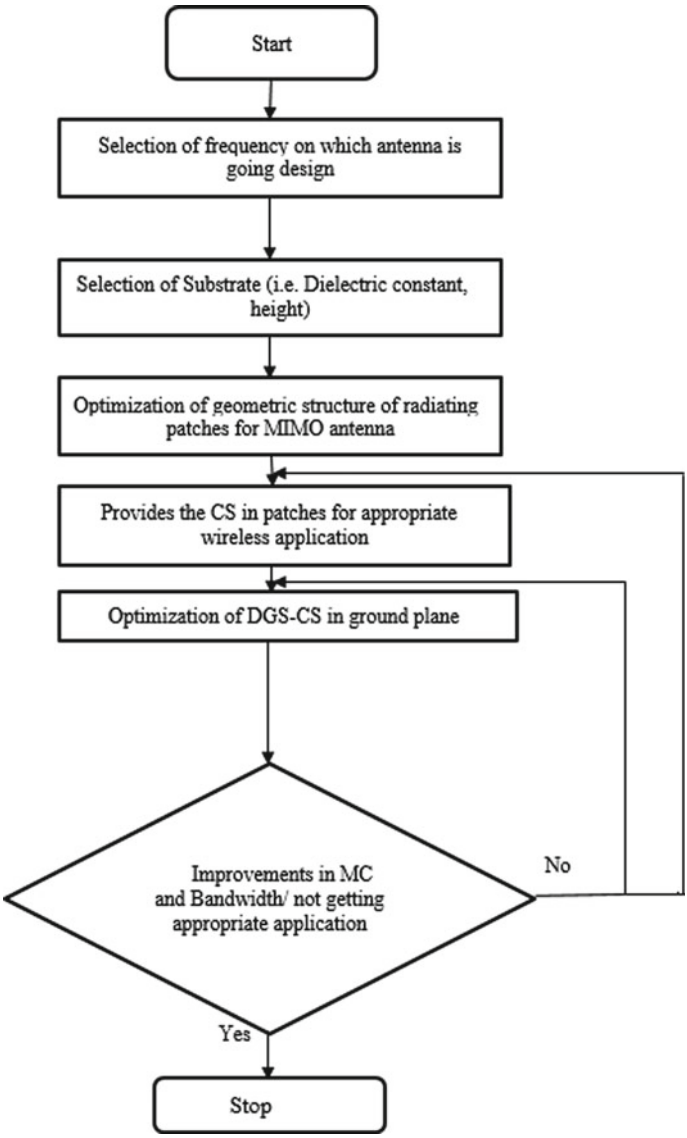

Flow Chart 2 Antenna design procedure

4 Conclusion

The different-shaped radiating elements massive MIMO antenna is investigated for multiband operation with wideband application. This antenna is operated on various frequency band, which are 3.6 GHz, 3.8 GHz, 4.7 GHz, 4.9 GHz, 5.2 GHz, 5.8 GHz, 6.1 GHz, 6.4 GHz, 6.5 GHz and 6.6 GHz. The analysis of antenna shows that, the return loss and isolation observed which is less than −10.20 dB. The total active reflection coefficients (TARC), correlation coefficient (CC) and envelope correlation coefficient (ECC) parameters of antenna which are observed, less than −10.98 dB, less than 0.00093 and less than 0.00000086 respectively. The operating bandwidth of proposed antenna is in between 182 MHz (3.02%) and 480 MHz (8%) with good directivity. This antenna operates on the various application of wireless communication such as 5G-band n77 and Wi-MAX, WLAN, 5G-band and C-band for satellite communication with wideband bandwidth.

References

1. Nadeem, D. Choi, Study on mutual coupling reduction technique for MIMO antennas. IEEE Access **7**, 563–586
2. Y. Liu, A. Ren, H. Liu, H. Wang, C.-Y. Sim, Eight-port MIMO array using characteristic mode theory for 5G smartphone applications. IEEE Access **7**, 45679–45692 (2019)
3. L. Cui, J. Guo, Y. Liu, C. Sim, An 8-element dual-band MIMO antenna with decoupling stub for 5g smartphone applications. IEEE Antennas Wirel. Propag. Lett. **18**(10), 2095–2099 (2019)
4. H.T. Chattha, 4-Port 2-element MIMO antenna for 5G portable applications. IEEE Access **7**, 96516–96520 (2019)
5. Y. Liu, X. Yang, Y. Jia, Y.J. Guo, a low correlation and mutual coupling MIMO antenna. IEEE Access **7**, 127384–127392 (2019)
6. Y. Li, C. Sim, Y. Luo, G. Yang, High-isolation 3.5 GHz eight-antenna MIMO array using balanced open-slot antenna element for 5G smartphones. IEEE Trans. Antennas Propag. **67**(6), 3820–3830 (2019)
7. J. Choi, W. Hwang, C. You, B. Jung, W. Hong, Four-element reconfigurable coupled loop MIMO antenna featuring LTE full-band operation for metallic-rimmed smartphone. IEEE Trans. Antennas Propag. **67**(1), 99–107 (2019)
8. S. Xiumei, Y. Liu, L. Zhao, G. Huang, X. Shi, Q. Huang, A miniaturized microstrip antenna array at 5G millimeter wave band. IEEE Antennas Wirel. Propag. Lett.
9. P. Garg, P. Jain, Isolation improvement of MIMO antenna using a novel flower shaped metamaterial absorber at 5.5 GHz WiMAX band. IEEE Trans. Circ. Syst. II
10. J. Guo, L. Cui, C. Li, B. Sun, Side-edge frame printed eight-port dual-band antenna array for 5G smartphone applications. IEEE Trans. Antennas Propag. **66**(12), 7412–7417 (2018)
11. X. Shi, M. Zhang, S. Xu, D. Liu, H. Wen, J. Wang, Dual-band 8-element MIMO antenna with short neutral line for 5G mobile handset. in *Proceedings 11th European Conference Antennas Propagation*, pp. 3140–3142
12. N.O. Parchin et al., Eight-element dual-polarized MIMO slot antenna system for 5G smartphone applications. IEEE Access **7**, 15612–15622 (2019)
13. Q. Chen et al., Single ring slot-based antennas for metal-rimmed 4G/5G smart- phones. IEEE Trans. Antennas Propag. **67**(3), 1476–1487 (2019)
14. J. Li et al., Dual-band eight-antenna array design for MIMO Applications in 5G mobile terminals. IEEE Access **7**, 71636–71644 (2019)

15. M.K. Khandelwal et al., Defected ground structure: fundamentals, analysis, and applications in modern wireless trends. IJAP (Hindawi). 2018527
16. Y. Ghazaoui, A. El Alami, M. El Ghzaoui, S. Das, D. Baradand S. Mohapatra, Millimeter wave antenna with enhanced bandwidth for 5G wireless application. J. Instrument. **15** (2020). https://doi.org/10.1088/1748-0221/15/01/T01003
17. B. Aghoutane, S. Das, H. El Faylali, B.T.P. Madhav, M. El Ghzaoui, A. El Alami, Analysis, design and fabrication of a square slot loaded (SSL) millimeter-wave patch antenna array for 5G applications. J. Circ. Syst. Comput. **30**(05), 2150086 (2021). https://doi.org/10.1142/S0218126621500869

Asset Allotment in Hybrid RF/VLC Communication in the 400–700 THz Band

Shivanshu Shrivastava, Sajal Agarwal, and Bin Chen

Abstract High data rate system is the most prominent version of communication systems require for the fifth generation mobile systems. Visible light communication (VLC) is one of the options to achieve the objective. Visible light communication works in the range of 400–700 THz and allows lower interference with radio frequency (RF) counterpart. However, VLC deployment suffers from some serious issues which can be overcome by the hybrid RF/VLC system. These hybrid systems provide promising mechanism for the problem in hand. Data rate maximizing can be done by constraining bandwidth, power, and user connection. We can opt for joint optimization of bandwidth, power, and user connection to maximize the data rate is non-concave and obtaining an optimal solution is hard with conventional algorithms. Normally, one optimization variable is presumed in the existing algorithms. A joint mechanism will be discussed in this chapter for hybrid RF/VLC systems. Basically, deep Q-network (DQN) learning-based algorithm is used in this chapter, which is an efficient learning-based mechanism for optimization. Multiple access points (APs) of VLC systems and only one RF AP will be taken. Idle APs are used and incorporated, and DQN algorithm is applied by finding an policy with action-value function. To carry out the simulation, a large data set has been taken with a multi-layered network to approximate the action-value function estimator. At the end, a algorithm has been proposed on transfer learning to maximize the data rate for new entered user equipments (UE). This system uses the reacquired data from already installed UE to learn and transfer the the information to new UE. It is aimed to provide an

S. Shrivastava (✉) · S. Agarwal
Department of Electronics Engineering, Rajiv Gandhi Institute of Petroleum Technology, Jais, Amethi, India
e-mail: sshrivastava@rgipt.ac.in

S. Agarwal
e-mail: sagarwal@rgipt.ac.in

B. Chen
College of Electronics and Information Engineering, Shenzhen University, Shenzhen, Guangdong Province, China
e-mail: bchen@szu.edu.cn

M. El Ghzaoui et al. (eds.), *Terahertz Wireless Communication Components and System Technologies*, https://doi.org/10.1007/978-981-16-9182-9_14

improvement in sum rate and number of iterations by 10 and 50 folds, respectively, as compared to the existing optimization algorithms.

Keywords Visible light communication · Deep Q-network learning · Bandwidth · Power · Connection parameter · Terahertz communication

1 Introduction

Dependency of our lives over electronic devices exerts an ever-growing need of energy and bandwidth for data radiation. These needs become more crucial with the growing interest of Internet of Things for interconnect and rapid data radiation, collection, and storage. Moreover, location estimation in indoor as well as outdoor environment requires satisfactory position which cannot be fulfilled by Global Positioning System. According to a survey by CISCO, it is estimated that the mobile data traffic would be 46% more in 2022 as compared to 2017, which will further break its record due to the current pandemic situation. Since, not only general communication but most of the communication, such as education, administrative, and personal communication is occurring over Internet. Apart from this interference and limited spectrum of radio frequency (RF), wireless communication is also an issue which has to be addressed.

Thus, to overcome the drawbacks of existing system and fulfill the current need with the option to address the coming demand, it is imperative to design a new communication system which will be able to accomplish all the task with better energy efficiency. Visible light communication (VLC) systems are such systems which works on the visible light present in the environment utilizing the light bandwidth varying from 380 to 750 nm. VLC emerges as an efficient candidate for telecommunication as well as energy-efficient systems [1, 2]. The corresponding frequency range of this wavelength is 430–790 THz, which provides large bandwidth. The basic concept of the VLC systems is to utilize the spectrum available in the confined spaces. Transmitter and recipients of VLC systems should be present in the same room for successful communication. Thus, transmitter or recipient present outside the particular confined space will not be able to transmit or receive waveforms, respectively. This makes VLC immune to security issues present in the RF counterpart. Since visible light is used for the waveform radiation and reception, thus, it saves extra power that was required by RF communication. One more positive point of with VLC communication is that it works in unlicensed band of the spectrum since it uses visible light for communication. Potential applications of VLC systems are Internet of Things (IoT), vehicular communication, robot communication, Li-Fi, and underwater communication, etc. This can also be used for the interference prone systems/spaces such as hospitals and aircraft . However, practical implementation of such systems is a big challenge like interference with the ambient light, interference between difference VLC devices, integration of this technology with the existing systems, etc. Basic VLC systems has two integral parts, i.e., transmitter and recipient

which consists of three layers. IEEE 802.15.7 is the standard used for the physical and MAC layer.

Although line of sight communication is a serious issue, which limits its stand-alone deployment [3, 4], hybrid RF/VLC systems emerged as a solution to the above problems of stand-alone VLC systems [5]. These hybrid systems incorporate concepts of RF and VLC into single system. Typical hybrid system consists of light source as the VLC access point (AP) in the setup. This whole set up is supported by RF APs (One or multiple). A recipient associated either with VLC or RF AP would be established in the same space. High data rate is provided by the access point of the visible light communication network, whereas RF AP is used for uninterrupted communication in the case of non-line of sight (blockage) condition. Thus, both networks complement each other. Apparently, hybrid systems provide a heterogeneous network. In heterogeneous and hybrid networks, asset allotment and their connection are a significant problem [6, 7]. Thus, maximum asset allotment is a challenge which can be addressed with different optimization methods. Deep Q-networks-based algorithms provide effective solution for the asset allotment problem jointly with the power allotment, down link bandwidth allotment, and their parameters for high data rate. Thus, this chapter is dedicated to the deep Q-networks-based algorithms. Before discussing the different models, a brief literature survey is given to understand the existing solutions for the asset allotment problem.

2 Existing Models

Asset allotment is a big challenge in the VLC communication technology. This problem is crucial in the hybrid systems since VLC and RF are two very different systems and their models are entirely different. Till now, various models are proposed by researchers to address the same problem. These models were proposed to maximize the sum rate and reduce energy-related issues, etc. [8–10]. In this section, a brief literature survey is given for the hybrid RF/VLC asset allotment models. In 2013, Ye et al. [6] proposed a user allotment scheme for load balancing in heterogeneous networks. To achieve the task, a distributed algorithm was designed via dual decomposition. Proposed scheme was also extended to the range expansion technique. Two factors were took into account, i.e., SINR and data rate. It was observed through the study that biasing factors are independent of the base station densities for different tiers.

In 2014, two distributed algorithms were proposed [11] for matching femtocell access points for different service providers. These algorithms were able to achieve a group stable matching and user equipment satisfaction level for centralized optimal solution. Moreover, the system complexity and delay are very less to achieve optimal solution due to less number of iterations that were required. Stefan [12] achieved a very high data rate hybrid system by optimizing the associated parameters using minimum separation condition in the same year. User connection was the focus for equal bandwidth among user equipment. It simulated the model for three tier

heterogeneous network with seven macrocells in hexagonal shape. The aim of this study was to develop solution for allotment of abundant assets of optical networks to allow off-load cellular systems for wireless data radiation.

In 2016, Kashef et al. [13] proposed an energy-efficient asset allotment model for hybrid system. This study displayed a very thorough study for the energy efficiency for various parameters.

This work was done for the indoor data network building block with multiple VLC and RF APs from different regions. This study proposed the efficient power and bandwidth allotment for energy efficiency maximization. From the results produced by this study, it proves that proposed method is much more efficient for energy saving than any other study done till that time. In 2017, Marzban et al. [14] proposed a solution of a very crucial problem of eavesdropping attacks on the physical layer. This study was dedicated to the physical layer security problems. To solve this problem, electrical power consumption was targeted to be minimized while securing the data simultaneously. For the taken hybrid network, zero forcing beamforming and minimum power allotment algorithm was proposed. From the results, it is confirmed that the solution provided by the proposed algorithm is promising.

It is depicted that the proposed algorithm outperforms the existing and popular algorithms in terms of consumed electrical power for indoor scenarios. In the same year, Kafafy et al. [15] identified the service disruption problem due to limited light coverage. To overcome this particular problem, hybrid RF/VLC networks are proposed with RF networks which can be exploited to resolve the limited VLC coverage. In the proposed study, a complex network was taken having multiple APs for VLC and RF both. The algorithm was dedicated to the asset allotment to maximize system power efficiency to improve throughput per unit power. Results showed that the deployment of access point of the visible light communication networks improves the power efficiency and improves the data rate per user. It was also depicted that uniform classification of access point of the visible light communication networks can further improve power efficiency.

The classification of access point of the visible light communication networks uniformly in the indoor environment can improve the power efficiency by 30% for same number of APs non-uniformly. In 2019, Kong et al. [16] discussed that the RF path gains change faster than VLC paths because that has small-scale fading. To overcome the problem in VLC/RF hybrid network, an two-timescale strategy was proposed to optimize the transmit power at both VLC and RF APs. To do so, Q-learning algorithm is used for multi-homing problem solution. It was confirmed from the simulation study that proposed technique successfully supports the users while satisfying their QoS requirements. Recently, Papanikolaou et al. [17] proposed a solution for the very crucial problem of, i.e., the coexistence of VLC and RF networks, and it was supposed that both networks are served by same network in backhaul, with both perfect and imperfect path state information. An optimal asset allotment algorithm was proposed to solve the said problem with effective solution. Apart from the above research, a number of different approaches were proposed by researchers for the improvement of the performance of the hybrid VLC/RF networks. In the next section, a solution is provided by the authors also.

3 Model of a Hybrid RF/VLC System

The system model of a typical hybrid RF/VLC setup consists of LED light sources installed on the ceiling of the room which acts as multiple access points of the visible light communication networks. As indicated in the diagram, ceiling is used to install the RF AP of the room with the CU as the co-locator. It uses the DQN algorithm to operate the network, APs bandwidth, and transmit power has been allocated to control APs. Along with this, UE connection was also done. The users who are carrying the UEs are exhibited randomly on the room's floor. A user with a UE who has just entered the room is also indicated at the room's floor's edge. Let $\mathscr{M}$ denote the collection of APs indexed as $i = 0, 1, 2, \ldots, |\mathscr{M}|$. The RF AP is represented by the index $i = 0$, whereas the access point of the visible light communication networks is represented by the indices $i = 1, 2, \ldots, |\mathscr{M}| - 1$. Let $\mathscr{N}$ be the number of UEs in the room, which are indexed as $j = 1, 2, \ldots, |\mathscr{N}|$. The UEs are measured from the floor at a height of h. The VLC and RF networks are used to communicate with a UE on the downlink. RF and VLC access points are used to connect with UE. The bandwidth is shared by all access point of the visible light communication networks. Inter-cell interference (ICI) exists in the VLC network as a result. For downlink communication, the tests will be carried out on a reference AP i-UE j pair. A backhaul circuit called [18] is used to communicate data between access point of the visible light communication networks and the RF AP. The underlying circuitry activities are likewise performed by the backhaul circuit. In this setup, a non-coordinated radiation has been investigated. Access points of the visible light communication network are connected to provide data to UE by using the concept of LOS and bounced light ray components (Table 1).

3.1 Light Propagation Model in THz Band

The access point of the visible light communication networks uses the downlink to send data to the UEs. The VLC models light propagation using diffused bouncion, where light scattering would be taken at various inclinations.

The Lambertian law [19] represents the optical power of light after diffused bouncion and is expressed as

$$P_o(\phi) = \frac{m+1}{2\pi} \cos^{m}(\phi) P_i, \quad \text{for } i \in \mathscr{M} \backslash \{0\}, \tag{1}$$

where P_i denotes total LED power, ϕ denotes gleam inclination, and m signifies Lambertian radiation profile order represented as

$$m = -\frac{\ln 2}{\ln \cos \psi_{1/2}}, \tag{2}$$

Table 1 Denotations

Denotation	Indication
i	The AP of interest
j	The UE Of interest
k	The AP causing interruptions
r_{ij}	The $i-j$ path data rate
r_i	Total data rate of any AP denoted by i
r	Summed data rate that is achievable
B^v_{maximum}	Upper VLC bandwidth limit
B^r_{maximum}	Upper RF bandwidth limit
P_i	Energy divided by time for an AP i
$\mathscr{M}$	Access points on the ceiling of the room
$\mathscr{N}$	User equipments on the floor
m	Lambertian coefficient
ϕ	Gleam inclination
ϕ_1, ϕ_2	Transmitter inclination of gleam at the point of bouncion
ψ	Projection inclination
ψ_1, ψ_2	Point of bouncion and recipient inclination of projection
$G^{(p)}$	Bouncion number p gain
A_s	Area of projection
G_{EffRef}	Net gain of path post getting bounced
$P_q^{(p)}$	Power of the bounced light wave at the bouncing point number p from the access point number q
C	Path capacity limit relevant to VLC
BW_{ji}	AP i allots bandwidth to the UE j
G_{ij}	Access point i and UE j gain
n^v_j	UE recipient noise during getting light waveforms
n^r_j	Radio frequency UE recipient noise for RF waveforms
ρ_j	Responsivity UE optical waveform receptor
pl_{0j}	Power term of RF link attenuation
α_{ji}	$\alpha_{ji} = 1$ means $i-j$ are connected $\alpha_{ji} = 0$ means $i-j$ are not connected
N^r_0	Unwanted waveforms power while receiving RF waveforms
N^v_0	Unwanted waveforms power while receiving VLC waveforms
P^r_{maximum}	Upper limit on energy/time of the radio waveforms AP
P^v_{maximum}	Upper limit on energy/time of the light waveforms AP

where $\psi_{1/2}$ denotes the LED's illuminance half-semi-inclination. This will help the LED to emit the required wavelength λ and $P_i(\lambda)$, where P_i can be written as

$$P_i = \int_{\lambda} P_i(\lambda) \mathrm{d}\lambda. \tag{3}$$

A path gain for downlink communication on $i - j$ path can be calculated for LOS DC path (1).

$$G_{ij}^{v} = \frac{(m+1)A_{\mathrm{pd}} \cos^{m} \phi_{ij} \cos \psi_{ij} T_{\mathrm{opt}}(\psi_{ij}) g(\psi_{ij})}{2\pi d_{ij}^{2}}, \tag{4}$$

where $T_{\mathrm{opt}}(\psi_i j)$ is the optical recipient filter gain, its value is constant or unity inside the recipient FOV, ϕ_{ij} represents the inclination of gleam at AP i, $\psi_i j$ is the inclination of projection at UE j, d_{ij} represents the separation between the UE j and AP i, and $g(\psi_{ij})$ is the converger gain as

$$g(\psi_{ij}) = \begin{cases} \frac{n^2}{\sin^2 \psi_{\mathrm{FOV}}} & \text{if } 0 \leq \psi_{ij} \leq \psi_{\mathrm{FOV}} \\ 0 & \text{if } \psi_{ij} > \psi_{\mathrm{FOV}}, \end{cases} \tag{5}$$

where n is the refractive index and $n = \frac{\text{speed of light in vaccum}}{\text{speed of light in that optical substance}}$ is the refractive index, where ψ_{FOV} is the FOV inclination of the recipient UE.

The NLOS path gain from the bounced light components was also calculated by photodiode of UEs. A ray of light from the $(l-1)$th bouncing point makes up the lth bounced light ray component. The virtual light source is the $(l-1)$th bouncing point, while the virtual recipient is the lth bouncing point. Effective path gain for DC path for multiple bounces can be calculated as in [19]. However, mathematically, cumulative path gain can be calculated for all pairs of bouncing points as G_{EffRef},

$$G_{\mathrm{EffRef}} = \sum_{p=0}^{\infty} G^{(p)}, \tag{6}$$

where p is the bounce index, $G(p)$ is the DC path gain after the pth bouncion from the source LED, and

$$G^{(p)} = \int_{S} G_1 G_2 \ldots G_{p+1} P_q^{(p)} dA_s, \tag{7}$$

where dAs represents the very small bounce surface area (approaching to zero) and $P_q^{(p)}$ represents the bounced light optical power after p bounces produced by the qth radiating access point of the visible light communication network. A very small part of the wall has been taken for the above integration of variables. The DC path gains

of the path tracked by each bounced component are $G_1, G_2, \ldots, G_{p+1}$ and are given as percent [19].

$$\begin{aligned} G_1 &= \tfrac{(m+1)A_s}{2\pi d_1^2}\cos^m(\phi_1)\cos(\psi_1), \\ G_2 &= \tfrac{A_s}{\pi d_2^2}\cos^m(\phi_2)\cos(\psi_2), \\ &\cdot \\ &\cdot \\ &\cdot \\ G_{p+1} &= \tfrac{A_s}{\pi d_{p+1}^2}\cos^m(\phi_{p+1})\cos(\psi_{p+1})T_{\text{opt}}(\psi_{p+1})g(\psi_{p+1}), \end{aligned} \tag{8}$$

where As is the projection surface area, ϕ_a and ψ_a $(a = 1, 2, \ldots, p+1)$ are the gleam and projection inclinations at the ath bounce (a is a dummy variable), ϕ_a and ψ_a $(a = 1, 2, \ldots, p+1)$ are the gleam and projection inclinations at the ath bounce, and G_{ij}^v is the DC path gain between the ith access point of the visible light communication network and the PD-based jth recipient in (4). Path gain can be taken as G_1 for ith access point of the visible light communication network and the first bouncing point, whereas path gains between 2^{nd} and 3^{rd} bouncing point are G_2, and G_{p+1} is the path gain between the pth bouncing point and the recipient PD in (8). All of the bouncing spots' path gains are almost identical mathematically. T_{opt} and $g(\psi_{p+1})$ receive PD properties. Hence, G_{p+1} is function of T_{opt} and $g(\psi_{p+1})$. G_{p+1} is the gain between the receiving PD and the last bouncing point. Let us say, spectral bounce of the substance at the pth bouncing point is $\Gamma_p(\lambda)$, and spectral bounce of the substance as pth bouncing point is $P_q^{(p)}$.

$$P_q^p = \int_\lambda P_i(\lambda)\Gamma_1(\lambda)\Gamma_2(\lambda)\ldots\Gamma_p(\lambda)\mathrm{d}\lambda. \tag{9}$$

All of the bouncing points' surfaces are presumed to be made of the same substance. Because Γ_p is a function of λ, $\Gamma_1(\lambda) = \Gamma_2(\lambda) = \ldots = \Gamma_p(\lambda) = \Gamma$ is supposed.

The total of the LOS and NLOS components in the effective received optical power P_{eff} from a single LED is expressed as

$$P_{\text{eff}} = G_{\text{EffRef}}P_i + G_{ij}^v P_i = G_{ij}P_i \text{ for } i \in \mathscr{M}\backslash\{0\}, \tag{10}$$

where VLC i transmits waveform with power P_i and AP i to UE j effective path gain is $G_{ij} = G_{\text{EffRef}} + G_{ij}^v$ for $i \in \mathscr{M}\backslash\{0\}$.

3.2 Model for RF Waveform Propagation

RF waveform propagation model can be used to receive the waveform by UE j from the RF AP, which includes fading and path loss in the power path gain. The WINNER-2 path model [20] is used to simulate the received RF waveform power.

$$G_{0j} = Ld_{0j}^{-pl_{0j}} \chi_{0j}, \tag{11}$$

where χ_{0j} represents the Nakagami fading path, pl_{0j} represents the path loss exponent, and d_{0j} is the separation between UE j and the RF AP indexed as $i = 0$. Here, $L = 10^{X/10}$, $X = M + N \log 10\left(\frac{fc}{5}\right)$, fc is the carrier frequency in GHz, and M and N are the propagation constants, which vary depending on the propagation model. $M = 46.8$ and $N = 20$ in a LOS environment, while $M = 43.8$ and $N = 20$ in a non-LOS environment. The fading strength of the Nakagami fading path χ_{0j} is based on the gamma classification. It is a fading classification in general. When $\kappa = 1$, it resembles the Rayleigh classification, and when $1 \geq \kappa \leq \infty$, it resembles the Rician fading classification.

3.3 Data Rate in THz Band-Based VLC

Because the goal of our research is to maximize the achievable sum rate of hybrid RF/VLC systems, apart from this, data rate of UE will also be calculated when it is connected to an RF or a access point of the visible light communication network is crucial. The Shannon's capacity formula will be used to express a UE's feasible data rate throughout its affiliation with the RF AP. When a UE is connected to a access point of the visible light communication network, however, communication is based on light intensity modulation/direct detection (IM/DD). The waveform amplitude bounces the immediate optical power in this diagram. As a result, there are restrictions on the waveform's real-valued and non-negative nature. Because of these limitations, applying the Shannon capacity formula directly may not be sufficient to get the desired data rate.

Gaussian noise damaged the capacity of an IM/DD path which was explored by the authors in [21–23]. According to [21], investigations demonstrate that the lowest bound of the path capacity in VLC networks can be calculated as

$$C = \frac{1}{2} B \log_2 \left(1 + w \frac{\rho^2 P_{\text{eff}}^2}{\sigma^2}\right), \tag{12}$$

where w is a constant equal to $w = e/2\pi$ (e is the Euler's number), ρ is the PD's responsivity, B is the modulation bandwidth, P_{eff} is the received optical power, and σ^2 is the Gaussian noise power A factor of $\frac{1}{2}$ emerges as a result of different limits in VLC, according to [21]. It was also discovered that the expression (12) is correct, and that it agrees with the top bound for a high SNR.

3.4 The Overall Communication Model

Data is sent to each UE by one of the access points of the visible light communication networks and RF AP. The DQN-based learning technique presented ahead will be used to determine its relationship. Some APs will most likely be idle, with no UE linked with them. The path gain vector for UE j linked with AP i for $i \in \mathscr{M}$ will be expressed as $\mathbf{G_j} = [G_{0j}, G_{1j}, G_{2j}, \ldots, G_{|\mathscr{M}|j}]$ where $G_{0j} \in \mathbb{C}$, $[G_{1j}, G_{2j}, \ldots, G_{|\mathscr{M}|j}] \in \mathbb{R}_{\geq 0}^{(|\mathscr{M}|-1)\times 1}$. The path gain between the UE j and the AP i is denoted as $G_{ij} \in \mathbf{G_j}$. The waveform put out by the APs will be expressed in vector form as follows: $\mathbf{x} = [x_0, x_1, x_2, \ldots, x_{|\mathscr{M}|}]$ where $x_0 \in \mathbb{R}$ and $[x_1, x_2, \ldots, x_{|\mathscr{M}|}] \in \mathbb{R}_{\geq 0}^{(|\mathscr{M}|-1)\times 1}$. Remember that the RF AP is represented by the index $i = 0$ in the above settings. Consider the case where the UE j is linked to the AP i. When UE j is connected to AP $i = 0$, i.e., the RF AP, it receives waveform yj, which is expressed as

$$y_j = \sqrt{G_{0j} P_0} \times x_0 + n_j^r, \text{ for } i = 0, \tag{13}$$

where n_j^r is the additive white Gaussian noise (AWGN). When UE j is connected to the ith access point of the visible light communication network, on the other hand,

$$y_j = \rho_j G_{ij} P_i x_i + \sum_{k \in N \setminus \{i\}} \rho_j G_{kj} P_k x_k D_k(\alpha_{kj'}) + n_j^v, \quad \text{for } i \in N \setminus \{0\}, \tag{14}$$

where ρ_j denotes the responsivity of the PD at the jth UE recipient as given in (12), n_j^v involves the shot noise and thermal noise, and

$$D_k(\alpha_{kj'}) = \left(1 - \prod_{j' \in \mathscr{N} \setminus \{j\}} (1 - \alpha_{kj'})\right), \tag{15}$$

where $\alpha_{kj'}$ is written as

$$\alpha_{kj'} = \begin{cases} 1 \text{ if AP } k \text{ is associated to UE } j' \\ 0 \text{ otherwise.} \end{cases} \tag{16}$$

$\alpha ij = 1$ in (14) indicates that UE j is connected with AP i. The desired AP-UE combination is AP i - UE j, but AP k is interfering with the jth receiving UE. The desired waveform is represented by the first term in (14), whereas interference is represented by the second term. The interference term in a standard version of the expression that does not have $Dk(\alpha k j')$. In the interference term, we multiply $Dk(\alpha k j')$ to account for idle APs that are not broadcasting. It assures that the interferer is only deemed AP k if it is radiating to minimum one UE j', where $j' \neq j$. $\alpha_{kj'}$ is a parameter. The parameter $\alpha_{kj'}$ denotes the connection of UE j' with AP k, with $D_k(\alpha_{kj'}) = 0$ if AP

k is not radiating and radiating to UE j' and 1 if AP k is broadcasting and radiating to UE j'. This factor takes into account the case where an AP is temporarily turned off owing to a hardware problem.

The instant achievable data rate at UE j for the input waveform that is continuous and follows a negative exponential classification expressed as [24] after (12), (13), and (14).

$$r_{ij} = \begin{cases} BW_{j0} \log_2 \left(1 + w\gamma_{0j}\right), & \text{for } i = 0 \text{ and} \\ \frac{1}{2} BW_{ji} \log_2 \left(1 + w\gamma_{ij}\right), & \text{for } i \in \mathscr{M} \backslash \{0\}, \end{cases} \tag{17}$$

where γ_{0j} and γ_{ij} are the lower bounds of SINR_{0j} and SINR_{ij} which are given as

$$\begin{aligned} SINR_{0j} &= \frac{P_0 G_{0j}}{N_0^r BW_{j0}}, \text{ and} \\ SINR_{ij} &= \\ &\frac{\rho_j^2 G_{ij}^2 P_i^2}{N_0^v BW_{ji} + \sum_{k \in N \backslash \{i\}} \rho_j^2 G_{kj}^2 P_k^2 \left(1 - \prod_{j' \in M \backslash \{j\}} (1 - \alpha_{kj'})\right)^2}, \end{aligned} \tag{18}$$

where BW_{j0} is the RF AP ($i = 0$) - UE j link's bandwidth and BW_{ji} is the bandwidth of the access point of the visible light communication network i - UE j link's bandwidth and $i \in \mathscr{M} \backslash \{0\}$. Because the model only considers one RF AP, it is supposed that the RF waveforms experience minimal interference. As a result, we are interested in the SNR when the UE j is linked to the RF AP. However, the SNR for the RF AP-UE j link is represented as SINR_{0j} for consistency in nomenclature. The RF AP is denoted by the subscript $i = 0$. SINR will be of importance when UE j is connected to a access point of the visible light communication network. In the case of RF waveforms, any broad statement of SINR will also indicate SNR. The throughput of AP i can be calculated using the above expression for instant data rate.

$$r_i = \sum_{j \in \mathscr{N}} \alpha_{ji} r_{ij}, \text{ for } i \in \mathscr{M}. \tag{19}$$

3.5 *Allocating the Assets in Hybrid RF/VLC*

The goal of this work is to discover the best user connection, AP transmits power allotment, and AP downlinks bandwidth allotment for the UEs that are connected to it. The asset allotment will be done with the goal of maximizing r_i from (19). The challenge of asset allotment is stated as follows:

$$\mathscr{P} : \max_{BW_{ji}, P_i, \alpha_{ji}} r_i, \qquad \text{for } i \in \mathscr{M}, j \in \mathscr{N}, \tag{20}$$

subject to the following constraints:

$$\mathscr{C}_1 : \sum_{j \in \mathscr{N}} \alpha_{ji} BW_{ji} \leq B^{v}_{\text{maximum}}, \quad \text{for } i \in \mathscr{M} \backslash \{0\}, \tag{21}$$

where B^{v}_{maximum} is the maximum allowable bandwidth for a access point of the visible light communication network. From $\mathscr{C}_1$, it is evident that the sum of bandwidths allocated to a access point of the visible light communication network's associated UEs should not be greater than B^{v}_{maximum}. The same consistency is required on the RF AP, which is written as follows:

$$\mathscr{C}_2 : \sum_{j \in \mathscr{N}} \alpha_{0j} BW_{j0} \leq B^{r}_{\text{maximum}}, \quad \text{for } i = 0, \tag{22}$$

Constraint $\mathscr{C}_2$ specifies that the entire bandwidth assigned to the RF AP cannot go beyond B^{r}_{maximum}. The radiation power is the next constraint, which is enforced to achieve power budget savings and eye safety considerations. An access point of the visible light communication network's radiation power has an upper limit P^{v}_{maximum}, which is defined as

$$\mathscr{C}_3 : 0 \leq P_i \leq P^{v}_{\text{maximum}}, \quad \text{for } i \in \mathscr{M} \backslash \{0\}, \tag{23}$$

Similarly, an RF AP's radiation power cannot exceed its maximum accessible power P^{r}_{maximum}, which is defined as follows:

$$\mathscr{C}_4 : 0 \leq P_0 \leq P^{r}_{\text{maximum}}, \quad \text{for } i = 0, \tag{24}$$

For $i \in \mathscr{M}$, $j \in \mathscr{N}$, SINR_{ij} is given more constraints in order to provide reliability. Let γ_{ij} be the least SINR needed on the AP i - UE j link for higher efficiency. As a result, the SINR restriction is as follows:

$$\mathscr{C}_5 : \text{SINR}_{ij} \geq \gamma_{ij}, \text{ for } i \in \mathscr{M}, j \in \mathscr{N}, \tag{25}$$

The minimal threshold for SINR_{ij} in the constraint $\mathscr{C}_5$ is $gammaij$. We use $\text{SINR}_i j = \gamma_i j$ for the calculations in this paper. To carry out the optimization of the variables BW_{ji}, P_i, and α_{ji}, equality is supposed. Taking equality as a starting point, the optimization of B_{ji}, P_i, and α_{ji} will lead to the optimization of γ_{ij}.

$$\text{SINR}_{ij} = \gamma_{ij} \tag{26}$$

facilitates the solution.

The following criteria for preventing SINR constraint violation are established when the constraint $\mathscr{C}_5$ in (25) holds with equality [25, 26]

$$\begin{array}{l} 1 - \sum_{i \in \mathscr{M}} \sum_{j \in \mathscr{N}} \xi_{ij} > 0, \text{ and} \\ \sum_{i \in \mathscr{M}} \sum_{j \in \mathscr{N}} \beta_i \xi_i \leq 1, \end{array} \tag{27}$$

where

$$\xi_{ij} = \left(1 + \frac{1}{\gamma_{ij}}\right)^{-1}, \text{ and} \tag{28}$$

$$\beta_{ij} = \frac{N_0 BW_{ji}}{(G_{ij} P_i / \gamma_{ij}) - N_0 BW_{ji}} + 1. \tag{29}$$

The constraints (25), (27), (28), and (29) are important for interference mitigation. Interference among APs forces the feasible data rates for distinct APs to interact with each other. As a result, optimizing the data rates that may be achieved for multiple APs at the same instants will be tough. The restriction (25) ensures that a minimum SINR threshold is maintained for each AP-UE pair. The minimal SINR threshold is indicated by the symbol γ_{ij}. By imposing a minimum SINR requirement on a AP-UE pair, the APs' interference is limited. The *state space vector* $\mathscr{S}_{ij}$ enables to do this. It will be constructed in the next section.

It is worth noting that summing logarithmic functions produces a concave function. However, in $\mathscr{P}$, BW_{ji}, P_i, and α_{ji} make the function r_i jointly non-concave.

4 Allotment of Bandwidth Power and Connection Parameter in the Systems with One RF and Multiple Access Point of the Visible Light Communication Networks

Now, a DQN-based learning algorithm to maximize the network throughput in (20) is developed.

4.1 Framework for Learning

We solved the problem in (20) using a DQN-based learning technique in this part. While respecting the limitations in (21)–(27), the suggested approach maximizes the attainable data rate of AP i in (20). The three vector variables *state*, *action*, and *reward* are used to operate learning-based algorithms. The environment's current state is defined by the state vector. The action vector specifies the course of action conducted in response to the current environment state. The reward vector specifies the reward that the system receives after it performs an activity. Let $\mathscr{S}_{ij} = \{s_{ij}^1, s_{ij}^2, \ldots, s_{ij}^l\}$ be the state vector and $\mathscr{A}_{ij} = \{a_{ij}^1, a_{ij}^2, \ldots, a_{ij}^m\}$ be the action space. At time t, the system in state $s_{ij}(t) \in \mathscr{S}_{ij}$ gets a reward $R_i(s, a)$. Then the player takes an action given by $a_{ij}(t) \in \mathscr{A}_{ij}$ on the system. This action takes the system to state $s_{ij}(t+1) \in \mathscr{S}_{ij}$. The result of action $a_{ij}(t)$ is obtained in the form of reward. The deep learning algorithm is trained by the CU on how to associate UEs and communicate with APs about

power and bandwidth classification. Iteratively, this process is repeated. The system gets closer to getting the maximum payout with each repetition.

4.1.1 Action Space ($\mathscr{A}_{ij}$)

α_{ji}, BW_{ji}, and P_i form the action space. As shown in (20), the action space $\mathscr{A}ij$ will be constructed with α_{ji}, BW_{ji}, and P_i for $i \in \mathscr{M}$ and $j \in \mathscr{N}$, respectively. Let $\mathbb{B}_{ij}$ and $\mathbb{P}_i$ represent the discretized form of BW_{ji} and P_i. For $\mathbb{B}_{ij}$ and $\mathbb{P}_i$, the following formula is used:

$$\mathbb{B}_{ij} = \left\{ 0, B_{\min}^{r/v} \left(\frac{B_{\text{maximum}}^{r/v}}{B_{\min}^{r/v}} \right)^{\frac{u}{(|\mathbb{B}_{ij}|-2)}} , u = 0, 1, 2, ..., |\mathbb{B}_{ij}| - 2, \right. \tag{30}$$

where $B_{\min}^{r/v}$ and $B_{\text{maximum}}^{r/v}$ represent the minimum and maximum BW_{ji} values. Likewise, $\mathbb{P}_i$ is calculated as

$$\mathbb{P}_i = \left\{ 0, P_{\min}^{r/v} \left(\frac{P_{\text{maximum}}^{r/v}}{P_{\min}^{r/v}} \right)^{\frac{u}{(|\mathbb{P}_i|-2)}} , u = 0, 1, 2, ..., |\mathbb{P}_i| - 2, \right. \tag{31}$$

where $P_{\min}^{r/v}$ and $P_{\text{maximum}}^{r/v}$ denote the minimum and maximum transmit power levels for the two different APs, namely the RF AP and the access point of the visible light communication network. α_{ji} will have a cardinality $2^{|\mathscr{M}|\times|\mathscr{N}|}$ for $i \in \mathscr{M}$ and $j \in \mathscr{N}$. The formulation of $\mathscr{A}_{ij}$ has $2^{|\mathscr{M}|\times|\mathscr{N}|}$ values of α_{ji} due to the occurrence of mathematical expression of interference in (18). $\mathscr{A}_{ij}$ is formulated with $|\mathbb{B}_{ij}| = |\mathbb{P}_i| = 2^{|\mathscr{M}|\times|\mathscr{N}|}$. The threshold γ_{ij} will be calculated with the discretized values $\mathbb{B}_{ij}$, $\mathbb{P}_i$, and α_{ji}, according to (18) on every $i - j$ link. The formulation of the action space will be done as

$$\mathscr{A}_{ij} = \{\gamma_{ij}^1, \gamma_{ij}^2, \ldots, \gamma_{ij}^{|\mathbb{B}_{ij}|\times|\mathbb{P}_i|\times|\alpha_{ji}|}\}. \tag{32}$$

The player, that is the CU, chooses a value, a value that belongs to $\mathscr{A}_{ij}$ and a value that the CU can assign for each AP. While opting a plan from $\mathscr{A}_{ij}$, it adjusts $\mathbb{P}_i$ and $\mathbb{B}_{ij}$ allotment for the ith AP (while satisfying $j \in \mathscr{N} \backslash \{\alpha_{ji} = 0\}$). It observes the environmental variations and those in its own radiation. Hence, choosing $\mathbb{B}_{ij}$ and $\mathbb{P}_i$ value to get a minimum SINR value, that is γ_{ij}, is the action of the player. Further, the design of state space vector is carried out.

4.1.2 State Space ($\mathscr{S}_{ij}$)

The state space is formulated with the constraints of the problem in (21)–(29). It is formulated as $\mathscr{S}_{ij} = \{I_1^{ij}, I_2^{ij}, \ldots, I_6^{ij}\}$, where

$$
\begin{aligned}
I_1^{ij} &= \begin{cases} 0 \text{ if } \sum\limits_{j\in\mathscr{N}} \alpha_{ij} BW_{ji} \le B^v_{\text{maximum}}, \text{ for } i \in \mathscr{M}\backslash\{0\}, j \in \mathscr{N}, \\ 1 \text{ otherwise.} \end{cases} \\
I_2^{ij} &= \begin{cases} 0 \text{ if } \sum\limits_{j\in\mathscr{N}} \alpha_{0j} BW_{j0} \le B^r_{\text{maximum}}, \text{ for } i = 0, j \in \mathscr{N}, \\ 1 \text{ otherwise.} \end{cases} \\
I_3^{ij} &= \begin{cases} 0 \text{ if } 0 \le P_i \le P^v_{\text{maximum}}, \text{ for } i \in \mathscr{M}\backslash\{0\}, j \in \mathscr{N}, \\ 1 \text{ otherwise.} \end{cases} \\
I_4^{ij} &= \begin{cases} 0 \text{ if } 0 \le P_0 \le P^r_{\text{maximum}}, \text{ for } i = 0, j \in \mathscr{N}, \\ 1 \text{ otherwise.} \end{cases} \\
I_5^{ij} &= \begin{cases} 0 \text{ if } \sum\limits_{i\in\mathscr{M}, j\in\mathscr{N}} \xi_{ij}(\gamma_{ij}) < 1, \text{ for } i \in \mathscr{M}, j \in \mathscr{N}, \\ 1 \text{ otherwise.} \end{cases} \\
I_6^{ij} &= \begin{cases} 0 \text{ if } \sum\limits_{i\in\mathscr{M}, j\in\mathscr{N}} \beta_{ij}\xi_{ij}(\gamma_{ij}) < 1, \text{ for } i \in \mathscr{M}, j \in \mathscr{N}, \\ 1 \text{ otherwise.} \end{cases}
\end{aligned} \tag{33}
$$

The expressions (25)–(29) form the state vector. The state vector enables the DQN algorithm and maintains a balance between the power of the waveform from the desired user and that from the interfering users.

4.1.3 Reward (r_i)

The action in a state facilitates a reward to the AP i immediately. For each $i \in \mathscr{M}$ and $j \in \mathscr{N}$ at t, actions are made at the CU $a_{ij}(t) \in \mathscr{A}_{ij}$ for the link $i - j$ post observation of $s_{ij}(t)$. The CU reports $\alpha_{ji}(t)$ via a underlying link to the ith AP for $j \in \mathscr{N}\backslash\{\alpha_{ji} = 0\}$. In s_{ij}, a_{ij}, and $\mathscr{A}_{ij}$, for clarity, the subscripts i and j have been removed. The instant reward $R_i(s, a)$ is received in the form of the AP i data rate and is defined as $R_i(s, a)$

$$
R_i(s,a) = \begin{cases} r_{\text{fix}}, & \text{if } \sum_{c=1}^{6} I_c^i > 0, \\ r_i, & \text{otherwise,} \end{cases} \tag{34}
$$

where r_{fix} is a lower reward than the reward gained after breaching the interference limits in any way. When the constraints are met, AP i receives r_i as a reward. The CU will try to determine the best policy for each AP in order to optimize its own r_i. For constraints (21) to (29), the CU makes decisions repeatedly until it finds the best policies for the APs to maximize their respective r_is.

Because r_is are never negative, maximization of $s \sum_{i \in \mathscr{M}} r_i$ may be accomplished by maximizing individual r_is for each AP i. As a result, the CU will use the DQN learning process to identify an optimal policy that maximizes the reward for AP i.

The three vectors, the first one is the action vector, the second one is the state vector, and the last one is the reward, were used to execute learning based on deep Q-network learning. A replay memory collected at the transition point of t and $t + 1$ is facilitated on the CU to store the experience $e_i(t) = \{a_{ij}(t), s_{ij}(t), r_i(t), and s_{ij}(t + 1)\}$. $s_{ij}(t)$, $r_i(t)$, and $s_{ij}(t + 1)$ are obtained by the replay memory from the network. On the other hand, $a_{ij}(t)$ is obtained from the DQN learning output. At each iteration, a small batch extracts training samples from the replay memory. As indicated in Algorithm 1, each iteration comprises of a set number of episodes EP_N, each of which uses one training sample and runs for T time slots. A DQN block is also illustrated, which is where DQN learning takes place. The DQN block's input switch alternates between connecting to the micro batch's output and connecting to the network. It gets the samples for training the time it is associated to the mini batch's output, and it gains information about the state $s_{ij}(t)$ when connected to the network's connection. The selected action $a_{ij}(t)$ is used to create the DQN learning output. The DQN block's output port swaps its connection between two input ports ahead of time. The replay memory receives $a_{ij}(t)$ from the first input port. The second input port sends $a_{ij}(t)$ to the loss, gradient, and parameter upgrading blocks, which results in an improved θ. With the micro batch output, the output of the parameter upgrading block is fed back to the input of the DQN block.

With the use of the state value function $V^{\pi}(s)$ [27], the CU develops an appropriate policy π for AP i to complete the DQN-based learning method. It is the largest discounted sum of immediate rewards $R_i(s, a)$ over a lengthy period of time while following the optimal strategy π. It's written like this in math:

$$V^{\pi}(s, a) = \max_{\pi} \left\{ \sum_{t=0}^{\infty} \zeta^t E(R(s, a))_t | s_t = s, a_t = a, \pi \right\}. \tag{35}$$

The optimal form of action-value function $Q^*(s, a) \triangleq \max_{\pi} V^{\pi}(s, a)$ is calculated using Bellman's equation as follows:

$$Q^*(s, a) = \max_{a \in \mathscr{A}} \{r(s, a) + \zeta Q^*(s', a')\}. \tag{36}$$

where $Q^*(s, a)$ is updated at ζ learning rate. $Q * (s, a)$ iteratively converges to its optimal value for $t \to \infty$ in (35).

As the goal of DQN learning is to build an environment for the agent to do particular behaviors in order to maximize the reward, maximization of $Q(s, a)$ leads to maximization of r_i. The ith AP's achievable data rate, r_i, is the incentive in this work. The state value function $V^{\pi}(s)$ is computed first. The state value function $V^{\pi}(s)$ indicates which state provides the greatest reward, i.e., the achievable data rate r_i, and is written as where

$$R_i(s,a) = \begin{cases} r_{\text{fix}}, & \text{if } \sum_{c=1}^{6} I_c^i > 0, \\ r_i, & \text{otherwise,} \end{cases} \tag{37}$$

The action-value function $Q(s,a)$ is then calculated, indicating the action or policy that the agent should follow in order to obtain the maximum state value. $Q(s,a) = \max_\pi V^\pi(s)$ is the mathematical formula. As a result, maximizing the action - value function maximizes the reward r_i.

Obtaining optimal $Q^*(s,a)$ becomes difficult when vectors are huge. As a result, a function estimator is used to estimate the optimal action-value function. In this approach, [27] was used, where a neural network for this estimation was proposed as $Q(s,a;\theta) \approx Q^*(s,a)$. This approximation is achieved using a fully linked feed-forward multilayer perception (MLP) network in this paper. The DQN-based approach has an advantage because it uses a neural network as the action-value approximator. It adds itexperience replay to increase learning performance in this approximation, in which the CU records the environment's experience at each time step for AP i as $e_i(t) = \{a_{ij}(t), s_{ij}(t), r_i(t), s_{ij}(t+1)\}$ in a replay memory. $D_i(t) = \{e_i(1), \ldots, e_i(t)\}$ represents the replay memory at different time instants. The action-value function approximator $Q(s,a)$ and the target action-value function approximator $Q(s,a;\theta)$ are the two MLP networks used as Q-network approximators. The parameters of the current and prior iterations are θ and θ^-, respectively. The action-state function's current iteration parameter θ is changed with each iteration. This is accomplished using the display memory D_i, which selects a random sample $(a, s, r, \widehat{s})$. After a certain number of iterations, θ^- is updated, and the parameters of the target value function are substituted with the updated θ of the action value function. The technique for updating is carried out using a gradient descent algorithm based on the following cost function:

$$L(\theta_i) = E\left[\left(r_i(s,a) + \zeta \max_{\hat{a}\in A}\left(\widehat{Q_i}(\hat{s},\hat{a},\theta_i^-)\right) - Q_i(s,a,\theta_i)\right)^2\right]. \tag{38}$$

5 Conclusion

The chapter studied the joint asset Allotment optimization problem in a hybrid RF/VLC system in the downlink. The problem is neither concave nor convex, as is observed. A centralized DQN-based learning method based on learning from the hybrid RF/VLC environment has been created to overcome the constraints of standard optimization algorithms in handling such a challenge. The state vector for DQN is based on the bandwidth, power, and connection parameter choices, whereas the action vector is based on the constraint terms in the optimization problem. With the use of an action-value function, the best policy is found. The CU selects the right

Algorithm 1 DQN Network Learning for Hybridized RF and VLC systems

for $i = 0, 1, 2, \ldots, |\mathscr{M}|$ **do**
  Start
  Start the memory vector that contains the state and action vectors
  Start $\pi(a_{ij}|s_{ij}; \theta_i)$ parameter θ_i
  Start the network based on neurons for Q_i with random θ_i
  Start the network based on neurons target action-value function $\widehat{Q}_i$ with $\theta_i^- = \theta_i$
end for
for Iteration =1:K_i **do**
  Get the initial state
  for Episode = 1: $\mathrm{EP_N}$ **do**
    for $t < T$ **do**
      for $i = 0, 1, 2, \ldots, |\mathscr{M}|$ **do**
        Opt $a_{ij}^*(t)$ according to the equation for maximization $j \in \mathscr{N}$
        Select an action

$$a_{ij}(t) = \arg\max_{a_{ij}(t)} Q(s_{ij}(t), a_{ij}(t); \theta_i) \tag{39}$$

        Else another random action has to be selected with probability ϵ
        Change $s_{ij}(t+1)$ and $r_i(t)$ as per (33) and (37)
        Store $e_i(t) = (a_{ij}(t), s_{ij}(t), r_i(t), s_{ij}(t+1)$ in the vector D_i designed for storing experience for ith AP.
        Change the present θ_i of $Q(s_{ij}(t), a_{ij}(t); \theta_i)$, by means of sampling of the mini batch of transitions from $D_i(t)$
        After every constant number of steps, change $\theta_i^- = \theta_i$
        Receive samples of batch which is mini sized from the replay memory
      end for
    end for
  end for
end for
Perform $r = \sum_{i \in \mathscr{M}} r_i$

bandwidth, power, and connection parameter values from the action vector set to choose the best action for optimal policy formulation.

References

1. P.H. Pathak, X. Feng, P. Hu, P. Mohapatra, Visible light communication, networking, and sensing: a survey, potential and challenges. IEEE Commun. Surveys Tutorials **17**(4), 2047–2077 (2015)
2. J. Luo, L. Fan, H. Li, Indoor positioning systems based on visible light communication: state of the art. IEEE Commun. Surveys Tutorials **19**(4), 2871–2893 (2017)
3. A.-M. Căilean, M. Dimian, Current challenges for visible light communications usage in vehicle applications: a survey. IEEE Commun. Surveys Tutorials **19**(4), 2681–2703 (2017)
4. O. Babatundi, L. Qian, J. Cheng, Downlink scheduling in visible light communications, in *2014 Sixth International Conference on Wireless Communications and Signal Processing (WCSP)* (IEEE, New York, 2014), pp. 1–6

5. M. Obeed, A.M. Salhab, M.-S. Alouini, S.A. Zummo, On optimizing VLC networks for downlink multi-user transmission: a survey. IEEE Commun. Surveys Tutorials **21**(3), 2947–2976 (2019)
6. Q. Ye, B. Rong, Y. Chen, M. Al-Shalash, C. Caramanis, J.G. Andrews, User association for load balancing in heterogeneous cellular networks. IEEE Trans. Wireless Commun. **12**(6), 2706–2716 (2013)
7. X. Qiu, K. Chawla, On the performance of adaptive modulation in cellular systems. IEEE Trans. Commun. **47**(6), 884–895 (1999)
8. A. Khreishah, S. Shao, A. Gharaibeh, M. Ayyash, H. Elgala, N. Ansari, A hybrid RF-VLC system for energy efficient wireless access. IEEE Trans. Green Commun. Networking **2**(4), 932–944 (2018)
9. L. Li, Y. Zhang, B. Fan, H. Tian, Mobility-aware load balancing scheme in hybrid VLC-LTE networks. IEEE Commun. Lett. **20**(11), 2276–2279 (2016)
10. R. Zhang, Y. Cui, H. Claussen, H. Haas, L. Hanzo, Anticipatory association for indoor visible light communications: light, follow me! IEEE Trans. Wireless Commun. **17**(4), 2499–2510 (2018)
11. S. Bayat, R.H.Y. Louie, Z. Han, B. Vucetic, Y. Li, Distributed user association and femtocell allocation in heterogeneous wireless networks. IEEE Trans. Commun. **62**(8), 3027–3043 (2014)
12. I. Stefan, H. Haas, Hybrid visible light and radio frequency communication systems, in *2014 IEEE 80th Vehicular Technology Conference (VTC2014-Fall)* (IEEE, New York, 2014), pp. 1–5
13. M. Kashef, M. Ismail, M. Abdallah, K.A. Qaraqe, E. Serpedin, Energy efficient resource allocation for mixed RF/VLC heterogeneous wireless networks. IEEE J. Sel. Areas Commun. **34**(4), 883–893 (2016)
14. M.F. Marzban, M. Kashef, M. Abdallah, M. Khairy, Beamforming and power allocation for physical-layer security in hybrid RF/VLC wireless networks, in *2017 13th International Wireless Communications and Mobile Computing Conference (IWCMC)* (IEEE, New York, 2017), pp. 258–263
15. M. Kafafy, Y. Fahmy, M. Abdallah, M. Khairy, Power efficient downlink resource allocation for hybrid RF/VLC wireless networks, in *2017 IEEE Wireless Communications and Networking Conference (WCNC)* (IEEE, New York, 2017), pp. 1–6
16. J. Kong, Z.-Y. Wu, M. Ismail, E. Serpedin, K.A. Qaraqe, Q-learning based two-timescale power allocation for multi-homing hybrid RF/VLC networks. IEEE Wireless Commun. Lett. **9**(4), 443–447 (2019)
17. V.K. Papanikolaou, P.D. Diamantoulakis, P.C. Sofotasios, S. Muhaidat, G.K. Karagiannidis, On optimal resource allocation for hybrid VLC/RF networks with common backhaul. IEEE Trans. Cogn. Commun. Networking **6**(1), 352–365 (2020)
18. M. Kashef, M. Abdallah, N. Al-Dhahir, K. Qaraqe, On the impact of PLC backhauling in multi-user hybrid VLC/RF communication systems, in *2016 IEEE Global Communications Conference (GLOBECOM)*, pp. 1–6 (2016)
19. J.R. Barry, D.G. Messerschmitt, *Wireless Infrared Communications* (Kluwer Academic Publishers, USA, 1994)
20. P. Kyosti, J. Meinila, et al. *WINNER II Channel Models* (D1.1.2 V1.2. IST-4-027756 WINNER II, USA, 2007)
21. A. Lapidoth, S.M. Moser, M.A. Wigger, On the capacity of free-space optical intensity channels, in *2008 IEEE International Symposium on Information Theory*, pp. 2419–2423 (2008)
22. A.A. Farid, S. Hranilovic, Capacity bounds for wireless optical intensity channels with Gaussian noise. IEEE Trans. Inf. Theory **56**(12), 6066–6077 (2010)
23. A. Chaaban, J. Morvan, M. Alouini, Free-space optical communications: capacity bounds, approximations, and a new sphere-packing perspective. IEEE Trans. Commun. **64**(3), 1176–1191 (2016)
24. X. Qiu, K. Chawla, On the performance of adaptive modulation in cellular systems. IEEE Trans. Commun. **47**(6), 884–895 (1999)

25. S.C. Chen, N. Bambos, G.J. Pottie, Admission control schemes for wireless communication networks with adjustable transmitter powers, in *Proceedings of INFOCOM '94 Conference on Computer Communications*, vol.1, pp. 21–28 (1994)
26. S. Pietrzyk, G.J.M. Janssen, Radio resource allocation for cellular networks based on OFDMA with QoS guarantees, in *IEEE Global Telecommunications Conference, 2004. GLOBECOM '04.*, vol. 4, pp. 2694–2699 (2004)
27. V. Mnih, K. Kavukcuoglu, D. Silver, A.A. Rusu, J. Veness, M.G. Bellemare, A. Graves, M. Riedmiller, A.K. Fidjeland, G. Ostrovski, S. Petersen, C. Beattie, A. Sadik, I. Antonoglou, H. King, D. Kumaran, D. Wierstra, S. Legg, D. Hassabis, Human-level control through deep reinforcement learning. Nature **518**(7540), 529–533 (2015)

Mechanical Engineering Challenges in Machining of Terahertz Waveguide Components

Rakesh Kumar Bhardwaj, V. P. Dutta, and Naresh Bhatnagar

Abstract The demand of high-speed wireless communication has increased, which needs the data rate of the order of Terabyte per second (Tbps) in near future. Terahertz (THz) band communication is a key wireless communication technology to satisfy this future demand. This will also reduce the spectrum scarcity and capacity limitation of current wireless systems. Micro fabricated folded waveguides are potential compact source of wideband and high-power terahertz radiation. This chapter primarily focuses on machining technology for THz waveguide components requiring ultra-high precision micromachining. Rectangular waveguides especially folded waveguides are even more difficult to manufacture using conventional machining techniques due to their small size and very tight tolerances. The criticalities in micromachining of Terahertz waveguide Components starting from 100 to 1100 GHz have been developed mechanically in this research work. Free cutting brass IS 319-H_2 and AL alloy IS:736 24345 WP were used as work materials due to its electrical and mechanical properties. Waveguide size as small as 0.254 × 0.127 mm was micro machined within ±3 to 5 μm linear tolerances, surface roughness of the order of 0.045 μm Ra and flatness less than 0.3 μm (<λ/2). The split top and bottom blocks of the waveguide were aligned by dowel pins which are matched within a tolerance of ±5 μm. The perpendicularity and parallelism were maintained within ±5 μm tolerance as per IS:8000-1975. This work explored and established the application of micro milling as reasonably suitable for the THz waveguides followed by ultrasonic cleaning. Waveguide above 1.1 THz having waveguide size as small as 75 μm × 37.5 μm was also realized using femtosecond laser within nanometer level accuracies.

R. K. Bhardwaj (✉)
Department of Mechanical Engineering, Indian Institute of Technology, Delhi 110016, India
e-mail: rk.bhardwaj.deal@gov.in

R. K. Bhardwaj · V. P. Dutta · N. Bhatnagar
Defence Electronics Applications Laboratory, Raipur Road, Dehradun, Uttrakhand 248001, India
e-mail: nareshb@mech.iitd.ac.in

M. El Ghzaoui et al. (eds.), *Terahertz Wireless Communication Components and System Technologies*, https://doi.org/10.1007/978-981-16-9182-9_15

1 Introduction to Terahertz Waves and Terahertz Technology

Terahertz technology is described under different subheadings as under.

1.1 EM Waves and Their Propagation

The Electromagnetic wave (EM wave) is created by a disturbance in electric or magnetic field locally. When magnetic field changes, it induces electric field, so that a series of electrical and magnetic oscillations are formed resulting in propagation of EM waves. From the origin (source), the wave propagates uniformly outward in all directions. An EM wave or radio wave propagates outward from the source such as antenna at the speed of light. The propagation of EM waves in a medium or vacuum is due to mutual changes between magnetic and electric field. All waves transmit energy through empty space. A medium is the material through which EM waves travel (Fig. 1) .

1.1.1 EM Spectrum

Electromagnetic energy is an arrangement of broad to short waves. The examples of broad waves are radio waves, whereas gamma rays are short waves. The electromagnetic radiations are reflected or absorbed by water vapors [1].

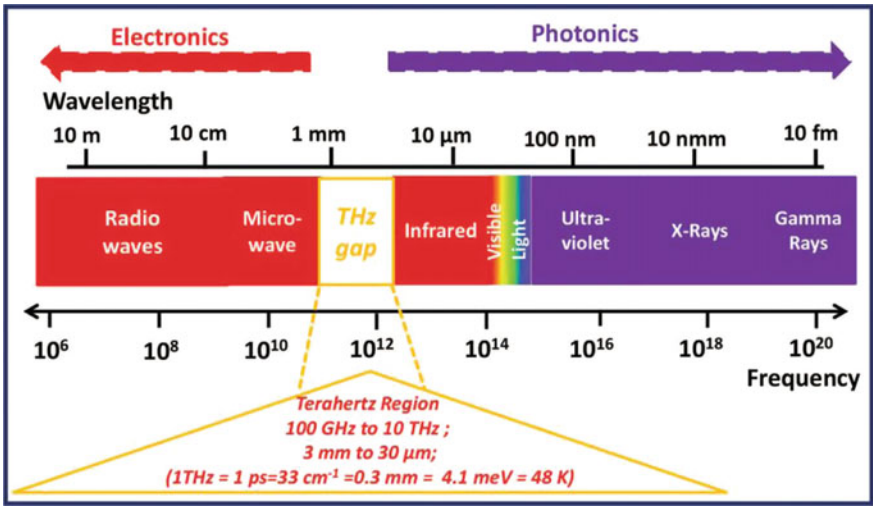

Fig. 1 Electromagnetic radiation spectrum [1]

1.2 Introduction to Waveguides

Waveguide is a device to guide electromagnetic energy from one region to another. In general, waveguides are hollow rectangular/circular metal tubes. The waveguide acts as a high pass filter in which most of the energy above the cutoff frequency will pass through the waveguide, whereas the energy below the cutoff frequency will be attenuated by the waveguide. Figure 2a shows the electric and magnetic fields of a wave whereas, Fig. 2b shows the waveguides.

Waveguides are often used at frequencies greater than 300 MHz being more common above 8 GHz. Waveguides are wideband devices used to transmit either power or communication signals [2]. A hollow metal rectangular waveguide is shown in Fig. 2c. Figure 3 shows different cross section geometries of waveguides.

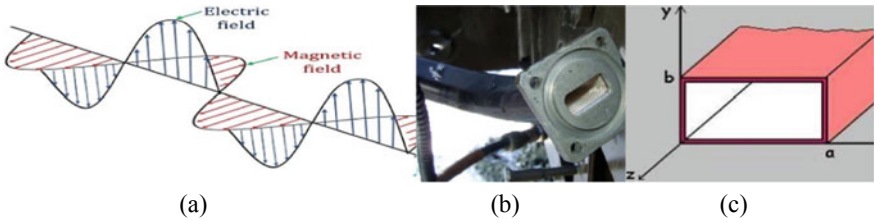

Fig. 2 **a** Electric and magnetic fields, **b** waveguide bend, **c** cross section of a waveguide

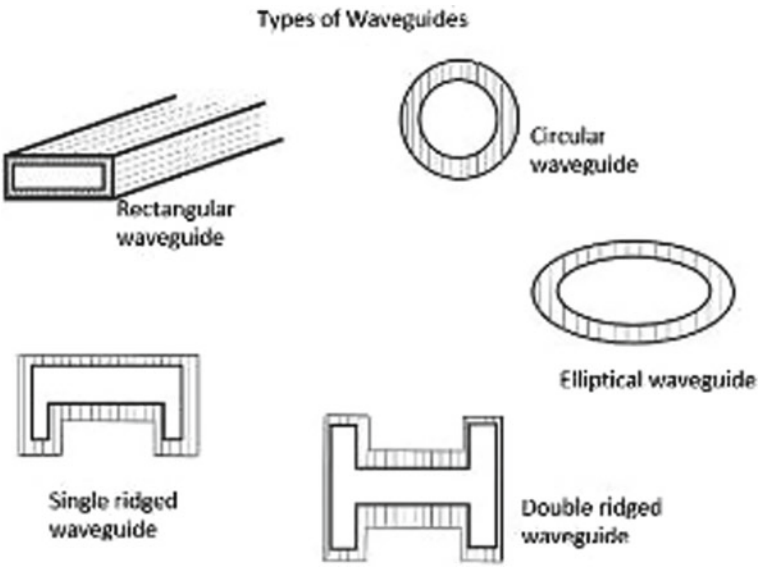

Fig. 3 Types of waveguide cross sections [3–6]

The waveguide has a width 'a' in the x-direction and a height 'b' in the y-direction with $a > b$ as shown in Fig. 2c. Power is transmitted in Z direction. The cutoff frequency f_c is the frequency at which all lower frequencies are attenuated by the waveguide. The formula for the cutoff frequency of a rectangular cross sectioned waveguide is given by:

$$f_c = \frac{1}{2a\sqrt{\mu\varepsilon}} = \frac{c}{2a} \quad \text{Rectangular cross section} \tag{1}$$

wherein, in Eq. (1), c is the speed of light within the waveguide, μ is the permeability of the material (air) that fills the waveguide and ε is the permittivity of the material (air) that fills the waveguide. Note that the cutoff frequency is independent of the short length 'b' of the waveguide.

1.2.1 Waveguide Cutoff Frequency for Rectangular Waveguide

The cutoff frequency of a waveguide varies according to its cross section. The cutoff frequency for a rectangular waveguide can be calculated using the formula given as [7, 8]:

$$f_c = c/2a$$

where:

f_c is rectangular waveguide cutoff frequency in Hz
c is the speed of light within the waveguide in meters per second, and
a is the large internal dimension of the waveguide in meters.

1.3 Frequency Bands and Designations

Hestler et al. [9] have recommended the waveguide sizes and interfaces at various frequency range up to 1.1 THz in his publication, which are backwards compatible with MIL-DTL 3922/67C. Table 1 gives the current standard series of waveguide bands starting from WR-10 up to WR-1 as specified in MIL-DTL-85/3C.

Rectangular Waveguides are denoted by WR, whereas the number that follows gives the width of the waveguide opening in mils divided by 10. EIA is environment impact assessment and ALMA stands for Atacama large millimeter/submillimeter wave array, which controls the environment under the guidelines of United Nation Environment protection (UNEP). Certain bands at higher frequencies are rounded off for convenience.

Tolerances can be calculated w.r.t. the tolerances at WR-10 using the formula as given in Eq. 2.

Table 1 Current and proposed waveguide bands, Hestler et al. [9]

Proposed band designation	EIA band designation	Internal dimensions (mils)	Internal dimensions (mm)	Frequency range (GHz)	TE (10) Cutoff (GHz)
WR-10	WR-10	100 × 50	2.540 × 1.270	75.0–110.0	59.0
WR-8	WR-8	80 × 40	2.032 × 1.016	90.0–140.0	73.5
WR-6.5	WR-6	65 × 32.5	1.651 × 0.826	110.0–170.0	90.8
WR-5.1	WR-5	51 × 25.5	1.295 × 0.648	140.0–220.0	116
WR-4.3	WR-4	43 × 21.5	1.092 × 0.546	170.0–265.0	137
WR-3.4	WR-3	34 × 17	0.864 × 0.432	220.0–300.0	174
WR-2.8	Undefined	28 × 14	0.711 × 0.356	265.0–400.0	211
WR-2.2	Undefined	22 × 11	0.559 × 0.279	330.0–500.0	268
WR-1.9	Undefined	19 × 9.5	0.483 × 0.241	400.0–600.0	311
WR-1.5	Undefined	15 × 7.5	0.381 × 0.191	500.0–750.0	393
WR-1.2	Undefined	12 × 6	0.305 × 0.152	600.0–900.0	492
WR-1.0	Undefined	10 × 5	0.254 × 0.127	750.0–1100.0	590

$$\text{Tolerances at any Freq. } f\,(\text{GHz}) = (\text{Tolerances at WR} - 10) \times (100/f) \quad (2)$$

1.4 Worldwide Status of Terahertz Technology

Tematys [10] a team of expert consultants, who provide consultation to various research and development organizations have published a market and technology trend report in 2016 on Terahertz components and systems. As shown in Fig. 4, Terahertz detectors were realized in 1985 and the THz source got developed in the next ten years. More compact detectors arrays were made in 2010 and now the world is working on low-cost and fast THz components. It is expected that by 2022, THz components will be available for the researchers to design systems for various applications in Defense, Biomedical, Industrial and other areas. The market

Industrial and other applications.

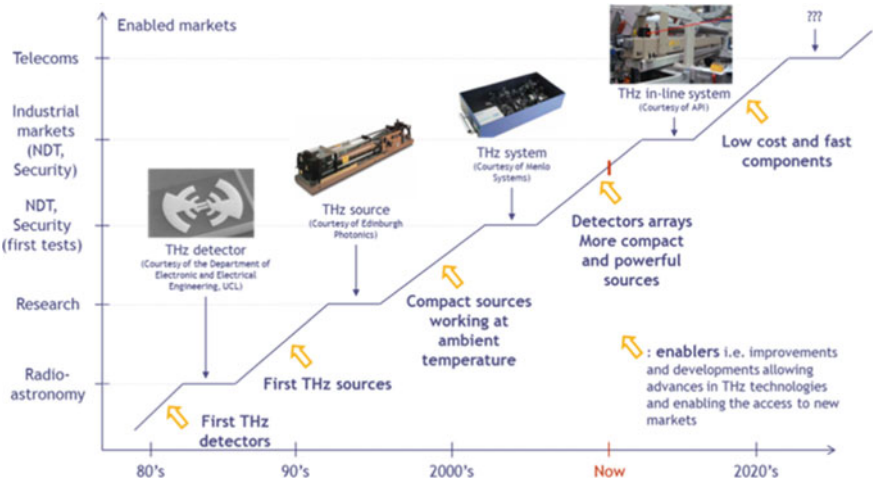

Fig. 4 Status of Terahertz techology and systems, © Tematys [10]

revenue of THz technology has grown to 40–100 million € in the last five years, which clearly indicates huge demand of this technology in the near future [10]. World over companies like Tera view, ADVENTEST, RP Photonics, Virginia Diode Inc., Toshiba and Zomega, etc. are working to develop THz technology. Also, some lab-level systems are being reported in the literature now a days.

1.5 Status of Terahertz Technology in India

Defence Research and Development organization (DRDO) one of the leading research and development organization working for Indian defense has published a paper in 2019 authored by Rehman et al. [11]. They gave the status of THz technology with future roadmap. Table 2 gives the institutions working in the field of Terahertz technology with research area.

1.6 Micromachining of Waveguide

Micromachining is a wider term, in the context of THz. Researchers [12–16] used different methods to realize lab-level THz components using micromachining. Bruneau et al. [17] of jet propulsion laboratory of NASA successfully realized THz metallic waveguides without sharing any of the mechanical manufacturing details. Deep reaction ion etching, Micro molding and Laser micromachining are another

Table 2 Institution wise status of THz technology in India [11]

	Institutes	Area of research
Sources and detectors	IIT Delhi	mm-wave electronic transmitters, spin-based THz sources, time domain, and CW THz set-up, THz waveguides machining and fabrication
	IISER, Trivandrum	Semiconductor hetero-structure alloys as THz sources
	TIFR, Mumbai	SI-GaAs THz sources, THz-ultrafast studies
Signal processing and devices	IIT Guwahati	THz metamaterial structures for the active–passive THz devices
	IIT Bombay	mm-wave signal processing
Channels	CEERI-Pilani	THz waveguides in Silicon for the short-range communication channel, multiplexer/demultiplexer
		mm-wave remote and atmospheric sensing, atmospheric transmission

popular method for realization of THz components. A deep understanding of chemical machining is required for the micro fabrication of components through them, and every material has different chemical affinity behavior and process parameters. The processes described so far can produce 2-D components in x–z plane, but tool based micro milling or conventional micro milling can produce 3-D components, in which linear, circular and helical interpolation is also possible with precise control of dimensions. Moreover, any material can be machined using micro milling and therefore it is very suitable for small lot size and research purposes. This research work will first focus only on tool based micro milling and Femtosecond laser machining for successful realization of THz waveguide components for the different frequency bands. Following are a few of the micromachining techniques for the development of waveguides at different frequencies.

1.6.1 Tool Based Micromachining/Mechanical Micromachining

Researchers [18, 19] have investigated various aspects of micromachining but there are no reported studies with regard to electromechanical components especially micromachining of THz components. Though all the aforementioned studies are of importance to carry out machining research work, these are adapted wherever possible in the machining of present THz waveguides. However Nordquest et al. [12] have successfully fabricated a metallic waveguide at 3THz, though they have also cut silicon substrate and placed it in a metallic cavity. Groenendijk et al. [13] have discussed the microstructure of metallic surface cut by Femtosecond laser. Micro milling can machine, metals, alloys, polymers, composites and ceramics into 3-D

shapes within accuracy of 10^{-3} to 10^{-5} (sub-micron). 3-D components for various applications can be machined using macro or micro machines at low or high production volume with much higher accuracies than MEMS based process which gives an accuracy of 10^{-1} to 10^{-3} only. As it is known that with an increase in frequency the wavelength reduces and hence waveguide size also reduces which makes the components much smaller in size and more sensitive to tolerances. For example, the cross section of a typical rectangular waveguide at 94 GHz is **2.54 × 1.27** mm, at 330 GHz, the size shrinks to **0.711 × 0.356 mm**. Similarly, the waveguide size reduces to **0.381 × 0.191** mm at 625 GHz and **0.254 × 0.127** mm at 1 THz.

1.6.2 MASK Based Micromachining/Silicon Micromachining

Mask Based micromachining is having following major technologies:

- Dry & Wet Etching
- Plasma Etching
- LIGA Process
- Electroforming

LIGA technology is well suited for the mass fabrication of parts, particularly in polymers. Many micro-systems benefit from the unique characteristics and advantages of the LIGA process in terms of product performance [14]. However, for metals like brass and copper, it may not be the right technique.

1.6.3 Micro Molding

Sammoura et al. [15] developed a waveguide with integrated flanges at 95 GHz and tested it. The plastic waveguide can be fabricated by hot embossing and electroplating technology. Plastic waveguides can be made in batches.

Signal transmission up to 77.8% is achieved by micro molding developed. This enables the use of components in all—weather conditions like weather monitoring, airplane radars, astronomy, etc. Conventional methods fabricate rectangular metal waveguides and later flanges are brazed. However, at high-frequency feature sizes are too small and micromachining is the right technology to meet the requirements. However, for such molding first of all micromachining of mold is required and later during mold filling, defects like shrinkage, sink marks, porosity may occur, which are serious at higher frequencies due to very small waveguide size. However, waveguide for Ka and Ku band has been reported in literature, which was made through micro molding.

1.6.4 Laser Micromachining

Laser micromachining is a general term used for making tiny features in parts measured in micrometer with extreme precision. It is also used for controlled cut, drill or scribe of material. Hence, Laser machining can be applied for machining the THz waveguides on metallic blocks without generating heating or mechanical damage like warping or loss of size and strength. It is also established that laser micromachining can fabricate metallic rectangular waveguides on Brass, Aluminum alloy, Magnesium alloy and 99% pure Copper. Therefore, these micromachining techniques can be used for fabricating waveguide of sizes corresponding to the frequency of 1 THz, 3 THz and 10 THz with desirable tolerances, surface roughness, flatness, perpendicularity and parallelism. One such laser micromachining technique is by using Femtosecond laser. The smallest duration of pulse makes femtosecond laser a feasible candidate for waveguide machining and it is also available at the Central Research Facility (CRF), IIT Delhi. Thus, efforts will be made to compare fabricated waveguide components at 1.1 THz by this technology with Kern micromachining. Researchers have worked on Lithography for development of waveguides, where they have developed a low frequency waveguide using micro molding. Researchers [20–29] have also used laser micromachining with CW fiber laser, Nanosecond laser and femtosecond laser for realizing various devices mostly on substrates and non-metallic materials.

1.7 Applications of Terahertz Band

Over the past several years, there has been increased interest in the potential of terahertz sensors for imaging of concealed weapons, explosives and chemical agents [16, 18, 30–35]. The THz application at the nano, micro and macro scale is discussed in the following sections and depicted in Fig. 5. Applications in the area of Defense, Industries, Biomedical and other areas are shown in detail.

1.8 Mechanical Engineering Challenges in THz Technology

Suppose the geometry of the waveguide was not maintained as per IEEE guidelines and MIL standards. In that case, the inside surface of waveguide dimensions will not be as desired and rough. Under these conditions, electromagnetic waves that are designed to an incident on smooth surface undergo reflection in the specular direction are scattered diffusely resulting in loss of intensity in the specular direction. THz components should satisfy all geometrical tolerances in addition to linear tolerances such as flatness, positional tolerances, cylindricity, parallelism, squareness, surface roughness, etc. need to be achieved according to standards.

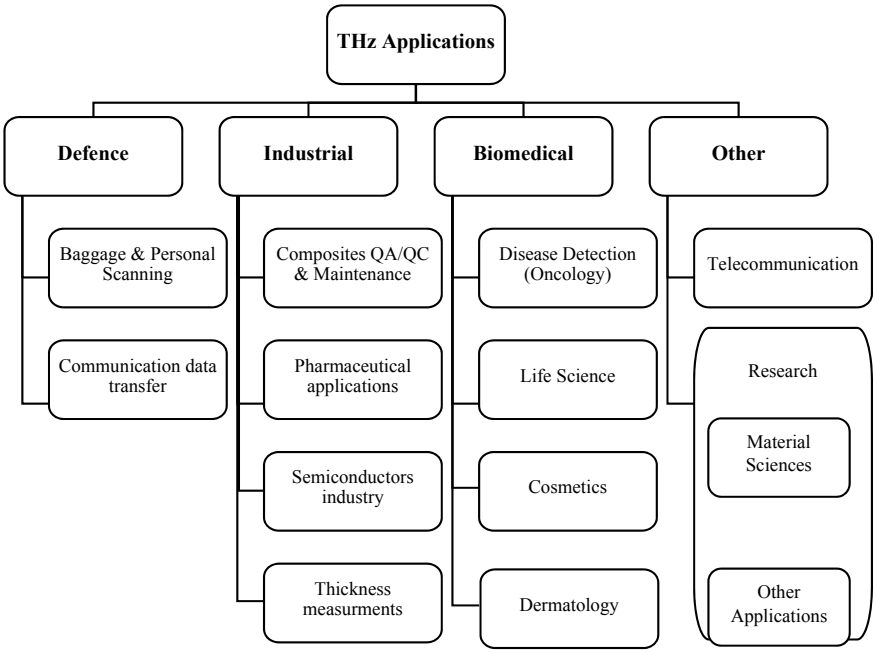

Fig. 5 Applications of terahertz technology [10]

1.8.1 Mechanical Design Methodology

Various open sources and book articles have elaborated the design and analysis of waveguides at different frequency bands [21–24]. The Software Ansoft Corporation, version 9, USA was used for the design of waveguides. The material selected for waveguides was Brass. The length of 25 mm was kept constant for all waveguide section. The theoretical design of waveguide is described in the textbooks Kulkarni [26], Kraus [27], Prasad [28], Mathew [29], Liao [36], Harrington [37], Balanis [38] and Collin [39]. Teja et al. [40] have studied the wave characteristics and field distribution traveling in different media in rectangular waveguides by using a High space structural system (HFSS). They explored different electrical as well as magnetic field strength parameters inside the waveguide and developed fundamental model distribution at the X-band. The two waveguide sizes considered by them were 32.86 × 20.16 mm and 22.86 × 10.16 mm, respectively. Researchers [3, 41–44] have designed and developed THz components based on analytical design and software simulations. The components designed by them are Filters in THz and Sub-THz region, Metal-dielectric-metal waveguide, Metal V-grove waveguide, Sub-THz channels for low-cost Interconnects and rectangular metal waveguide with and without ridges. Sudhamani et al. applied these design and analysis strategies to develop variety of THz components [4–6, 45–48].

1.8.2 Material Selection

The properties of material like electrical conductivity, permeability and permittivity play a very important role for the propagation of electromagnetic waves. Hence it is very important to choose materials according to the electrical requirements in addition to structural properties. The half-hard free cutting brass IS 319–H2 (Cu: 61%, Zn: 36%, Pb: 3%) was selected for straight and folded waveguide structure (FWS) due to its high strength, corrosion resistance and good dimensional stability over a long period [49]. In the same way, some researchers [50–56] define the properties and advantages of using Al-Alloy, OFHC, Mg Alloy, Silicon family, Graphene and polymeric materials for waveguides. In addition to that many-more researchers have used different materials for realization of THz waveguide components and their characterization [57–63].

1.8.3 Waveguide Interface Standards

Hadeel et al. [64] in 2020 emphasized the importance along with status of technology and a very good review of literature stream wise. He has described time line standardization shown in Fig. 6. They compiled the data of achievable data rate and propagation distance at frequency starting from 100 to 625 GHz along with the technology through which it was achieved. According to the data presented, a propagation distance as high as 1500 m was achieved at 140 GHz using 16QAM modulation with the power of −5 dBm through CMOS SHM technology. Similarly,

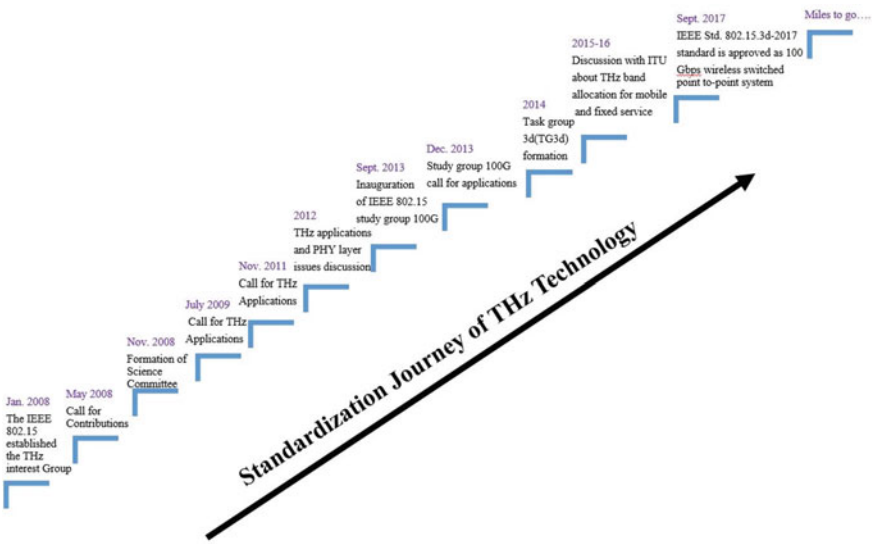

Fig. 6 Standardization journey of THz technology

a propagation distance of 850 m at 240 GHz and 3.8 m at 450 GHz was obtained using various modulation schemes and technologies. Most of the papers published between 2014 and 2019 were focusing on modulation schemes, technologies and source developments.

1.8.4 Misalignments in Waveguides

Kerr et al. [64, 65] have studied the configuration of the waveguide and measured the waveguide losses due to misalignment at connection through flanges. Cases like misalignment in the *x*-direction, *y*-direction, *x* and *y*-direction, rotation about a point or combinations of misalignments were presented in his study. It was learned that misalignment of 75–250 μm in *x*-direction leads to a loss S11 of the order of −40 to −20 dB. All the possible cases are shown in Fig. 7. Though the measurements were done at the W band, hence the impact of misalignments will be much higher at THz frequency. If the corners of the waveguide are not sharp, the nose radius should be minimum possible and does not exceed 2% of dimension '*a*' as shown in Fig. 7.

Similarly, the error in waveguide during micromachining due to mismatching of lower and upper block called misalignment. Literature shows that bilateral tolerances are better in terms of electric performance, where any misalignment should not be greater than 2% of dimension '*a*'. On the other hand, the Geometrical tolerances like surface roughness, perpendicularity between '*a*' and '*b*', the flatness of mating surfaces of the upper and lower part, positional tolerances of the flange dowel pins also need to be maintained with close tolerance to the target values depending on the respective frequency band. Measuring residual stresses is not a trivial matter. A large number of researchers have concentrated on improving the measurement technologies. By far, the most popular type of measurement is based on diffraction methods as reported by Jawahir et al. [66], Withers et al. [67], Fitzpatrick et al. [68] and Noyan et al. [3]. The Bragg's law was adopted from [68] as it explained the science behind X-Ray diffraction. Residual stresses were not measured directly from this measurement as we only get 'd' the new spacing from which strain is calculated and then stress was computed by the software available on measurement system.

Fig. 7 Effect of misalignment of waveguide ports on power losses

1.8.5 Tolerances

All the Linear dimensions of waveguide crossection were adopted from Hestler et al. [9]. It is evident from his study that when the frequency increases tolerance become stringents. For example, at WR-10 the linear tolerance is ±12 μm, which becomes ±1 μm at WR-1. Whereas, the gemotrical tolerance like surface roughness, flatness, positiobnal tolerence prallelism and perpendicularity also infulance the perforamce of waveguides. As per the study of Kerr et al. [65], if the cross section configuration of waveguide is not maintained will result to power losses.

Linear Tolerances

Since, the waveguide size depends on the wavelength (λ) hence variation os waveguide size is critical. The waveguide size governs the cutoff frequency of the waveguide. If the size '*a*' and '*b*' is not maintained close to the design values, the characteristics of waveguide such as cutoff frequency will not be maintained and cause the power loss [69].

Geometrical Tolerances

The complete configuration of the waveguide depends not only on the linear tolerances but the geometrical tolerances are equally important to establish cutoff frequency and effective propagation of EM waves. The important geometrical tolerances like surface roughness, flatness, perpendicularity, parallelism, straightness and positional tolerances are discussed in following sections.

Effect of Surface Roughness and Skin Depth

Wang et al. [69] studied the effect of surface roughness on the conductor and reported three basic types of losses in THz guiding structures named Radiation, dielectric and conductor loss. Absorption ratio increases with the increase in roughness height. At different frequencies, the power absorption was observed for different root mean square (RMS) heights and it was deduced that with increasing RMS height (up to 0.1 μm), the power absorption goes higher. The trend is similar for both the metals studied i.e., Copper and Aluminum. Chen et al. [71] have studied the Lossy rectangular waveguide and effect of surface roughness on their performance. They have found that as the correlation length and frequency increase, the attenuation decreases and propagation constant increases. Chen et al. [72] have analyzed lossy rectangular waveguide on similar lines, containing rough inner surface. Popalghat et al. [73], Sau rez et al. [74] and Li et al. [75] also contributed a lot in the study of surface roughness and its effects on propagation. Klein et al. Diana Gamzina et al. [76] published a research paper in 2015 highlighting the Nano surface roughness effect on THz vacuum.

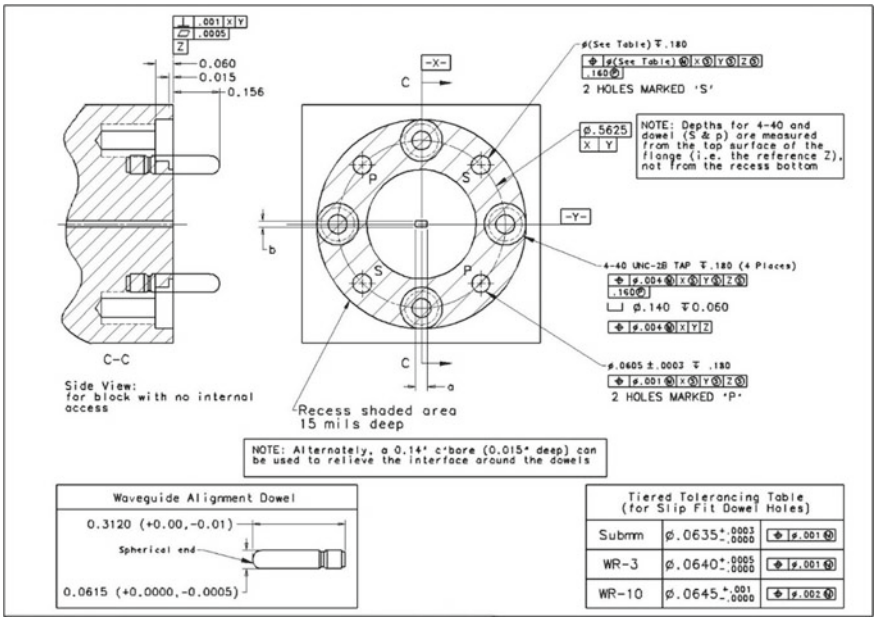

Fig. 8 Recommended waveguide interface from WR-10 to WR-1 [9]

Flatness

The flatness of two mating waveguide blocks is important to minimize the power losses occurring due to leakage of energy. It should be of the order of half the wavelength. The flatness can be measured using interference of monochromatic light [77].

Other Geometrical Tolerances

Figure 8 shows the importance of positional and form tolerances for proper mating of discrete components to avoid any misalignments between two components. The alignment pin and pin-hole tolerances at the interface are crucial for proper matching of two waveguides in order to minimize the plumbing losses.

The achievable angular alignment limit is generally set by the skill of humans and the accuracy of jigs and fixtures being used at the manufacturing facility. Reflection at the interface can be minimized by achieving tight tolerances on the interface being an integral part of waveguide through CNC machines. The desired linear and geometrical tolerances are shown in Fig. 8.

1.9 Micromachining

Since to achieve desirable magnitude of linear and geometrical tolerances for fabricating THz waveguide falls beyond the capability of conventional machining. According [7, 8, 13, 14, 78–85] the micromachining can be the only available method to achieve the critical parameters of THZ waveguides. Few reported studies are published with regard to electromechanical components especially micromachining of THz straight as well as folded waveguide (FWG) structures [4, 45–48, 86]. Though all the aforementioned studies are of importance to carry out machining research work, these are adapted wherever possible in the machining of present THz waveguides. Prakash et al. [79] used CO_2 laser for creating microfluidic channels which are geometrically like waveguides. Researchers [13] have worked on Lithography for development of waveguides, whereas [14] have developed a low frequency waveguide using micro molding. Researchers [7, 8, 78–84] have used laser micromachining like CW fiber laser, Nanosecond lase and femtosecond laser for realizing various devices mostly on substrates and non-metallic materials. However, Ganti et al. [83] have successfully fabricated a metallic waveguide at 3THz, though they have also cut silicon substrate and placed it in a metallic cavity. Groenendijk et al. [13] have discussed the microstructure of metallic surface cut by femtosecond laser. More details on micro milling and Femtosecond laser machining are provided in subsequent articles. The specific contributions of following authors helped to plan the micromachining strategies in particular. Bruneau et al. [17] in his research paper has successfully developed and demonstrated the metallic THz waveguide using tool based micro milling.

1.9.1 Micro Milling

Micro milling can machine, metals, alloys, polymers, composites and ceramics into 3-D shapes within accuracy of 10^{-3} to 10^{-5}(sub-micron). 3-D components for various applications can be machined using macro or micro machines at low or high production volume with much higher accuracies of order 10^{-1} to 10^{-3}, better than MEMS based process.

Many researchers [87–98] have studied various aspects of micro milling such as surface roughness, minimum uncut chip thickness (MUCT), ploughing, size effect, vibration, burr formation, force measurements, minimum quantity lubrication, etc. Aramcharoen et al. [99], Vazquez et al. [85] and Jain [49] have achieved and described stringent tolerances using tool based micro cutting.

According to Zhang et al. [100], the vibration occurring is active and negative. He suggested strategies for reducing vibrations during micro milling. Guillem et al. [101] presented chatter and strategies for suppression of chatter to get better surface finish. Researchers [102–106] discussed burr formation in details along with their location of occurrence. Strategies for minimization burr formation were also discussed. Machine tool construction for micromachining and error sources were discussed by Lamikiz

et al. [107] and Hashmi et al. [108] especially the Abb's error and correction methods along with isolation from external vibrations.

1.9.2 Femtosecond Micromachining

Bookey et al. [78] had used Femtosecond laser for producing THz waveguide having insertion loss below 3.5 dB at 1550 nm. To fabricate the waveguide, he used 370-nJ pulses focused on approximately 150 μm below the surface of sample. Shafique et al. [7] created microwave trenches for substrate integrated waveguides in low temperature confined ceramics (LTCC) technology for micro and nano drilling. Li et al. [109] could micromachine two-anode frequency tippler at 900 GHz consisting feature size as small as 30 μm to 60 μm. Another important work was published by Nordquist et al. [12] in which waveguide of size 75 μm × 35 μm at 3THz was micromachined. This was probably the smallest metal waveguide reported in literature. On the other hand, Groenendijk et al. [13] have reported surface microstructure by femtosecond laser pulses. On the similar lines [83] and [84] have also explored and described femtosecond laser for high tech use and have explained the science behind it.

1.9.3 Importance of Geometrical Tolerances in Context of THz Waveguides

Suppose the geometry of the waveguide was not maintained as per IEEE guidelines and MIL standards. In that case, the inside surface of waveguide dimensions will not be as desired and rough. The subsequent sections describe almost all geometrical tolerances in addition to linear tolerances, named Flatness, positional tolerances, cylindricity, parallelism, squareness, surface roughness, etc. They need to be achieved in totality and not partially. This is a classic example of criticality in realizing THz waveguide components.

1.9.4 Effect of Surface Roughness

Wang et al. [85] investigated the influence of surface roughness on the conductor at terahertz frequency and reported three basic types of losses in THz guiding structures named Radiation, dielectric and conductor loss. It was observed from work carried by Wang that the absorption ratio increases with frequency. At different frequencies, the power absorption was observed for different root mean square (RMS) heights, and it was deduced with increasing RMS height (up to 0.1 μm), the power absorption goes higher. The trend is similar for both the metals studied, i.e., Copper and Aluminum. From this, it can be concluded that there is a direct effect of surface roughness on the waveguide characteristic. Figure 9a, b show the variation of power absorption ratio with the increase of frequency at different (RMS) for Copper and Aluminum, respectively.

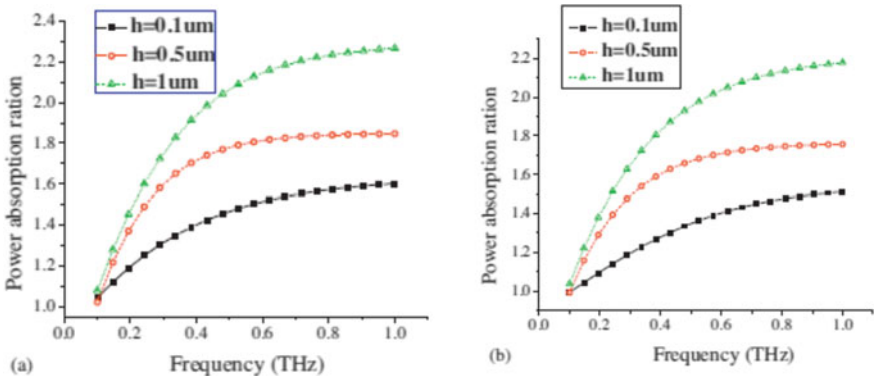

Fig. 9 **a** Power absorption ratio for different RMS height for Copper. **b** Power absorption ratio for different RMS height for Aluminum [70]

Therefore, a firm understanding of the scattering behavior of terahertz waves from rough surfaces is of importance while developing terahertz machined components and systems. Figure 10a, b show the reflectivity at vertical incidence depending on frequency for different rough surfaces. This phenomenon is not significant at low frequencies but, with the increase in frequency, the reflectivity sharply decreases, which indicates higher losses in both the metals under study. Figure 11a, b show the normalized power spectral density of Aluminum and Copper for different rough heights. Chen et al. [71] have studied the effect of surface roughness on the Lossy rectangular waveguide. They have found that as the correlation length and frequency increase, the attenuation decreases and propagation constant increases. Chen et al. [72] have analyzed lossy rectangular waveguides on similar lines containing rough inner surfaces. Popalghat et al. [73], Sau Rez et al. [74] and Li et al. [75] also contributed a lot in the study of surface roughness and its effects on propagation. Gmzina et al. [76] reported scattering of spoof surface plasmon polaritons in defect-rich THz waveguide.

1.9.5 Interface Tolerances

The alignment pin and pin-hole tolerances at the interface are crucial for accurate mating of two waveguides to minimize the reflection at the waveguide interface (Fig. 12).

The achievable angular alignment limit is generally set by the skill of humans and the accuracy of jigs and fixtures being used at the manufacturing facility. Reflection at the interface can be minimized by achieving tight tolerances on the interface being an integral part of waveguide through CNC machines. The desired linear and geometrical tolerances are shown in Fig. 13b

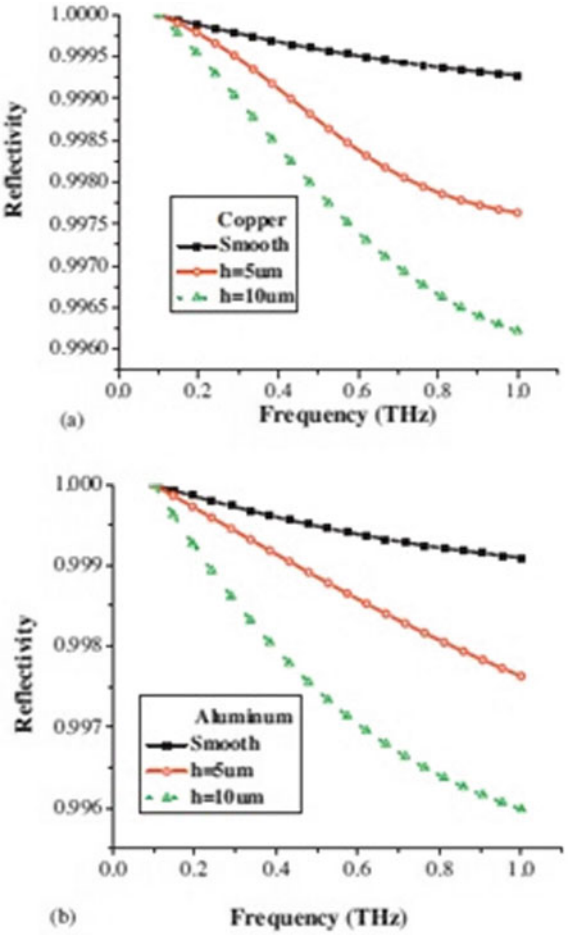

Fig. 10 Reflectivity versus frequency for different rough samples **a** for Copper and **b** for Aluminum

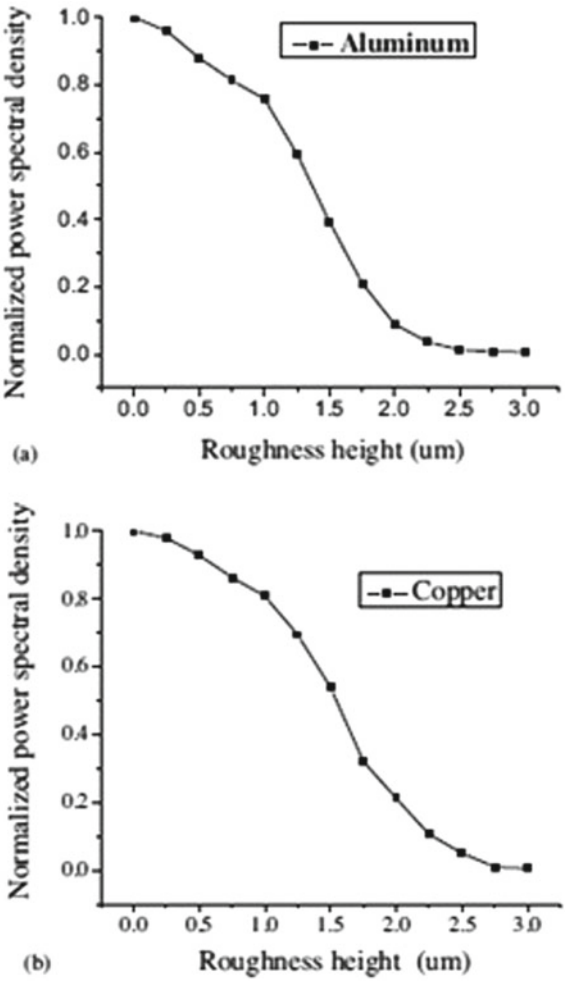

Fig. 11 Normalized power spectral density of Aluminum and Copper for different rough height **a** for Aluminum and **b** for Copper

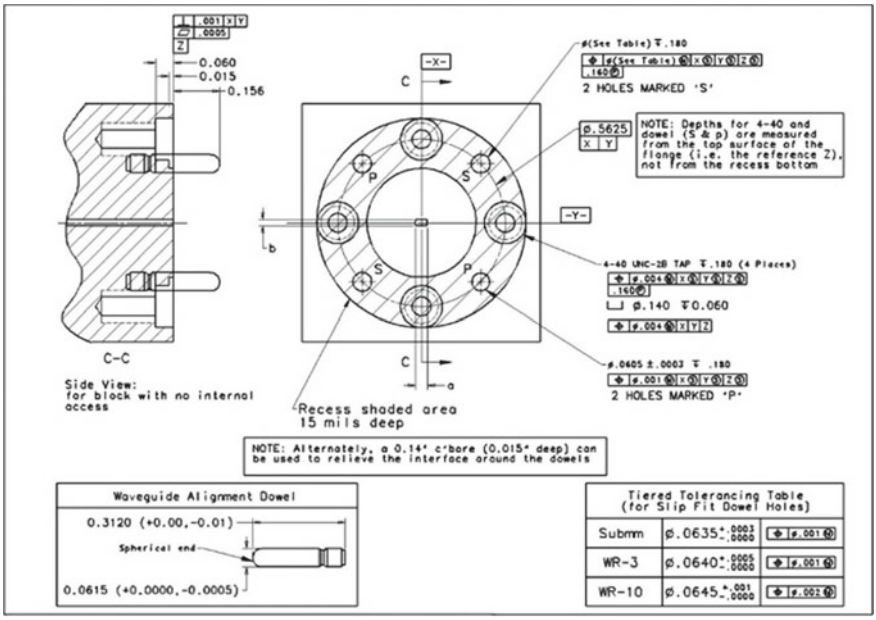

Fig. 12 Recommended waveguide interface from WR-10 to WR-1 [9]

	Submm	WR3 Tol	WR10 Tol
	(in.)	(in.)	(in.)
Min. Pin Diameter	0.061	0.061	0.061
Max. Pin Diameter	0.0615	0.0615	0.0615
Min. Hole Diameter	0.0635	0.064	0.0645
Max. Hole Diameter	0.0638	0.0645	0.0655
Pin Tolerance Range (PLTZF)	0.001	0.001	0.001
Hole Tolerance Range (PLTZF)	0.001	0.001	0.002
Pin Tolerance Range (FRTZF)	0.001	0.001	0.001
Hole Tolerance Range (FRTZF)	0.001	0.001	0.002
Maximum Total Offset	0.0024	0.0028	0.0038
Fit Tolerance	0	0.0005	0

	Frequency of Min Return Loss Due to Misalignment (GHz)		
	Submm	WR3 Tol	WR10 Tol
Minimum RL (23 dB) at	275	240	176
Minimum RL (7 dB) at	825	720	528

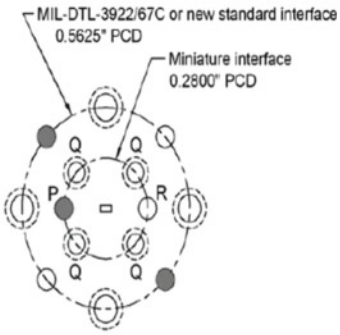

Fig. 13 **a** Dimensions and tolerances of Dowel pins and pinholes, **b** The miniature interface [9]

References

1. W. Ghann, J. Uddin, *Terahertz Spectroscopy—A Cutting Edge Technology* (2017).https://doi.org/10.5772/62805
2. R. Zamorano Ulloa, Ma. Guadalupe Hernandez Santiago, V.L. Villegas Rueda, The interaction of microwaves with materials of different properties, in *Electromagnetic Fields and Waves* (2019), pp. 1–29. https://doi.org/10.5772/intechopen.83675
3. H.S. Sudhamani, R. Bhardwaj, S.U.M. Reddy, J. Balakrishnan, Study of passband and stopband properties of sheet-beam folded waveguide structures. IEEE Trans. Electron Devices

66(5), 2401–2408 (2019). https://doi.org/10.1109/TED.2019.2905774
4. S. Hrabar, J. Bartolic, Z. Sipus, Miniaturization of rectangular waveguide using uniaxial negative permeability meta-material, in *IEEE MELCON 2004*, May 12–15, Dubrovnik, Croatia
5. H.S. Sudhamani, J. Balakrishnan, S.U.M. Reddy, L. Kumar, Analysis of sheet beam folded waveguide slow wave structure for THz TWT's, in *Proceedings of 16th IEEE Int. Vac. Electron, Conf. (IVEC)*, Beijing, China (2015), p. 45
6. H.S. Sudhamani, J. Balakrishnan, S.U.M. Reddy, PIC simulations of folded waveguide slow wave structure for THz TWT's, in *Proceedings of the 4th International Conference on Electronic Warfare (EWCI)*, Bangaluru, India (2016), pp. 95–97
7. D. Shan, Y. Shi, S. Duan, Y. Wei, Q. Cai, X. Yang, Electrospumn magnetic poly(l-lactide) (PLLA) nanofibers by incorporating PLLA-stabilized Fe_3O_4 nanoparticles. Mater. Sci. Eng., C **33**(6), 3498–3505 (2013). https://doi.org/10.1016/j.msec.2013.04.040
8. S. Prakash, S. Kumar, Fabrication of microchannels on transparent PMMA using CO_2 Laser (10.6 μm) for microfluidic applications: an experimental investigation. Int. J. Precis. Eng. Manuf. **16**(2), 361–366 (2015). https://doi.org/10.1007/s12541-015-0047-8
9. J.L. Hesler, A.R. Kerr, W. Grammer, E. Wollack, Recommendations for waveguide interfaces to 1 THz, in *Proceedings of the Eighteenth International Symposium on Space Terahertz Technology 2007, ISSTT 2007* (2007), pp. 100–103
10. https://www.tematys.fr/reports/fr/accueil/31-terahertz-components-systems-technology-and-market-trends-update-2016.html
11. M.H. Rahaman, A. Bandyopadhyay, S. Christopher, K.P. Ray, S. Pal, THz communication technology in India: present and future. Def. Sci. J. **69**(5), 510–516 (2019). https://doi.org/10.14429/dsj.69.14471
12. M.N.W. Groenendijk, J. Meijer, Surface microstructures obtained by femtosecond laser pulses. CIRP Ann. **55**(1), 183–186 (2006). https://doi.org/10.1016/S0007-8506(07)60394-1
13. X. Liu, R.E. DeVor, S.G. Kapoor, K.F. Ehmann, The mechanics of machining at the microscale: assessment of the current state of the science. J. Manuf. Sci. Eng. **126**(4), 666–678 (2005). https://doi.org/10.1115/1.1813469
14. F. Sammoura et al., Plastic 95-GHz rectangular waveguides by micro molding technologies. Sens. Actuators, A **127**(2), 270–275 (2006). https://doi.org/10.1016/j.sna.2005.07.020
15. P.J. Bruneau, H.D. Janzen, J.S. Ward, Machining of terahertz split-block waveguides with micrometer precision, in *33rd International Conference on Infrared and Millimeter Waves and the 16th International Conference on Terahertz Electronics, 2008, IRMMW-THz 2008* (2008), pp. 7–8. https://doi.org/10.1109/ICIMW.2008.4665435.
16. Y. Peng, C. Shi, X. Wu, Y. Zhu, S. Zhuang, Terahertz imaging and spectroscopy in cancer diagnostics: a technical review. BME Frontiers **2020**, 1–11 (2020). https://doi.org/10.34133/2020/2547609
17. J. Chae, S.S. Park, T. Freiheit, Investigation of micro-cutting operations. Int. J. Mach. Tools Manuf **46**(3–4), 313–332 (2006). https://doi.org/10.1016/j.ijmachtools.2005.05.015
18. K. Iwaszczuk, Terahertz Technology for Defense and Security-Related Applications by A thesis submitted in partial fulfillment for the (2012)
19. T. Narytnik, Possibilities of using THz-band radio communication channels for super high-rate backhaul. Telecommun. Radio Eng. **73**, 1361–1371 (2014)
20. The Antenna Theory Website. https://www.antenna-theory.com/. Accessed Jul 07, 2021
21. Northwest Engineering Solutions|Electronics Design & PCB Layout Company, Embedded Systems, Aerospace and Defense Electronics in Portland, OR. https://www.nwengineeringllc.com/. Accessed Jul 07, 2021
22. https://www.microwaves101.com
23. https://www.electronicsdesk.com
24. Ansoft Corporation, *User's Guide—High Frequency Structure Simulator* (2005), p. 801
25. M. Kulkarni, *Microwave and Radar Engineering* (Umesh Publication, New Delhi, 2020)
26. J.d. Kraus, *antennas.pdf*, 2nd ed. (McGraw-Hill, 1988)

27. K.D. Prasad, *Antennas and Wave Propagation* (Satya Prakashan, Tech India Publications, New Delhi, New Delhi, 2009)
28. A.P. Mathew, K. Oksman, M. Sain, The effect of morphology and chemical characteristics of cellulose reinforcements on the crystallinity of polylactic acid. Wiley InterScience (2005). https://doi.org/10.1002/app.23346
29. S.Y. Liao, *Microwave Devices and Circuits*, 3rd edn. (Pearson Prentice Hall, 2008)
30. NASA's jet Propulsion Laboratory, An all solid state, room-temperature, heterodyne receiver for atmospheric spectroscopy at 1.2 THz. Electron. Comput. 1–5 (2013)
31. M. Supriya, A.V. Samuel, Terahertz technology: a review on dental perspective, **12**(10), 1320–1325 (2020)
32. A.Y. Pawar, D.D. Sonawane, K.B. Ernade, D.V. Derle, Terahertz technology and its applications. Drug Invention Today **5**, 157–163 (2013)
33. L. Yu et al., The medical application of terahertz technology in non-invasive detection of cells and tissues: opportunities and challenges. RSC Adv. **9**(17), 9354–9363 (2019). https://doi.org/10.1039/C8RA10605C
34. S.U. Hwu, K.B. Desilva, C.T. Jih, Terahertz (THz) wireless systems for space applications, in *2013 IEEE Sensors Applications Symposium, SAS 2013—Proceedings* (2013), pp. 171–175. https://doi.org/10.1109/SAS.2013.6493580
35. I.F. Akyildiz, J.M. Jornet, The internet of nano-things. IEEE Wirel. Commun. **17**(6), 58–63 (2010). https://doi.org/10.1109/MWC.2010.5675779
36. R.F. Harrington, *Time Harmonic Electromagnetic Fields* (Wiley-IEEE Press, 2001)
37. L. Tripodi et al., Broadband terahertz and sub-terahertz CMOS modules for imaging and spectroscopy applications. Procedia Eng. **47**, 1491–1497 (2012). https://doi.org/10.1016/j.proeng.2012.09.435
38. R.E. Collin, *Foundation for Microwave Engineering* (Wiley-IEEE Press, 2001)
39. M.L.R. Teja, V.D. Rao, G.B. Sri, Designing and studying the characteristics of rectangular rectangular waveguide using HFSS. Int. J. Electric. Electron. Data Commun. **5**(6), 8–10 (2017)
40. V.S. Syzranov, A.S. Ermolov, S.P. Lebedev, V.N. Murzin, Designing and studying waveguide filters of terahertz and subterahertz frequency ranges. Instrum. Exp. Tech. **55**(6), 673–679 (2012). https://doi.org/10.1134/S0020441212050077
41. X. Li, J. Song, J.X.J. Zhang, Design of terahertz metal-dielectric-metal waveguide with microfluidic sensing stub. Optics Commun. **361**, 130–137 (2016). https://doi.org/10.1016/j.optcom.2015.10.007
42. H. Xiao-Yong, Simulation investigation on channel surface plasmon guiding by terahertz wave through subwavelength metal V-groove. Opt. Laser Technol. **41**(5), 535–538 (2009). https://doi.org/10.1016/j.optlastec.2008.11.005
43. B. Yu, Y. Liu, Y. Ye, J. Ren, X. Liu, Q.J. Gu, High-efficiency micromachined sub-THz channels for low-cost interconnect for planar integrated circuits. IEEE Trans. Microw. Theory Tech. **64**(1), 96–105 (2016). https://doi.org/10.1109/TMTT.2015.2504443
44. M. Gerhard, R. Beigang, M. Rahm, Comparative terahertz study of rectangular metal waveguides with and without a ridge. J. Infrared Millimeter Terahertz Waves **36**(4), 327–334 (2015). https://doi.org/10.1007/s10762-015-0145-9
45. H.S. Sudhamani, J. Balakrishnan, S.U.M. Reddy, Investigation of instability in a folded-waveguide sheet beam TWT, *IEEE Transactions on Electron Devices*, vol. 64, no. 10 (2017), pp. 4266–4277
46. R.K. Bhardwaj, H.S. Sudhamani, V.P. Dutta, N. Bhatnagar, Micromachining and characterisation of folded waveguide structure at 0.22THz. J. Infrared Millimeter Terahertz Waves **42**(3), 229–238 (2021). https://doi.org/10.1007/s10762-021-00767-w
47. H.S. Sudhamani, J. Balakrishnan, S.U.M. Reddy, Investigation of Instabilities in a Folded-Waveguide Sheet-Beam TWT. IEEE Trans. Electron Devices **64**(10), 4266–4271 (2017). https://doi.org/10.1109/TED.2017.2736065
48. H. Elayan, O. Amin, B. Shihada, R.M. Shubair, M. Alouini, Terahertz band : the last piece of RF, in *IEEE Open Journal of the Communications Society*, vol. 1, no. November 2019 (2020), pp. 1–32

49. X. Wu, L. Li, N. He, C. Yao, M. Zhao, Influence of the cutting edge radius and the material grain size on the cutting force in micro cutting. Precis. Eng. **45**, 359–364 (2016). https://doi.org/10.1016/j.precisioneng.2016.03.012
50. M.J.J.J. Paulo Davim, *Nano and Micromachining* (Wiley Online Library, 2009)
51. T. Chatti, S., Laperrière, L., Reinhart, G., Tolio, *CIRP Encyclopedia of Production Engineering, 2014* (Springer Publishing Company, Incorporated C.I.R.P., Berlin, 2014)
52. P. Rodríguez et al., Size effect and minimum chip thickness in micromilling. Int. J. Mach. Tools Manuf **51**(2), 39–54 (2011). https://doi.org/10.1016/j.ijmachtools.2011.01.003
53. M.A. Câmara, J.C.C. Rubio, A.M. Abrão, J.P. Davim, State of the art on micromilling of materials, a review. J. Mater. Sci. Technol. **28**(8), 673–685 (2012). https://doi.org/10.1016/S1005-0302(12)60115-7
54. M.B.G. Jun, R.E. DeVor, S.G. Kapoor, Investigation of the dynamics of microend milling—part II: model validation and interpretation. J. Manuf. Sci. Eng. **128**(4), 901–912 (2006). https://doi.org/10.1115/1.2335854
55. X. Liu, R.E. DeVor, S.G. Kapoor, An analytical model for the prediction of minimum chip thickness in micromachining. J. Manuf. Sci. Eng. **128**(2), 474–481 (2005). https://doi.org/10.1115/1.2162905
56. H. Weule, V. Hüntrup, H. Tritschle, Micro-cutting of steel to meet new requirements in miniaturization. CIRP Ann. Manuf. Technol. **50**(1), 61–64 (2001). https://doi.org/10.1016/S0007-8506(07)62071-X
57. X. Sun, K. Cheng, Chapter 2—Micro-/Nano-Machining through Mechanical Cutting, in *Micro-Manufacturing Engineering and Technology*, ed. by Y. Qin (William Andrew Publishing, Boston, 2010), pp. 24–38. doi: https://doi.org/10.1016/B978-0-8155-1545-6.00002-8
58. N. Chen et al., Advances in micro milling: from tool fabrication to process outcomes. Int. J. Mach. Tools Manuf. **160**, 103670 (2021). https://doi.org/10.1016/j.ijmachtools.2020.103670
59. F. Klocke, *Manufacturing Processes 1* (Springer, 2011)
60. X. Cheng, Z. Wang, K. Nakamoto, K. Yamazaki, A study on the micro tooling for micro/nano milling. Int. J. Adv. Manuf. Technol. **53**(5), 523–533 (2011). https://doi.org/10.1007/s00170-010-2856-3
61. G. Chen, C. Ren, P. Zhang, K. Cui, Y. Li, Measurement and finite element simulation of micro-cutting temperatures of tool tip and workpiece. Int. J. Mach. Tools Manuf **75**, 16–26 (2013). https://doi.org/10.1016/j.ijmachtools.2013.08.005
62. B. Boswell, M.N. Islam, I.J. Davies, A review of micro-mechanical cutting. Int. J. Adv. Manuf. Technol. **94**(1), 789–806 (2018). https://doi.org/10.1007/s00170-017-0912-y
63. K. Yang, Y. Liang, K. Zheng, Q. Bai, W. Chen, Tool edge radius effect on cutting temperature in micro-end-milling process. Int. J. Adv. Manuf. Technol. **52**(9), 905–912 (2011). https://doi.org/10.1007/s00170-010-2795-z
64. A.R. Kerr, E. Wollack, N. Horner, Waveguide flanges for ALMA instrumentation waveguide flanges for ALMA instrumentation. ALMA Report **278**, 1–14 (1999)
65. I.S. Jawahir et al., Surface integrity in material removal processes: recent advances. CIRP Ann. Manuf. Technol. **60**(2), 603–626 (2011). https://doi.org/10.1016/j.cirp.2011.05.002
66. P.J. Withers, H.K.D.H. Bhadeshia, Residual stress part 1—measurement techniques. Mater. Sci. Technol. **17**(4), 355–365 (2001). https://doi.org/10.1179/026708301101509980
67. M.E. Fitzpatrick, A.T. Fry, P. Holdway, F.A. Kandil, J. Shackleton, L. Souminen, NPL good practice guide no. 52: determination of residual stresses by x-ray diffraction Determination of Residual Stresses by X-ray Diffraction—Issue 2, no. 52 (2002)
68. J.B. Noyan, I.C. Cohen, Measurement by diffraction and interpretation, in *Residual Stress* (Springer, 1987)
69. Z. Wang, The influence of surface roughness on conductor at terahertz frequencies. Optik **125**(13), 3237–3240 (2014). https://doi.org/10.1016/j.ijleo.2013.12.051
70. J. Chen, B. Huang, *Effects of Surface Roughness on Lossy Rectangular Waveguide* (2012)
71. C.-D. Chen, C.-K.C. Tzuang, S.T. Peng, Full-wave analysis of a lossy rectangular waveguide containing rough inner surfaces. IEEE Microwave Guided Wave Lett. **2**(5), 180–181 (1992). https://doi.org/10.1109/75.134347

72. S.K. Popalghat, A. Chaudhari, P.B. Patil, Effect of surface roughness on electromagnetic propagation through waveguides. Indian J. Pure Appl. Phys. **37**(11), 848–852 (1999)
73. A. Mendoza-Suárez, U. Ruíz-Corona, R. Espinosa-Luna, Effects of wall random roughness on TE and TM modes in a hollow conducting waveguide. Optics Commun. **238**(4), 291–299 (2004). https://doi.org/10.1016/j.optcom.2004.05.007
74. J. Li, L.X. Guo, H. Zeng, FDTD investigation on electromagnetic scattering from two-dimensional layered rough surfaces. Appl. Comput. Electromagn. Soc. J. **25**(5), 450–457 (2010)
75. N.C. Luhmann et al., Nanoscale surface roughness effects on THz vacuum electron device performance, in *IEEE-NANO 2015—15th International Conference on Nanotechnology*, vol. 15, no. 1 (2015), pp. 55–58. https://doi.org/10.1109/NANO.2015.7388675
76. A.K. Klein et al., Scattering of spoof surface plasmon polaritons in defect-rich THz waveguides. Sci. Rep. **9**(1), 6288 (2019). https://doi.org/10.1038/s41598-019-42412-6
77. E. Vazquez, J. Gomar, J. Ciurana, C.A. Rodríguez, Analyzing effects of cooling and lubrication conditions in micromilling of Ti6Al4V. J. Clean. Prod. **87**, 906–913 (2015). https://doi.org/10.1016/j.jclepro.2014.10.016
78. M. Farhan Shafique, I.D. Robertson, Laser machining of microvias and trenches for substrate integrated waveguides in LTCC technology, in *European Microwave Week 2009, EuMW 2009: Science, Progress and Quality at Radiofrequencies, Conference Proceedings—39th European Microwave Conference, EuMC 2009*, no. October (2009), pp. 272–275. https://doi.org/10.1109/EUMC.2009.5295980
79. C.W. Cheng, S.Y. Wang, K.P. Chang, J.K. Chen, Femtosecond laser ablation of copper at high laser fluence: modeling and experimental comparison. Appl. Surf. Sci. **361**, 41–48 (2016). https://doi.org/10.1016/j.apsusc.2015.11.055
80. E.C. Santos, M. Shiomi, K. Osakada, T. Laoui, Rapid manufacturing of metal components by laser forming. Int. J. Mach. Tools Manuf **46**(12), 1459–1468 (2006). https://doi.org/10.1016/j.ijmachtools.2005.09.005
81. D. Drummer, S. Cifuentes-Cuéllar, D. Rietzel, Suitability of PLA/TCP for fused deposition modeling. Rapid Prototyping J. **18**(6), 500–507 (2012). https://doi.org/10.1108/13552541211272045
82. S. Ganti et al., Characterization and modeling of laser micromachined periodically corrugated metallic terahertz wire waveguides. J. Infrared Millimeter Terahertz Waves **33**(11), 1104–1116 (2012). https://doi.org/10.1007/s10762-012-9926-6
83. https://www.industrial-lasers.com/cutting/article/16488567/femtosecond-laser-micromachining-a-backtobasics-primer
84. Y. Li, I. Mehdi, A. Maestrini, R.H. Lin, J. Papapolymerou, A broadband 900-GHz silicon micromachined two-anode frequency tripler. IEEE Trans. Microw. Theory Tech. **59**(6), 1673–1681 (2011). https://doi.org/10.1109/TMTT.2011.2123112
85. S. Hrabar, J. Bartolic, Z. Sipus, Waveguide miniaturization using uniaxial negative permeability metamaterial. IEEE Trans. Antennas Propag. **53**, 110–119 (2005)
86. D.H. Kai Cheng, *Micro-Cutting: Fundamentals and Applications*, 1st edn. (Wiley, Chichester, 2013)
87. C. Brecher, M. Esser, S. Witt, Interaction of manufacturing process and machine tool. CIRP Ann. Manuf. Technol. **58**(2), 588–607 (2009). https://doi.org/10.1016/j.cirp.2009.09.005
88. F.B. de Oliveira, A.R. Rodrigues, R. Coelho, A.F. de Souza, Size effect and minimum chip thickness in micromilling. Int. J. Mach. Tools Manuf. **89**, 39–54, (2015)
89. A.J. Mian, N. Driver, P.T. Mativenga, Identification of factors that dominate size effect in micro-machining. Int. J. Mach. Tools Manuf. **51**(5), 383–394 (2011). https://doi.org/10.1016/j.ijmachtools.2011.01.004
90. R. Neugebauer, D. Weidlich, U. Mahn, Modelling of the clamping mark formation in manufacturing processes with extremely high axial forces. Int. J. Mach. Tools Manuf. **45**(3), 279–284 (2005). https://doi.org/10.1016/j.ijmachtools.2004.08.009
91. M. Malekian, M.G. Mostofa, S.S. Park, M.B.G. Jun, Modeling of minimum uncut chip thickness in micro machining of aluminum. J. Mater. Process. Technol. **212**(3), 553–559 (2012). https://doi.org/10.1016/j.jmatprotec.2011.05.022

92. H.T. Yun, S. Heo, M.K. Lee, B.-K. Min, S.J. Lee, Ploughing detection in micromilling processes using the cutting force signal. Int. J. Mach. Tools Manuf. **51**(5), 377–382 (2011). https://doi.org/10.1016/j.ijmachtools.2011.01.003
93. K.M. Li, S.Y. Chou, Experimental evaluation of minimum quantity lubrication in near micro-milling. J. Mater. Process. Technol. **210**(15), 2163–2170 (2010). https://doi.org/10.1016/j.jmatprotec.2010.07.031
94. E. Creighton, A. Honegger, A. Tulsian, D. Mukhopadhyay, Analysis of thermal errors in a high-speed micro-milling spindle. Int. J. Mach. Tools Manuf. **50**(4), 386–393 (2010). https://doi.org/10.1016/j.ijmachtools.2009.11.002
95. P. Rodríguez, J.E. Labarga, A new model for the prediction of cutting forces in micro-end-milling operations. J. Mater. Process. Technol. **213**(2), 261–268 (2013). https://doi.org/10.1016/j.jmatprotec.2012.09.009
96. K. Egashira, S. Hosono, S. Takemoto, Y. Masao, Fabrication and cutting performance of cemented tungsten carbide micro-cutting tools. Precis. Eng. **35**(4), 547–553 (2011). https://doi.org/10.1016/j.precisioneng.2011.06.002
97. H.-C. Möhring, C. Brecher, E. Abele, J. Fleischer, F. Bleicher, Materials in machine tool structures. CIRP Ann. **64**(2), 725–748 (2015). https://doi.org/10.1016/j.cirp.2015.05.005
98. H.T. Bookey et al., Femtosecond laser inscription of low insertion loss waveguides in Z-cut lithium niobate. IEEE Photonics Technol. Lett. **19**(12), 892–894 (2007). https://doi.org/10.1109/LPT.2007.897534
99. V.K. Jain, *Introduction to Micromachining* (CR Press, India, 2001)
100. G. Quintana, J. Ciurana, Chatter in machining processes: a review. Int. J. Mach. Tools Manuf. **51**(5), 363–376 (2011). https://doi.org/10.1016/j.ijmachtools.2011.01.001
101. R. Lekkala, V. Bajpai, R.K. Singh, S.S. Joshi, Characterization and modeling of burr formation in micro-end milling. Precis. Eng. **35**(4), 625–637 (2011). https://doi.org/10.1016/j.precisioneng.2011.04.007
102. J.C. Aurich, D. Dornfeld, P.J. Arrazola, V. Franke, L. Leitz, S. Min, Burrs-analysis, control and removal. CIRP Ann. Manuf. Technol. **58**(2), 519–542 (2009). https://doi.org/10.1016/j.cirp.2009.09.004
103. B.Z. Balázs, N. Geier, M. Takács, J.P. Davim, A review on micro-milling: recent advances and future trends. Int. J. Adv. Manuf. Technol. **112**(3), 655–684 (2021). https://doi.org/10.1007/s00170-020-06445-w
104. P. Kumar, M. Kumar, V. Bajpai, N.K. Singh, Recent advances in characterization, modeling and control of burr formation in micro-milling. Manuf. Lett. **13**, 1–5 (2017). https://doi.org/10.1016/j.mfglet.2017.04.002
105. R. Piquard, A. D'Acunto, P. Laheurte, D. Dudzinski, Micro-end milling of NiTi biomedical alloys, burr formation and phase transformation. Precis. Eng. **38**(2), 356–364 (2014). https://doi.org/10.1016/j.precisioneng.2013.11.006
106. L.N. López de Lacalle, A. Lamikiz, *Machine Tools for High Performance Machining* (Springer, 2009)
107. S. Hashmi, *Comprehensive Materials Processing* (Elsevier, 2014)
108. W. Grzesik, Sensor-Assisted Machining, Advanced Machining Processes of metallic Materials. Elsevier Science Ltd (2008). https://doi.org/10.1016/B978-0-08-044534-2.X5001-2
109. https://terasense.com/applications/

Rakesh Kumar Bhardwaj is working as Scientist: F at Defense Electronics Applications Laboratory (DEAL) of Defence Research and Development Organisation (DRDO) at Dehradun Uttrakhand. He has obtained his B.Tech. in Mechanical Engineering from College of Engineering Thiruvananthapuram, Kerala University in 1996 and M.Tech. in Production Engineering from IIT Delhi in 2006. He submitted his Ph.D. thesis at IIT Delhi in 2021. He joined DRDO as Scientist B in 1997, since then he is working in Design and Development of microwave and mm-Wave components ranging from X, L, S, Ku, Ka and W band. He is recipient of Padamshee M M Suri Project award at IIT Delhi in 2006, National Science Day oration and Gold medal in 2007, Agni Award for Excellence in Self Reliance of Defence Technology in 2011 and National Technology Day Oration and Titanium Medal in 2015. He has published 27 technical papers in Journals and conferences. His Area of Specialization is Production Engineering, CAD/CAM, Composite materials, Precision Engineering, Micro and nano manufacturing. His current activity includes design and development mm-Wave and terahertz waveguide components within desired tolerances. He is a member of ASME, SSME and Fellow of Institution of Engineers India. In addition to academics, he is Vice President of EcoGroup Society and Secretary of IIT Alumni association, Dehradun, Uttrakhand Chapter. He is also associated to Art of Living.

Dr. V. P. Dutta is Scientist G has obtained his B.E. in production Engineering from Punjab Engineering College, Chandigarh in 1980. He worked initially for six years in private industries like Escort, Godrej and Samtel and joined DRDO as Scientist: B in 1986. He conferred MBA from IGNOU in 1995 and Ph.D. in Mechanical Design from IIT Delhi in 2005. Presently he is Scientist: G and Group Director, Center for Advance Mechanical Engineering Group of DEAL, DRDO, Dehradun. He has published number of papers in International and National journals.

Prof. Naresh Bhatnagar obtained his B.Tech. in Mechanical Engineering from REC Trichy, M.Tech. and Ph.D. in Production Engineering from IIT Bombay. Presently he is working as Professor in Mechanical Engineering Department of IIT Delhi, and Associated DEAN R&D of IIT Delhi. He has published more than 150 International Journal Papers. He has patents to his credit. His area of expertise is Production, Composite materials, Biomaterials and their processing. He is authored chapters and books of International repute. He has guided more than 21 Ph.D. theses.

Material Selection, Micromachining, and Measurements of THz Waveguide Components

Rakesh Kumar Bhardwaj, V. P. Dutta, and Naresh Bhatnagar

Abstract The criticalities in micromachining of Terahertz waveguide Components starting from 100 to 1100 GHz have been developed mechanically in this research work. Free cutting brass IS 319-H_2 and AL Alloy IS:736 24,345 WP were used as work materials due to its electrical and mechanical properties. Waveguide size as small as 0.254 × 0.127 mm was micromachined within ± 3–5 μm linear tolerances, surface roughness of the order of 0.045 μm Ra and flatness less than 0.3 μm (<λ/2). The split top and bottom blocks of the waveguide were aligned by dowel pins which matched within a tolerance of ±5 μm. The perpendicularity and parallelism were maintained within ±5 μm tolerance as per IS:8000, 1975. This work explored and established the application of micro-milling as reasonably suitable for the THz waveguides followed by ultrasonic cleaning. Waveguide above 1.1 THz having waveguide size as small as 75 μm × 37.5 μm was also realized using femtosecond LASER within nanometer level accuracies. Measurements of folded waveguide at 0.22 THz waveguide losses were close to simulated values.

Keywords THz · Waveguide · Micromachining · Terahertz waveguide components

1 Introduction

Micro-milling is a versatile micro-cutting process for producing micro-level components in small and medium quantities. CNC controllers and CAD/CAM software have made it possible to generate highly complex micro-components and microstructures. The size, geometry, and composition of micro tools are vital to micro-milling as they determine the minimum feature size and surface quality. Micro-milling tools ranging

R. K. Bhardwaj · N. Bhatnagar (✉)
Department of Mechanical Engineering, Indian Institute of Technology, Delhi 110016, India
e-mail: nareshb@mech.iitd.ac.in

R. K. Bhardwaj
e-mail: rk.bhardwaj.deal@gov.in

R. K. Bhardwaj · V. P. Dutta
Defence Electronics Applications Laboratory, Raipur Road, Dehradun, Uttrakhand 248001, India

M. El Ghzaoui et al. (eds.), *Terahertz Wireless Communication Components and System Technologies*, https://doi.org/10.1007/978-981-16-9182-9_16

from 25 to 1000 μm are available for micro-milling of miniature components like THz waveguides on conventional and micro-milling machines. These machines have got ultra-high-speed low run-out spindles that can run at 100,000 rpm if required. In order to minimize the thermal errors, the spindle is generally temperature-controlled, and a better surface finish can be achieved on these machines. The spindle speeds have greatly enhanced the machining rates to acceptable levels even with low feed/tooth values used in micro tools. Recent micro-milling machines use high damping material characteristics like polymer concrete and have high dynamic stiffness. They also employ glass scales of sub-micron resolutions in place of linear encoders for better control and fewer motion errors. Materials like polymer concrete also provide good thermal stability when compared to cast iron. Multi-axis machine configuration reduces the setup change errors and increases productivity. Mechanical micromachining and particularly micro-milling process, when utilized as a THz machining process, deliver many advantages over its counterparts due to the possibility of applications to a variety of materials, lesser number of setups to generate stepped geometries, complex machining of 3D geometries, lower setup costs, a good accuracy, and high surface quality. However, size effect, rapid tool wear, inherent burr formation, and low stiffness of tool that causes deflection, limitation of the minimum feature size, and higher surface roughness compared to Lithographic techniques possess a number of challenges. The machining of THz waveguide geometries requires a very high level of geometrical tolerances and surface quality which can only be achieved through micro-milling. The generated topography of the micro-milled surface inside the waveguide is mainly influenced by the tool, machining parameters, and strategy of cutting. Advanced CNC machine tools with an online tool and workpiece measurements have reduced positioning inaccuracies, can achieve high levels of precision. Hence, micro-milling represents a suitable technique to manufacture THz waveguide components.

1.1 Materials and Design Selection of Waveguide

Waveguides are made from Brass, Copper, Aluminum, or metal with low bulk resistivity and high electric conductivity. Although poor conducting metals and alloys can be used, they need to be plated correctly to increase conductivity. An example—gold-plated microwave and millimeter wave components were produced. According to the literature, it is even possible to make plastic or polymeric waveguides.

However, electromagnetic materials have long been an interest, which attracted the research community to fabricate the devices for the THz frequency band. The main characteristics of these materials are permittivity (ε) and permeability (μ), also known as constitutive parameters. Some waveguide materials and their properties are discussed below.

Table 1 The properties of brass IS: 319 H_2

Density	8.49 g/cm^3
Melting point	885 °C
Tensile strength	338–469 MPa
Yield strength (depending on temper)	124–310 MPa
Elongation at break (in 457.2 mm)	53%
Elastic modulus	117 GPa
Poisson's ratio	0.34
Machinability (UNS C36000 (free cutting brass)=100)	100
Shear modulus	37 GPa
Thermal Expansion co-efficient @ 20–300 °C/68–572°F)20.5 µm/m°	20.5 µm/m°
Electrical conductivity (Siemens/m)	1.59×10^7 S/m
Permeability	1.60 m^2

1.1.1 Free Cutting Brass IS 319-H_2

Free cutting brass IS 319-H_2 (Cu: 61%, Zn: 36%, Pb: 3%) half hard was selected for waveguide structures due to its high strength, corrosion resistance, and good dimensional stability over a long period. This alloy is suitable for waveguides at higher frequencies due to its electrical conductivity and machinability. To increase the conductivity of Brass, we finally gold plate the components. To relieve the locked-in stresses, alpha (α) brass alloy is annealed and subjected to stress relief. The inclusion of 2–4% Lead in the alloy makes it free cutting, and Zinc at 36% completely dissolves in the solution and makes a continuous solid solution. Refer: [1]

The Properties of Brass IS: 319 H_2 are shown in Table 1:

1.1.2 Aluminium (Al) Alloy: IS 736-24345WP as a Material for the Waveguide

The excellent heat and electrical conductivity, as well as lightweight characteristics, make Al alloys suitable material for waveguides. It is also non-corrosive, easily machinable, low cost, non-magnetic, and recyclable making it the first choice for many structural and communication applications. The Aluminum alloy is an alternative for the manufacturing of waveguide filters shows a very good thermal stability with respect to standard Aluminum. The electric conductivity of Aluminum can be enhanced by metal coating (e.g., silver, gold). The tensile strength of pure Aluminum is around 90 MPa, but this can be increased to over 690 MPa for some heat-treatable alloys. Al Alloy IS: 736-24345WP can be used for machining THz waveguide structure due to its superior electrical conductivity, permeability, and machinability, as this is a Copper-based alloy. Refer [2]

The Properties of Al Alloy: IS 736-24345WP are shown in Table 2:

Table 2 The properties of Al Alloy: IS 736-24345WP

Density	2.6898 g/cm^3
Melting point	660.2 °C
Tensile strength	395 MPa
Yield strength (depending on temper)	276 MPa
Elongation at break (in 457.2 mm)	12%
Elastic modulus	73GPa
Poisson's ratio	0.34
Machinability (UNS C36000 (free cutting brass)=100)	Good machinability
Shear modulus	28GPa
Thermal Expansion co-efficient @ 20–300 °C/68–572°F)20.5 µm/m°	8.9×10^{-3} µm/m°C
Electrical conductivity (Siemens/m)	3.7×10^7 S/m
Permeability	10^{-9} m^2

1.1.3 Oxygen-Free High Conductive Copper (OFHC)

The main characteristics are high ductility, high electrical and thermal conductivity, high impact strength, good creep resistance, ease of welding, and low volatility under a high vacuum. It contains less than10 ppm oxygen in the metal and is completely free from copper oxide particles. OFHC contains less than 10 ppm of oxygen, deserves superior electrical and thermal conductor, passes close bend tests, and easily welded. OFHC is used in electrical energy, power transmission, magnet windings, etc. Refer [3]

The Properties of OFHC are shown in Table 3:

Table 3 The properties of OFHC

Property	Metric
Tensile strength, ultimate (varies with heat treatment)	400 MPa
Tensile strength, yield (varies widely with heat treatment)	150 MPa
Elongation at break (in 101.6 mm (4 in.))	25%
Modulus of elasticity	115 GPa
Poissons ratio	0.31
Machinability (UNS C36000 (free cutting brass)=100%)	20%
Shear modulus	45 GPa
Density	8.86 g/cm^3
Melting point	1083 °C
Thermal Expansion co-efficient @ 20–300 °C/68–572°F)20.5 µm/m°	9.8×10^{-3} µmm/m°C
Electrical conductivity	5.9×10^7 S/m
Permeability	2.74×10^{-6} m^2

1.1.4 Mg Alloy AZ 91

Magnesium alloy, the lightest structural metal, is alloyed with Aluminium, Zinc, Manganese, Silicon, Copper, rare earth, and Zirconium. It has a hexagonal lattice structure, affecting the properties of the alloy. AZ 91 is a cast alloy, which improves mechanical properties due to plastic formation, where temperature plays an important role in yield stress and flow stress. Refer [4].

The properties of Mg Alloy AZ91 are shown in Table 4:

1.2 Silicon Family

Various materials based on silicon are used to make waveguides because of the low loss due to low absorption in the wavelength range 1.1–8.5 μm. Silicon, Silica, and Silicon nitride as an insulator are used to fabricate waveguides by electron beam lithography (EBL). Due to limitations of the fabrication process, large section silicon waveguides were reported in the literature to achieve low propagation losses with 1 μm wafer thickness, but the bending radius was limited to 100–1000 μm. Silicon materials are not helpful at shorter wavelengths, such as 850 nm in communication. Subsequently, advanced fabrication processes can make nanoscale silicon wire waveguides as per literature. The transparent window of silicon nitride was from 400 nm to mid-infrared; hence it is useful for wavelengths shorter than 1.1 μm. On the other hand, the fabrication processes for Silica exhibit low absorption makes suitable for waveguide materials in the visible region. The processes like EBL are for large quantity fabrication with control of dimensions is still an issue, it needs a deep understanding of the process and their parameters. One option of processing is to have a silicon wafer cut into waveguide geometry and fix on a metal cavity

Table 4 The properties of Mg Alloy AZ91

Density	1.75 g/cm^3
Melting point	533 °C
Tensile strength	262 MPa
Yield strength (depending on temper)	200 MPa
Elongation at break (in 457.2 mm)	35%
Elastic modulus	40.2 GPa
Poisson's ratio	0.35
Machinability (UNS C36000 (free cutting brass)=100)	Good machinability
Shear modulus	17 GPa
Thermal Expansion co-efficient @ 20–300 °C/68–572°F)20.5 μm/m°	8.48 × 10^{-3} μmm/m°C
Electrical conductivity (Siemens/m)	2.3 × 10^7 S/m
Permeability	2.2 × 10^{-6} m^2

for interface and holding. It has been seen practically that the moment number of components increases, achieving interface tolerances was difficult to even at lower THz frequency. The high thermo-optic co-efficient of silicon makes the microcavity of the waveguide strongly sensitive to temperature variation. Refer [5, 6].

1.2.1 Graphene on Silicon

Graphene is a 2D material that can seamlessly be integrated with silicon waveguides without hexagonal structure. Moreover, it has high carrier mobility at room temperature is 100 times higher than silicon. If a hybrid waveguide is suitably polarized, the loss of the waveguide can be reduced. Mittendroff et. al. [7] have developed a Graphene-based waveguide-integrated THz modulator. It used two methods to produce ridges with a height of 100 μm through deep reaction-ion etching (DRIE) with a dicing saw. Refer [7].

1.2.2 Polymer Materials

Kaur et al. [8] have reported the use of polymer materials for affordable fabrication of THz components for 0.15–0.5 THz using polymer jetting UV resin in 3D printing technology. Dielectric waveguides having ridges were fabricated through 3D printing technology. They have reported that transmission loss was dominated by loss characteristics of the polymer material used. Many more researchers have used different materials for the realization of THz waveguide components and their characterization [9–16]. Importance of geometrical tolerances in context of THz waveguides.

Suppose the geometry of the waveguide was not maintained as per IEEE guidelines and MIL standards; In that case, the inside surface of waveguide dimensions will not be as desired and rough. Under these conditions, electromagnetic waves that are designed to incident on smooth surface undergo reflection in the specular direction and are scattered diffusely, resulting in loss of intensity in the specular direction. In the subsequent sections contain almost all geometrical tolerances in addition to linear tolerances, named Flatness, positional tolerances, cylindricity, parallelism, squareness, surface roughness, etc., they need to be achieved in totality and not partially. This is a classic example of criticality in realizing THz waveguide components.

1.3 Micro-manufacturing and Micro-milling

The development of micro and nanotechnology has taken place due to the rising demand for micro and miniature parts. Micro-manufacturing is generally employed to realize parts or feature sizes ranging from tens or hundreds of micrometers. Typical examples of micro-manufacturing are non-lithography-based micro-manufacturing like micro EDM, micro-milling, laser cutting/patterning/drilling, micro-extrusion,

micro embossing, microstamping, micro injection molding, etc. These processes are based on different working principles and have their own respective characteristics in terms of achievable accuracy, surface finish, and production rate. But they all are capable of producing 3D shape micro parts using a variety of materials. This chapter will only focus on the micro mechanical-cutting process, in which tool geometry is defined. Micromachining can machine metals, alloys, polymers, composites, and ceramics into 3D shapes within 10^{-3} to 10^{-5} (sub-micron) accuracy. 3D components for various applications can be machined using macro or micro machines at low or high production volume with much higher accuracies than MEMS-based processes, which give accuracy of 10^{-1} to 10^{-3} only. Micro cutting is generally used for machining 3D parts demanding high accuracy on a variety of engineering materials. To characterize micro-cutting, we need to study minimum uncut chip thickness (MUCT), dimensions and accuracy of micro parts or features, cutting tool geometry, underlying cutting mechanism, and application area. If the uncut chip thickness of mechanical cutting falls to the nonmetric level, less than tens of nanometers, the cutting process is regarded as nonmetric cutting [17].

1.4 Micro-milling

Micro-milling is a versatile micro-cutting process for producing micro-level components in small and medium quantities. CNC controllers and CAD/CAM software have made it possible to generate highly complex micro-components and microstructures. The size, geometry, and composition of micro tools are vital to micro-milling as they determine the minimum feature size and surface quality. Micro-milling tools ranging from 25 to 1000 μm are available for micro-milling of miniature components like THz waveguides on conventional and micro-milling machines. These machines have got ultra-high-speed low run-out spindles that can run at 100,000 rpm if required. In order to minimize the thermal errors, the spindle is generally temperature-controlled, and a better surface finish can be achieved on these machines. The spindle speeds have greatly enhanced the machining rates to acceptable levels even with low feed/tooth values used in micro tools [18, 19]. Recent micro-milling machines use high damping material characteristics like polymer concrete and have high dynamic stiffness. They also employ glass scales of sub-micron resolutions in place of linear encoders for better control and fewer motion errors. Materials like polymer concrete also provide good thermal stability when compared to cast iron. Multi-axis machine configuration reduces the setup change errors and increases productivity. Mechanical micromachining and particularly micro-milling process, when utilized as a THz machining process, deliver many advantages over its counterparts due to the possibility of applications to a variety of materials, lesser number of setups to generate stepped geometries, complex machining of 3D geometries, lower setup costs, a good accuracy, and high surface quality. However, size effect, rapid tool wear, inherent burr formation, and low stiffness of tool that causes deflection, limitation of the minimum feature size, and higher surface roughness compared to Lithographic techniques possess a

number of challenges. The machining of THz waveguide geometries requires a very high level of geometrical tolerances and surface quality which can only be achieved through micro-milling [20]. The generated topography of the micro-milled surface inside the waveguide is mainly influenced by the tool, machining parameters, and strategy of cutting. Advanced CNC machine tools with an online tool and workpiece measurements have reduced positioning inaccuracies, can achieve high levels of precision. Hence, micro-milling represents a suitable technique to manufacture THz waveguide components. Kern micro-milling was used for precision machining of THz waveguide components. The machine is shown in Fig. 1, and the features are described as follows:

1.5 Micromachining Setup

The micromachining of the waveguide was carried on Kern CNC Micro-milling machine as shown in Fig. 1a, having Heidenhain TNC 530 Controller. Tool of diameter as small as 70 μm–100 μm with tool nose radius of 2 μm was used. It is important to use the actual instantaneous diameter and reducing the length of the tool during cutting through online measurement and compensation. Machining parameters like cutting speed, feed, and depth of cut were optimized using ANOVA as well as the Taguchi method and were experimentally verified to achieve the required linear tolerances, geometrical tolerances especially surface roughness. Long-term distortion in the waveguide can result in a loss of tolerance of the waveguide, although its initial flatness meets the specifications. To take care of distortion during and after machining and to prevent the work hardening effect due to cutting forces, well-sharpened cemented solid carbide end mills were used on the CNC milling machines. In order to prevent distortion and overheat in the thin sections, a controlled feed rate and depth of cut along with an MQL were used. This has also prevented the burnishing-glazing effect on the machined surface. The free cutting brass block was machined on six faces, using a high-precision milling machine within 5 μm parallelism. 'Kern' recommended collets and tool holders were used for the micro-milling of all the folded waveguides. The upper and lower block are aligned by dowel pins having positional tolerances within ±5 μm under a tool maker's microscope having a magnification of 50–100X. Lapping was done on the mating surfaces of the upper and lower block using Speedfam double-sided lapping machine with abrasive up to 4000 grit size in kerosene vehicle. The fitment of dowel pins is critical work and required a clean environment and operator's skill.

The experiments were conducted on a machine tool, KERN Micro 2522. Due to the high working accuracy of 1–2 μm and the speed range of the spindle (VSC 4084 Precise), up to 50,000 rpm, the machine tool is highly suitable for micro-milling processes. The acceleration of the axes is specified with $a = 2000$ mm/s^2, and a feed rate of $v_f = 6000$ mm/min is available. In order to realize high accuracy, the machine tool was placed in a thermally controlled environment (20° ± 2°) on a polymer concrete foundation to reduce the effects of heat and vibration. It has

(a)

(b)

Resource	Description
CAM System	Edge CAM
Machine Tool	KERN Micro-2522 , CNC Micromilling and drilling Machine, iTNC 530 Heidenhain Controller
Cutting tools	Ultrafine grade (<0.5µm) WC-Co Solid Carbide Endmill Cutters
Cutting tool adapter	Balanced HSK 25 tool adapter and collet with runout less than 1 µm.(KERN-Schaublin make)
Cutting tool length and diameter calibration	Blum Micro Compact NT laser pre-setting system, repeatability ±1 µm
Workpiece holding	High Precision grinding vice
Configurations	Three linear axes
Base structure	Polymer concrete
Controller	Heidenhain iTNC 530
Speed range	Up to 50,000rpm
Resolution	<0.1µm
Work volume	250×220×200mm

(c)

(d)

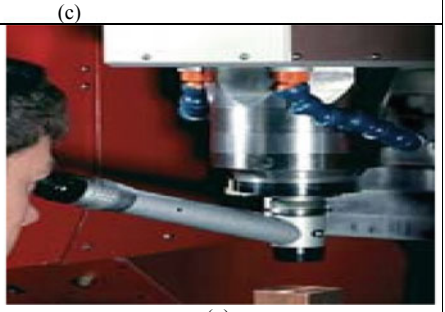

(e)

Fig. 1 **a** Kern Micro-milling, **b** different systems of micro milling-machine, **c** features of Kern Micro milling machine, **d** polymeric concrete construction, **e** centering microscope

a water-cooling system (refrigeration unit) for the milling spindle and a separate electrical cabinet to avoid thermal deformations. The machine body is made from polymer concrete to eliminate vibrations and avoid thermal deformations. This type of machine is more robust as compared to micro-factories. It can provide better static and dynamic stiffness and makes it easier to integrate complementing equipment such as monitoring (Non-contact tool measurement, Touch trigger probes for job measurement and compensation, etc.) and tool handling system (Automatic tool changer). A laser tool measurement system is installed on the table of the machine to measure both the length and diameter of the cutting tools in a dynamic state i.e., while rotating at high speeds. The laser beam has got a beam diameter of 30 μm, which enables it to measure the length, radius, and run-out of tools up to 50 μm diameter at high spindle speeds. Repeatability ±1 μm. The use of a touch probe (tactile sensor) enables the automatic centering, part zeroing, and part alignment of the workpiece. This infrared touch probe measures the height and position of the workpiece. Repeatability ±1 μm. The machine bed is made of polymer concrete, and the C frame of the machine is filled with polymer concrete to increase damping and absorbs most of the vibrations induced by cutting. Polymer concrete is ten times more vibration resistant than cast iron and provides higher dynamic and static rigidity than the latter. It has got much better thermal stability due to the addition of resins, which is critical for achieving higher accuracy on micro features.

1.6 Cutting Tools and Their Geometry Effect on Micro-cutting

Micro-milling tool is important to achieve desired dimensions and, its geometry and microstructure directly relate to the achieved surface roughness and accuracy.

Cemented Carbide tools have high hardness, acceptable wear resistance, and strength and are affordable. The performance of solid carbide tools is chiefly dependent upon the composition (i.e., cobalt content) and grain size, as the smaller grain size enables lower values of cutting-edge radius on the tool. The most popular choice for the micro tools is fine grain size (<0.6 μm) cobalt bonded tungsten carbide [21–23].

The geometry of the cutting tool is shown in Fig. 2, and raw material properties are given in Table 5.

1.7 Cutting Parameters (Feed, Speed, and DOC) and Their Importance

The experiments were repeated several times for three sets of waveguide slots at 0.33 THz, 0.625 THz, and 1.1 THz, respectively, keeping the cutting parameters the same for each set of THz waveguide as per the regression analysis equation:

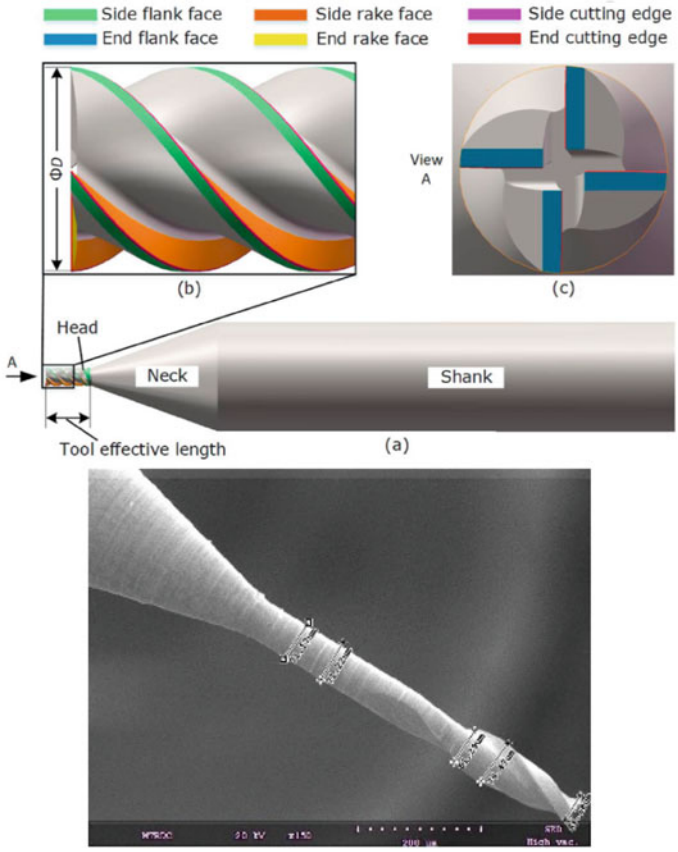

Fig. 2 Generic geometry of micro-milling cutters containing **a** head, neck, and shank, and the magnification of tool heads from **b** front and **c** side views, [23], **d** SEM Image of cutter having a diameter of 70 μm

$$\begin{aligned}\mathrm{RS(MPa)} &= 2991 - 0.0960\,\mathrm{S(rpm)} + 27.2\,\mathrm{F(mm/min)} \\ &\quad - 94,650\,\mathrm{D(mm)} * 0.000001\mathrm{S(rpm)} * \mathrm{S(rpm)} \\ &\quad - 3.51\mathrm{F(mm/min)} * \mathrm{F(mm/min)} + 1,446,667\,\mathrm{D(mm)} * \mathrm{D(mm)} \\ &\quad + 0.00278\mathrm{S(rpm)} * \mathrm{F(mm/min)} + 2.80\mathrm{S(rpm)} * \mathrm{D(mm)} \\ &\quad + 956\mathrm{F(mm/min)} * \mathrm{D(mm)}.\end{aligned}$$

The final parameters were achieved through trial and error.

Table 5 Raw material types for micro-milling cutters and their properties [23]

Materials	Cemented carbide
Specification	HW K10
Composition	WC-6Co
Density (g/cm^3)	14.9
Hardness (HV)	1580
Fracture toughness (MPa m$^{1/2}$)	9.6
Flexural strength (GPa)	2
Compression strength (GPa)	5.4
Young's modulus (GPa)	630
Poisson constant	0.22
Heat conductivity (W m^{-1} K^{-1})	80
Coefficient of thermal expansion, 293–1073 K (10^{-6} K^{-1})	5.5
Specific heat capacity 293 K (J g^{-1} K^{-1})	0.95

1.8 Accuracy and Thermal Effects

In the microdomain, the cutting forces are extensively affected by the normally overlooked issues in conventional milling, such as tool wear, tool run-out, and chatter [24]. Tool wear in micro-milling is high because of the lower chip loads and large effective rake angles, which increases the friction between workpiece and tool. Tool run-out is on the higher side in micro-milling due to the low rigidity of the tool and higher cutting speeds and has a significant effect when compared to the conventional domain, which leads to deteriorated surface quality (surface roughness and burr generation) due to excessive vibrations [21] and [22]. As the micro tool can be considered as a cantilever, when the diameter of the cutter is halved, the stiffness of the cutter is reduced 16 times. Also, micro-milling itself is an interrupted cutting process where cutting forces vary with the rotation angle of the cutter. As we decrease the size of the micro tool, its lowered stiffness will result in increased tool deflections and which will lead to deteriorated surface roughness and loss of precision (Fig. 3). Cutting paths and machining strategies should be selected and optimized in micro-scale milling to maintain tighter tolerances, reduce the cutting force, maintain constant chip load, and avoid premature tool failure [25] and [26]. In their research, Gracia et al. [25] have shown the Fish Bone diagram indicating the sources of geometrical and superficial errors affecting the machining accuracy in Micro-milling, covering all the major domains of process temperature control, handling, and metrology. Apart from the critical cutting parameters i.e., feed, speed, depth of cut, cutter type, tool path, etc., the micro-milling processes depend broadly on work material, tooling, and the machine tool. The key aspects of micro-milling are shown in Fig. 4, which listed all aspects of work material, tooling, and machine tools.

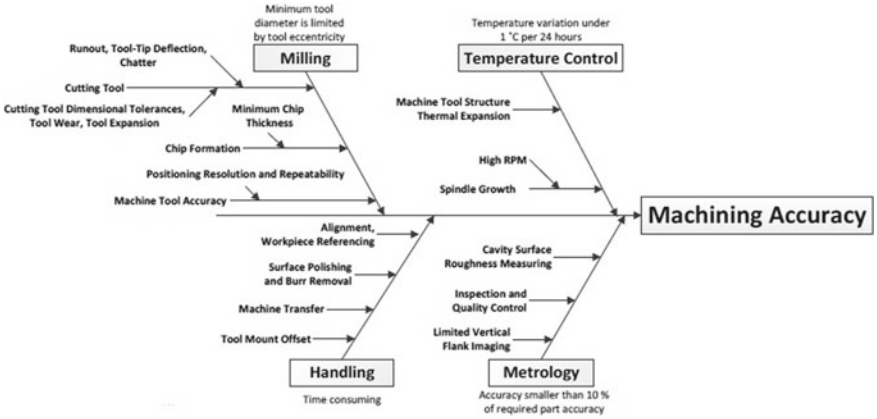

Fig. 3 Sources of geometrical errors [25]

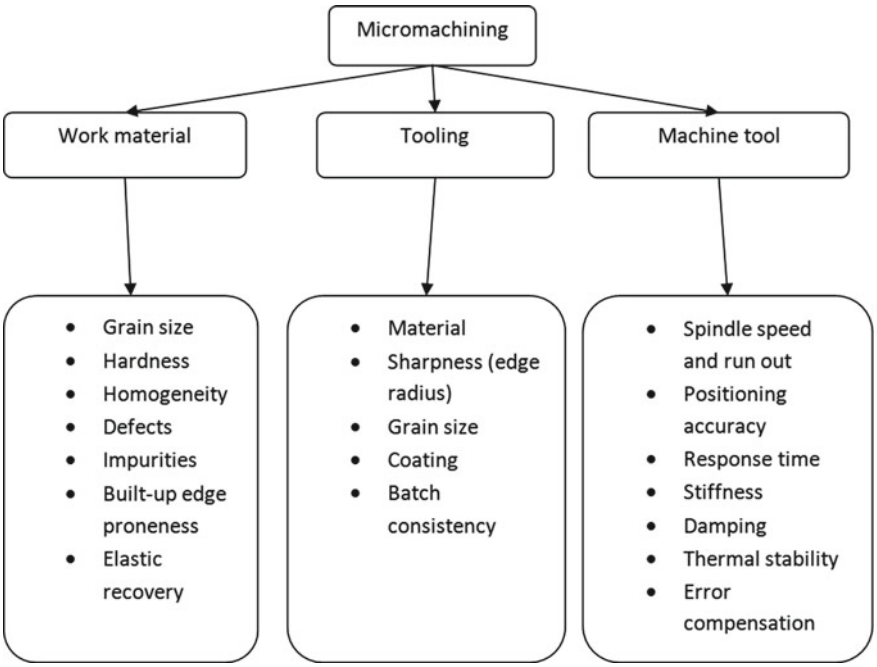

Fig. 4 Key aspects in micro-milling [27]

Micromachining processes for THz waveguide are particularly sensitive to the surface roughness and the precision of achieved machining geometrical accuracies.

1.9 Machining Strategies to Minimize Surface Roughness

Sub-millimeter waveguide technology is used in deep space signal retrieval where the highest detection efficiencies are needed and therefore, every possible signal loss in the receiver has to be avoided and stringent tolerances achieved. With a sub-standard surface finish, the signals traveling along the waveguides dissipate away faster than with perfect surfaces where the residual roughness becomes comparable with the electromagnetic skin depth. Therefore, the higher the radio frequency, the more critical this becomes [28].

Surface roughness and burr generation are the critical parameters for deciding the quality of the generated surface. Unlike conventional milling, micro-milling needs to have a minimum cut thickness for the dominance of the shearing mechanism below, which due to plastic deformation and elastic recovery, the quality of surface deteriorates. This is directly related to the size effects as discussed earlier; on cutter geometry i.e., edge radius, cutting parameters like speed, feed, axial and radial depth of cuts, etc., with strong influence on resulting accuracy and surface quality of micro features [27]. In the literature, the best value for the magnitude of cut has been associated with the minimum chip thickness, below which plowing and rubbing govern the cutting mechanism and result in bigger burr sizes, rougher surfaces, and elastic recovery of the workpiece [21, 29, 16]. Issues such as tool wear, deflection due to low stiffness, run-out, chatter are also very influential in microdomain for achieving high precision and surface quality and are related to properties of tool material and machine tool utilized [24].

1.10 Laser Micromachining

The features of THz waveguides were to be machined on metallic blocks without generating heating or mechanical damage that could create warping or loss of size and strength. Laser micromachining was done to fabricate metallic rectangular waveguides on free cutting brass, Aluminium alloy, Magnesium alloy, and 99% pure Copper. The waveguide sizes corresponding to the frequency of 1 THz, 3 THz, and 10 THz were chosen to study achieved tolerances, surface roughness, flatness, perpendicularity, and parallelism [30–39].

1.11 CW Fiber Laser Cutting

Continuous-wave (CW) operation of a light source means that it is continuously operated. It is not pulsed. For a laser, a continuous-wave operation implies that it is continuously pumped and continuously emits light. CW Fiber laser engraving was initially tried, and some free cutting brass was cut on this machine using 200 W,

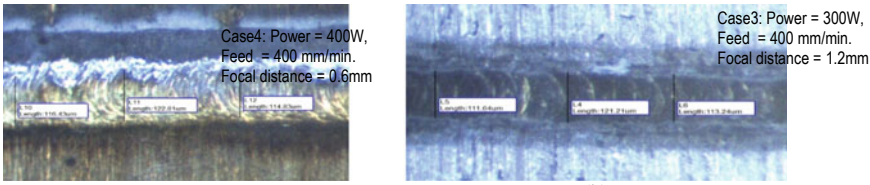

(a) (b)

Fig. 5 **a** SEM Image of sample cut on CW fiber laser [free cutting brass IS: 319 H_2] and **b** SEM Image for [Al alloy IS: 736 24345WP]

300 W, and 400 W power with a constant feed of 400 mm/min and focal distance of 0.6, 0.6, and 1.2 mm, respectively. Al Alloy samples were also cut using 100 W, 200 W, 300 W, and 400w at a feed of 400 mm/min and focal distance of 0.6 mm. Linear tolerances were ±10–15 μm and surface roughness of the order of 1.5 μm Ra. Surface roughness on the inside surface and tolerances of the cross section were poor, showing recast layers. Waveguide edges were not sharp. The SEM images are shown in Fig. 5a, b for free cutting brass and Al alloy, respectively.

1.12 Nanosecond Laser Cutting

A nanosecond is one-billionth of a second. In that one-billionth second pulsed nanosecond laser can interact with a range of materials to melt, ablate, clean, cut, engrave, and drill. Nanosecond Laser, which on average removes more material per pulse than femtosecond laser but at the expense of heat damage and greater recast on the cut edges. The heat damage may be in the form of residual stresses resulting in the change in the waveguide cross section. The surface roughness achieved was of the order of 300 nm Ra which is poor, and the recast layer was observed beyond the acceptance limit of higher frequency components especially above 1 THz. The recast is due to thermal heating. However, the biggest advantage is that the non-thermal ablation process leaves a clearer surface with minimum recast after machining and imparts less heat into the part during machining, thereby reducing residual stresses and hence stable part fabrication within desired tolerances. The surface roughness is shown in Fig. 6 for free cutting brass.

Femtosecond Laser Cutting and Process Parameters

The femtosecond laser is a laser that emits optical pulses with a duration of femtosecond (1 fs = 10^{-15} s). It is also known as ultrafast laser or ultra-short pulse laser. The characteristics of femtosecond laser cutting make it suitable for higher frequency components, particularly at and above 1 THz frequency band, where the waveguide size becomes 0.075 mm × 0.037 mm and 0.025 mm × 0.012 mm within ± 0.001- ± 0.002 at 3 THz and 10 THz respectively.

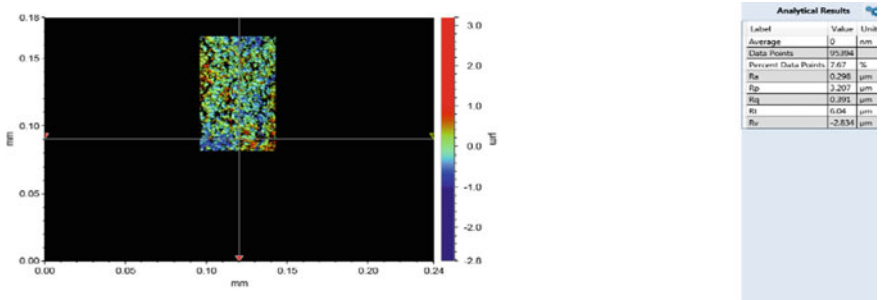

Fig. 6 Surface roughness of free cutting brass IS: 319 H_2

The pulse width was kept constant at 249 femtoseconds, and other parameters were strictly kept as tabulated in Table 6. The experiments were repeated for Al Alloy, free cutting brass, Magnesium alloy, and 99% Copper using the same parameters. Laser micromachining offers advantages over contact mechanical material removal for THz waveguide components at and above 1 THz. Figure 7a shows the Star cut tube model of the Coherent femtosecond laser machine, which is primarily for cutting tubular samples to make various components like heart stents. It has a flat sample attachment as shown in Fig. 7b, which can be attached and used for flat cutting.

Table 6 Sample-wise cutting parameters for Al alloy, brass, magnesium alloy, and 99% pure copper

Sample No Frequency	1A 10 THz	1B 10 THz	1C 3 THz	1D 1 THz	1E 0.625 THz	1F 0.33 THz
Laser Power (µJ)	5	5	5	5	10	15
Speed (mm/s)	6	4	3	2	2	2
Sample No	**2A**	**2B**	**2C**	**2D**	**2E**	**2F**
Laser Power	5	10	15	20	25	30
Speed	6	4	3	2	2	2
Sample No	**3A**	**3B**	**3C**	**3D**	**3E**	**3F**
Laser Power	5	5	5	10	15	20
Speed	6	4	3	2	2	2
Sample No	**4A**	**4B**	**4C**	**4D**	**4E**	**4F**
Laser Power	5	5	5	10	15	20
Speed	6	4	3	2	2	2
Sample No	**5A**	**5B**	**5C**	**5D**	**5E**	**5F**
Laser Power	5	5	5	10	15	20
Speed	6	4	3	2	2	2
Sample No	**6A**	**6B**	**6C**	**6D**	**6E**	**6F**
Laser Power	5	5	5	10	15	20
Speed	6	4	3	2	2	2

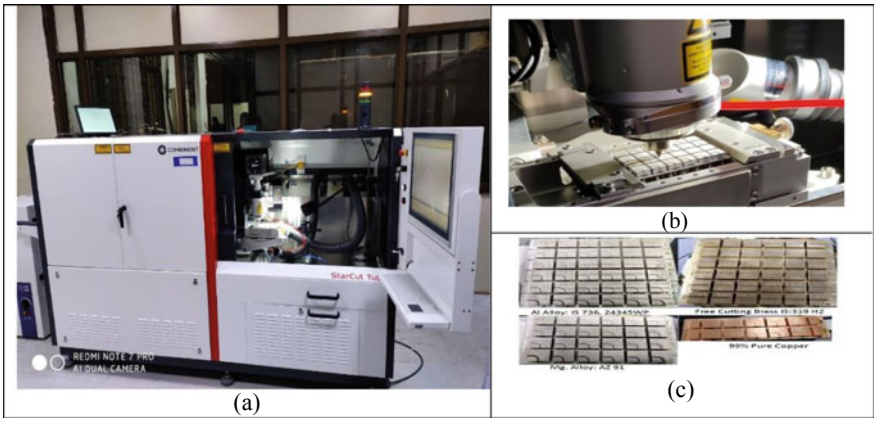

Fig. 7 **a** Femtosecond laser cutting machine (star cut tube)**, b** flat cutting attachment, **c** samples of Al alloy, free cutting brass, Mg alloy, and 99% pure copper, and **d** sketch of waveguide cross section

The motion in the *x*-axis is on this attachment through a link provided, and the Y and *z*-axis are on the laser head; in addition to this, one rotary axis is also available. The cutting parameters are laser power, laser speed, pulse width/duration. Argon gas pressure is kept constant at 15 bar throughout the experimentation. Various laser cuts were performed on a variety of materials, as shown in Fig. 7c, in the shape of the straight waveguide and 90º bend at different frequency ranges to study the effect of laser power and laser speed on the archived parameters like waveguide sizes, surface roughness, etc. For efficient cutting beam, dia was established after making few cuts and subsequently measuring them on the microscope and through SEM images. It was deduced that the beam diameter is about 20 μm, and sufficient overlap is required for smooth cutting.

1.13 Measuring Instruments for Linear and Geometrical Tolerances

The mechanical measurements of THz waveguides involve linear and geometric tolerances along with the configuration of the waveguide, which is desired for their efficient working. The measuring instruments used are described below, along with their features. The measurements are linear dimensions, geometrical tolerances like surface roughness, flatness, straightness, perpendicularity, parallelism, circularity, cylindricity, location, etc., which need very precise and non-contact type instruments supported with high-end technology and software for computation of errors because the waveguide dimensions are very small and approach of contact type instruments is limited.

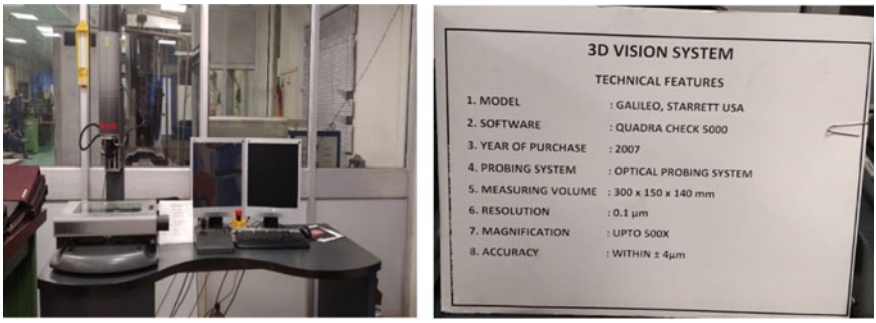

Fig. 8 Starrett 3D vision system and its features [Curtsy CAME, DEAL, DRDO]

1.14 Galileo Starrett 3D Vision System

Galileo Starrett 3D vision system as shown in Fig. 8 measures all geometrical parameters like straightness, perpendicularity, parallelism, circularity, etc. The resolution of this system is 0.1 µm. The inbuilt software is Quadra Check 5000 is capable of computing the abovementioned parameters from the image. The accuracy of the measurement is of the order of ±4 µm.

1.15 Optical Surface Profiler

The optical surface profiler works on the principle of topographical characterization of the surface of an object using a non-contact measurement method. It is used for the measurement of surface roughness and waviness. It scans the surface using an incident light source, interferometry objectives of different magnifications, and a detector measures the amount of light reflected, refracted by the surface. The high-precision data acquisition and processing system provide information about the surface topography in macro, micro, and sub-micron levels. The Contour GT-X Optical Profiler delivers the highest performing non-contact surface measurements for laboratory research and production process control. With white light interferometry (WLI), this metrology system can provide a high vertical resolution of 0.1 nm with a large field of view.

For precise measurement of surface roughness, the surface profile as shown in Fig. 9a was used, whose features and resolution are shown in Fig. 9b, and the measured surface roughness is displayed on the screen provided.

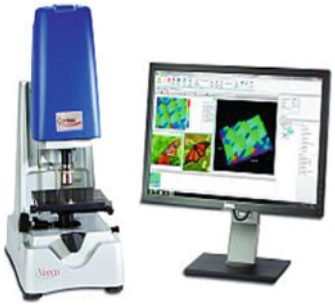

(a)

Make	Bruker, USA
Z Scan Range	0.1 nm to 10 mm
Vertical Resolution	0.1 nm
XY Stage	150mm manual with ±6° manual tip/tilt
Z focusing Stage	100 mm manual Z axis
Objectives	2.5x, 20x, 50x
Parameters	Surface Roughness, waviness & form errors.

(b)

Fig. 9 **a** Optical surface profiler and technical features of contour GT-X optical profiler. Curtsy CAME, DEAL, DRDO

1.16 Surface Flatness Checking

Based on the light interference principle, the flatness of the finished surfaces was checked using a monochromatic light source for the flatness of the surface. It gives precise measurements, which is one of the most accurate measurements. One of the conditions for using a monochromatic light source is that the component's surface must reflect the respective light bands.

The measurement system, along with its features, is shown in Fig. 10. Flatness was also measured using non-contact measurement methods. Flatness is required while lapping the mating surfaces of waveguide blocks to avoid leakage of energy. The mating blocks are lapped on low pressure until the flatness of λ/2 is achieved for a particular frequency of operation.

Monochromatic light source	Sodium Vapo Lamp
Optical Flat	Fused Quartz
1 Light Band	0.3 um

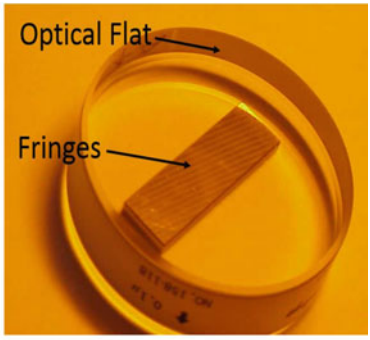

Fig. 10 Surface Flatness checking setup and its features Curtsy CAME, DEAL, DRDO

1.17 Measurement of Linear and Geometrical Tolerances

All the linear dimensions were measured using non-contact measurement methods for better accuracy. The waveguide is tabulated in Table 7. All the measurements are tabulated based on an average of 5–6 readings because the accuracy requirements are stringent. Linear dimensions of the broad side of waveguide '*a*' and narrow side of waveguide cross-section 'b' were measured using mechanical and optical methods. The linear tolerances were found within ± 2 to 5 μm for THz waveguides components. Refer [40–46] gives the procedures of using measurement system.

1.18 Measurement of Surface Roughness

Surface roughness (R_a) less than 40–50 nm was achieved for THz waveguide components on free cutting brass and Al Alloy. In Fig. 11, the roughness measurement of the waveguide surface.

The sample was placed under the lens, as shown in Fig. 11b, and the surface roughness value is shown in Fig. 11c. The average roughness parameter (Ra) was taken for the study because most of the literature has reported Ra only. However, the measurement system also provides other parameters like Ra, Rp, Rq, Rt, Rz, and surface parameters like Sa.

1.19 Measurement of Straightness

The straightness of the waveguide is a crucial parameter that depends on the linear scale or encoder of the machine tool. The measurement of straightness is shown in Fig. 12, where (a) shows the straight edge selection from the waveguide and (b) gives the value of straightness in micrometer.

1.20 Measurement of Perpendicularity

The waveguides are so kept that cross section is visible and the edge of the waveguide can be selected, perpendicularity can be measured using Starrett measuring system**.** It can also be measured on the multi-sensor system using a non-contact probe. The value of perpendicularity and edge selection is shown in Fig. 13a, b, respectively.

Table 7 Measured waveguide sizes, linear and geometrical tolerances

Frequency	Waveguide size (mm)	Tol (μm)	D.P. Alli (μm)	Ra (nmRa)	Flatness (μm)	Straightness (μm)	Parallelism (μm)	Perpendicu-larity (μm)
94 GHz	2.540 × 1.270	±5	±12	200	0.3	±20	±20	±20
140 GHz	1.650 × 0.830	±5	±10	150	0.3	±15	±15	±15
220 GHz	1.092 × 0.546	±5	±5	80	0.3	±10	±10	±10
0.330 THz	0.711 × 0.356	±5	±5	60	0.3	±5	±5	±5
0.400 THz	0.559 × 0.279	±5	±5	50	0.3	±5	±5	±5
0.500 THz	0.483 × 0.241	±5	±5	50	0.3	±5	±5	±5
0.625 THz	0.381 × 0.191	±5	±3–5	45	≤ 0.3	±5	±5	±5
0.750 THz	0.305 × 0.152	±5	±3–5	45	≤0.3	±5	±5	±5
1100 THz	0.254 × 0.127	±5	±2–3	45	≤0.3	±5	±5	±5
3000 THz	0.0750X0.0375	±5	±2–3	42	≤0.3	±5	±5	±5
10,000 THz	0.0254 × 0.0127	±5	±2	45	≤0.3	±5	±5	±5

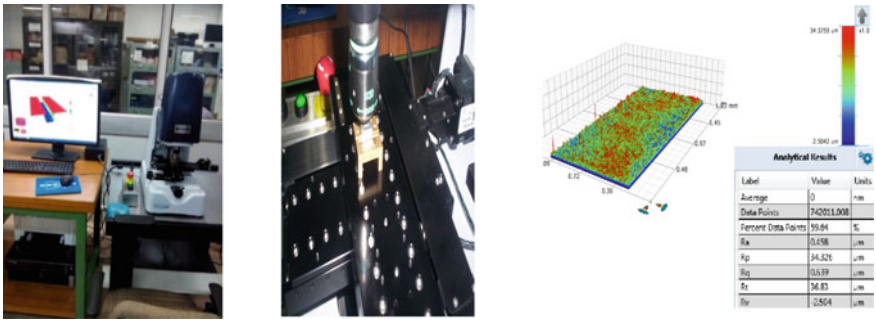

(a) (b) (c)

Fig. 11 **a** Surface profiler, **b** sample placed under the lens, **c** surface roughness achieved inside WG

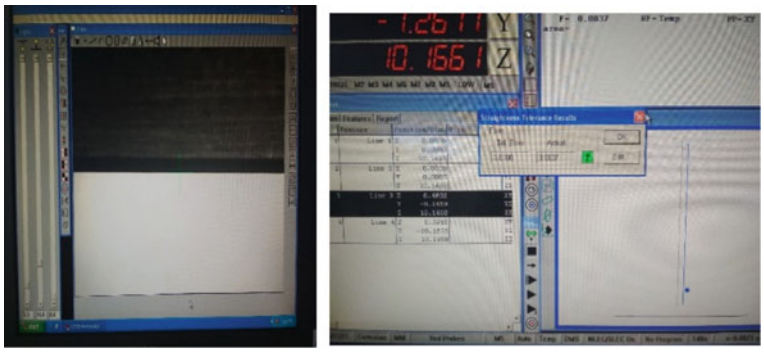

(a) (b)

Fig. 12 **a** Straightness of waveguide edge, **b** measured value

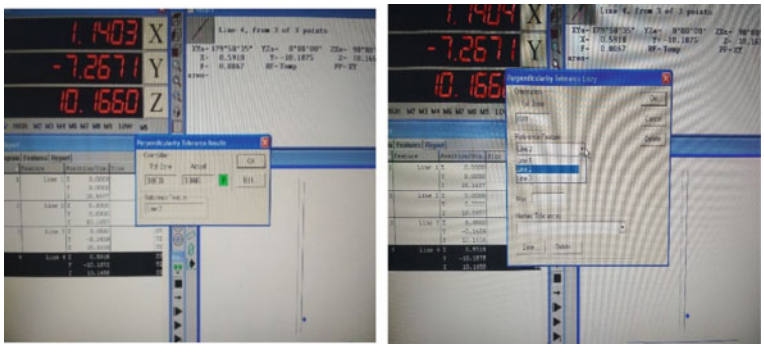

(a) (b)

Fig. 13 **a** Perpendicularity of waveguide edges, **b** measured value

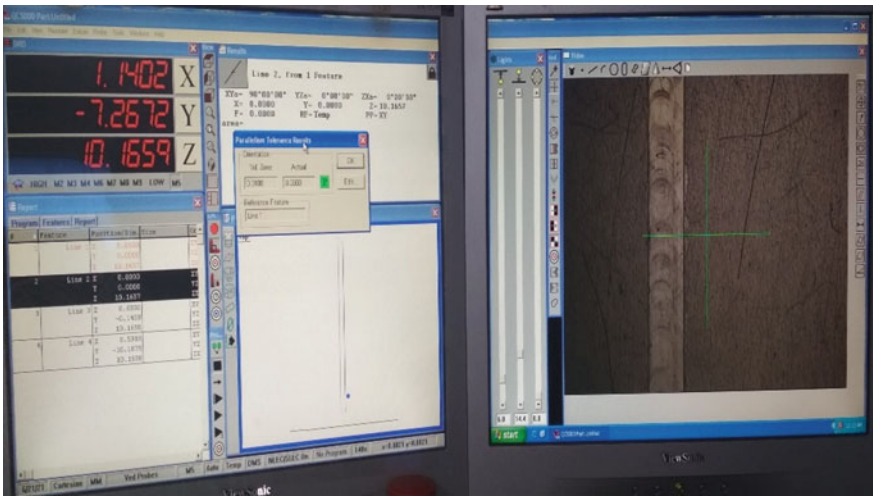

Fig. 14 Measurement of parallelism between two sides of W/G

1.21 Measurement of Parallelism

A similar setup was used for evaluating the parallelism. The two edges were selected to find parallelism between them, as shown in Fig. 14.

1.22 Measurement of Circularity

Circularity is critical for dowel pinholes, in which the dowel pin slides under precision slide fit conditions. Not only circularity, but also its cylindricity is also important from a precision point of view. If the cylindricity is maintained, the dowel pin positional tolerances are met which are required for precise alignment of two waveguide blocks resulting in the minimization of interfacing losses. The selection of hole and value of circularity is shown in Fig. 15a, b, respectively.

1.23 Measurement of Dowel Pin Diameter

The diameter of any pin or external feature can be measured precisely using a laser micrometer. The diameter of the dowel pin is a critical dimension in addition to its cylindricity for precise alignment of upper and lower blocks of the same waveguide and two different components at the time of assembly.

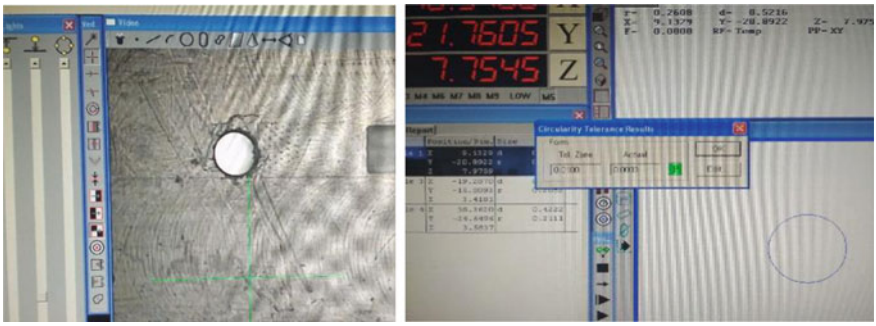

(a) (c)

Fig. 15 **a** Starrett measuring station, **b** measured of circularity, **c** circularity value

(a) (b)

Fig. 16 **a** Laser micrometer, **b** V blocks for keeping the measurement sample like dowel pin

The equipment for measuring diameter is shown in Fig. 16a, whereas the v block arrangement for keeping the pin or component under measurement is shown in Fig. 16b. Digital readout is there on the machine, which gives the value of diameter within few seconds. The tuning pins, filter, disk, sleeves, etc., are measured on this laser micrometer within a short time of high accuracy.

1.24 S-parameters Measurement

To simplify the description of the types of measurements a VNA can make, the reflection and transmission measurements are defined in terms of scattering parameters or S-parameters (Fig. 17).

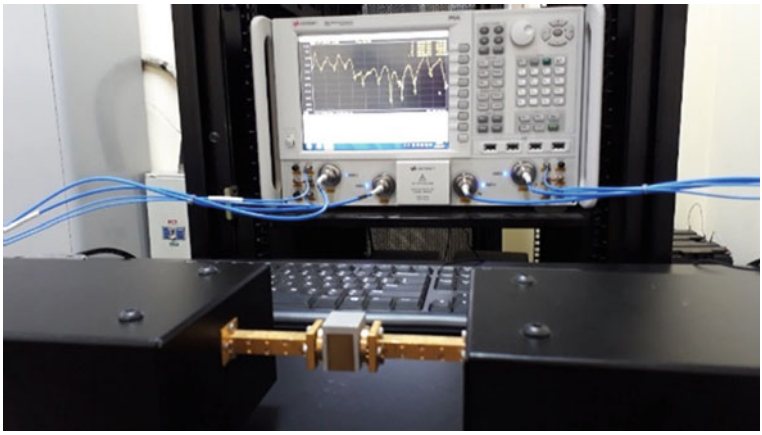

Fig. 17 Network analyzer setup for measurements

1.25 Waveguide Loss (S_{21}-Parameter) and Dispersion Measurements

The folded waveguide was designed for the operating frequency 220 GHz and the cold passband 170–280 GHz. In order to verify the design, 6 periods folded waveguide structure was manufactured using micro-milling. Two halves were fabricated and assembled using alignment pins. Table gives the dimensions of the folded structure.

Table 8 shows the reasonably good agreement between the design values and the achieved dimensions with micro-milling method. The maximum deviation observed is less than 10 μm. The fabricated pieces were assembled after aligning with alignment pins as shown in Fig. 18.

The structure was connected to PNA using WR-4 waveguide straight which operates from 170 to 260 GHz. The loss measurement for 220 GHz FWS is reported in the present study considering the effect of circular interpolation. Electrical measurements show that the measured values of resonances were within 1.5% of design values. Refer Fig. 19.

1.26 Dispersion Measurements

Dispersion characteristics depict the variation of phase velocity with frequency. This characteristic is important from the design of slow-wave structure for a TWT/amplifier. This gives the values of operating bandwidth for any device. This is basically measured by the method of resonances [1]. The structure is shorted at both ends to make it a resonant structure, and S-parameter measurement is carried out to observe the N resonances.

Table 8 Mechanical parameters of folded waveguide structure

Design parameter	Design value (mm)	Measured value (mm)	Deviation (mm)	Surface roughness (R_a)
Period	0.560	0.563	0.003	42 nm
Broad side waveguide dimension '*a*'/2 for each half part (depth)	0.425	0.430	0.005	45 nm
Narrow dimension of the waveguide '*b*'	0.120	0.125	0.005	41 nm
Value '*b*' at depth (each halves—measure of taper)	0.120	0.090	0.030	45 nm
Beam hole width 'a_1'/2 (each half part)	0.15	0.153	0.003	
Beam hole height, 'b_1'	0.075	0.078	0.003	–
Peak—Peak height of Folded waveguide structure	0.726	0.723	0.003	–
Inner height of the FWS	0.513	0.518	0.005	–

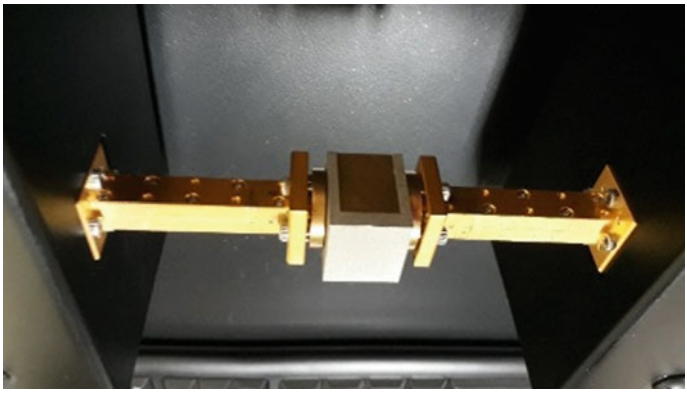

Fig. 18 Waveguide holder for measurement

Fig. 19 Assembly of FWS and dispersion measurements using PNA N5222A

Table 9 Measurement of folded waveguide resonances

Sl. No.	Design values of resonances	Measured values of resonances	Deviation (%)
1	178.28	177.65	0.35
2	180.17	181.7	−0.85
3	184.13	186.65	−1.37
4	189.71	192.5	−1.47
5	196.55	198.35	−0.92
6	204.47	204.2	0.13
7	213.38	212.75	0.30
8	223.1	222.2	0.40
9	233.36	233.9	−0.23
10	244.07	244.7	−0.26
11	254.51	254.15	0.14

Table 9 shows the comparison between design value and measured values of resonances Refer [47–50].

The corresponding dispersion characteristics (plot of frequency versus phase shift) are shown in Fig. 20. It is seen that the maximum deviation is 1.47% in the entire passband and less than 0.5% within the operating band (210–260 GHz).

1.26.1 Measurement of Insertion Loss of FWS

The same setup is used for S_{12}/S_{21} measurements. The measurement includes the losses due to the mismatch at both ends (abrupt transitions from FWS to the WR-4 dimensions). This loss has to be subtracted from the actual measured ones. This adapter loss was estimated using simulations and subtracted from the measurements. The loss due to FWS alone is shown in Fig. 21. The return loss is shown in Fig. 22. The total loss due to 12 periods is varying from 5 to 10 dB. The minimum loss achieved per period is from 0.42 dB. The results are very good with respect to the dimensions,

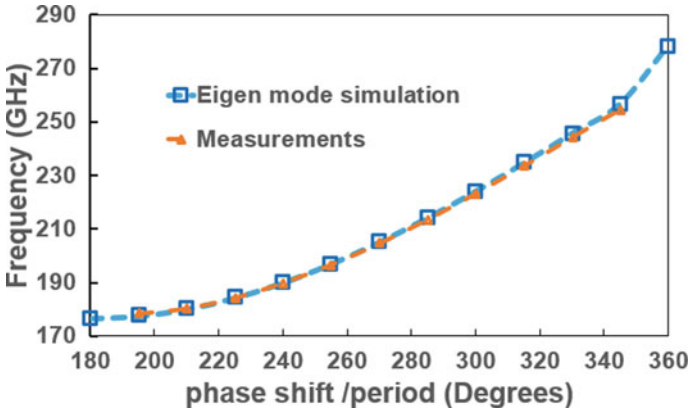

Fig. 20 Comparison of dispersion characteristics with measurements [48]

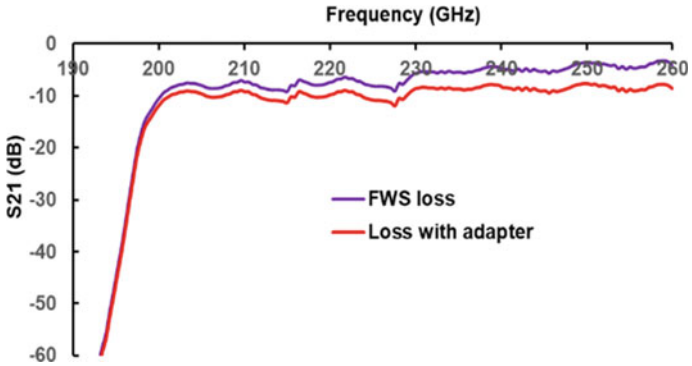

Fig. 21 Insertion loss measurements [48]

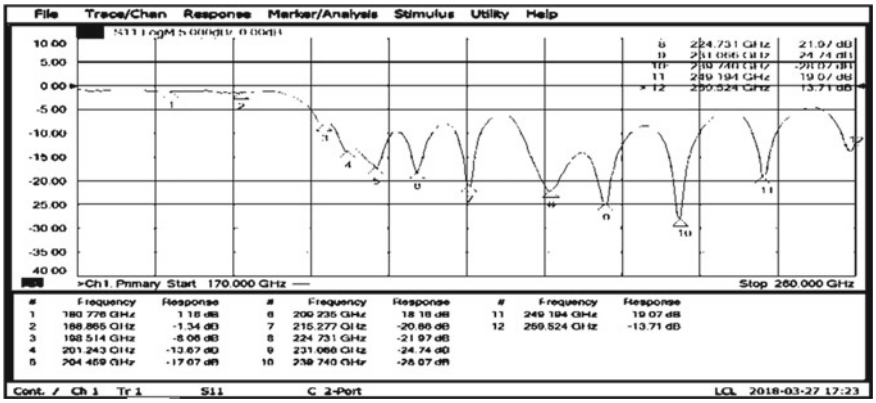

Fig. 22 Return loss measurement

and there is still scope to improve them, especially the waveguide narrow dimension 'b' becoming tapered to 0.09 mm from 0.120 mm in few samples.

As for as the results are concerned, dispersion characteristics are closely matching with the design. Maximum variation is less than 1.5%. One more frequency beyond 260 GHz could not be measured as the measurement capability is up to 260 GHz in MTRDC. This can be measured in RCI only. The main observation is the burrs that are seen in SEM images. The process of machining can be improved to reduce the machining burrs in the fabricated samples or there should be a method to super finish the fabricated parts. The loss per period is found approximately 0.42 dB. Various straight as well as folded waveguide measurements were carried out at different frequencies for loss measurements refer [47–50].

2 Conclusion

The main objective of this research work was to develop Terahertz waveguide components ranging from 100 Ghz to 1 THz, which was met successfully. Practically, waveguide components are made for some particular requirement like power divider, short slot coupler, or circulator, etc., based on geometric configuration of waveguide channels. The channels are the passages having either straight cross section, a bend of waveguide cross section, or a twist of cross section. Hence it was planned that if we can develop straight waveguide, waveguide bend, waveguide twist, and waveguide bend-cum-twist, any component can be developed. A series of components were developed at 0.22 THz, 0.33 THz, 0.625 THz, and 1.1 THz and tolerances close to or better than the requirements were achieved successfully. Since the technology is in infancy stage and we need to develop components in a batch size of less than 10, so tool-based micro-milling was considered to demonstrate working THz waveguide components. The electrical requirements were studied and their dependency on mechanical parameters was found out. These mechanical parameters were then controlled through other engineering characteristics, which are like process parameters, material parameters, machine tool parameters, programming skills, machining strategies, alignment and fitment strategies, and finally the verification methods. Waveguide made of metal and alloys are not only lab models, they are rugged and can be used in systems directly. The machining parameters were identified and strategized in such a way to minimize the effect of residual stresses, which distort the waveguide cross section and reduce the electromagnetic wave transmission.

References

1. D.B. and R.P. Sujit Kumar Jha, Experimental Analysis of Microstructure and Mechanical. Int. J. Automot. Mech. Eng. (IJAME) **11**, 2317–2331 (2015)

2. I. Gunes, M. Erdpan, B. Cengelci, Mechanical and electrical properties of artificially aged aluminium alloy AA 2024. Metallic Mater. **54**, 379–387 (2016)
3. R. Kočiško et al., The mechanical properties of OFHC copper and CuCrZr alloys after asymmetric rolling at ambient and cryogenic temperatures. Open Eng. **8**(1), 426–431 (2018). https://doi.org/10.1515/eng-2018-0041
4. R.C. Bonnah, Y. Fu, H. Hao, Microstructure and mechanical properties of AZ91 magnesium alloy with minor additions of Sm, Si and Ca elements. China Foundry **16**(5), 319–325 (2019). https://doi.org/10.1007/s41230-019-9067-9
5. M.K. Mustafa, U. Majeed, N. Nayan, Characterization of silicon nitride waveguide produced by R. F. sputtering technique. ARPN J. Eng. Appl. Sci. **11**(16), 9694–9698 (2016)
6. L. Su, Y., Zhang, Y., Qiu, C., Guo, X., Sun, Silicon photonics: silicon photonic platform for passive waveguide devices: materials, fabrication and applications. Adv. Mater. Technol. **5**(8) (2020). https://doi.org/10.1002/admt.202070046
7. D. Urbonas, R.F. Mahrt, T. Stöferle, Low-loss optical waveguides made with a high-loss material. Light: Sci. Appl. **10**(1), 15 (2021). https://doi.org/10.1038/s41377-020-00454-w
8. A. Kaur, J.C. Myers, M.I.M. Ghazali, J. Byford, P. Chahal, Affordable terahertz components using 3D printing, in *2015 IEEE 65th Electronic Components and Technology Conference (ECTC)* (2015), pp. 2071–2076. https://doi.org/10.1109/ECTC.2015.7159888
9. K.K. Tung, W.H. Wong, E.Y.B. Pun, Polymeric optical waveguides using direct ultraviolet photolithography process. Appl. Phys. A **80**(3), 621–626 (2005). https://doi.org/10.1007/s00339-003-2248-8
10. Y. Shirakata, N. Hidaka, M. Ishitsuka, A. Teramoto, T. Ohmi, High permeability and low loss Ni–Fe composite material for high-frequency applications. IEEE Trans. Magn. **44**(9), 2100–2106 (2008). https://doi.org/10.1109/TMAG.2008.2001073
11. A. Verma, A.K. Saxena, D.C. Dube, Microwave permittivity and permeability of ferrite–polymer thick films. J. Magn. Magn. Mater. **263**(1), 228–234 (2003). https://doi.org/10.1016/S0304-8853(02)01569-X
12. S. Anand, D.S. Kumar, R.J. Wu, M. Chavali, Graphene nanoribbon based terahertz antenna on polyimide substrate. Optik **125**(19), 5546–5549 (2014). https://doi.org/10.1016/j.ijleo.2014.06.085
13. L. Zhu, Y. Fan, S. Wu, L. Yu, K. Zhang, Y. Zhang, Electrical control of terahertz polarization by graphene microstructure. Optics Commun. **346**, 120–123 (2015). https://doi.org/10.1016/j.optcom.2015.02.032
14. H. Němec, P. Kužel, J.-L. Coutaz, J. Čtyroký, Transmission properties and band structure of a segmented dielectric waveguide for the terahertz range. Optics Commun. **273**(1), 99–104 (2007). https://doi.org/10.1016/j.optcom.2006.12.016
15. J. Yang, B. Yang, Z. Wang, W. Liu, Design of the low-loss wide bandwidth hollow-core terahertz inhibited coupling fibers. Optics Commun. **343**, 150–156 (2015). https://doi.org/10.1016/j.optcom.2015.01.020
16. G. Quintana, J. Ciurana, Chatter in machining processes: a review. Int. J. Mach. Tools Manuf. **51**(5), 363–376 (2011). https://doi.org/10.1016/j.ijmachtools.2011.01.001
17. D.H. Kai Cheng, *Micro-Cutting: Fundamentals and Applications*, 1st edn. (Wiley, Chichester, 2013)
18. A. Aramcharoen, P.T. Mativenga, Size effect and tool geometry in micromilling of tool steel. Precis. Eng. **33**(4), 402–407 (2009). https://doi.org/10.1016/j.precisioneng.2008.11.002
19. E. Vazquez, J. Gomar, J. Ciurana, C.A. Rodríguez, Analyzing effects of cooling and lubrication conditions in micromilling of Ti6Al4V. J. Clean. Prod. **87**, 906–913 (2015). https://doi.org/10.1016/j.jclepro.2014.10.016
20. V.K. Dr, *Jain, Introduction to Micromachining* (CR Press, India, 2001)
21. J. Chae, S.S. Park, T. Freiheit, Investigation of micro-cutting operations. Int. J. Mach. Tools Manuf. **46**(3–4), 313–332 (2006). https://doi.org/10.1016/j.ijmachtools.2005.05.015
22. X. Sun, K. Cheng, Chapter 2—Micro-/Nano-Machining through Mechanical Cutting, in *Micro-Manufacturing Engineering and Technology*, ed. by Y. Qin (William Andrew Publishing, Boston, 2010), pp. 24–38. https://doi.org/10.1016/B978-0-8155-1545-6.00002-8

23. N. Chen et al., Advances in micro milling: from tool fabrication to process outcomes. Int. J. Mach. Tools Manuf. **160**, 103670 (2021). https://doi.org/10.1016/j.ijmachtools.2020.103670
24. T. Gietzelt, L. Eichhorn, *Mechanical Micromachining by Drilling, Milling and Slotting* (IntechOpen, 2012). https://doi.org/10.5772/34124
25. A. García, G. Siller, H. R. Medrano-téllez, Micromanufacturing engineering and technology, in *ICOMM (8)*, (2013), pp. 658–664
26. E. Kuram, B. Ozcelik, Effects of tool paths and machining parameters on the performance in micro-milling of Ti6Al4V titanium with high-speed spindle attachment. Int. J. Adv. Manuf. Technol. **84**(1), 691–703 (2016). https://doi.org/10.1007/s00170-015-7741-7
27. M.A. Câmara, J.C.C. Rubio, A.M. Abrão, J.P. Davim, State of the art on micromilling of materials, a review. J. Mater. Sci. Technol. **28**(8), 673–685 (2012). https://doi.org/10.1016/S1005-0302(12)60115-7
28. W. Chen, W. Xie, D. Huo, K. Yang, A novel 3D surface generation model for micro milling based on homogeneous matrix transformation and dynamic regenerative effect. Int. J. Mech. Sci. **144**, 146–157 (2018). https://doi.org/10.1016/j.ijmecsci.2018.05.050
29. H. Weule, V. Hüntrup, H. Tritschle, Micro-cutting of steel to meet new requirements in miniaturization. CIRP Ann. Manuf. Technol. **50**(1), 61–64 (2001). https://doi.org/10.1016/S0007-8506(07)62071-X
30. H.T. Bookey et al., Femtosecond laser inscription of low insertion loss waveguides in Z-cut lithium niobate. IEEE Photonics Technol. Lett. **19**(12), 892–894 (2007). https://doi.org/10.1109/LPT.2007.897534
31. M. Farhan Shafique, I.D. Robertson, Laser machining of microvias and trenches for substrate integrated waveguides in LTCC technology, in *European Microwave Week 2009, EuMW 2009: Science, Progress and Quality at Radiofrequencies, Conference Proceedings—39th European Microwave Conference, EuMC 2009*, no. October (2009), pp. 272–275. https://doi.org/10.1109/EUMC.2009.5295980
32. T.L. See, Z. Liu, L. Li, X.L. Zhong, A comparison of the characteristics of excimer and femtosecond laser ablation of acrylonitrile butadiene styrene (ABS). Appl. Surf. Sci. **364**, 467–476 (2016). https://doi.org/10.1016/j.apsusc.2015.12.173
33. S. Ganti et al., Characterization and modeling of laser micromachined periodically corrugated metallic terahertz wire waveguides. J. Infrared Millimeter Terahertz Waves **33**(11), 1104–1116 (2012). https://doi.org/10.1007/s10762-012-9926-6
34. S. Prakash, S. Kumar, Fabrication of microchannels on transparent PMMA using CO2 Laser (10.6 μm) for microfluidic applications: an experimental investigation. Int. J. Precis. Eng. Manuf. **16**(2), 361–366 (2015). https://doi.org/10.1007/s12541-015-0047-8
35. C.W. Cheng, S.Y. Wang, K.P. Chang, J.K. Chen, Femtosecond laser ablation of copper at high laser fluence: Modeling and experimental comparison. Appl. Surf. Sci. **361**, 41–48 (2016). https://doi.org/10.1016/j.apsusc.2015.11.055
36. E.C. Santos, M. Shiomi, K. Osakada, T. Laoui, Rapid manufacturing of metal components by laser forming. Int. J. Mach. Tools Manuf **46**(12), 1459–1468 (2006). https://doi.org/10.1016/j.ijmachtools.2005.09.005
37. X. Yu et al., Study of engineered low-modulus Mg/PLLA composites as potential orthopaedic implants: An in vitro and in vivo study. Colloids Surf. B Biointerfaces. **174** (2019), pp. 280–290. https://doi.org/10.1016/j.colsurfb.2018.10.054
38. C.D. Nordquist, M.C. Wanke, A.M. Rowen, C.L. Arrington, M. Lee, A.D. Grine, Design, fabrication, and characterization of metal micromachined rectangular waveguides at 3 THz. IEEE Antennas Propag. Soc. Int. Symp. **2008**, 1–4 (2008). https://doi.org/10.1109/APS.2008.4619761
39. M.N.W. Groenendijk, J. Meijer, Surface microstructures obtained by femtosecond laser pulses. CIRP Ann. **55**(1), 183–186 (2006). https://doi.org/10.1016/S0007-8506(07)60394-1
40. Operation manual, Fast tool measurement with Werth 3-D multisensor coordinate measuring machine, Werth Messtechnik GmbH, Siemensstr. 19, D-35394, GieBen
41. Taylor Hobson's, machine manual, Talysurf 10, 401 Congress Ave #1760, Austin, TX 78701, USA

42. https://www.bruker.com/en/products-and-solutions/test-and-measurement/3d-optical-profilers/contourgt-x.html
43. J.F.W. Galyer, Charles reginal Shotbolt, Metrology for Engineers, Cengage Learning EMEA; 5th Revised edition (22 March 1990)
44. Operaton manual, Cimcore 3000i Series, Release 07/02/2003, Cimcore ®, Cimcore Carlsbad, California
45. QC5000, Metrology Software for multi-Sensor systems User Guide, Metronics, Inc., Bedford, New Hampshire, USA, 2004
46. N. V. Raghvendra, *Engineering Metrology and Measurements* (Oxford University Press, 2013)
47. H.S. Sudhamani, R. Bhardwaj, S.U.M. Reddy, J. Balakrishnan, Study of passband and stopband properties of sheet-beam folded waveguide structures. IEEE Trans. Electron Devices **66**(5), 2401–2408 (2019). https://doi.org/10.1109/TED.2019.2905774
48. R.K. Bhardwaj, H.S. Sudhamani, V.P. Dutta, N. Bhatnagar, Micromachining and characterisation of folded waveguide structure at 0.22THz. J. Infrared Millimeter Terahertz Waves **42**(3), 229–238 (2021). https://doi.org/10.1007/s10762-021-00767-w
49. H.S. Sudhamani, J. Balakrishnan, S.U.M. Reddy, Investigation of instabilities in a folded-waveguide sheet-beam TWT. IEEE Trans. Electron Devices **64**(10), 4266–4271 (2017). https://doi.org/10.1109/TED.2017.2736065
50. H.S. Sudhamani, J. Balakrishnan, S.U.M. Reddy, PIC simulations of folded waveguide slow wave structure for THz TWT's, in Proc, 4th Int. Conf. Electron. Warfare (EWCI), Bangaluru, India (2016), pp. 95–97

Rakesh Kumar Bhardwaj is working as Scientist: F at Defence Electronics Applications Laboratory (DEAL) of Defence Research and Development Organisation (DRDO) at Dehradun Uttrakhand. He has obtained his B.Tech. in Mechanical Engineering from College of Engineering Thiruvananthapuram, Kerala University in 1996 and M.Tech. in Production Engineering from IIT Delhi in 2006.He submitted his Ph.D. thesis at IIT Delhi in 2021. He joined DRDO as Scientist B in 1997, since then he is working in Design and Development of microwave and mm-Wave components ranging from X, L,S, Ku,Ka and W band. He is recipient of Padamshree M M Suri Project award at IIT Delhi in 2006, National Science Day oration and Gold medal in 2007, Agni Award for Excellence in Self Reliance of Defence Technology in 2011 and National Technology Day Oration and Titanium Medal in 2015. He has published 27 technical papers in Journals and conferences. His Area of Specialization is Production Engineering, CAD/CAM, Composite materials, Precision Engineering, Micro and nano manufacturing. His current activity includes design and development mm-Wave and terahertz waveguide components within desired tolerances. He is a member of ASME, SSME, and Fellow of Institution of Engineers India. In addition to academics, he is Vice President of EcoGroup Society and Secretary of IIT Alumni association, Dehradun, Uttrakhand Chapter. He is also associated to Art of Living.

Dr. V. P. Dutta , Scientist G has obtained his B.E. in Production Engineering from Punjab Engineering College, Chandigarh in 1980. He worked initially for six years in private industries like Escort, Godrej, and Samtel and joined DRDO as Scientist B in 1986. He conferred MBA from IGNOU in 1995 and Ph.D. in Mechanical Design from IIT Delhi in 2005. Presently he is Scientist: G and Group Director, Centre for Advance Mechanical Engineering Group of DEAL, DRDO, Dehradun. He has published number of papers in International and National journals.

Prof. Naresh Bhatnagar obtained his B.Tech. in Mechanical Engineering from REC Trichy, M.Tech. and Ph.D. in Production Engineering from IIT Bombay. Presently he is working as Professor in Mechanical Engineering Department of IIT Delhi, and Associated DEAN R&D of IIT Delhi. He has published more than 150 International Journal Papers. He has patents to his credit. His area of expertise is Production, Composite materials, Bio materials and their processing. He is authored chapters and books of International repute. He has guided more than 21 Ph.D. thesis.

A Comparative Analysis of Optical and Electrical Control of High Frequency Properties of Si IMPATT in W-band

Suranjana Banerjee

Abstract Electrical control of IMPATT (Impact Avalanche Transit Time) diode by applying varying bias currents results in frequency tuning and power enhancement of the device but if the device is irradiated by optical energy then the optical control terminal provides an additional control due to which various interesting properties emerge like frequency chirping and power reduction which can be exploited in applications like phased array radars, optoelectronic integrated circuits and high frequency signal processing systems. Initially, bias current optimization is done by varying the currents from 4.5×10^8 Am^{-2} to 8.5×10^8 Am^{-2}. The value of current at which efficiency and power output are maximum is taken as the optimum value of current for comparison of electrical and optical properties of the device at the window frequency of 94 GHz in W-band. For optical illumination, two configurations of the double drift region (DDR) ATT device are taken: Flip Chip (FC) and Top Mount (TM) and their behaviors are compared for various incident photon flux densities near bandgap absorption of Si which is nearly 1.1 μ. An analytical model is used to establish a relation between the electron and hole current density of the device taking into account the normalized values of the current densities and the flux density of optical energy incident on the device. Comparison outcomes show RF power and efficiency reduction in optically controlled FC or TM structures as compared with the un-illuminated device which is electrically controlled. An interesting observation is frequency shift in the admittance characteristics which is utilized in frequency modulation and its applications. Outcomes also reveal that light irradiation effects show better visible results for electron dominated photocurrent (TM) than that for hole dominated photocurrent (FC).

Keywords Bias current modulation · Frequency chirping · Bandgap absorption · Flip chip · Top mount

S. Banerjee (✉)
Department of Electronics, Dum Dum Motijheel College, Kolkata, India

M. El Ghzaoui et al. (eds.), *Terahertz Wireless Communication Components and System Technologies*, https://doi.org/10.1007/978-981-16-9182-9_17

1 Introduction

Optically irradiated IMPATT diode leads to various modifications of the important high frequency characteristics of the device which make them appealing to researchers for applications like optoelectronic integrated circuits, signal processing systems and phased array antennas for imaging and space communication. Electrical control of the selected device with bias current provides frequency tuning and strengthens the RF power output of the device while optical control with optical illumination provides frequency chirping and power reduction which property is utilized in numerous applications, some of which are mentioned before. The device selected here for electrical and optical tuning is Impact Avalanche Transit Time (IMPATT) diode. Silicon based IMPATT diodes have already been accepted as a reliable solid-state source of high power generation with a good efficiency factor covering a vast range of frequencies from microwave to millimeter wave regions i.e., 3–300 GHz of the electromagnetic spectrum [1–6]. These Si diodes under dc bias modulation and optical modulation show different fascinating properties which have captivated research interest of experimenters and researchers to further explore them in various application regimes.

Literature reports [7–10] reveal experimental realization of optical control functions of the photo-illuminated device like high frequency power modulation, injection locking and frequency tuning. Photocurrent generation and rise of leakage current in the reverse biased diode form the basis for all these optical functions.

Various methods can be adopted to accomplish frequency tuning: (i) electrical tuning with a dc bias current (ii) mechanical tuning by varying the diameter and height of the resonant cap and the position of the sliding tuner of the resonant cap of an IMPATT oscillator and (iii) optical tuning by photo-illumination of the IMPATT device. An analytical model is used to establish a relation between the electron and hole current density of the device taking into account the normalized values of the current densities and the flux density of optical energy incident on the device. Simulation is done in MATLAB platform to obtain the admittance characteristics, resistivity profiles, RF output power and efficiency profiles with small amplitude of ac signal for un-illuminated device and also illuminated device for various incident photon flux densities near bandgap absorption of Si which is approximately 1.1 μm. Two configurations are considered for optical illumination i.e., Flip Chip (FC) structure where the photocurrent is influenced by mobile carrier holes and Top Mount (TM) structure where the photocurrent is influenced by mobile carrier electrons. Then the outcomes are compared for both the cases. The optimized bias current density is obtained for the un-illuminated structure and also the output power, efficiency of conversion and other dc and small signal parameters are obtained for the optimized bias current. Results are also analyzed after photo irradiation of the concerned device for two configurations as mentioned above. IMPATT diode is used as the solid-state device for optical illumination at 94 GHz in the W-band.

Various dc and small signal parameters obtained after simulation help the author to choose the particular configuration which provides good efficiency and adequate

amount of power at the output. The configuration which provides better results can be used for further research and development of optically irradiated ATT device with even further modifications. Gummel and Blue [11] have reported revolutionary work on the analysis of the IMPATT device with ac signal of small amplitude using a random doping profile and ionization rates of the carriers which are electric field dependent parameters. This model steered research interests among various researchers who made further developments in the analysis using the platform created by Gummel and Blue. Various studies are reported by Dash et al. [12] and Roy et al. [13, 14] using the well-established field maximum simulation method. But all these reports are associated with the RF characteristics of the un-illuminated IMPATT device. An analytical model has been used to carry out the avalanche noise behavioral analysis of the ATT device in FC and TM structures of double drift layered Si IMPATT device.

2 IMPATT Oscillator

Figure 1 shows the cross-sectional view of a resonant cap oscillator comprising of a cap and post structure below which the IMPATT diode is entrenched and the whole thing is enclosed in a rectangular waveguide which results in generation of high frequency waves when the diode is tuned to achieve resonance in the cavity. At the resonant frequency, the electromagnetic fields confined within the RF cavity in the microwave or millimeter wave region of the electromagnetic spectrum reinforce to form standing waves within the cavity. The cap structure behaves like an impedance transformer which is used to match the impedance of the device and the load necessary for resonance.

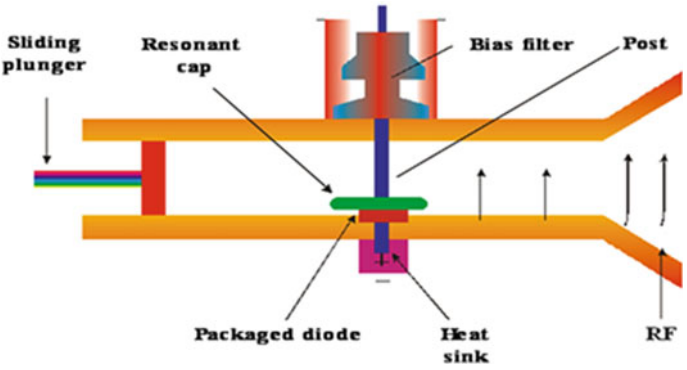

Fig. 1 IMPATT oscillator with cap and post arrangement

2.1 Tuning Mechanisms

Tuning of the cap oscillator can be done mechanically by tuning of the RF cavity and also by properly positioning the sliding plunger [15]. Cavity tuning is done by changing both the cap height and diameter to attain optimization of oscillator performance. During this process of cavity optimization, the oscillation frequency is varied around the design frequency of operation. The condition for optimization of the cavity resonator is related by the following expression [15]:

$$D = \lambda/2 \tag{1}$$

where, D is the cap diameter and λ is the operating wavelength.

Hence, for practical realization of the device oscillator, the cap diameter must be properly designed at half the wavelength at the operating frequency for getting optimum performance of the oscillator.

The cavity structure can be fashioned as a cylindrical cavity bounded above and below by electric enclosure and the side walls by magnetic enclosure [16–18].

Variation of the sliding short position in small steps provides tuning of power and the frequency of oscillation. The oscillation frequency varies around the design frequency. Literature reports [15] reveal an early frequency leap due to the adopted tuning mechanism accompanied by an abrupt drop of frequency with successive power increase at the output. The position of the sliding plunger can be varied over a range of $\lambda/2$ enables smooth mechanical tuning around the design frequency of operation [15].

Electronic tuning of the oscillator can be attained by varying the dc bias current to modify the output power and the frequency at which oscillation takes place giving rise to optimized cavity parameters like diameter and height of the RF cavity.

3 Design Procedure for Electrical Control of the Si IMPATT Diode

The input doping parameters for the chosen base semiconductor of the IMPATT diode and the design frequency of 94 GHz can be approximated from the empirical formula given by Sze and Ryder as follows:

$$W_{n,p} = 0.37\, v_{sn,sp}/f\ . \tag{2}$$

where, $W_{n,p}$ = depletion layer thickness for the n and p sides, $v_{sn,sp}$ = carrier saturation velocity and f = operating frequency.

Table 1 shows the design parameters of electrically controlled Si IMPATT at the design frequency of 94 GHz which shows the n and p layer epitaxial thickness and doping along with the substrate layer doping.

Table. 1 Design parameters for Si IMPATT at 94 GHz design frequency

Design frequency, f_d (GHz)	n-epitaxial layer thickness, W_n (μm)	p-epitaxial layer thickness, W_p (μm)	n-epitaxial layer doping, $n_{n0} = N_D$ ($\times 10^{23}$ m^{-3})	p-epitaxial layer doping, $p_{p0} = N_A$ ($\times 10^{23}$ m^{-3})	Substrate layer doping, N_{sub} ($\times 10^{26}$ m^{-3})
94	0.3200	0.3000	1.450	1.650	1.0

3.1 Device Model

The two models used for accomplishing effective device performance especially at a high frequency range like in the W-band are Classical Drift–Diffusion (CDD) model and Energy Relaxation (ER) model. Out of these, CDD model is desirable than ER model for dc and RF analysis of the Si IMPATT at 94 GHz as shown by Dalle and Rolland [19].

A device model will be used in the simulation software to obtain the aforementioned dc properties. The computation is initiated from the location where electric field gives the peak value in the active layer depleted of mobile carriers near p–n junction. Concentration of impurities per unit volume in the n-side and p-side of the junction is considered as the input parameters assuming symmetrical doping profile, doping functions in the n and p regions are uniform and those at the epitaxy-substrate interfaces are considered to be exponential functions given as:

$$\begin{aligned} N(x) &= N_{n^+}\exp\left(-1.08\lambda_n(x) - 0.78\lambda_n(x)^2\right) && x \le 0 \\ &= N_D && 0 > x \ge x_1 \\ &= N_D\left[1 - \exp\left(\tfrac{x}{s}\right)\right] && x_1 > x \ge x_j \\ &= -N_A\left[\exp\left(-\tfrac{x}{s}\right) - 1\right] && x_j > x \ge x_2 \\ &= -N_A && x_2 > x \ge W \\ &= -N_{p^+}\exp\left(-1.08\lambda_p(x) - 0.78\lambda_p(x)^2\right) && x > W \end{aligned} \tag{3}$$

where, N_A is the acceptor concentration and W_p is the width of p-epitaxial layer, x_j is the junction location measured from the surface.

Near the junction the doping profiles are considered to be steeply rising exponential functions because the junctions are produced by MBE (Molecular beam epitaxy) technique. The important physical parameters governing the material behavior are carrier saturation velocity, rate of ionization of the carrier, permittivity of the semiconductors, diffusion constant, carrier mobility, etc.

3.2 DC Analysis

The important one-dimensional device equations under dc conditions will be solved numerically. Figure 2 shows the one-dimensional schematic diagram of DDR

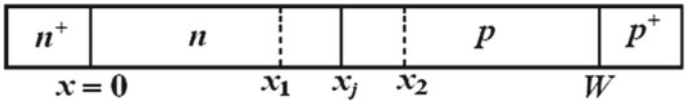

Fig. 2 1-D structure of DDR IMPATT diode

IMPATT device. These equations are Poisson's equation, carrier transport equation, current density equations and space charge equations. The effects of cloud of carrier charge accumulated in the active layer and carrier diffusion due to concentration gradient will be incorporated in the simulation program. All these equations are simultaneously solved numerically by using Finite Difference Technique. A double iterative field maximum method reported in [20] will be used here. The method used for simulation of the steady state characteristics of the device is based on double iteration commencing from the location of the maximum electric field [20].

The computation starts from the point having peak electric field value, then it continues to the rightmost extremity of the active layer, returning to the center peak field position and then pursuing the same to the leftmost extremity of the active layer.

The next step is to test whether the boundary conditions of the electric field and the difference of carrier current density normalized with respect to the total current density match with those obtained from the computation at the boundaries of the depletion layer. Iteration is done over two parameters: location of the peak field and the peak field value subject to proper limiting conditions at the edges of the active layer and this continues till the conditions are satisfied. The simulation program enables the convergence to reach within 20 iterations. Once the convergence is obtained, the solution for distributions of field, $\xi(x)$ and current normalized with respect to the maximum value, $P(x)$ can be obtained. The avalanche zone width can also be obtained from the current density profile.

E-field integrated over the entire width of the active region gives the breakdown voltage V_B and that integrated over the thickness of the avalanche zone gives the avalanche layer voltage V_A. The drift zone voltage V_d is the difference of V_B and V_A. Efficiency of conversion from static to high frequency can be obtained using Scharfetter-Gummel formula given below:

$$\eta = 2m/\pi \times V_D/V_B. \tag{4}$$

where, m = modulation factor, V_D = drift voltage and V_B = breakdown voltage.

3.3 RF Analysis for Small Amplitude AC Signal

The analysis for small amplitude RF signal will be carried out using the dc parameters obtained from the dc analysis by using Gummel-Blue model described in [11]. The admittance (G-B; G-conductance, B-susceptance) plots and the negative impedance

(R and X; R-resistance and X-reactance) plots will be produced for this small amplitude signal by varying the external current excitation. The plots will provide a deep physical insight into the RF power generation in the depletion layer. Negative conductance reaches the peak at the optimum frequency while the frequency at which B makes a transition from positive (inductive) to negative (capacitive) is the avalanche resonance frequency. For oscillation to occur, negative G and positive B condition must be fulfilled. Integration of the impedance profiles over the active layer using numerical method gives the total resistance and reactance from which the G and B can be obtained using the equations given below. Thus,

$$Z_R(\omega) = \int_0^W R(x,\omega)\mathrm{d}x;\; Z_X(\omega) = \int_0^W X(x,\omega)\mathrm{d}x. \tag{5}$$

$Z_D(\omega)$ and $Y_D(\omega)$ is obtained from Eqs. (15) and (16) respectively as a function of a specified frequency ω=2πf and for an injected current density J_0.

$$Z_D(\omega) = \int_0^W Z(x,\omega)\mathrm{d}x = Z_R(\omega) + iZ_X(\omega). \tag{6}$$

$$Y_D(\omega) = \frac{1}{Z_D(\omega)} = G(\omega) + iB(\omega) = \frac{1}{(Z_R(\omega) + iZ_X(\omega))} \tag{7}$$

The small signal simulation provides the admittance characteristics of the device which enables determination of the peak optimum frequency, f_p corresponding to peak negative conductance, G_p. Then the negative resistance plots and Q-factor are simulated at the peak frequency. Immediate necessary conditions for obtaining proper design parameters are procured from the outcomes of the device simulation at millimeter and terahertz frequency regime by modulating the injected current density. The expressions given below help procurement of the conductance (−ve) and susceptance (+ve).

$$\left.\begin{aligned} |-G(\omega)| &= Z_R(\omega)/\left(Z_R(\omega)^2 + Z_X(\omega)^2\right) \\ |B(\omega)| &= -Z_X(\omega)/\left(Z_R(\omega)^2 + Z_X(\omega)^2\right) \end{aligned}\right\} \tag{8}$$

Power obtained at THz frequency operation is given as.

$$P_{\mathrm{RF}} = \frac{1}{2}(V_{\mathrm{RF}})^2\left|G_p\right|A_j \tag{9}$$

where, V_{RF} (=$m_x V_B$) is the voltage obtained at the particular THz frequency, $\mathrm{m_x}$ is the percentage of modulation (<30%), $\mathrm{V_B}$ is the static voltage at breakdown and A_j is the circular cross-sectional area of the device.

4 Analytical Model to Analyze the RF Properties of the Optically Irradiated Device

Two vertical configurations: Top Mount (TM) and Flip Chip (FC) are taken to investigate the optically irradiated characteristics of the mesa device. In TM configuration, light irradiation is done over the p^+ layer which acts as the topmost layer for TM whereas in FC configuration, the topmost layer is n^+ layer which is irradiated with light through a controlled optical window [7, 9, 21, 22] as shown in Fig. 3. The photocurrent arising from TM configuration is primarily due to electrons as light is incident over the p^+ layer while that from FC is due to holes as the topmost n^+ layer is irradiated by light. A relation is obtained between the photon flux incident on the mesa structure and the normalized difference of hole and electron current density at the edges of the depletion layer which is substituted in the program to obtain the variations of RF properties due to optical illumination with different photon flux densities.

The electron and hole multiplication factors (M_n & M_p) are given by,

$$M_n = J_0/J_{ns\,(\text{Total})} \quad \text{and} \quad M_p = J_0/J_{ps\,(\text{Total})} \tag{10}$$

where, $J_{ns/ps(\text{Total})}$ is the total electron/hole reverse saturation current having two components, i.e., (a) thermally generated saturation current and (b) optically generated saturation current. Thus,

$$J_{ns\,(\text{Total})} = J_{ns(\text{Th})} + J_{ns(\text{Opt})} \quad \text{and} \quad J_{ps(\text{Total})} = J_{ps(\text{Th})} + J_{ps(\text{Opt})} \tag{11}$$

The expression for thermally generated electron and hole reverse saturation currents is given by,

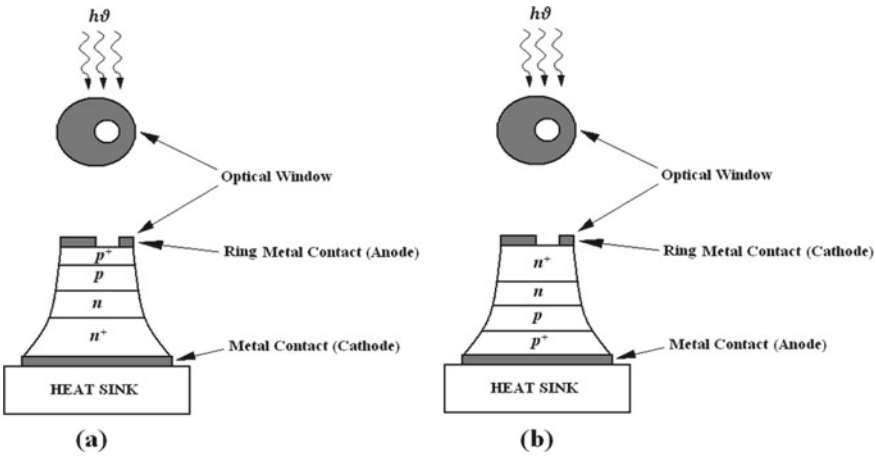

Fig. 3 Schematic diagram of optically illuminated **a** TM and **b** FC IMPATT device structures

$$J_{ns(\mathrm{Th})} = q D_n n_{p0}/L_n \quad \text{and} \quad J_{ps(\mathrm{Th})} = q D_p p_{n0}/L_p \tag{12}$$

$D_{n/p}$ are the diffusion coefficients which are obtained from [23] at 500 K. L_n and holes L_p are the diffusion lengths of Si at 500 K which are 35.4 μm and 10.0 μm respectively [23]. $\varphi_0(\lambda)$ m^{-2} s^{-1} is the photon flux of wavelength λ be incident on either p^+ or n^+-layer of vertical IMPATT device. Presuming 100% internal quantum efficiency which means creation of an electron–hole pair (EHP) from a photon.

The generation rate of EHPs as a function of distance x from the surface is obtained from [24] as,

$$G_L(x) = \alpha(\lambda)\varphi_0(\lambda)[1 - R(\lambda)]\,\mathrm{e}^{-\alpha(\lambda)x} \tag{13}$$

where, $\alpha(\lambda)$ and $R(\lambda)$ are the absorption coefficient (m^{-1}) and reflectance [$R = (n_2 - n_1)/(n_2 + n_1)$; n_2 = refractive index of the semiconductor, n_1 = refractive index of air] of the semiconductor material respectively at a wavelength of λ. For DDR MITATTs, the photon flux φ_0 may be incident on either p^+ or n^+ surfaces depending on Top Mount (TM) or Flip Chip (FC) structure respectively. So, EHP generation rate at the leading edge of p or n-drift layers is obtained from Eq. (4) by substituting,

$$x = W_{p+} \,\text{for TM} \quad \text{and} \quad x = W_{n+} \,\text{for FC} \tag{14}$$

Now, optically generated electron and hole reverse saturation current densities at the edges of the depletion layer are given by,

$$J_{ns(\mathrm{Opt})} = q G_L L_n \quad \text{and} \quad J_{ps(\mathrm{Opt})} = q G_L \mathrm{L}_p \tag{15}$$

By using Eqs. (10), (11), (12) and (15), the normalized difference of electron and hole current density at the edges of the depletion layer is given by,

$$\begin{aligned} P(0) &= \left(2q\left(D_p p_{n0} + G_L L_p^2\right) - J_0 L_p\right)/J_0 L_p \quad \text{and} \\ P(W) &= \left(J_0 L_n - 2\mathrm{q}\left(D_n n_{p0} + G_L L_n^2\right)\right)/J_0 L_n \end{aligned} \tag{16}$$

A relation between the incident photon flux and the normalized difference of electron and hole current density at the edges of the depletion layer is obtained from Eq. (16). This relationship provides the boundary conditions in the proposed simulation model for obtaining the variation of RF properties of the optically illuminated device. Table 2 shows the bandgap absorption wavelength of different semiconductors like Ge, Si, InP, GaAs, 4H-SiC and Wz-GaN which indicates the minimum wavelength of the optical radiation required to overcome the bandgap of the particular semiconductor so that the carriers can cross the bandgap and go to the conduction band to give rise to photocurrent in the reverse biased device. The value of bandgap absorption wavelength is extremely essential to choose the proper optical source. The same absorption wavelength is also shown in Fig. 4 which gives the variation of

Table 2 Bandgap absorption wavelength of different semiconductors at 300 K

Materials	Bandgap, E_g (eV)	Bandgap absorption wavelength, λ_{max} (μm)
Ge	0.66	1.8690
Si	1.12	1.1080
InP	1.34	0.9260
GaAs	1.43	0.8680
4H-SiC	3.23	0.3840
Wz-GaN	3.20	0.3880

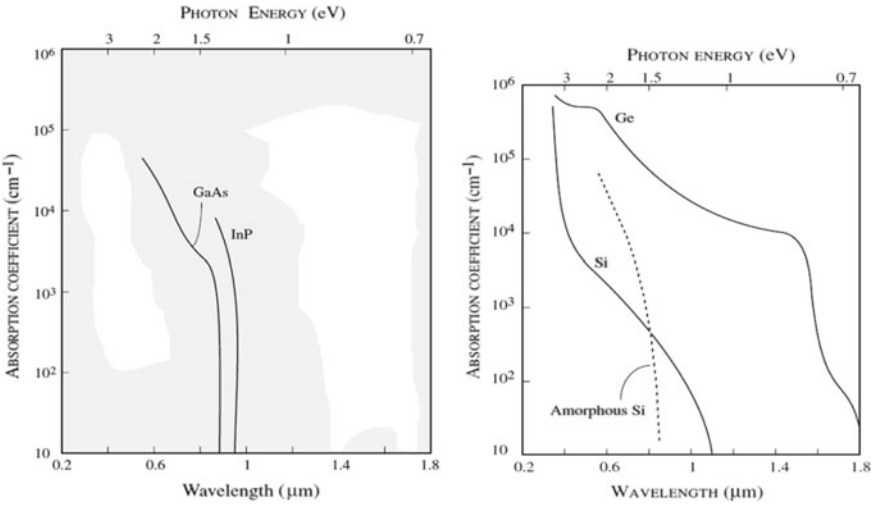

Fig. 4 Variation of absorption coefficient with wavelength of different semiconductors at 300 K

the absorption coefficient with wavelength for the same different semiconductors at 300 K.

5 Simulated Results for the Electrical Control of Un-illuminated IMPATT Diode

The results obtained after simulation of the un-illuminated or electrically controlled IMPATT device with bias currents varying from 4.5×10^8 Am^{-2} to 8.5×10^8 Am^{-2} are provided in Figs. 7, 8, 9, 10 and 11. Electric field profile in Fig. 5 shows the highest peak for the lowest bias current. Figure 6 shows the variation of the breakdown voltage, peak electric field and conversion efficiency with varying current densities. Peak electric field slightly decreases with increasing bias current as is also obvious from Fig. 5 and breakdown voltage increases slightly with current bias. Conversion

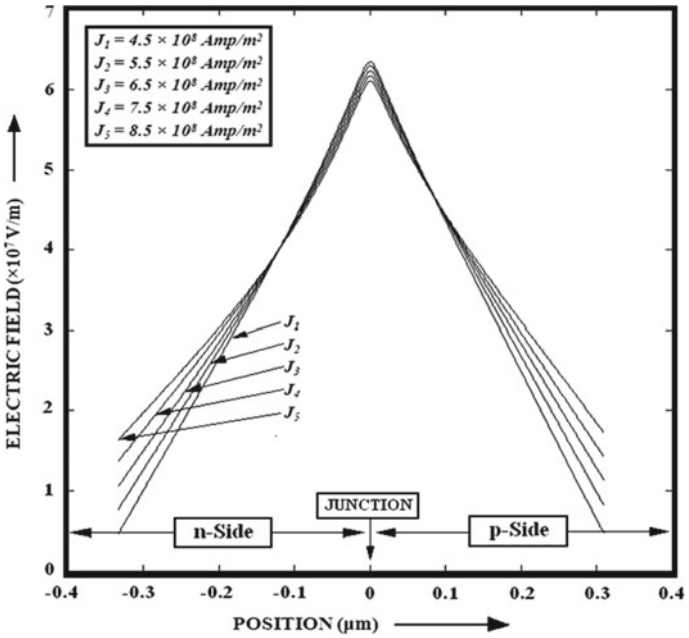

Fig. 5 Electric field profile for different bias current densities

efficiency increases gradually with increasing bias current, attains a peak at 5.5 × 10^8 Am^{-2} and then gradually decreases. Hence, current density value of 5.5 × 10^8 Am^{-2} is considered as the optimum value of bias current.

Figures 7 and 8 show the admittance plots and negative resistivity plots for bias current variation from 4.5 × 10^8 Am^{-2} to 8.5 × 10^8 Am^{-2}. In Fig. 7, the admittance plot corresponding to J_2 which is 5.5 × 10^8 Am^{-2} gives the peak optimum frequency very close to the design frequency of 94 GHz which also validates the choice of the optimum current density. Figure 9 shows the variation of the peak optimum frequency and the RF power output with varying current densities i.e., the electrical control of the aforementioned RF parameters. It is obvious from the plot that the two curves for peak frequency and RF output power intersect at 5.5 × 10^8 Am^{-2} which again corresponds to the design frequency of 94 GHz.

6 Simulated Results for the Optical Controlled Si IMPATT diode at 94 GHz

Tables 3 and 4 show the dc and RF parameters (under low amplitude ac signal) for various photon flux densities under dark and two optically illuminated configurations: FC (hole dominated photocurrent) and TM (electron dominated photocurrent). The

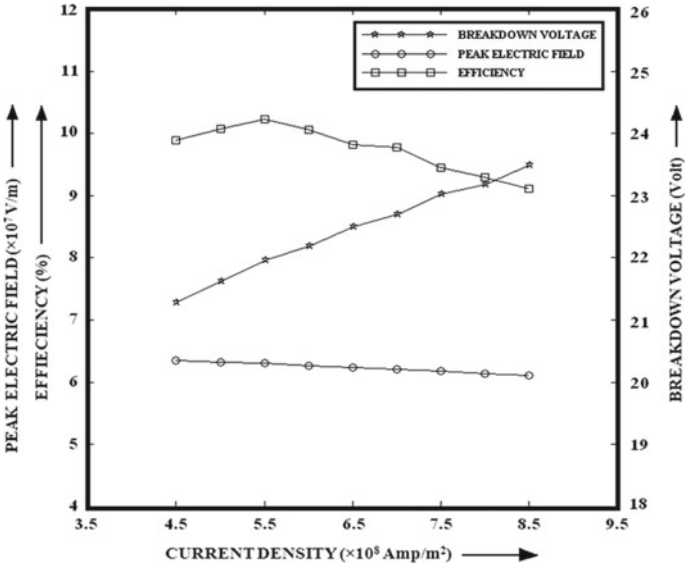

Fig. 6 Peak electric field, efficiency and breakdown voltage with bias current density

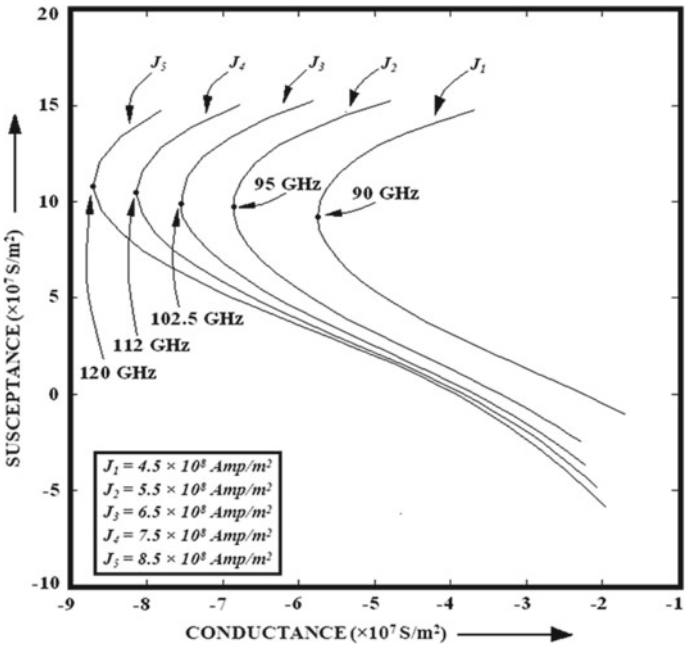

Fig. 7 Admittance plots for different bias current densities

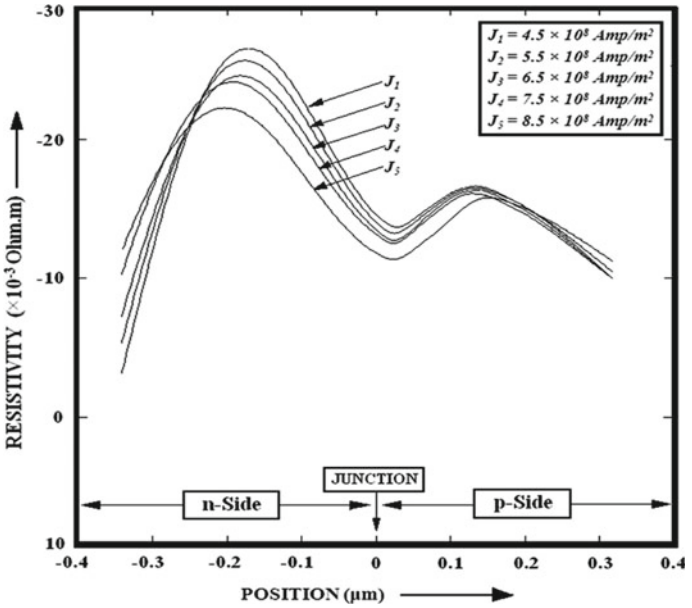

Fig. 8 Negative resistivity plots with varying bias current densities

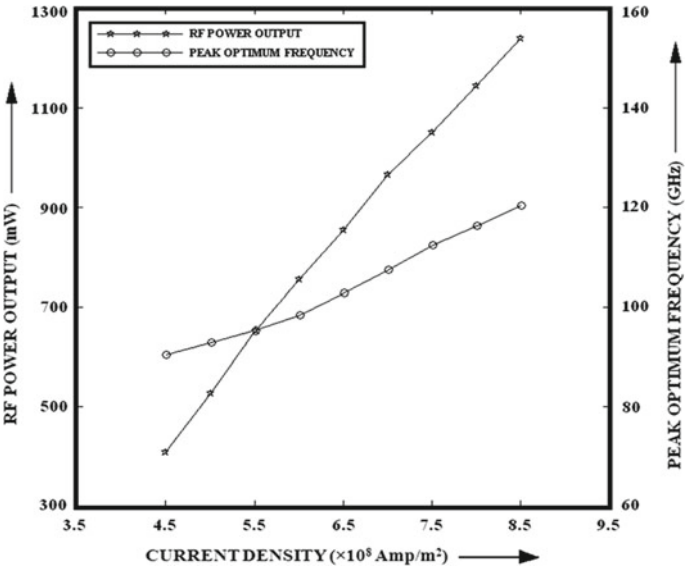

Fig. 9 Peak optimum frequency and RF power output with varying bias current densities

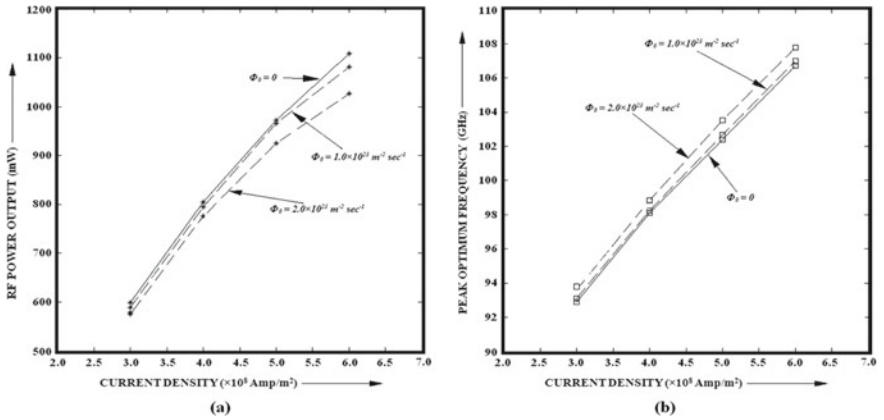

Fig. 10 Effect on the **a** RF power output and **b** peak optimum frequency for FC configuration

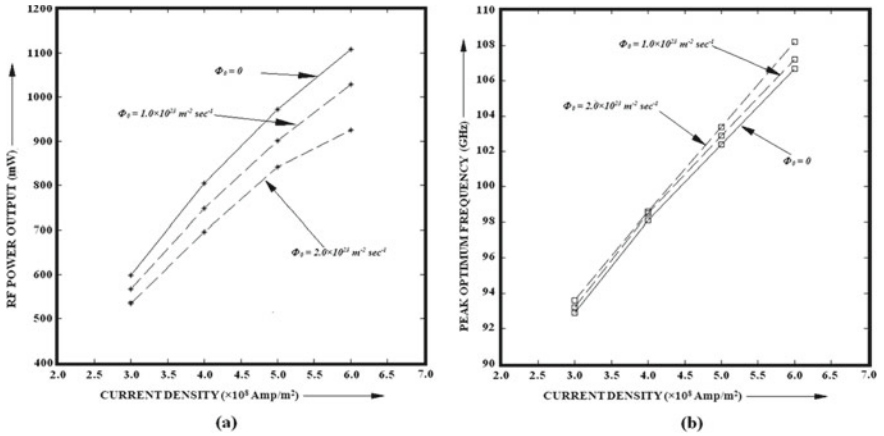

Fig. 11 Effect on the **a** RF power output and **b** peak optimum frequency for TM configuration

Table 3 DC Parameters of DDR Silicon IMPATTs under dark and two illumination configurations for different photon flux densities

Optical Illumination Conditions	$\Phi_0(\lambda)$ ($\times 10^{23}$ m^{-2} s^{-1}) (λ = 400 nm)	$I_{ns(opt)}$ (mA)	$I_{ps(opt)}$ (mA)	BIAS current density (J_0 = 3.0 × 10^8 Amp/m^2)		
				ξ_m ($\times 10^7$ V/m)	V_B (Volt)	η (%)
Dark	0	0	0	6.4178	20.63	9.41
Hole dominated photo current	1	0	1.3453	6.4078	20.51	9.53
	2	0	2.6406	6.3778	20.39	9.42
Electron dominated photo current	1	4.3692	0	6.3818	20.46	9.17
	2	8.9583	0	6.3709	20.34	8.83

Table 4 Small-signal parameters of DDR silicon IMPATTs under dark and two illumination configurations for different photon flux densities

Optical illumination conditions	$\Phi_0(\lambda)$ ($\times 10^{23}$ m^{-2} s^{-1}) ($\lambda = 400$ nm)	Bias current density ($J_0 = 3.0 \times 10^8$ Amp/m^2)				
		f_p (GHz)	G_p ($\times 10^7$ S/m^2)	$Q_p = (-B_p/G_p)$	Z_R ($\times 10^{-8}$ Ω m^2)	P_{RF} (mW)
Dark	0	93.00	−6.5783	1.69	−0.3954	586.3
Hole dominated photo current	1	93.15	−6.5187	1.70	−0.3937	577.3
	2	93.50	−6.5175	1.72	−0.3881	562.7
Electron dominated photo current	1	93.29	−6.5371	1.72	−0.3906	554.5
	2	93.77	−6.4153	1.74	−0.3870	521.6

same results are shown graphically in Figs. 10, 11, 12 and 13. End results are rather more conspicuous for TM configuration where the photocurrent is dominated by electrons. Tables 3 and 4 show that the efficiency and RF power are more in the dark condition but for illuminated conditions the results are more pronounced for the TM structure as compared to the FC structure. Figures 10 and 11 show the effect of optical energy on the peak optimum frequency and the RF power obtained at the output for FC and TM configurations respectively. It is quite clear from the aforementioned plots that the graphs for different photon flux densities show more prominent effects for TM as compared to FC structure. Another important observation is that RF power gets reduced when optical energy is incident over the device which can be utilized in phased array radars and optoelectronic integrated circuits etc. Figures 12 and 13 show the effect of incident light on the admittance plots and negative resistivity plots respectively for FC and TM configurations. The observation is quite similar to the

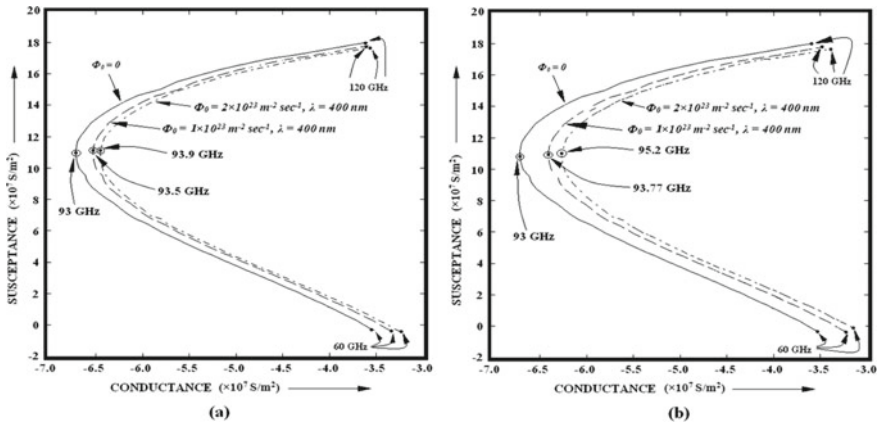

Fig. 12 Admittance characteristics for **a** FC (hole dominated photocurrent) and **b** TM (electron dominated photocurrent)

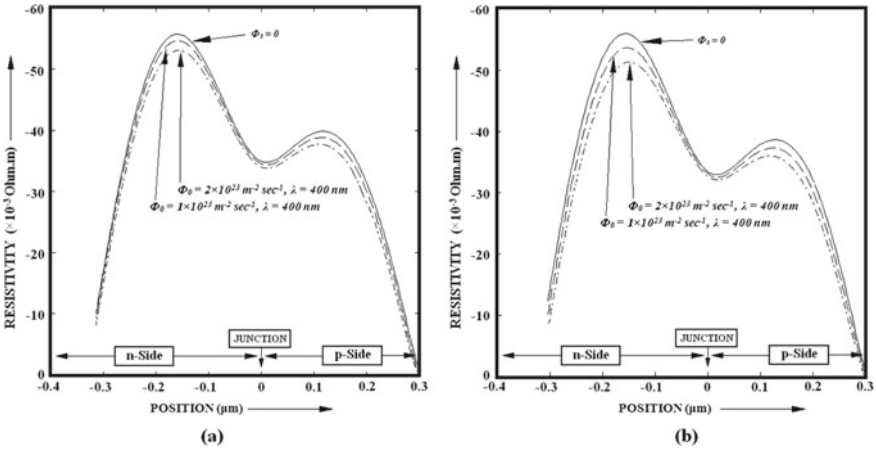

Fig. 13 Negative resistivity characteristics for **a** FC (hole dominated photocurrent) and **b** TM (electron dominated photocurrent)

previous observations i.e., the effect of optical energy is rather more conspicuous for TM configuration where the photocurrent is dominated by electrons as compared to FC configuration where the photocurrent is dominated by holes. The admittance plots also show frequency chirping i.e., there is a slight deviation of peak optimum frequency from the designed value of frequency.

7 Conclusion

The dc and RF properties of Si IMPATT diode are compared under dark and illuminated conditions at 94 GHz. The device is used in two modes: (i) FC producing hole dominated photocurrent and (ii) TM producing electron dominated photocurrent. Optical control furnishes the device with an additional control terminal over electrical control. Electrical control provides frequency tuning and power enhancement of the device by varying the input bias current density while optical control provides power reduction. This reduction of power occurs due to faster buildup of avalanche current pulse which decreases the avalanche phase delay under the effect of incident optical energy. This crucial observation can be exploited in various applications like phased array radars, optoelectronic integrated circuits and high frequency signal processing systems. In the first instance, current density is varied from 4.5×10^8 Am^{-2} to 8.5×10^8 Am^{-2} to provide bias current optimization at the window frequency of 94 GHz in the W-band. The optimized value of current density is that at which the conversion efficiency and power output is maximum. For optical illumination, two configurations of the double drift region (DDR) ATT device are taken: Flip Chip (FC) and Top Mount (TM) and their behaviors are compared for different photon flux

densities near bandgap absorption of Si which is nearly 1.1 μ. A relation is obtained between the electron and hole current density of the device and the photon flux on it using an analytical model. End results reveal RF power and efficiency reduction in optically controlled FC or TM structures as compared with the un-illuminated device which is electrically controlled. An interesting observation is frequency shift in the admittance characteristics which is utilized in frequency modulation and its applications. Effects of optical irradiation are noteworthy for TM configuration with respect to FC configuration. So, TM configuration of vertical DDR Si IMPATT device is better to use over FC configuration to obtain more perceivable effects of optical interaction of the RF properties of the device. These outcomes will be of immense favor to researchers and fabricators to continue further research on the optical modulation of RF characteristics and realize the suitable configuration of the device in the real world scenario.

References

1. S.K. Roy, Transit time device, in *Encyclopaedia of Electron Devices*, vol. 24, ed. by J.G. Webster (Wiley, New York 1999)
2. J.P. Banerjee, J.F. Luy, F. Schaffler, Comparison of theoretical and experimental 60 GHz silicon Impatt diode performance. Electron. Lett. (UK) **27**(12), 1049–1051 (1991)
3. T.A. Midford, R.L. Bernick, Millimeter wave CW IMPATT diodes and oscillators. IEEE Trans. Microwave Theory Tech. **27**(5), 483–492 (1979)
4. A. Acharyya, M. Mukherjee, J.P. Banerjee, Studies on the millimeter-wave performance of MITATTs from avalanche transit time phase delay, in *IEEE Applied Electromagnetics Conference 2011*. Kolkata (India), December 18–22, 2011
5. A. Acharyya, M. Mukherjee, J.P. Banerjee, Influence of tunnel current on DC and dynamic properties of silicon based terahertz IMPATT source. Terahertz Sci. Technol. **4**(1), 26–41 (2011)
6. A. Acharyya, J.P. Banerjee, Potentiality of IMPATT devices as terahertz source: an avalanche response time based approach to determine the upper cut-off frequency limits. IETE J. Res. Accepted, to be published March-April (2013)
7. H.P. Vyas, R.J. Gutmann, J.M. Borrego, Leakage current enhancement in IMPATT oscillator by photoexcitation. Eletron. Lett. **13**, 189–190 (1977)
8. H.W. Yen, M.K. Barnoski, R.G. Hunsperger, R.T. Melville, Switching of GaAs IMPATT diode oscillator by optical illumination. Appl. Phys. Lett. **31**, 120 (1977)
9. A. Schweighart, H.P. Vyas, J.M. Borrego, R.J. Gutmann, Avalanche diode structure suitable for microwave-optical interaction. Solid-Sate Electron. **21**, 1119–1121 (1978)
10. J.R. Forrest, A.J. Seeds, Optical injection locking of impatt oscillators. Electron. Lett. **14**(19), 626–627 (1978)
11. H.K. Gummel, J.L. Blue, A small-signal theory of avalanche noise in IMPATT diodes. IEEE Trans. Electron Devices **14**(9), 569–580 (1967)
12. G.N. Dash, J.K. Mishra, A.K. Panda, Noise in mixed tunneling avalanche transit time (MITATT) diodes. Solid-State Electron. **39**(10), 1473–1479 (1996)
13. S.K. Roy, M. Sridharan, R. Ghosh, B.B. Pal. Computer methods for the dc field and carrier current profiles in impattdevices starting from the field extremum in the depletion layer, in *Proceedings of NASECODE-I Conference on Numerical Analysis of Semiconductor Devices* (Boole Press, Dublin, 1979), p. 266
14. S.K. Roy, J.P. Banerjee, S.P. Pati, A computer analysis of the distribution of high frequency negative resistance in thedepletion layers of Impatt diodes, in *Proceedings of NASECODE-IV*

Conference on Numerical Analysis of Semiconductor Devices (Boole Press, Dublin, 1985), p. 494
15. T.K. Pal, J.V. Prasad, J.P. Banerjee, Study of various tuning properties and injection locking of resonant-cap IMPATT oscillator. Int. J. Eng. Technol. **2**(5), 329–335 (2010)
16. I.J. Bahl, P. Bhartia, *Microstrip Antennas* (Artech House, Dedham, 1980)
17. A.G. Derneryd, Analysis of microstrip disc antenna elements, in *IEEE Trans. on Antennas and Propagation*, vol. AP-27 (1979), p. 660
18. J. Watkins, Circular resonant structures in microstrip. Electron. Lett. **5**, 524 (1969)
19. C. Dalle, P.A. Rolland, Drift-diffusion versus energy model for millimetre-wave IMPATT diodes modelling. Int. J. Numer. Model. Electron. Networks Devices Fields **2**, 61–73 (1989)
20. S.K. Roy, M. Sridharan, R. Ghosh, B.B. Pal, Computer method for the dc field and carrier current profiles in the IMPATT device starting from the field extremum in the depletion layer, in Proceedings of the 1st Conference on Numerical Analysis of Semiconductor Devices (NASECODE I), ed. By J.H. Miller (Dublin, Ireland, 1979), pp. 266–274
21. H.P. Vyas, R.J. Gutmann, J.M. Borrego, Effect of hole versus electron photocurrent on microwave-optical interactions in impatt oscillators. IEEE Trans. Electron Devices **26**(3), 232–234 (1979)
22. A. Acharyya, J.P. Banerjee, A comparative study on the effect of optical illumination on $Si_{1-x}Ge_x$ and Si based DDR IMPATT diodes at W-band. Iran. J. Electr. Electron. Eng. **7**(3), 179–189 (2011)
23. "Electronic Archive: New Semiconductor Materials, Characteristics and Properties," http://www.ioffe.ru/SVA/NSM/Semicond
24. D.A. Neamen, *Semiconductor Physics and Devices* (The McGraw Hill Companies, 2007), p. 606